Dissertation
submitted to the
Combined Faculty for Natural Sciences and Mathematics
of Heidelberg University, Germany
for the degree of
Doctor of Natural Sciences

put forward by
Justin Albert Grewe
born in Hannover
Oral examination: 29.07.2020

Modeling the interplay of mechanics and self-assembly in the actin cytoskeleton

Referees: Prof. Dr. Ulrich Schwarz
Prof. Dr. Rasmus Schröder

Physikalische Modelle für das Zusammenspiel von Mechanik und Selbstassemblierung im Aktin Zytoskelett

Viele zelluläre Prozesse wie Zellmigration oder Zellteilung erfordern einen Kompromiss aus struktureller Stabilität und dynamischer Reorganisation der belasteten Elemente. Für tierische Zellen hat das Aktinzytoskelett diese Funktion entwickelt, allerdings fehlt es am physikalischem Verständnis des Zusammenspiels von mechanischen Prozessen und Selbstassemblierung. Hier modelliere ich zwei paradigmatische Situationen dieser Art. Zuerst untersuche ich die Selbstassemblierung von Nichtmuskel Myosin II Minifilamenten, besonders im Hinblick auf stochastische Effekte, die aufgrund der kleinen Systemgröße von ca. 30 tragenden Elementen auftreten, die zugleich dynamisch ausgetauscht werden und Kraft generieren. Das Selbstassemblierungsmodell beruht auf einer Konsensarchitektur, wodurch es die geometrischen Nachbarschaftsbeziehungen der Myosin II Monomere mit Bindungsenergien zwischen ihnen in Beziehung setzt. Es zeigt sich durch Simulation der Master-Gleichung des Systems, sowie durch eine Mean-Field Theorie, die die komplexe Assemblierungsstruktur mit einem Monomer Additionsschema in Beziehung setzt, dass der Austausch von Monomeren vom mechanochemischen Querbrückenzyklus abhängt. In einem rheologischen Rahmen charakterisiere ich die verschiedenen mechanischen Eigenschaften von Nichtmuskel Myosin II Minifilamenten, die aufgrund der Unterschiede in den Querbrückenzyklen der verschiedenen Myosin II Isoformen auftreten, die in Heterofilamenten koassemblieren können. Die frequenzabhängige mechanische Antwort kann durch den komplexen Modulus eines Maxwell Elements beschrieben werden und zeigt einen Übergang von viskosem zu elastischem Verhalten durch Erhöhung des Anteils der langsamen Isoform eines gemischten Ensembles. Danach untersuche ich die dynamische Stabilität einer peripheren Stressfaser, in Abhängigkeit des Zusammenspiels von Myosin II Minifilamenten, Polymerisation von neuen Aktinfilamenten an beiden Enden der Stressfaser und kortikaler Spannung. Zusammen mit Experimentatoren, konnten wir zeigen wie sich die Zusammensetzung der Stressfaser aus den verschiedenen Isoformen von Nichtmuskel Myosin II im Phänotyp der Stressfaser widerspiegelt und konnten die Position im Stabilitätsphasendiagramm der Stressfaser darstellen. Diese Ergebnisse zeigen quantitativ wie mechanische Prozesse und Selbstassemblierung auf verschiedenen Skalen im Aktinzytoskelett interagieren.

Modeling the interplay of mechanics and self-assembly in the actin cytoskeleton

Many cellular processes such as cell migration or division require a trade-off between structural integrity and dynamic reorganization of the load-bearing elements. The actin cytoskeleton has evolved to provide this function for animal cells, but a physical understanding of the interplay between its mechanics and self-assembly is missing. Here I model theoretically two paradigmatic situations of this kind. First, I consider the self-assembly of non-muscle myosin II minifilaments, with a special focus on the stochastic effects that arise due to the small system size of around 30 load bearing elements that turn-over simultaneously to producing contractile force. The self-assembly model follows a consensus architecture, thereby relating the geometrical neighborhood relations of the myosin II monomers with associated binding energies. I find that the turn-over of monomers depends on the mechanochemistry of the cross-bridge cycle by simulating the associated master equation explicitly and by a mean-field approach that maps the complex assembly structure to a simple monomer-addition scheme. Using a rheological framework, I characterize the distinct mechanical properties of non-muscle myosin II minifilaments that arise due to differences in the cross-bridge cycle of the different myosin II isoforms, that can co-assemble in one hetero-filament. Quantitative analysis of the frequency dependent response by a complex modulus, reveals a cross over from viscous to elastic behavior as the ratio of slow to fast isoforms working together is increased. Second I consider the dynamical stability of a peripheral stress fiber, that depends on the interplay of contraction by myosin II minifilaments, self-assembly of new actin filaments at both ends of the fiber and cortical tension. In collaboration with an experimental group, we could show how the myosin II isoform content is differentially reflected by the phenotype of peripheral stress fibers and show their position in a stability phase diagram of the stress fiber. These results demonstrate quantitatively how mechanics and self-assembly interact on different scales in the actin cytoskeleton.

Contents

1. Introduction **1**

2. Mechanics and self-assembly in the actin cytoskeleton **5**
- 2.1. The cytoskeleton . . . 5
  - 2.1.1. The three filament systems . . . 5
  - 2.1.2. Molecular motors . . . 9
  - 2.1.3. Myosin II . . . 12
- 2.2. Theoretical concepts . . . 19
  - 2.2.1. Master equation . . . 19
  - 2.2.2. Self-assembly and chemical rate-equations . . . 21
  - 2.2.3. Linear viscoelasticity . . . 23
- 2.3. Experimental techniques . . . 26
  - 2.3.1. Micropatterning on two-dimensional substrates . . . 27
  - 2.3.2. Fluorescence recovery after photobleaching . . . 28
  - 2.3.3. Microrheological methods . . . 30
  - 2.3.4. Laser cutting . . . 32

3. Becker Döring model for finite size clusters **35**
- 3.1. Introduction . . . 35
- 3.2. Model outline . . . 36
- 3.3. Ensemble dynamics near equilibrium . . . 37
  - 3.3.1. Equilibrium . . . 37
  - 3.3.2. Relaxation behavior . . . 39
- 3.4. Single cluster dynamics near equilibrium . . . 43
  - 3.4.1. Equilibrium . . . 43
  - 3.4.2. Relaxation behavior . . . 44
- 3.5. Comparison of bulk and single cluster dynamics . . . 44
- 3.6. Relation to constant total concentration case . . . 48
- 3.7. Conclusion . . . 50

4. Mechanosensitive self-assembly of myosin II minifilaments **53**
- 4.1. Introduction . . . 53
- 4.2. Models and methods . . . 56
  - 4.2.1. Minifilament organization . . . 56
  - 4.2.2. Minifilament assembly . . . 58
  - 4.2.3. Crossbridge model . . . 59
  - 4.2.4. Coupling of self-assembly and force generation . . . 61
  - 4.2.5. Mean-field theory . . . 61

4.2.6. FRAP-experiments 63
4.3. Results 63
4.3.1. Assembly dynamics 63
4.3.2. Steady state results 65
4.3.3. Comparison with experiments 68
4.4. Discussion 69

5. Rheology of mixed motor ensembles 73
5.1. Introduction 73
5.2. Mechanical setup & simulation 74
5.3. An alternative mean-field approach 81
5.4. Nonlinear behavior 82
5.5. Conclusion 87

6. Tension Viscosity Model 89
6.1. Introduction 89
6.2. Active contractile flows may control cell shape 90
6.2.1. Constant polymerization speed 92
6.2.2. Force-dependent polymerization speed 94
6.2.3. Comparison of $R(d)$ relation 96
6.3. Summary 99

7. Interplay of non-muscle myosin II isoforms in live-cells 101
7.1. Introduction 101
7.2. Phenotypical characterization of NM II-KO and NM IIB-KO cell lines 103
7.3. Quantitative analysis of NM II A/B-KO phenotypes show signatures of isoform-specific force-velocity relation 105
7.4. Isoform specific differences in turn-over depend on the crossbridge cycle 109
7.5. Discussion 116

8. Conclusion 119

A. Appendix 123
A.1. List of abbreviations 123
A.2. Supplementary figures to chapter 4 125
A.3. Supplemental material to chapter 7 128
A.3.1. Focal adhesion quantification 128
A.3.2. FRAP analysis 128
A.3.3. Balancing of Forces 128
A.3.4. FRAP simulation 130

Bibliography 130

List of publications 153

Acknowledgements **155**

1. Introduction

Self-assembly and mechanical processes are often considered to occur with no temporal overlap: First a machine is build, then it performs its work. In biology this is sometimes very different. The human, as one example for a higher developed organism, is composed of $\sim 10^{13}$ cells that, in addition to constantly having to renew, have to arrange in a very specific way for the organism to function correctly [1]. Renewal and correct arrangement – key concepts of dynamic self-assembly – in this case are critically dependent on migration of cells on deformable media, which is clearly an interesting mechanical problem. Thus, at the scale of entire organisms self-assembly and mechanics both play central roles.

On smaller length scales, biological load bearing structures are normally self-assembled from smaller constituents. On the one hand, changes within the regulation of self-assembly of these structures lead to distinct changes in mechanical behavior [2]. On the other hand, and perhaps more surprisingly, biological cells respond to changes in mechanical stresses by either reinforcing (when stress is increased) or partly dissolving their load bearing structures (when stress is decreased) [3–5]. Thus mechanical cues can lead to changes in self-assembly and vice versa. This is very reminiscent of the motor-generator duality, where from an electrical current either torque can arise or from torque an electrical current arises, and, similarly, is a sign for a feedback loop, which is an omnipresent motif in mechanobiology [6, 7]. Clearly, also at this scale there is a temporal overlap of self-assembly and arising mechanical processes, as mechanical tasks have to be performed during remodeling of the structure at hand by self-assembly.

The fact, that biological load-bearing structures are often reinforced after being stressed is a remarkable observation in itself: Standard materials we know from our typical environment either bend, deform or shatter when applying appreciable amounts of force to them, with self-healing properties staying reserved to the newly emerging metamaterials [8]. In the actin cytoskeleton, a network of the biopolymer actin that gives mechanical stability to biological cells, the *catch bond* is the central kinetic motif that is thought to lead to reinforcement of stressed structures [9, 10]. Both, the *slip bond* and the *catch bond* describe the force dependent stability of a receptor-ligand connection. While the slip bond more intuitively decreases its stability with increasing force, i.e. the stochastic rupturing rate of a bond increases with force, the catch bonds show an increased stability with increasing force up to a certain maximal force, where increasing the force further destabilizes the force. Accordingly, the catch bond is thought to be implemented biologically in a large array of proteins that have to function under load with examples including molecular motors such as non-muscle myosin II or the bacterial flagellar motor [5, 9] and network-crosslinkers such as α-actinin [9].

This thesis models phenomena involving concurrent self-assembly and force-generation with a strong focus on the role of myosin II in the actin cytoskeleton. Dependent on the size of the system studied, modeling approaches either take into account the stochastic nature of molecular processes such as the assembly of single myosin II minifilaments which are mechanically active structures formed from ~ 30 monomers, or they neglect them in the case of stress fibers, actin bundles containing many minifilaments and being constructed from a huge amount actin monomers.

Outline

Chapter 2 lays down the biological and theoretical background providing the basis of the following chapters. After introducing the cytoskeleton, an interacting network of dynamically self-assembling polymers, many facets of myosin II molecular motors are described. Following this, theoretical concepts important to the work are introduced. Finally, some experimental methods, that probe assembly and mechanics are highlighted.

Chapter 3 discusses a classical approach to self-assembly, a modified version of the Becker-Döring system. Here the dynamics of growth of a complex with a distinct maximum size, that grows or shrinks by adding or subtracting monomers is described by chemical rate equations. After outlining the equilibrium behavior of the model, I follow a perturbative approach to approximate timescales relevant to the relaxation to equilibrium and finally compare to numerical results. The central result of this chapter is that of self-assembly processes slow down near a critical monomer concentration, the critical aggregation concentration (CAC).

Chapter 4 introduces a model for force-dependent self-assembly of myosin II minifilaments. A stochastic assembly model that builds upon a consensus architecture of myosin II minifilaments and bond energies neighboring monomers is coupled to a stochastic crossbridge model in order to study the interplay of mechanics and self-assembly at the small scale of minifilaments. Similar to the previous chapter, there is a critical monomer concentration where assembly dynamics slows down. This concentration depends the availability of actin and force and shows that force can facilitate assembly. The model introduced here is also used to simulate fluorescence recovery after photobleaching (FRAP) experiments as a means to show agreement with experimental results.

Chapter 5 describes the response of an ensemble of slow and fast myosin II molecular motors to an oscillatory force in a rheological framework. The combination of short term resistance to deformation and long term remodeling of the actin cytoskeleton has often been connected to viscoelastic material properties. Here we show, that the mean response a crossbridge model is also viscoelastic. I further investigate the dependence of this phenomenon on the speed of the motors and the size of the system and outline arising non-linear effects.

Motivated by the previous chapter, chapter 6 introduces a dynamical self-assembly model of a contractile viscous stress fiber that is subject to a normal force. The deterministic model describes the length change introduced by motor contraction and disassembly in the center of the stress fiber and self-assembly of additional cytoskeletal material at the boundary points. By searching for stable solutions one finds a correlation between spanning distance and radius of curvature of the fiber that is dependent on the motor properties.

Chapter 7 describes collaborative work with experimentalists. We investigate cells with deficiencies in the slow and fast non-muscle myosin II (NM II) isoforms respectively. Using phenotypical characterization and the model introduced in the previous chapter we consistently connect the experimental observations with the known motor properties of the two isoforms. FRAP experiments also reveal a dynamic turnover in myosin minifilaments that is dependent on the force generating crossbridge cycle as suggested by the model introduced in chapter 4.

Finally, chapter 8 concludes and summarizes the work done in this thesis and offers some future perspectives.

2. Mechanics and self-assembly in the actin cytoskeleton

2.1. The cytoskeleton

In order to function correctly cells must be able to mechanically interact with their environment and each other. Often it is crucial, that they maintain and control their shape and position in space in some way. All cells however must be able to reorder their inner constituents, when they grow, divide or have to adapt to changes in their environment. The very dynamic mechanical stability needed for this is provided by a system of filaments called the cytoskeleton [11]. The cytoskeleton performs its various tasks by utilizing three filament subsystems: *actin filaments*, *microtubules* and *intermediate filaments*. Each filament system has its characteristic mechanical traits and biological function, however typically all three are required for providing the cell with its shape, mobility and stability. Here we introduce all three filament families briefly, but later discuss mainly the *actin filaments* since the focus of this thesis lies on contraction of actin filaments by myosin II motors and related phenomena.

2.1.1. The three filament systems

The three biological filament types occuring in eucaryotic cells by their mechanics all qualify as semi-flexible polymers that are very resistant to stretch. Semi-flexible polymers can be described by the worm-like chain model which from comparing the bending rigidity of a flexible rod to the thermal energy predicts a length scale, the so called persistence length, along which these filaments are relatively straight in a thermal environment [12]

$$l_p = \frac{EI}{k_B T}, \tag{2.1}$$

where E is the Young's modulus, I is the geometric moment and $k_B T$ is the thermal energy. Eq. (2.1) can already give an intuition about the typical behavior: Thick or short filaments will be straight, while long or thin filaments will buckle under

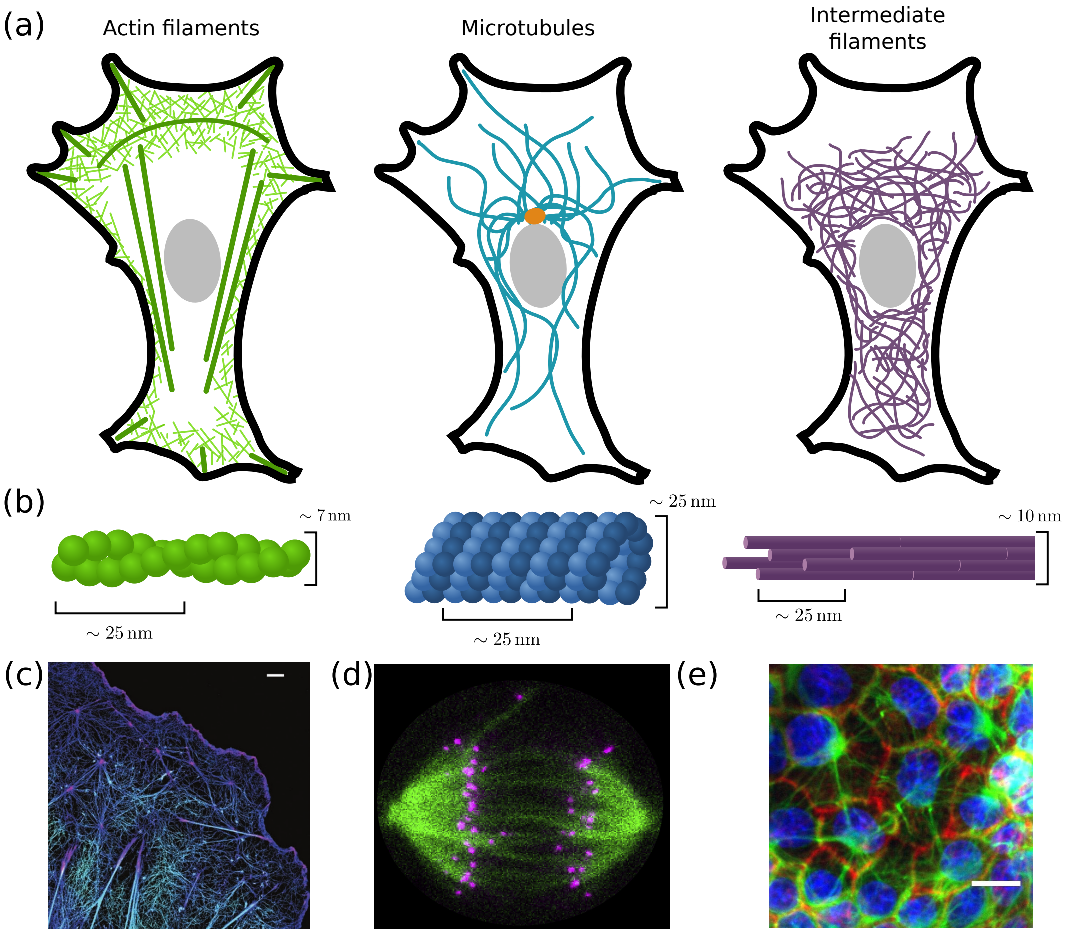

Figure 2.1.: Three types of filaments with different traits make up the cytoskeleton. (a) Schematic drawing of the localization and qualitative organization of actin filaments (left), microtubules with the centrosome in orange (center) and intermediate filaments (right). (b) Close-up cartoon of the three different filaments with typical length scales. (c) STORM microscopy image of the ventral actin fibers. (d) In cell mitosis the kinetochores (pink) are pulled apart by an assembly of microtubules (green). (e) Intermediate filaments (green) can stabilize cells are strained. In this case they become straight. Adapted from [13–16].

thermal fluctuations if they are longer than their persistence length. The overall mechanical properties of the cytoskeleton of course do not only depend on the filaments themselves but also on associated proteins, that crosslink filaments, seed polymerization of new filaments, disassemble or contract filaments. Each filament system has its own specialized proteins that are able to perform these tasks on the specific filament. There are of course also proteins that mediate interactions between two different filament families [13] by e.g. crosslinking them with each other. Fig. 2.1

shows a schematic of the typical organization of the three different filaments alongside a sketch of their appearance on the nano-scale and exemplary microscopy images of the filament systems in distinct situations where they are vital.

Actin filaments Actin filaments are double-stranded helical polymers with a diameter of $\sim 7\,\mathrm{nm}$ (see Fig. 2.1(b)) that have a persistence length of $l_p \approx 15\,\mu\mathrm{m}$, made of the globular protein G-actin [12]. They also show a sense of directionality, i.e. they are *polar*, which stems from the asymmetry in G-actin. This is apparent from their fast and slow growing end which are called their plus or barbed end and their minus or pointed end respectively. It is this polarity, that enables the molecular motor myosin, that walks along actin filaments, to give rise to directed motion. Typically myosins walk form the pointed to the barbed end. So far only one exeption to this rule has been found, myosin VI [17, 18].

In the cytoskeleton actin filaments occur in many different supramolecular organizations, that are determined from the actin associated proteins that interact with

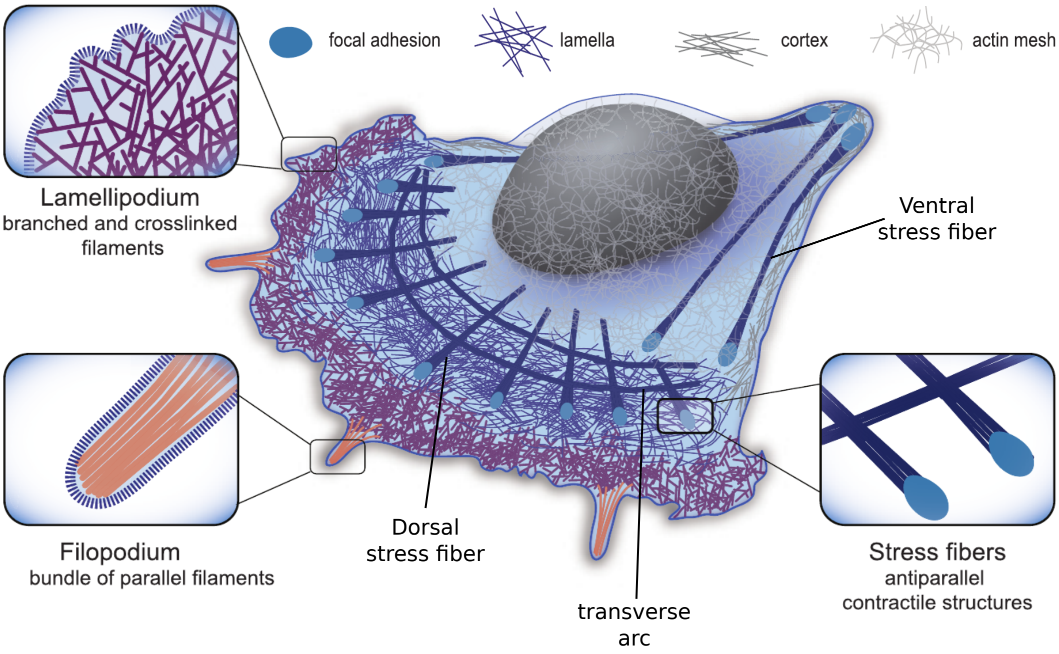

Figure 2.2.: The actin cytoskeleton. Actin together with associated proteins forms very diverse structures. Examples include filopodia, bundeled parallel actin filaments forming fingerlike cell protrusions, lamellipodia, branched networks, driving the advancement of the leading edge of the cell, the cortex, a crosslinked network stabilizing the plasmamembrane and stress fibers, contractile actin bundles powered by myosin. Adapted from [19].

any given actin structure such as cross linkers (e.g. α-actinin), polymerization agents (e.g. formins) and molecular motors (e.g. myosin) [11]. The spatial organization of these actin structures is shown in Fig. 2.2. In the cell periphery Arp2/3-dependent branched networks push forward the plasma membrane of a migrating cell by polymerizing against it. This structure is called the lamellipodium and defines the leading edge of migrating cells. At the leading edge also filopodia emerge. These are bundles of parallel actin filaments that form fingerlike protrusions in the plasma membrane. Also in the periphery, crosslinked contractile networks, the actin cortex, stabilize the fragile plasma membrane against mechanical perturbations from the environment. In the center so called stress fibers form, which can be categorized into four groups from the front to the back of the cell: dorsal stress fibers, transverse arcs, ventral stress fibers and the perinuclear actin cap [20]. Dorsal stress fibers are anchored to focal adhesions, that mediate interactions between the cell and the extracellular matrix, at one side. They are not contractile [21] but connect to the transverse arcs that are contractile but are not anchored to focal adhesions. Instead, the contraction of the transverse arcs leads to the flat phenotype of the lamellum. This occurs as the focal adhesions of the dorsal stress fiber attaches to acts as a fulcrum[21, 22]. Ventral stress fibers, that are situated at the rear of the cell are contractile and are considered to be the strongest with typical forces of 10 nN they apply to the extra cellular matrix (ECM) via the focal adhesions they are anchored to on both sides[23, 24]. In addition to mechanical sensing and signaling, they also pull the trailing edge of the cell forward during cell migration. Fig. 2.1(c) shows a super resolution microscopy image highlighting the different organizations of actin filaments coexisting in the ventral cytoskeleton of a cultured cell adhering to a glass slide. One can clearly discern the highly crosslinked and disordered cortical actin network from the relatively long straight and thick actin stress fibers.

Microtubules Microtubules are stiff tubular filaments with a thickness of $\approx 25\,\mathrm{nm}$ and a much longer persistence length than actin filaments of $l_p \approx 3\,\mathrm{mm}$ [12]. They are made up of 13 protofilaments that are helically arranged around a hollow core and themselves polymerize from a dimer of α- and β-tubulin as illustrated in Fig. 2.1(b). The asymmetry in the tubulin dimer also leads to a polarity of the microtubules which – as with actin filaments – enables the molecular motors kinesin and dynein walking on microtubules to sense their direction. Kinesins typically walk towards the plus-end of the microtubule, which is typically located in the periphery of the cell, while dyneins walk in the other direction, typically towards the center [25].

Similar to actin filaments there exist also so called microtubule-associated proteins that regulate polymerization, depolymerization and the organization of microtubules.

Key players in this regard are the microtubule-organizing centers, from where microtubules can spread throughout the cell in an aster-like fashion. Mammalian cells have one microtubule-organizing center called the centrosome, which is located near the nucleus [11]. The typical organization is sketched in Fig. 2.1(a).

Microtubules play a central role in many key cellular processes, such as the intracellular transport of vesicles or even entire organelles [26] or splitting of the genomic information during cell divisions, which is shown in Fig. 2.1(d). Both of these processes require molecular motors.

Intermediate filaments Intermediate filaments are a diverse family of many different proteins that have been lumped together into one class. These different proteins are expressed in a cell-type specific manner [11]. In stark contrast to actin and microtubules the monomers are elongated proteins that are also non-polar, which implies that there should not be able to act as tracks for translational molecular motors [27]. By a hierarchical self-assembly the monomers, e.g. keratins or vimentins, of a typical thickness of 2 nm and a length of ~ 50 nm, form rope like filaments of thickness ~ 10 nm, as sketched in Fig. 2.1(b) [28]. The mechanism by which they provide tear strength to cells has been investigated in detail. In essence, the monomers contain domains that unfold upon being stretched. The mechanical response to force naturally depends on the type of intermediate filament and has been found to depend on differences in lateral coupling of subunits to each other in vimentin and keratin fibers [29]. Fig. 2.1(e) shows the tear strength inducing process in action in Madison-Darby Canine Kidney cells. Here, the intermediate filaments that are normally quite disordered as sketched in Fig. 2.1(a)

are loaded and become straight as the cell is strained to a multiple of its typical area [16].

2.1.2. Molecular motors

In this section different molecular motors are classified by the type of movement they generate. What all molecular motors have in common is, that they use useful energy, i.e. non-thermal energy, that is typically stored as chemical energy, in order to move different objects in a directed manner. The two archetypal storage forms utilized by cells are the chemical compound adenosine triphosphate (ATP), which can be hydrolyzed to adenosine diphosphate (ADP) and phosphate at an energy gain, and concentration gradients of ions. The three different molecular motors types introduced here are shown in Fig. 2.3: *Cargo motors*, that typically move biomolecules enclosed in a vesicle to their target location, *filament translation motors*, that move their respective tracks against each other, and *rotary motors*, that act to

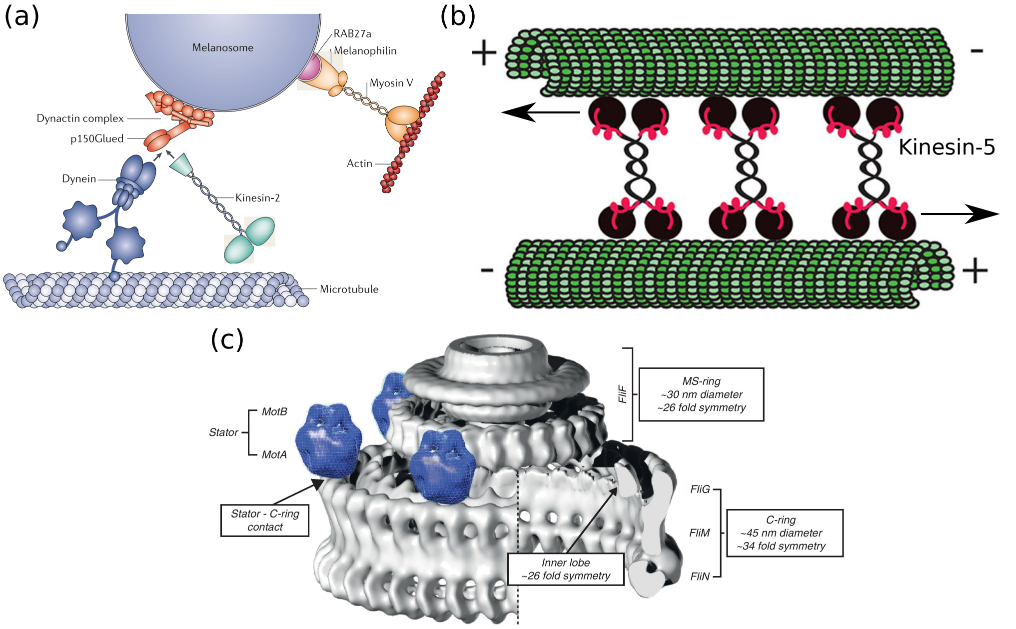

Figure 2.3.: Three different motor classes by type of action. (a) Three different cargo motors: The microtubule motors kinesin-2 and dynein and the actin motor myosin V. These can connect to vesicles, that enclose cargo and transport it along their respective filament tracks. (b) Filament translation motors: Kinesin-5 translocates microtubules by walking towards the plus end of the microtubules with both of its head groups and thereby pushes the minus ends of the microtubules appart from each other. (c) Rotary motors: The bacterial flagellar motor, a large complex that is mechanically fixed to the cell wall of bacteria, rotates the flagellum in order to propel the bacterium. Adapted from [30–32].

rotate a central structure around its axis in order to e.g. generate a hydrodynamic flow.

Another overarching theme in molecular motors is the fact that they move in a stepwise fashion, with each step being tightly connected to a discrete amount of fuel used – be it one hydrolyzed ATP or the movement of a set amount of molecules down the concentration gradient.

Cargo motors Cargo motors move vesicles along their respective substrate track into a preferred direction. There are two big families of molecular motors moving on microtubules: the kinesin and the dynein family [11]. While kinesins typically walk towards the plus end of the microtubules, dyneins walk towards the minus end. Together with the location of the centrosome this means, that kinesins (with few exceptions) transport cargo towards the periphery of the cell while dyneins transport cargo towards the nucleus of the cell. Cargo motors are not exclusive to microtubules as the myosin family provides several motors that perform this action. Myosin V is a very universal example for such a motor, that moves its cargo by processively walking along the actin filaments, i.e. at least one head is bound to actin at each point in time [33], with $\sim 36\,\mathrm{nm}$ steps and generating a maximum force of $\sim 3.6\,\mathrm{pN}$ when both heads are bound to actin. The melanosome is a well studied model system in which motors of all three families of cargo motors mentioned here work together in concert with a variety of regulatory proteins to control the pigmentation of our skin [32] (see Fig. 2.3(a)).

Filament translation motors Filament translation motors are arguably a type of cargo motor, their cargo are however cytoskeletal filaments themselves. Thereby they play a central role in the morphology and mechanical properties of the filament network they are connected to. The most prominent example of this sort of motor is myosin II, which is responsible for the contraction in muscle cells and also for the – albeit much smaller – contractile forces in platelets or fibroblasts [34, 35]. There are also microtubule based filament translation motors, one example being kinesin-5, which plays a vital role in cell division, as it pushes the duplicate genomic information apart by moving its heads towards the plus direction of two anti-parallely arranged microtubules [31] (see Fig. 2.3(b)). While both of these two systems slide filaments against each other one might ask, why in the microtubule system the sliding leads to pushing two objects apart, while in the actin system this leads exclusively to contraction. The reason for the difference has been found to lie fundamentally in the fact that the persistence length of microtubules is much larger than the persistence length of actin filaments. This leads to actin filaments buckling more easily under pushing forces. In an initially disordered network of crosslinked actin filaments this leads to a selection of actin filaments bearing contractile load and to an overall contraction by severing actin filaments that buckle under compressive forces [36–39]. This effect does not occur in the much more rigid microtubules.

Rotary motors Contrary to the previously presented motor classes, where the direction of movement was linear along a polymer track, these motors rotate subdomains of proteins or larger structures as flagella around a stationary axis as in the ATP synthase or the flagellar motor respectively [12]. These are the two main examples of rotary motors.

The ATP synthase that produces ATP actually consists of two distinct rotary motors, the so called F_0 and F_1 motor. The F_0 motor utilizes a concentration transmembrane gradient in hydrogen ions in order to rotate. The F_1 motor rotates in the opposite direction via ATP hydrolysis. In typical conditions the torque produced by the F_0 motor surpasses the torque of the F_1 motor, which forces the F_1 to rotate in reverse, which produces ATP. If the driving force, i.e. the transmembrane gradient, is weak however, ATP is hydrolyzed in order to pump hydrogen ions against their concentration gradient [12].

The flagellar motor shown in Fig. 2.3(c) is similar to the F_0 motor as it also uses a hydrogen ion transmembrane gradient to power a rotation. It is tightly fixed in the cell wall of bacteria and rotates the flagellum to provide motility to the bacterium. The flagellar motor consists of a reasonably complex arrangement of many proteins. In particular there is the so called C-ring, that is anchored to the cell wall and the MS-ring, which is anchored to the flagellum. In between, stator units are the elements that produce the torque. They can reversibly bind to the MS-ring and it has been shown, that increasing the total torque the flagellum is leads to increases in the number of stator units bound to the MS-ring [5, 40]. This intriguing phenomenon can be interpreted as a mechanism that increases efficiency: At low torque only a low amount of stators – and thereby only a low flux of hydrogen ions, a measurement of power in this context – is needed for rotation. By dynamic self-assembly of additional stator units the torque can be increased which in turn increases the flux of hydrogen ions.

2.1.3. Myosin II

Motor proteins that travel along actin tracks are called myosins. They form a very diverse superfamily of molecular motors [17] that share a common mechanism to convert chemical energy in the form of ATP to mechanical work [42], their task within cells however differ greatly from each other. These tasks range from generation of strong contractile forces in skeletal muscles or the heart muscle (by numerous different types of myosin II [43, 44]) over length regulation of the stereocilia in hair cells (by myosin IIIa/b [45] and myosin XVa [46]) to mechanosensors (notably myosin IC in hair cells [47, 48], but also non-muscle myosin II (NM II) in migratory cells [49]). This wealth of different tasks surely comes with a wealth of different biological challenges that evolution has addressed by introducing the astonishing amount of slightly different myosin proteins. Biologists have classified these into 17 classes as the phylogenetic tree in Fig. 2.4 visualizes.

The structure of most myosins can be best described by the serial arrangement of three functional units [17]

1. the motor domain, that interacts with actin and hydrolyses ATP
2. the neck domain, that can bind additional proteins

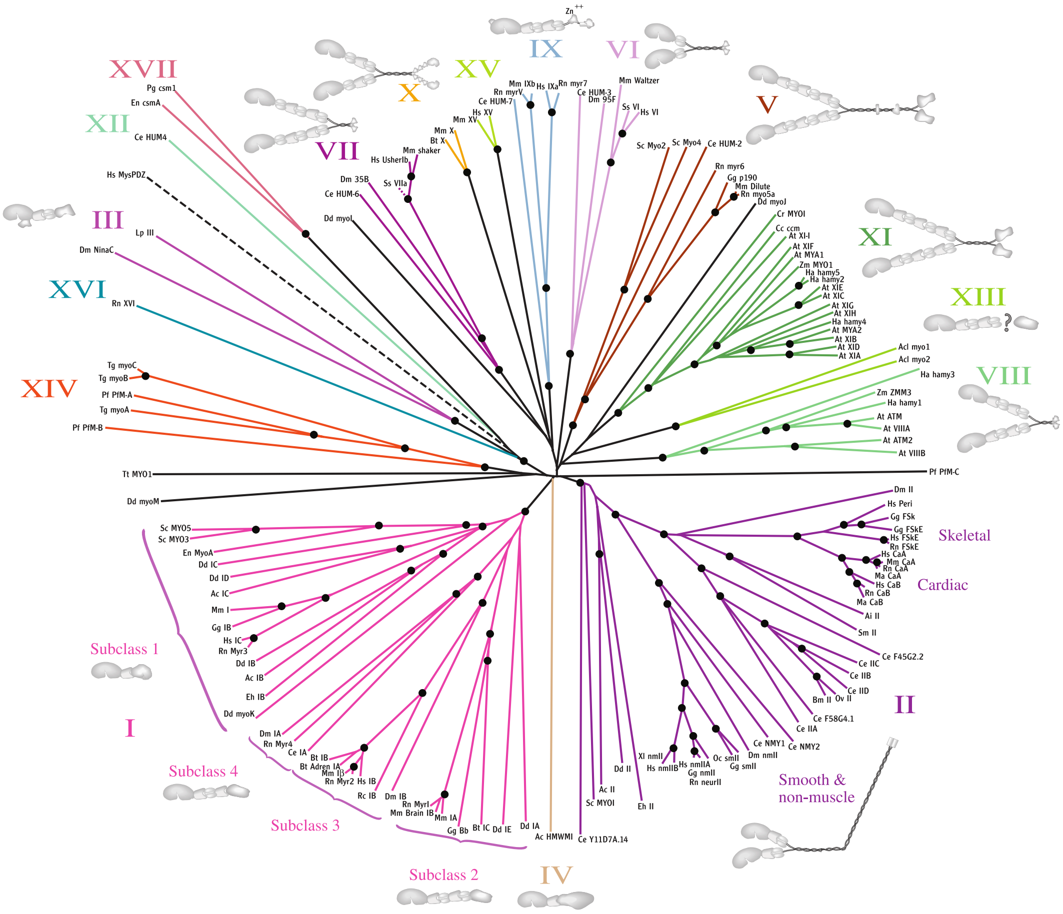

Figure 2.4.: The phylogenetic tree of myosins proteins. Depending on their construction from subdomains, myosins are classified into 17 classes. Adapted from [41].

3. the tail domain, which is meant to position the head in such a way, that it can productively interact with actin.

While the motor domains are quite well conserved, the neck domain contains different amounts of repeats the so-called IQ motiv, which leads to varying lengths of this region. The most diverse domain is the tail region, perhaps because it defines to which structures myosin can bind. In the case of myosin V – a cargo motor – clearly has to bind something different (namely vesicle adaptor proteins [50]) than myosin II which should contract actin filaments and thereby should bind to actin at two points that can travel into different directions.

Assembly In order to be able to connect and later contract two actin filaments, myosin II assembles larger structures by virtue of the long helical coiled-coil domain

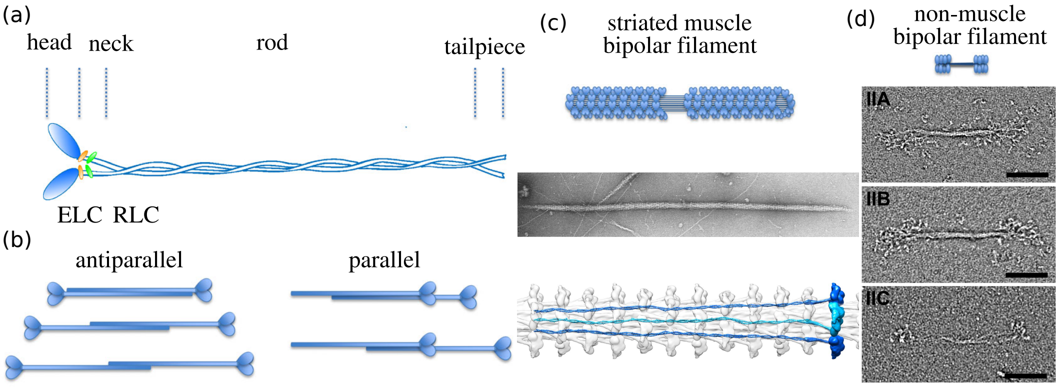

Figure 2.5.: Myosin II and its assemblies. (a) Structure of the myosin hexamer consisting of two heavy chains (blue), two ELCs (orange) and two RLCs (green). The heavy chain can be subdivided into three regions, the head, the neck and the α-helical coiled-coil rod, which ends with a non-helical tailpiece. (b) The charge distribution along the rod of myosin supports antiparallel and parallel arrangement of rods with distinct staggering. (c) Striated muscle bipolar filaments, an example for a very large myosin assembly. A schematic is shown together with an electron microscopy image of scallop thick filaments and a cryo-electron tomography of the *Lethocerus* flight muscle. (d) Non-muscle myosin bipolar filaments are an example of a small assembly of myosin II. A schematic is shown together with negative stain electron microscopy images of the three isoforms of NM II. Adapted from [51–54].

along which electrical charge is organized such, that it allows for association of additional myosin II [51, 54]. The structure of myosin II is depicted in Fig. 2.5(a). The myosin II hexamer – which is often called the *monomer*, as it can be seen as the functional unit of myosin II – is formed by two heavy chains (blue), two essential light chains (ELC) and two regulatory light chains (RLC). Myosin II monomers can associate to each other in an antiparallel and parallel fashion with distinct staggers as depicted in Fig. 2.5(b). These arise due to the charge distribution along the myosin rod [55]. Near the tailpiece there is a predominantly positively charged region, while the rest of the rod is predominantly negatively charged. Thereby this region is critical for self-assembly to occur [56]. Presumably dependent on the details of the charge distribution, which varies between isoforms [57], different higher order structures of myosin II form.

Fig. 2.5(c) shows an example for a very large and higly ordered myosin II assembly: the straited muscle bipolar filament. These are very long myosin filaments with heads splaying to the outside, that produce the high forces required for muscle contraction and the beating of our heart [11]. In the middle of the thick filament there is a bare zone, where no heads splay outwards. In the core of the thick filament the myosin rods are densely packed. Since the geometrical arrangement of the rods is of central importance for the electrostatic interaction, it was hypothesized on how the myosin rods could be packed inside the core of the filament [58] and for some species, the rod packing could be investigated experimentally in detail by electron tomography [53].

A much smaller and presumably much less ordered assembly of myosin II is depicted in Fig. 2.5(d), the NM II bipolar filament, which was first discovered in human platelets [34]. It takes a central role in many different cellular processes, such as cell division, cell adhesion, migration and the organization of the actin cytoskeleton, and is present in almost all mammalian cells [59]. It is also important in muscle cells, as in heart muscle cells non-muscle myosin takes the role of a pioneer filament, that cooperatively aligns actin filaments during maturation leading to a highly structured actin cytoskeleton in mature cells [60]. NM II occurs in three different isoforms in mammals, NM IIA, NM IIB, NM IIC. From electron microscopy of the purified protein there is no phenotypical difference between NM IIA and NM IIB. Both filaments are $\sim 300\,\mathrm{nm}$ long and the bare zone has a thickness of $\sim 12\,\mathrm{nm}$. Together with the typical thickness of the rod of $\sim 2\,\mathrm{nm}$ this indicates that there are around ~ 30 myosin monomers in one NM II filament of isoforms A or B. NM IIC filaments have a similar length, however are much thinner, consistent with less myosin heads pointing outward compared to NM IIA/B filaments (see Fig. 2.5(d))[54].

The crossbridge cycle Once assembled, bipolar myosin II filaments can perform their actual task: the contraction of actin filaments. The contraction mechanism is typically explained by a sequence of mechanochemical states of the myosin head region, based on the *crossbridge model*, which was pioneered by Huxley [61]. The crossbridge cycle – sometimes also the actomyosin ATPase cycle [62] – has been studied in great detail via dynamical experiments [63–67] together with numerous modeling studies [68–78] as well as via structural investigations [62, 79]. It is shown schematically in Fig. 2.6.

The crossbridge cycle can be summarized as follows:

- Starting from the unbound state where ATP is already hydrolyzed the myosin head binds to actin. The motor domain is now reversibly bound to actin.
- Subsequent phosphate release and movement of the lever arm lead to a movement of $\sim 5.5\,\mathrm{nm}$ along the actin fiber. This transition is often termed the first powerstroke.
- Now ADP can dissociate from the motor head and the second, shorter power-

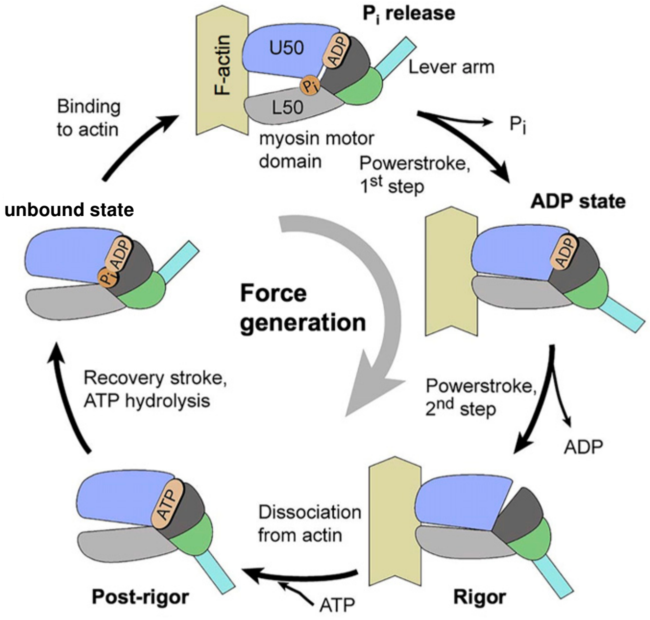

Figure 2.6: The cross-bridge cycle shows the mechanochemical states of the myosin motor domain and its subdomains while it interacts with actin. It links the ATPase chemistry with the mechanics of force generation. Modified from [62].

stroke ($\sim 2.5\,\mathrm{nm}$) is performed.

- From the so-called rigor state dissociation from actin happens as soon as fresh ATP binds to the head. In rigor mortis, it is the depleted ATP, which blocks myosin in an actin attached state, which leads to stiff muscles.
- The newly bound ATP is hydrolyzed and the lever arm returns to its original position, i.e. the recovery stroke is performed. Sometimes this transition is also called repriming of the lever arm.

Similar to the motor domain, also the crossbridge cycle is well conserved, however the transition rates and affinities highly vary, which allows for tuning myosin to perform many different functions [42]. Myosin can also perform its crossbridge cycle without actin, however in this case it is much slower [49]. For this reason myosin ist often called an actin-activated ATPase.

Regulation As most cellular processes, also the assembly and force generation of myosin II have to be regulated in space and time. In muscle cells the thick bipolar filaments come already assembled into the higher order structure of sarcomeres, highly ordered actomyosin structures with additional linking proteins. Here, regulation of contractile forces occurs primarily by a Ca^{2+}-dependent blocking of actin binding sites by tropomyosin [11], which is additionally modulated by phosphorylation of the RLC and other regulatory proteins. This additional regulation may transition motor domains of a thick filament in the super-relaxed state [80], in which myosin heads are

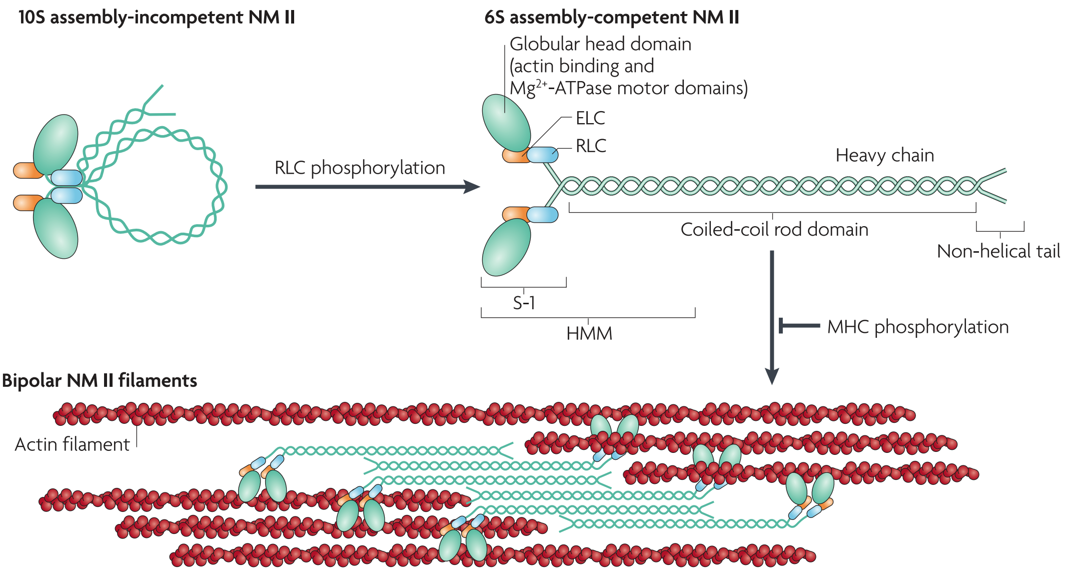

Figure 2.7.: Regulation scheme of NM II. From the assembly-incompetent form, phosphorylation of the RLC (by e.g. MLCK or ROCK) leads to a transition into the assembly-competent form, which can self-assemble into NM II minifilaments. Adapted from [49].

trapped very close to the backbone structure and cannot interact with actin [81, 82].

NM II is regulated in a spatio-temporally different way, as forces have to be dynamically produced on demand. Here contraction is regulated by assembly itself: if NM II is not assembled into bipolar filaments, no appreciable force can be produced. Assembly of NM II dependends critically on the phosphorylation of the RLC. If it is unphosphorylated, the myosin rod folds onto itself. This configuration is called the 10S assembly-incompetent NM II and is characterized by inhibition of most functionalities of NM II such as ATPase activity and binding to actin [83]. Upon phosphorylation of the RLC the rod can unfold into the 6S assembly-competent form as shown in Fig. 2.7. It is this form that can assemble into bipolar filaments that can contract anti-parallel actin filaments. The assembly is additionally regulated by phosphorylation of the tail region in an isoform dependent manner [49]. The viewpoint, that only the assembly-competent NM II can assemble into oligomeres, has been challenged by a study which identified folded oligomeres in electron microscopy images of *in vitro* assemblies [84]. It is however unclear, how big of a role this phenomenon plays *in vivo*, where it could lead to faster filament assembly [59, 84, 85]. Notably, the upstream regulation of the RLC phosphorylation by the RhoA-pathway concurrently upregulates actin assembly by activating formins, which means, that motor tracks and the motors themselves are built on-the-fly as needed by the cell [86, 87], which is in stark contrast to the rather static assembly situation in muscle cells. This motivates the modeling approach of simulating concurrent assembly and force generation of myosin minifilaments that is presented in chapter 4.

The different isoforms of non-muscle myosin II As mentioned above, non-muscle myosin II occurs in three different isoforms in mammals, NM IIA, NM IIB and NM IIC, encoded by three different genes for the heavy chain *Myh9*, *Myh10* and *Myh14*. The assembled hexamers only differ in their heavy chain, while their ELC and RLC remain the same, indicating that RLC-regulation is not isoform specific [59]. In turn, the regulation heavy-chain phosphorylation may be isoform specific as distinct phosphorylation loci exist along the myosin rod [49]. NM IIA and IIB is expressed by most cells, while NM IIC is only expressed by a few specialized cell types [59]. As little is known about the details of the mechanics of NM IIC we here focus on the other two isoforms NM IIA and NM IIB.

For assessing the mechanical capabilities of molecular motors there are two central quantities that link mechanics and motor chemistry and thereby dictate whether the motors are slow, fast, weak or strong: the *duty ratio* and the rate of ATP-hydrolysis [71]. The duty ratio describes the fraction of time spent attached to actin and can be interpreted as a measure for how strong a motor is, since one myosin head can carry a maximum force of $\sim 2\,\mathrm{pN}$ [64] only if it is attached. The rate of ATP-hydrolysis characterizes how much time a motor needs to complete one crossbridge cycle and thereby can be interpreted as a measure for speed. Compared to skeletal muscle myosin, non-muscle myosins are very slow and attach to actin quite strongly. Of the two, NM IIA can be characterized as the faster but weaker motor as it cycles through the actin bound states of the crossbridge cycle faster than NM IIB but spends less time in actin attached states. It was shown that different NM II isoforms can co-assemble into one bipolar filament yielding hetero-filaments [88, 89]. A theoretical study has shown, that these filaments show an intermediate behavior between pure NM IIA or NM IIB filaments [72].

Many cellular processes, such as cell migration, rely on the differences in mechano-chemical properties between the two major NM II isoforms. NM IIB is more often incorporated more ordered and long lived structures such as ventral stress fibers, that have to exert forces over long periods of time [49, 59, 90]. In contrast NM IIA can be found in more dynamic actin structures such as transverse arcs, where its higher contraction speed compared to NM IIB is vital to flatten the lamellum [22, 59]. Overall in migrating cells, there exists a well known front to back pattern of more NM IIA in the front and more NM IIB in the back of the cell [22, 90, 91]. An appealing mechanistic model mechanistically explaining the emergence of this pattern is described in [90]. NM IIA and NM IIB coassemble stochastically at the cell front and follow the retrograde flow of actin towards the cell rear. During this movement, higher turnover of NM IIA versus NM IIB, that has been found experimentally [91, 92], leads to an increased dissociation of NM IIA, which in turn leads to more NM IIB in the cell rear, than in the cell front. This process is likely additionally steered by differential regulation via the myosin tail region [49, 59].

2.2. Theoretical concepts

In the following theoretical concepts are introduced that are useful for the description of assembly and mechanics in the actin cytoskeleton.

2.2.1. Master equation

Due to the small size of the constituents of the cell and the energy scales involved in cellular processes being near the thermal energy $k_B T$, biological processes are often subject to appreciable fluctuations. In the case of molecular motors a reason for appreciable fluctuations lies also within the small number of motors that work together. Processes like these, that can be captured by a discrete set of states, are best described in the framework of master equations, that are introduced here following [93].

Suppose X_t is a random variable of a time dependent stochastic process, which could be the position of a diffusive brownian particle or the size of a self-assembling complex. If we collect this value at many discrete time steps we have obtained a so called *trajectory* $\{x_1, x_2, ...\}$ for the times $\{t_1, t_2, ...\}$. The probability distribution function for each time t assigns a probability $p(x,t)\mathrm{d}x$ for the random variable be in the interval between x and $x + \mathrm{d}x$ to each time. Importantly for the interpretation as a probability, $p(x,t)$ is normalized such that $\int p(x)\mathrm{d}x = 1$ and non-negative $p(x) \geq 0$. One can now also define the joint probability distribution function of n points $p_n(x_1, t_1; x_2, t_2; ...)$, which describes the probability for the system to have taken a specific trajectory. Often systems have no memory of their complete trajectory and thereby future states only depend on the present state, but not on the entire history of the system. These are called *Markov processes.* The following relation holds

$$p_n(x_{n+1}, t_{n+1}|x_n, t_n; x_{n-1}, t_{n-1}, ...) = p_2(x_{n+1}, t_{n+1}|x_n, t_n). \tag{2.2}$$

The conditional probability of whether state x_{n+1} is reached at time t_{n+1} given that it is in state x_n at t_n can be interpreted as a *transition probability.* This implies, for the three times $t_1 \leq t_2 \leq t_3$ that

$$p_2(x_3, t_3|x_1, t_1) = \int \mathrm{d}x_2 p_2(x_3, t_3|x_2, t_2) p_2(x_2, t_2|x_1, t_1), \tag{2.3}$$

which is called the Chapman-Kolmogorov equation. It states that the transition probability from state x_1 at t_1 to x_3 at t_3 can be calculated as a sum of transition probabilities over all intermediate steps x_2.

For small time differences τ between states x_1 and x_2 the Chapman-Kolmogorov equation implies

$$p_2(x_2, t_1 + \tau|x_1, t_1) = (1 - a\tau)\delta(x_2 - x_1) + \tau w(x_2|x_1) + \mathcal{O}(\tau^2), \tag{2.4}$$

which in essence states, that if the time difference is zero, no state change will occur, while at small τ the probability that a change occurs is given by $w(x_2|x_1)$. The Chapman-Kolmogorov equation together with the limit $\tau \to 0$ now implies

$$\frac{\partial p_2(x_3|x_1)}{\partial t} = \int \Big(w(x_3|x_2) p_2(x_2|x_1) - w(x_2|x_3) p_2(x_3|x_1) \Big) \mathrm{d}x_2, \tag{2.5}$$

which is the master equation. It should be interpreted as a time evolution equation for the probability to find the system in state x at time t when it was in state x_1 at time t_1. Bearing this in mind, one typically writes this equation in a less convoluted way by dropping the conditional probabilities. Additionally, when reasoning about a system with discrete states rather than continuous ones the integral becomes a sum and the equation is now

$$\frac{\mathrm{d}p_n(t)}{\mathrm{d}t} = \sum_n \left(w_{nn'} p_{n'}(t) - w_{n'n} p_n(t) \right), \tag{2.6}$$

where $w_{nn'}$ is the transition probability per unit time from state n' to state n. From this equation it becomes clear, that the master equation is a balance equation of probability fluxes. This equation can be further simplified by introducing the $\mathbb{W}$ matrix

$$\mathbb{W}_{nn'} = w_{nn'} - \delta_{nn'} \sum_{n''} w_{n''n}, \tag{2.7}$$

which can be used to rewrite eq. (2.6) as

$$\frac{\mathrm{d}\vec{p}(t)}{\mathrm{d}t} = \mathbb{W}\vec{p}(t). \tag{2.8}$$

$\mathbb{W}$ can be diagonalized, since $-\mathbb{W}$ is a non-singular M-matrix (for more details see [94, 95]), solutions to the master equation are now given by the ansatz

$$\vec{p}(t) = \sum_i C_i \mathrm{e}^{\lambda_i t} \vec{v}_i, \tag{2.9}$$

where λ_i and $\vec{v}_i$ are the eigenvalues and right eigenvectors of $\mathbb{W}$ respectively, while C_i are coefficients. Since the probability is conserved, the column sum of $\mathbb{W}$ vanishes, which implies, that $(1, 1, ..., 1)$ is a *left* eigenvector of $\mathbb{W}$ to the eigenvalue $\lambda_0 = 0$. The corresponding *right* eigenvector corresponds to the stationary state of the system.

The other eigenvalues cannot be given in general, however their real value is negative [94], which corresponds to a damping of non steady state probability distributions. Since $\mathbb{W}$ is not generally symmetric, in principle also complex eigenvalues can occur, however if detailed balance is fulfilled, i.e. there exists a steady state p_n^{eq} where all fluxes $p_n^{\mathrm{eq}} w_{nn'}$ are balanced with fluxes in the opposite direction $p_{n'}^{\mathrm{eq}} w_{n'n}$, the eigenvalues are real and thereby no oscillations occur in the solution of the master equation.

A special example of a master equation that is often studied is the one-step master equation. In these processes states can be numbered by an integer n and the $\mathbb{W}$ matrix only permits transitions between adjacent sites. These can be written in the form

$$\frac{\mathrm{d}p_n(t)}{\mathrm{d}t} = r_{n+1} p_{n+1} + g_{n-1} p_{n-1} - (r_n + g_n) p_n. \tag{2.10}$$

$r_n = w_{nn-1}$ and $g_n = w_{nn+1}$ are the probability per unit time that a transition from state n to state $n-1$ and $n+1$ occur respectively. It can be used to model a wide variety of stochastic processes such as recombination and generation of charges in semiconductors and birth-and-death problems, as arise in the dynamics of adhesion clusters [96, 97], in the load-dependent self-assembly of the bacterial flagellar motor [5] or in adhesion mediated cellular uptake of particles [98, 99].

2.2.2. Self-assembly and chemical rate-equations

Self-assembly of multiple individual constituents to a functioning whole is at the heart of many biological processes. Be it the assembly of a virus capsid [100], the assembly of cytoskeletal filaments [101] or the synthetic biology approach of DNA-origami [102], the single constituent does not fullfil a purpose (apart from being able to assemble that is), but the assembled structure can sometimes be a quite intriguing. In the advent of larger-scale computer simulations, that model self-assembly from diffusion and reaction of explicit particles in three dimensions [103], more simple models of self-assembly that model only the size of complexes may sometimes be overlooked. However in some scenarios it is not the exact geometric arrangement that is important for the self-assembled to perform its job, but it is the size. Examples for these sorts of complexes include lipid membranes, that – essentially for biological cells – compartmentalize an aqueous environment and have to provide large enough compartments to fit all cellular constituents, adhesion clusters, that are only stable to force if they contain enough adhesion proteins [97], ensembles of non-processive motors, that can move processively if enough motors join the ensemble [69], or synthetic fibers, where the tensile strength of a fiber depends strongly on the typical molar weight of the polymers [104].

To capture the essential features of the self-assembly of these complexes, as they do not depend strongly on explicit geometry, a description in terms of a network of distinct chemical reactions is often sufficient. The Smolochowski-Kolmogorov coagulation fragmentation equation is a classical example for such a network, that is based on the law of mass action [105–107]. It describes the time evolution of concentrations during reversible reactions of clusters consisting of n and s monomers of the form $C_n + C_s \rightleftharpoons C_{n+s}$ and is given by

$$\begin{aligned}\frac{\mathrm{d}c_n}{\mathrm{d}t} = \frac{1}{2}\sum_{s=1}^{n-1} a_{s,n-s} c_s c_{n-s} - \sum_{s=1}^{\infty} a_{n,s} c_n c_s \\ - \frac{1}{2} c_n \sum_{s=1}^{n-1} b_{s,n-s} + \sum_{s=1}^{\infty} b_{n,s} c_{n+s}.\end{aligned} \tag{2.11}$$

The coagulation and fragmentation kernels are $a_{s,n}$ and $b_{s,n}$ respectively and describe the chemical rates of each of the reactions. Mathematical research typically focuses on the situation where clusters can grow indefinitely (as is indicated by the upper limit ∞ in the second and last sum) and asks questions about the long time behavior [106]. However, there are also applications of this equation to systems with a maximal cluster size, such as the assembly SASS-6 proteins that to rings that later serve as scaffolds for microtubule nucleation [108–110].

The Smolochowski-Kolmogorov aggregation-fragmentation equation can be simplified if one assumes clusters can only grow or shrink by addition or dissociation of one monomer. This reaction network is described in the literature as the Becker-Döring equation [111] and can be written as

$$\frac{\mathrm{d}c_1}{\mathrm{d}t} = -2J_1 - \sum_{n=2}^{\infty} J_n \tag{2.12}$$

$$\frac{\mathrm{d}c_n}{\mathrm{d}t} = J_{n-1} - J_n, \qquad n \geq 2 \tag{2.13}$$

with $J_n = k^n_{\mathrm{on}} c_1 c_n - k^n_{\mathrm{off}} c_{n+1}$. The evolution of the monomer concentration is much more complex, since monomers participate in reactions of all cluster sizes. Again, mathematical research focuses on the situation where clusters can grow infinitely large [112] and investigates predominantly long time behavior and the existence of steady states [113]. While earlier typically the monomer concentration was held constant for ease of calculations, in more recent work eq. (2.12) is into account which should ensure mass conservation. Surprisingly, in situations of high initial mass the equilibrium solution which is approached can become zero for all finite cluster sizes. This implies that at $t \to \infty$ all initial monomers have formed a *superparticle* [112, 114].

As stated above, a maximal cluster size with dynamical systems in mind, such as assembling viruses, where the respective monomers are produced concurrently to self-assembly and release of finished clusters from the system, the Becker-Döring model can be used in a modified version to model open molecular self-assembly [115, 116]. Here, an influx of monomer and outflux of complexes of different sizes are introduced to the system of equations and the changed behavior is studied. Remarkably, also oscillatory solutions are found [116].

2.2.3. Linear viscoelasticity

Many different experiments indicate that the mechanics of animal cells is neither purely elastic, nor purely viscous, but depends on the experiment. Be it the reaction of red blood cells to prolonged deformation in a microchannel [117], time-dependent contraction of stress fibers using opto-genetics [2] or the mechanical response of subcutaneous adipose tissue [118], the mechanics of cells is best described as viscoelastic, i.e. a combination of both elastic and viscous response. Myosin II, as it is the main molecular motor that affects the actin cytoskeleton, has been found to play a central role in determining the mechanical behavior of the cell [119–122]. As chapter 5 makes use of viscoelastic theory, to relate the chemical properties of myosin II to viscoelastic properties, basic theoretical results are given here.

This chapter follows [123, 124] in laying the basis for understanding the linear viscoelastic behavior of materials. A general linear response of a viscoelastic system to an applied strain $\varepsilon(t)$ or an applied stress $\sigma(t)$ can be written as

$$\sigma(t) = \int_{-\infty}^{t} G(t-t')\mathrm{d}\varepsilon(t') \tag{2.14}$$

$$\varepsilon(t) = \int_{-\infty}^{t} J(t-t')\mathrm{d}\sigma(t'). \tag{2.15}$$

The functions $J(t)$ and $G(t)$ are called the *creep compliance* and the *relaxation modulus* respectively, or also the *material functions* of the viscoelastic material. They describe the response of the viscoelastic material to a unit step in force or strain respectively, i.e. $\varepsilon(t) = \Theta(t) \Rightarrow \sigma(t) = G(t)$ and $\sigma(t) = \Theta(t) \Rightarrow \varepsilon(t) = J(t)$. Since the current response of a material should not depend on an applied strain or stress in the future – this would violate causality – the material functions should vanish for $t < 0$. Experimental evidence shows, that the material functions are non-negative monotonic functions. While $J(t)$ is increasing, $G(t)$ is monotonically decreasing. The limiting values of the material functions at $t \to 0^+$ and $t \to +\infty$ can already be used to qualitatively classify a viscoelastic material. The values for $t \to 0^+$ relate to the instantaneous (glass) response and are denoted by J_g and G_g, while the values for long times $t \to +\infty$ are related to the equilibrium response and are denoted by J_e and G_e. It can be shown, that the material functions are not independent of each other but there is a one-to-one correspondence between the two. For the limiting values of the material functions one in particular finds $J_g = G_g^{-1}$ and $J_e = G_e^{-1}$. For a derivation see [123]. This allows to classify viscoelastic materials according to their instantaneous and equilibrium responses into four types, as shown in Table 2.1. Type I materials can be deformed elastically on very short time scales and still exhibit some elastic resistance to deformation at long timescales. Type II materials behave elastically on short timescales, but flow on long timescales. Type III materials cannot be deformed at short timescales, but behave elastically at long timescales. Finally, Type IV materials cannot be deformed instantly, but flow at long timescales.

Type	$J_g := J(0^+)$	$J_e := J(+\infty)$	$G_g := G(0^+)$	$G_e := G(+\infty)$
I	> 0	$< \infty$	$< \infty$	> 0
II	> 0	$= \infty$	$< \infty$	$= 0$
III	$= 0$	$< \infty$	$= \infty$	> 0
IV	$= 0$	$= \infty$	$= \infty$	$= 0$

Table 2.1.: The four types of viscoelasticity following [125].

Animal cells should fall into the the material type II category, as for small times they are deformable but remember their original configuration and are able to return to it, while reorganization of the cytoskeleton makes them flow on long timescales. This is also consistent with the description of cells as exhibiting a soft-glassy rheology [126, 127] with a power-law creep compliance $J(t) \sim (t/\tau_0)^\beta$ with typical values for β between 0.1 and 0.5.

In experimental situations sample materials are often not subjected to a step in strain or stress but to a sinusoidal excitation. One can calculate the corresponding *dynamic functions* from the material functions by assuming a loading history of $\varepsilon(t;\omega) = \mathrm{e}^{i\omega t}$ and $\sigma(t;\omega) = \mathrm{e}^{i\omega t}$ in eqns. (2.14) and (2.15) respectively. Here a complex notation is used for convenience and ω denotes the angular frequency. One finds

$$\sigma(t) = G^*(\omega)\mathrm{e}^{i\omega t}, \text{ with } G^*(\omega) := i\omega \int\limits_0^\infty G(t)\mathrm{e}^{-i\omega t}\mathrm{d}t \tag{2.16}$$

$$\varepsilon(t) = J^*(\omega)\mathrm{e}^{i\omega t}, \text{ with } J^*(\omega) := i\omega \int\limits_0^\infty J(t)\mathrm{e}^{-i\omega t}\mathrm{d}t. \tag{2.17}$$

The functions $G^*(\omega)$ and $J^*(\omega)$ are called *complex modulus* and *complex compliance*. For consistency of eqns. (2.14) and (2.15) it also follows that $G^*(\omega)J^*(\omega) = 1$. Since these functions are complex of course the stress and strain response of the material is phase shifted by the so called *loss angle* $\delta(\omega)$ compared to the sinusoidal excitation. If one separates the real and imaginary parts of the dynamic functions one can write

$$G^*(\omega) = G'(\omega) + i\omega G''(\omega) = |G^*(\omega)|\mathrm{e}^{i\delta(\omega)} \tag{2.18}$$

$$J^*(\omega) = J'(\omega) - i\omega J''(\omega) = |J^*(\omega)|\mathrm{e}^{-i\delta(\omega)}, \tag{2.19}$$

with $\tan\delta(\omega) = G''(\omega)/G'(\omega) = J''(\omega)/J'(\omega)$. The real parts G' and J' are called *storage* modulus and compliance respectively, while the imaginary parts G'' and J'' are termed *loss* modulus and compliance.

While the material and dynamic functions can be used easily to describe experimental results, classical mechanical models composed of linear springs and dashpots can be helpful to gain a better intuition of the meaning of these functions. The mechanical models always relate to a so called *constitutive equation* which relates stress and strain (along with their derivatives w.r.t. time). From these it is possible to obtain the material functions via eqns. (2.14) and (2.15). We here focus on the *Maxwell model*, a serial arrangement of a spring with spring constant k and a dashpot with friction coefficient η as shown in the inset of Fig. 2.8, which is the simplest

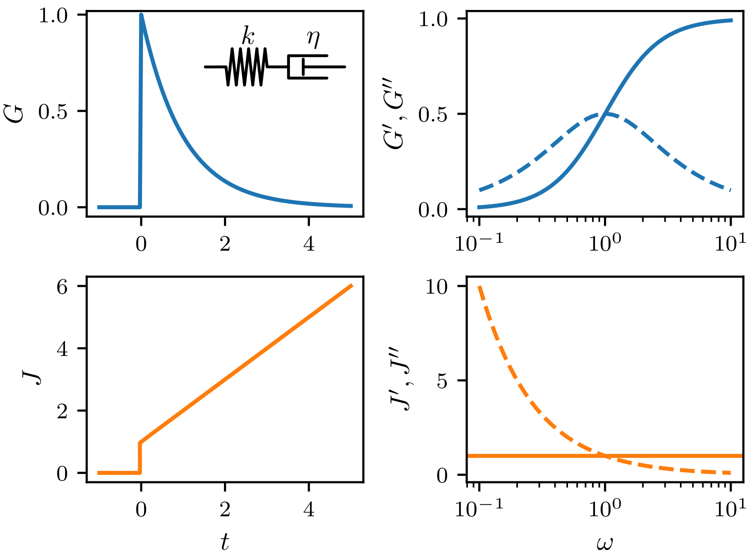

Figure 2.8.: Visualization of the the material functions (left) and the dynamic functions (right) of the Maxwell model, where solid lines denote the real part and dashed lines denote the imaginary part.

viscoelastic material of type II. For more examples of mechanical models refer to [123].

The *constitutive equation*, which relates stress to strain and their derivatives w.r.t. time, for the Maxwell model is given by

$$\sigma(t) + \frac{\eta}{k}\frac{\mathrm{d}\sigma}{\mathrm{d}t} = \eta\frac{\mathrm{d}\varepsilon}{\mathrm{d}t}. \tag{2.20}$$

Hence the material functions are given by

$$G(t) = k\mathrm{e}^{-t/\tau} \qquad G^*(\omega) = \frac{k(\eta\omega)^2 + i\omega k^2\eta}{(\eta\omega)^2 + k^2} \tag{2.21}$$

$$J(t) = \frac{1}{k} + \frac{t}{\eta} \qquad J^*(\omega) = \frac{1}{k} - i\frac{1}{\omega\eta} \tag{2.22}$$

with relaxation time $\tau = \eta/k$. All functions are visualized in Fig. 2.8.

2.3. Experimental techniques

The following section highlights some central experimental methods that have been utilized to characterize the mechanics or self-assembling behavior of the actomyosin system.

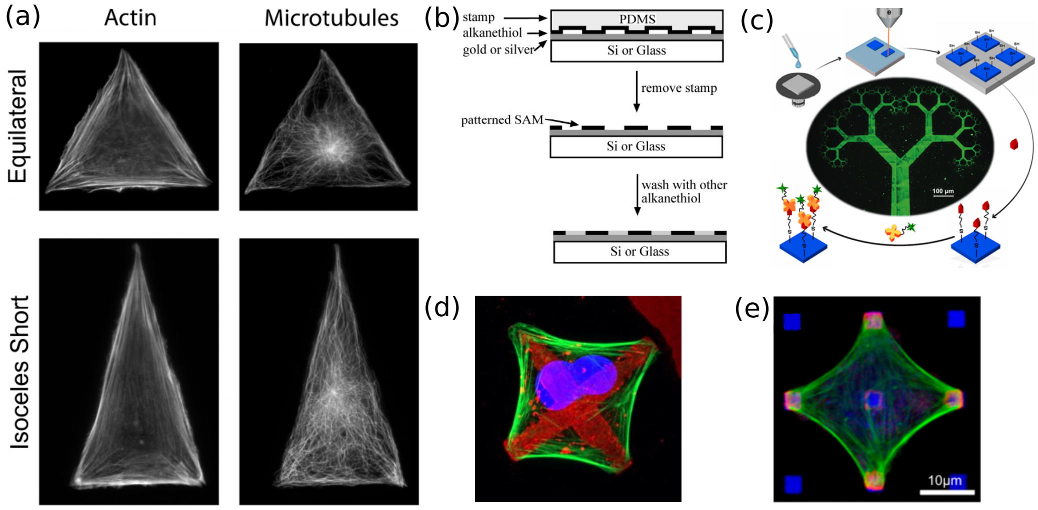

Figure 2.9.: Micropatterning techniques and applications. (a) Changes of cytoskeletal organization due to adhesion constraints can be investigated using micropatterning. (b) Principle of microcontact printing: A micro inked with alkanethiol is brought into contact with a thin gold/silver surface and leaves a functionalized mark for protein absorption. The remaining surface is washed with another alkanethiol not suitable for protein absorption. (c) A more recent technique uses electron beam lithography to selectively functionalize a surface is technically more involved but is able produce smaller features. (d) U2OS cell on a cross-pattern of fibronectin. Image is courtesy of Kai Weißenbruch. (e) Cell on a dotted substrate showing invaginated arcs between the adhesive dots. Adapted from [128, 129, 131, 132].

2.3.1. Micropatterning on two-dimensional substrates

Biological cells are often cultivated on adhesive surfaces where even one cell line typically shows a variety of phenotypes that are difficult to quantify in a meaningful way. In order to conduct well controlled experiments that probe the cytoskeletal organization it has been found to be instructive to control the area the cells can adhere to by fixing proteins normally found in the extracellular matrix (as e.g. fibronectin [11]) to constrained areas [128–130]. Fig. 2.9(a) shows how the actin and microtubule cytoskeleton organization changes depending on the shape of the adhesive surface, which only gives a glimpse of the possibilities for controlled investigation of cell behavior. This section gives an overview of the different techniques that have been developed to fabricate such substrates.

Microcontact printing, a technique of soft lithography, has been utilized to produce microfluidic devices or bendable microelectronics [133]. Microcontact printing can be used to chemically functionalize a metal surface for protein absorption and has been used very early to confine cell spreading to a predefined area [134]. In brief, a stamp, which has been produced from a master and is typically made of polydimethylsiloxane (PDMS), a transparent elastomer, is inked and used to leave a pattern predetermined by the master on a given surface as shown in Fig. 2.9(b). For biological applications one can use glass slides with a thin gold film as the surface and stamp on alkanethiols that form self-assembled monolayers that can adsorb proteins. A subsequent washing step with a different sort of alkanethiol also forming self-assembled monolayers, that importantly resist the adsorption of protein concludes the patterning. In a last step purified protein can be introduced to the surface and after excess protein is washed away we receive a surface with a well defined pattern of attachment points for cells [132]. This is a quite cost-effective and simple method to generate micropatterned surfaces in a lab environment without a clean room and hence has been used in numerous studies from stress fibers [128, 135] (see Fig. 2.9(d) and (e)) to the influence of cell shape on stem cell differentiation [136].

Direct photolithographic processes have also become available where, using a photomask, extracellular matrix protein is more directly coated to a glass surface [137]. These procedures allow for a production of large quantities of patterned surfaces. Another technique, which focuses on the production of very small patterns, uses electron beams to directly write free thiolene functional groups patterns to glass surfaces (see Fig. 2.9(c)). In subsequent steps these can used to immobilize biomolecules on the predefined pattern with features as small as 250 nm.

2.3.2. Fluorescence recovery after photobleaching

FRAP makes use of the normally unfavorable behavior of photobleaching that typical fluorescent markers used in biological experiments show. Shining light onto these fluorophores over time leads to a permanent loss of the fluorophores ability to fluoresce. In FRAP experiments this property is utilized by purposely bleaching a small domain using a focused laser beam. The recovery of the fluorescence that may be observed in the target area stems from the stochastic exchange of permanently damaged fluorophores with undamaged ones [138]. This turnover can be either driven by active transport or diffusion [139] and can be slowed down significantly if the fluorescent particle is bound to a stationary object [140]. In the theoretical description of FRAP therefore two limits which are described in the following can be distinguished assuming active transport does not play a major role: The diffusion-limited case and the reaction-limited case [141].

Diffusion-limited recovery In this regime fluorescent particles are assumed to not bind to any other particle. Thus the fluorescence recovery is only governed by diffusion and therefore should be modeled using the diffusion equation

$$\frac{\partial C}{\partial t} = D\Delta C, \tag{2.23}$$

where C is the concentration of fluorophore and D is the diffusion constant, with appropriate starting conditions for the bleached spot [139]. The exact solution depends on the starting condition and other conditions, such as the dimensionality of the space that is available for diffusion. For a circular bleach spot of radius w of a fluorophore diffusing in two dimensions there is an analytical formula for the detected FRAP dynamics with the modified Bessel functions I_0 and I_1

$$FRAP(t) = \mathrm{e}^{-\frac{\tau_D}{2t}}\left[I_0\left(\frac{\tau_D}{2t}\right) + I_1\left(\frac{\tau_D}{2t}\right)\right] \text{ with } \tau_D = \frac{w^2}{D}. \tag{2.24}$$

Other closed form recovery dynamics emerging from different dimensionalities can be found in [142] together with a thorough discussion about the impact of the choice of boundary conditions on the physical properties estimated from experimental profiles.

Reaction-limited recovery In this regime reversible attachment of the fluorescent particle to a stationary object is important and diffusion is expected to be fast. The simplest reaction that can be considered is the reversible binding of free diffusible protein F to vacant immobile binding sites S, with binding rate k_{on} and unbinding rate k_{off}, forming the complex C

$$F + S \underset{k_{\mathrm{off}}}{\overset{k_{\mathrm{on}}}{\rightleftharpoons}} C.$$

The recovery dynamic has here been given in the literature [141]

$$FRAP(t) = 1 - \frac{k^*_{\mathrm{on}}}{k^*_{\mathrm{on}} + k_{\mathrm{off}}}\mathrm{e}^{-k_{\mathrm{off}}t} \tag{2.25}$$

where $k^*_{\mathrm{on}} = S_{\mathrm{eq}}k_{\mathrm{on}}$ is the effective first-order rate constant given the solution is in equilibrium prior to performing the bleaching (which is assumed to be true in typical scenarios). This formula assumes, that free proteins fully contribute to the fluorescence signal, which however may not apply in a confocal microscope, if the studied complex fully fills up the focal plane such that free proteins are not detected.

In these situations often the fluorescence does not recover fully, which is attributed to only a fraction of the fluorophores being able to be exchanged in the timescale

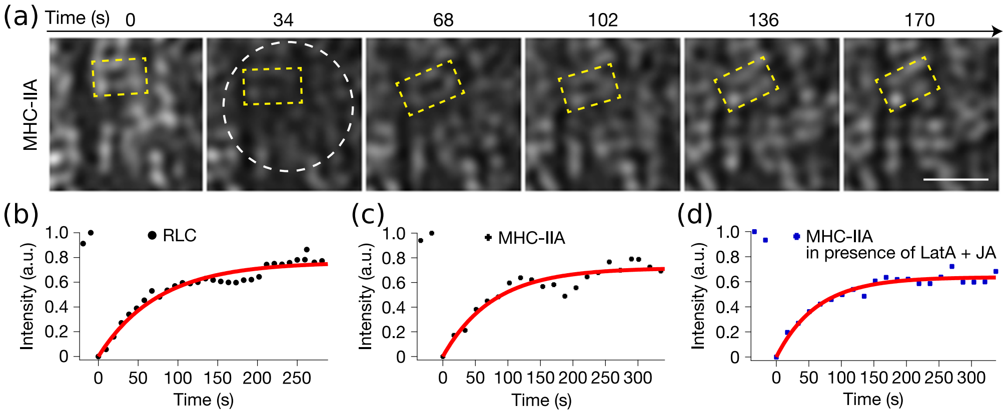

Figure 2.10.: FRAP of non-muscle myosin IIA. (a) SIM imaging of GFP tagged NM IIA heavy chain after photobleacing the white circle. (b-d) FRAP data of the RLC, the heavy chain with and without suppressed actin polymerization dynamics are similar, suggesting, that the recovery is due to complete exchange of myosin hexamers. Adapted from [143].

probed by the experiment. In practice recovery profiles of the form

$$FRAP(t) = \delta \left(1 - \mathrm{e}^{-k_{\mathrm{off}}t}\right) \tag{2.26}$$

with the mobile fraction of fluorophores δ are observed [143]. This approach has been used to study NM II turnover dynamics (see Fig. 2.10) in conjunction with structured illumination microscopy (SIM), a super resolution microscopy technique. The FRAP dynamics neither depended on the specific fluorescently tagged protein in the myosin II hexamer, as the tagged RLC (Fig. 2.10(b)) and the tagged heavy chain (Fig. 2.10(c)) recover similarly, nor on actin dynamics, as inhibition using two chemical compounds known for inhibiting actin dynamics did not change the FRAP dynamics (see Fig. 2.10(d)). Thus, this study indicates, that myosin II hexamers are in dynamic turnover with a small fraction – the immobile fraction – which does not exchange with the environment on the timescale probed by the experiment.

2.3.3. Microrheological methods

This section briefly describes some approaches that have been utilized to investigate the rheology of the cytoskeleton. All approaches build upon the idea that thermal or non-thermal forces act upon the cytoskeleton and the response can be recorded. They can probe different substructures of the cytoskeleton, depending on the location and magnitude of the stress they exert. They are shown in a very schematic way in Fig. 2.11.

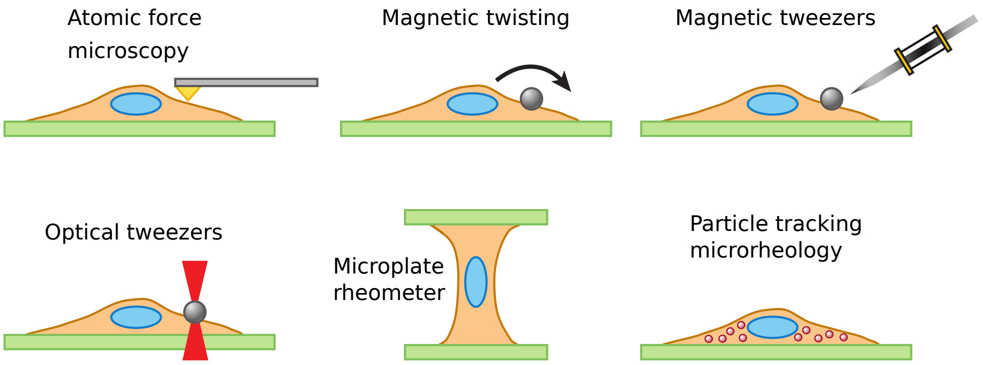

Figure 2.11.: Sketches of standard microrheological measurement methods. Adapted from [127].

Atomic force microscopy uses a tip attached to a soft cantilever to press down on a material and measure the force dependent on the indentation of the material [144]. Due to its high spatial resolution, which is primarily limited by the tip sharpness, it is often viewed as an imaging technique but can also shed light on mechanical properties of a biological sample. By utilizing tipless cantilevers, also the whole cell can be deformed at once, thereby probing a more global response of the cell to pressure [122].

Magnetic twisting has been conceived very early for probing the rheology of biological cells [145]. Protein-coated ferromagnetic but non-magnetized beads are allowed to bind to the cell. After magnetization of the cell bound beads, the beads can be rotated by an external field and the orientation of the beads magnetic field can be recorded with a magnetometer. This setup allows to measure many cells in parallel, the twisting can be done over a large frequency domain from $0.01 \sim 1000\,\mathrm{Hz}$ [127].

Magnetic tweezers can be utilized to pull on protein-coated paramagnetic beads that have been brought into close contact with the cell membrane in order to probe the mechanics of the actin cytoskeleton below the plasma membrane [146]. Beads can be subject to a maximum force of $\sim 100\,\mathrm{nN}$ using this method [127]. Since magnets either pull or push on the same para- or diamagnetic bead forces can only be applied in one direction and probing the response to oscillatory forces is not possible.

Optical tweezers can manipulate microbeads using a focused laser light [147]. Beads are always pushed towards the focal point of the laser. Only small forces of up to $\sim 50\,\mathrm{pN}$ can be generated, however therefore it is a very precise method, which can be used to study the mechanics of single molecular motors [33]. They have also been used to measure the shear response of the cytoskeleton, by fixing an adherent bead in space with optical tweezers and applying an oscillatory force by moving the sample slide via a piezoelectric motor [148].

A microplate rheometer investigates the cellular rheology by pushing and pulling on a cell attached to two glass plates [149]. Due to the setup it is possible to control the prestress the cell is subject to by controlling the distance between the two plates. With this approach it has been shown that cells are typically stress stiffening [150].

Particle tracking microrheology relies on thermal forces rather than forces produced by a measurement apparatus [151]. Instead – after bringing marker beads to the points of measurement – one follows the thermal fluctuations of the marker beads as they move together with the cytoskeleton. Remarkably, it is possible to obtain the complex modulus of the material in which the beads have been embedded from the mean squared displacement $\Delta r^2(t)$ as

$$G^*(\omega) = \frac{2k_B T}{3\pi a i \omega F_u[\Delta r^2(t)]},$$

where a is the radius of the bead and $F_u[\cdot]$ is the unilateral Fourier transform [151]. As the above formula relates fluctuations – quantified by $\Delta r^2(t)$ – with an impedance $G^*(\omega)$ in a thermodynamic equilibrium situation, it can be interpreted as a form of the fluctuation dissipation theorem. While the method has been developed with equilibrium fluctuations in mind, particle tracking microrheology has also been applied to systems in which molecular motors play a central role. By comparison of results with and without motor action it was shown that additional fluctuations by motors occur at specific slower timescales [152].

2.3.4. Laser cutting

In order to extract meaningful information about the mechanical properties of a material the typical approach is deforming it by a prescribed protocol and recording the response of the material [153]. This is also true for the cytoskeleton or cells in general, as numerous such techniques exist that stress the cell mechanically [127] as pointed out in the previous section. Additionally, since the cytoskeleton is typically prestressed by molecular motors such as myosin II, it is possible to probe the mechanics by partly disrupting the structure. This can be done in practice by laser cutting, a technique where a focused femtosecond laser is aimed at a cytoskeletal filament in order to laser-ablate it [154].

An often performed experiment that is performed with this technique is simply ablating part of a fiber and observing the retraction with confocal microscopy [154, 156–158] (see Fig. 2.12(a)). The retraction is often found to be divided in a virtually instant elastic retraction and a following exponential retraction with a typical timescale on the order of tens of seconds [159]. The standard linear solid model includes both instant elastic relaxation and viscoelastic retraction in its response to a sudden release of strain.

Peripheral stress fibers can be isolated by 'shaving' off cortical actin in the periphery as shown in Fig. 2.12(b). In this study an active standard linear solid model could describe the mechanics of the isolated stress fibers inside cells in response to micromanipulation with an intracellular bead as depicted in Fig. 2.12(c) [155]. Additionally they could show, that myosin contraction and crosslinking leads to an increase in stiffness of the peripheral stress fiber as the same elongation of the stress fiber leads to a lower force when myosin is inhibited (see Fig. 2.12(d)).

A very recent study The laser cutting and 'shaving' of the cortex approach has since also been applied in conjunction with traction force microscopy [160], a method to quantify the traction forces cells exert on their substrate [161]. By measuring changes in traction force due to cutting and shaving the peripheral stress fibers in several

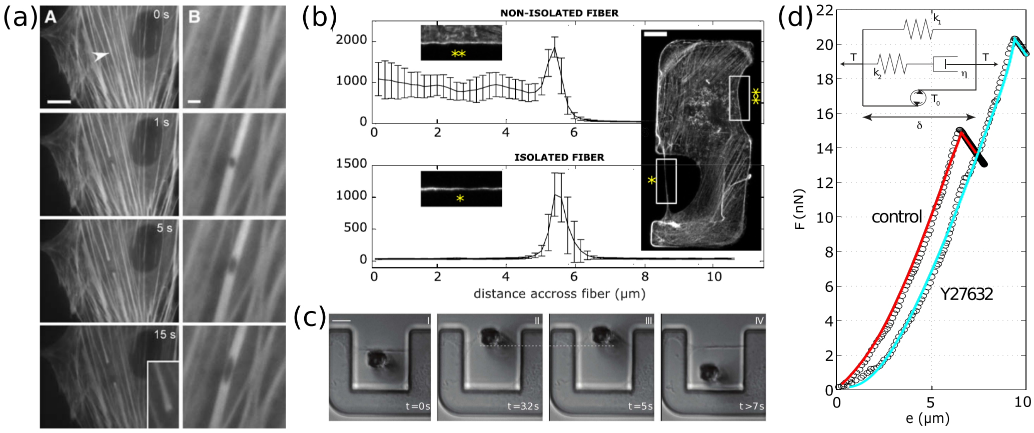

Figure 2.12.: Applications of lasercutting of actin filaments. (a) (left) A fluorescently labeled actin filaments that is cut at the arrow head shows a retraction. (right) A 300 nm hole is punched into a filament which elongates over time into an elliptical shape. (b) The peripheral stress fiber that bridges the lower part of an S-shaped micropattern has been isolated by cutting/'shaving' off the cortical actin network. (c) A microbead that was inserted into the cells is used to manipulate the isolated stress fiber. (d) The strain-stress response curve can be modeled by an active standard linear solid material law. Inhibition of actomyosin with Y27632 leads to a decrease in force at similar elongations. Adapted from [154, 155].

geometries and comparing to theoretical modeling, the authors conclude that stress fibers should be considered as well embedded contractile structures into a contractile actin network.

Recapitulating, laser cutting has developed to be a versatile tool to probe the mechanical properties, the organization and force transduction within the cytoskeleton. Especially in conjunction with rigorous methods for force measurements this method is very powerful.

3. Becker Döring model for finite size clusters

3.1. Introduction

The Becker-Döring equations, as introduced briefly in section 2.2.2, have been studied in great detail [106] in the past as they are a simple and generic approach to describe the dynamics of self-assembly of very different systems from phospholipid micelles [162] to viral capsids [163], while also correctly predicting critical phenomena such as Ostwald ripening [164].

In many classical systems such as the originally studied super-saturated vapor [111] or binary alloys, in principle clusters of infinite size can form. In the realm of biology there is however often a maximum cluster size at which the cluster is either fully assembled or the dynamics change. Examples for such self-assemblies include viral capsids, where a set amount of proteins assembles into a shell that closes onto itself [163, 165], or prion fibrils that nucleate from individual missfolded proteins and are stabilized once a threshold size is reached [166]. NM II minifilaments are also such an example, as they contain a well defined number of $\lesssim 30$ non-muscle myosin II (NM II) monomers [34, 54]. Systens like these have also been studied with mathematical rigour mainly motivated by numerical approaches[167, 168].

Independent of the specific system studied, there is typically a great interest in the timescale on which self-assembly occurs. These can vary widely even in the realm of biology. While β-amyloid fibrils, protein aggregates which have been related to neurodegenerate diseases such as Alzheimer's, Huntington's and Parkinson's disease [169, 170], assemble on very long timescales of multiple hours, virus capsids and NM II minifilaments can assemble within minutes [54, 165].

In their form, where monomer concentrations are held constant and there is a maximum cluster size, the Becker-Döring equations are a finite dimensional linear system of equations and hence timescales can be extracted from the eigenvalues of their Jacobian matrix. Here, I investigate such a modified version of the Becker-Döring equations, where the maximum sized cluster is stabilized. Investigaton of the equilibrium properties of this system, in particular of the dependence of total monomers in the system on free monomer concentration, reveals that there is a monomer concentration at which this scaling changes dramatically, the critical aggregation concentration (CAC), which is a typical occurence in self-assembling systems [171]. I approximate the eigenvalues of the system using a perturbative approach supported with numerical calculations. Furthermore, the stochastic dynamics of the size of one cluster of this system is modeled by a one step-master equation. Analysis of the equilibrium and dynamic properties of the one-cluster system reveals a maximum in relaxation time very close to the CAC, which is in contrast to the bulk system, where the relaxation time only increases with increasing monomer concentration. Finally, the applicability of these results to situations where the total monomer concentration is conserved is discussed briefly.

3.2. Model outline

The Becker-Döring equations [111] describes the dynamic growth of clusters with rate equations

$$\begin{aligned} \dot{c}_1 &= -2J_1 - \sum_{n=2}^{\infty} J_n \\ \dot{c}_n &= J_{n-1} - J_n, \quad n \geq 2 \\ J_n &= k_{\text{on}} c_1 c_n - k_{\text{off}} c_{n+1}, \end{aligned} . \tag{3.1}$$

where c_n is the concentration of clusters containing n monomers, i.e. n-mers, k_{off} is the off-rate, k_{on} is the second order rate constant for association of a monomer to a cluster and J_n are the net fluxes of concentration from n-mers to $n+1$-mers. For clusters with maximum size N with a stabilized fully assembled cluster this changes to

$$\begin{aligned} \dot{c}_1 &= -2J_1 - \sum_{n=2}^{N-1} J_n & & \\ \dot{c}_n &= J_{n-1} - J_n, & & 2 \leq n < N \\ \dot{c}_N &= J_{N-1} = k_{\text{on}} c_{N-1} - \varepsilon k_{\text{off}} c_N & & \\ J_n &= k_{\text{on}} c_1 c_n - k_{\text{off}} c_{n+1} & & 2 \leq n < N-1, \end{aligned} \tag{3.2}$$

where the small constant $\varepsilon > 0$ was introduced. The reaction network of this system of equation is shown in Fig. 3.1.

This system can be non-dimensionalized by using the rescaled time $\tau = t k_{\text{off}}$ and

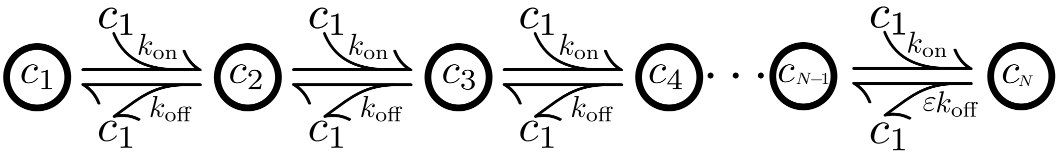

Figure 3.1.: Schematic of the rate equation studied in this chapter. The off-rate of the fully assembled cluster $\varepsilon k_{\text{off}}$ is assumed to be small compared to k_{off}.

measuring concentration in units of $k_{\text{off}}/k_{\text{on}}$, which yields

$$\begin{aligned}
\dot\theta_1 &= -2J_1 - \sum_{n=2}^{N-1} J_n \\
\dot\theta_n &= J_{n-1} - J_n, \quad 2 \le n < N \\
\dot\theta_N &= J_{N-1} = \theta_1\theta_{N-1} - \varepsilon\theta_N \\
J_n &= \theta_1\theta_n - \theta_{n+1}, \quad \theta_n = \frac{k_{\text{on}}c_n}{k_{\text{off}}},
\end{aligned} \tag{3.3}$$

with the dimensionless concentrations θ_n. We call $\theta_1 = \theta$ the reduced monomer concentration.

3.3. Ensemble dynamics near equilibrium

3.3.1. Equilibrium

The behavior of this nonlinear set of equations can be analyzed by holding the reduced monomer concentration θ constant, which removes the nonlinearity. The rough experimental protocol to achieve this would be:

1. Allocate volume V of solvent and put in x amount of monomer.

2. While the reaction occurs record the n-mer concentrations and add new monomer to the solution such that the monomer concentration stays constant.

The time evolution equation can be written as a matrix vector equation

$$\dot{\vec\theta} = J\vec\theta + \vec f, \tag{3.4}$$

where J is the Jacobian and the vector $\vec{\theta}$ contains the concentration of n-mers for $n \geq 2$. J and $\vec{f}$ have the form

$$J = \begin{pmatrix} -(1+\theta) & 1 & 0 & \cdots & 0 & 0 \\ \theta & -(1+\theta) & 1 & \ddots & \vdots & \vdots \\ 0 & \theta & -(1+\theta) & \ddots & 0 & 0 \\ \vdots & \ddots & \ddots & \ddots & 1 & 0 \\ 0 & \cdots & 0 & \theta & -(1+\theta) & \varepsilon \\ 0 & \cdots & 0 & 0 & \theta & -\varepsilon \end{pmatrix}_{(N-1)\times(N-1)} \tag{3.5}$$

$$\vec{f} = \begin{pmatrix} \theta^2 \\ 0 \\ \vdots \\ 0 \end{pmatrix}. \tag{3.6}$$

Note, that J is a tridiagonal Toeplitz matrix up to the entries in the last column, which arise due to the missing flux to bigger clusters for finite maximum size clusters and the reduced dissociation rate.

Enforcing detailed balance on (3.4) with updated J yields

$$\begin{aligned} \theta_n^{\mathrm{eq}} &= \theta^n, \quad 2 \leq n < N \\ \theta_N^{\mathrm{eq}} &= \frac{1}{\varepsilon}\theta^N. \end{aligned} \tag{3.7}$$

The total concentration of monomer θ_{tot} can now be calculated

$$\begin{aligned} \theta_{\mathrm{tot}}(\theta) &= \sum_{n=1}^{N} n\theta_n^{\mathrm{eq}} = \sum_{n=1}^{N-1} n\theta^n + \frac{1}{\varepsilon}N\theta^N \\ &= \frac{\theta - N\theta^N + (N-1)\theta^{N+1}}{(\theta-1)^2} + \frac{1}{\varepsilon}N\theta^N. \end{aligned} \tag{3.8}$$

Here we used the derivative of the geometric sum in the last step. The monotonically increasing function $\theta_{\mathrm{tot}}(\theta)$ is visualized in Fig. 3.2. There is a kink in the function where the power-law scaling changes. This kink can be found numerically by maximizing

$$\frac{\mathrm{d}^2}{\mathrm{d}\xi^2} \ln \theta_{\mathrm{tot}}(\mathrm{e}^{\xi}) \tag{3.9}$$

with respect to the reduced monomer concentration $\theta = \mathrm{e}^{\xi}$. We call this concentra-

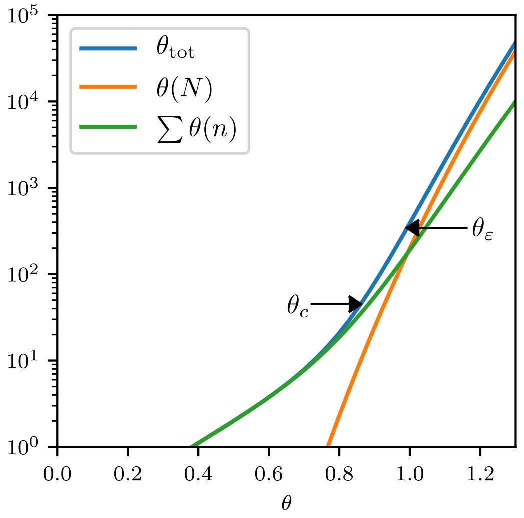

Figure 3.2: Different terms in the total concentration $\theta_{\mathrm{tot}}(\theta)$. The orange and green line denote the amount of monomers in maximum size clusters and the sum of all other monomers respectively. θ_c is the critical aggregation concentration, where θ_{tot} has a kink and θ_ε is the concentration where half of the monomers are in maximum sized clusters.

tion the CAC $\theta_c(N, \varepsilon)$. At lower θ, increases in the total concentration are accompanied by sizable increases in the equilibrium monomer concentration, while beyond θ_c, increases in θ_{tot} go almost exclusively towards generating new clusters. In addition to the critical monomer concentration we define the monomer concentration where half of all monomers are build into maximum size clusters as θ_ε. Both of these concentrations are also visualized in Fig. 3.2.

Fig. 3.3(a) shows the CAC as a function of ε and maximum cluster size N. θ_c typically increases for increasing ε and N. Holding ε constant θ_c increases and approaches $\theta_c = 1$ for increasing N as shown in Fig. 3.3(b). Conversely, for constant N and decreasing ε, θ_c decreases and scales approximately as $\theta_c \sim \varepsilon^{\frac{1}{N}}$ for $\varepsilon \ll 1$ (see Fig. 3.3(c)). This can be seen by investigating the power law scaling $\theta_c \sim \varepsilon^\alpha$ as a function of N at low ε. Here we determine the powerlaw by comparing θ_c at two different (low) ε extracting the power law exponent as

$$\alpha(N) = \frac{\ln \theta_c(N, \varepsilon_1) - \ln \theta_c(N, \varepsilon_2)}{\ln \varepsilon_1 - \ln \varepsilon_2}, \text{ with } \varepsilon_1 = 10^{-6},\ \varepsilon_2 = 10^{-7}. \tag{3.10}$$

The result in Fig. 3.4 suggests, that indeed the exponent of the power law again scales with a power law.

3.3.2. Relaxation behavior

We now look for the eigenvalues of J in the case that ε is small, later we will approximate the contribution of ε as a linear perturbation. The eigenvalue problem can be solved by using the known eigenvalues of tridiagonal Toeplitz matrices and

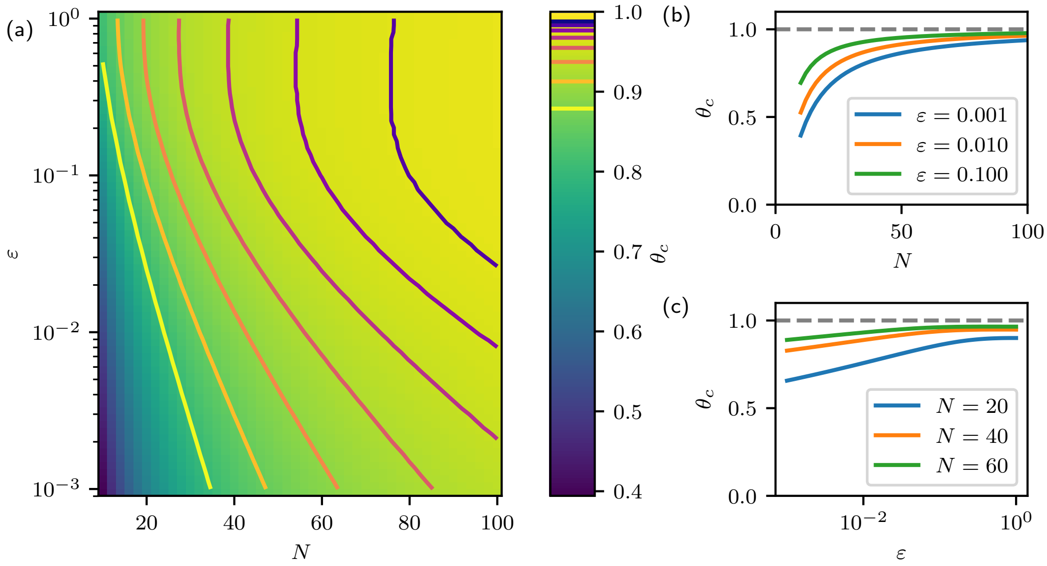

Figure 3.3.: The critical aggregation concentration θ_c (a) as a function of ε and N, (b) as a function of N and (c) as a function of ε.

Laplace Expansion of J along the last column

$$\begin{aligned} \det(J - \lambda E) &= -\lambda \det(T - \lambda E) \overset{!}{=} 0 \\ \Leftrightarrow \quad & \lambda = 0 \vee \det(T - \lambda E) = 0. \end{aligned} \tag{3.11}$$

Thus the eigenvalues are $\lambda_0 = 0$ (with right eigenvector $\vec{v}_0 = (0, \dots, 1)^T$) and the eigenvalues of the matrix T which is the matrix J where the last row and the last column are omitted. The eigenvalues λ, right eigenvectors $\vec{v}$ and the left eigenvectors $\vec{w}^T$ of T are

$$\begin{aligned} \lambda_n &= -(1+\theta) - 2\sqrt{\theta}\cos\left(\frac{\pi n}{N-1}\right) \\ v_n^k &= \theta^{k/2} \sin\left(\frac{k\pi n}{N-1}\right) \\ w_n^k &= \theta^{-k/2} \sin\left(\frac{k\pi n}{N-1}\right), \qquad n,\, k \in \{1, ..., N-2\} \end{aligned} \tag{3.12}$$

Now we construct the right eigenvectors of J that correspond to the eigenvalues we obtained from T. Assume $\vec{d}$ is an eigenvector of J for the eigenvalue λ and $\vec{v}$ is the

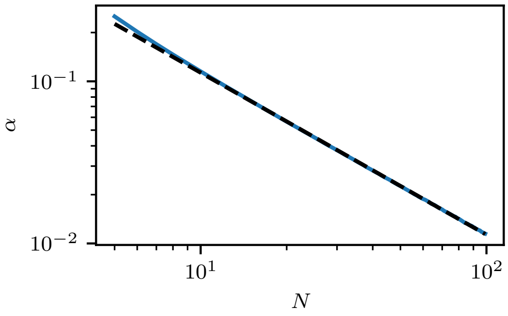

Figure 3.4: Power law scaling exponent of $\theta_c \sim \varepsilon^{\alpha}$ as a function of N. The blue line denotes the numerical result, while the dashed black line denotes γN^{-1} with $\gamma = 1.131$.

corresponding eigenvector of T, then $\vec{d}$ is

$$\vec{d} = \begin{pmatrix} | \\ \vec{v} \\ | \\ x \end{pmatrix} \tag{3.13}$$

with the condition that x must fulfill

$$\left(\begin{array}{cccc|c} & & T & & 0 \\ & & & & \vdots \\ \hline 0 & \cdots & 0 & \theta & 0 \end{array}\right) \begin{pmatrix} | \\ \vec{v} \\ | \\ x \end{pmatrix} = \begin{pmatrix} | \\ \lambda\vec{v} \\ | \\ \lambda x \end{pmatrix} \tag{3.14}$$

i.e. (v^{N-2} is the last element of $\vec{v}$):

$$x = \frac{v^{N-2}\theta}{\lambda} \tag{3.15}$$

For the left eigenvectors $\vec{f}^T$ of J a similar calculation yields

$$\vec{f}^T = \left(\vec{w}^T, 0\right) \tag{3.16}$$

for the eigenvalues pertaining to T. The left eigenvector for λ_0 can be obtained by solving the recurrence relation

$$\begin{aligned} -(1+\theta)f_1 + \theta f_2 &\overset{!}{=} 0 \\ f_n - (1+\theta)f_{n+1} + \theta f_{n+2} &\overset{!}{=} 0. \end{aligned} \tag{3.17}$$

This yields

$$f_n^0 = -\frac{\theta^{-n} - 1}{\theta - 1}. \tag{3.18}$$

Now we can calculate the perturbation of the eigenvalues of J that ε induces to first order as:

$$\delta\lambda_n = \frac{\vec{f}_n^T \delta J \vec{d}_n}{\vec{f}_n \vec{d}_n}, \tag{3.19}$$

where $\vec{d}_n$ and $\vec{f}^T$ are right and left eigenvectors corresponding to the eigenvalue λ_n respectively. We obtain:

$$\begin{aligned} \vec{f}_n \vec{d}_n &= \sum_{k=1}^{N-2} \sin^2\left(\frac{k\pi n}{N-1}\right) = \frac{1}{2}(N-1) \\ \delta\lambda_n &= 2\varepsilon \frac{\theta \sin^2\left(\frac{(N-2)\pi n}{N-1}\right)}{(N-1)\lambda_n} + \mathcal{O}(\epsilon^2) \end{aligned} \tag{3.20}$$

$$\begin{aligned} \vec{f}_0 \vec{d}_0 &= -\frac{\theta^{-(N-1)} - 1}{\theta - 1} \\ \delta\lambda_0 &= -\epsilon\theta^{-(N-1)} \frac{1-\theta}{\theta^{-(N-1)} - 1} + \mathcal{O}(\epsilon^2) \end{aligned} \tag{3.21}$$

Solutions to the starting value problem of (3.4) could now be approximated by

$$\vec{\theta}(\tau) \approx \vec{\theta}_{\text{eq}} + \sum_{n=0}^{N-2} C_n (\vec{d}_n + \delta\vec{d}_n) \mathrm{e}^{(\lambda_n + \delta\lambda_n)\tau}, \tag{3.22}$$

where C_n are constants that are determined by the starting condition, $\vec{\theta}_{\text{eq}}$ contains the equilibrium concentrations of n-mers starting from $n = 2$ and $\delta\vec{d}_n$ are the perturbations of the eigenvectors, which were not calculated here.

The largest non zero eigenvalue will yield the primary relaxation time as $\tau_0 = -1/\lambda_0$, which becomes the most important prominent relaxation for longer timescales, i.e. towards equilibration of the system. It is easy to convince yourself, that $\tau_0(\theta)$ shows a biphasic behavior. Starting from (3.21), for large enough N it follows that

$$\tau_0 = \frac{1}{\varepsilon(1-\theta)}\left(1 - \theta^{N-1}\right) \approx \begin{cases} \frac{1}{\varepsilon(1-\theta)}, & \theta \ll 1 \\ \frac{\theta^{N-2}}{\varepsilon}, & \theta \gg 1 \end{cases}. \tag{3.23}$$

3.4. Single cluster dynamics near equilibrium

3.4.1. Equilibrium

In order to compare the calculations made so far to simulations of a single cluster in a solution that has reached equilibrium, we here look at the situation where we follow one cluster and describe its probability to be of a certain size. The probability p_n follows

$$\begin{aligned} \dot{p}_1 &= -\tilde{J}_1 \\ \dot{p}_n &= \tilde{J}_{n-1} - \tilde{J}_n, \quad n \geq 2 \\ \dot{p}_N &= \tilde{J}_{N-1} \\ \tilde{J}_n &= \theta p_n - p_{n+1}. \end{aligned} \tag{3.24}$$

Note the similarity to equation (3.4) – with the exception of the dynamics of $\dot{p}_1$, that have been adapted in such a way, that the sum of all probabilities is a conserved quantity. This system can be rewritten as

$$\dot{\vec{p}} = \tilde{J}\vec{p} \tag{3.25}$$

$$\tilde{J} = \begin{pmatrix} -\theta & 1 & 0 & \cdots & 0 & 0 \\ \theta & -(1+\theta) & 1 & \ddots & \vdots & \vdots \\ 0 & \theta & -(1+\theta) & \ddots & 0 & 0 \\ \vdots & \ddots & \ddots & \ddots & 1 & 0 \\ 0 & \cdots & 0 & \theta & -(1+\theta) & \varepsilon \\ 0 & \cdots & 0 & 0 & \theta & -\varepsilon \end{pmatrix}_{N\times N} . \tag{3.26}$$

This system is in equilibrium if all fluxes J_n are zero, yielding

$$p_n = \theta^{n-1} p_1 \quad n \neq N \tag{3.27}$$

$$p_N = p_{N-1}\frac{1}{\varepsilon}, \tag{3.28}$$

where p_1 is given by the normalization $1 = \sum p_n$. Note that in contrast to the bulk solution system, where we worked with a $(N-1) \times (N-1)$ sized Jacobian, the dimension of the Jacobian is now $N \times N$, since the dynamics of the probability for the cluster being of size $n = 1$ has to be taken into account.

3.4.2. Relaxation behavior

In a similar fashion to the preceeding section we want to perturbatively calculate the eigenvalues of $\tilde{J}$. Because of the entry $J_{1,1}$ however, the relations from the Toeplitz matrices cannot be used. Instead the eigenvalues of the submatrix $\tilde{T}$ can only be calculated analytically if $\theta = 1$ [172]. They read

$$\lambda_k = -2\theta + 2\theta \cos \frac{(2k-1)\pi}{2N-1}, \quad k \in 1, ..., N-1. \tag{3.29}$$

The corresponding left and right eigenvectors are

$$v_j^k = w_j^k = \cos \frac{(2k-1)(2j-1)\pi}{2(2N-1)}. \tag{3.30}$$

Together with equation (3.15) the last entry of the right eigenvectors of $\tilde{J}$ can be constructed as in equation (3.13). The left eigenvectors last entry is zero as enforced by the second to last row of $\tilde{J}^T$.
The right and left eigenvectors corresponding to $\lambda_0 = 0$ are $u_0^k = \delta_{N,k}$ and $w_0^k = 1$ respectively. Employing equation (3.19) for the linear perturbation yields

$$\delta\lambda_0 = 0 \tag{3.31}$$

$$\vec{f}_n \vec{d}_n = \frac{2N-1}{4} \tag{3.32}$$

$$\delta\lambda_n = \frac{4\varepsilon\theta \cos^2 \frac{(2n-1)(2N-3)\pi}{2(2N-1)}}{\lambda_n(2N-1)} + \mathcal{O}(\varepsilon^2). \tag{3.33}$$

with the approximate knowledge of the eigenvalues one can approximate the temporal evolution of the probability similar to eq. (3.22). Note that eq. (3.31) is in fact exact, as the total probability is conserved, as explained in section 2.2.1.

3.5. Comparison of bulk and single cluster dynamics

The question we want to address in this section is what can we learn from the relaxation behavior of the bulk about the relaxation dynamics of a single cluster? What are the main differences and similarities?

We start our analysis by revisiting the total monomer concentration $\theta_{\text{tot}}(\theta)$. In a typical experimental scenario, the experimenter will predefine the total concentration θ_{tot} and from this, the equilibrium monomer concentration θ will follow according to $\theta_{\text{tot}}(\theta)$. From this perspective $\theta_{\text{tot}}(\theta)$ can be interpreted as a control curve. Figs. 3.5(a) and (d) show this control curve at varying ε and maximum cluster size

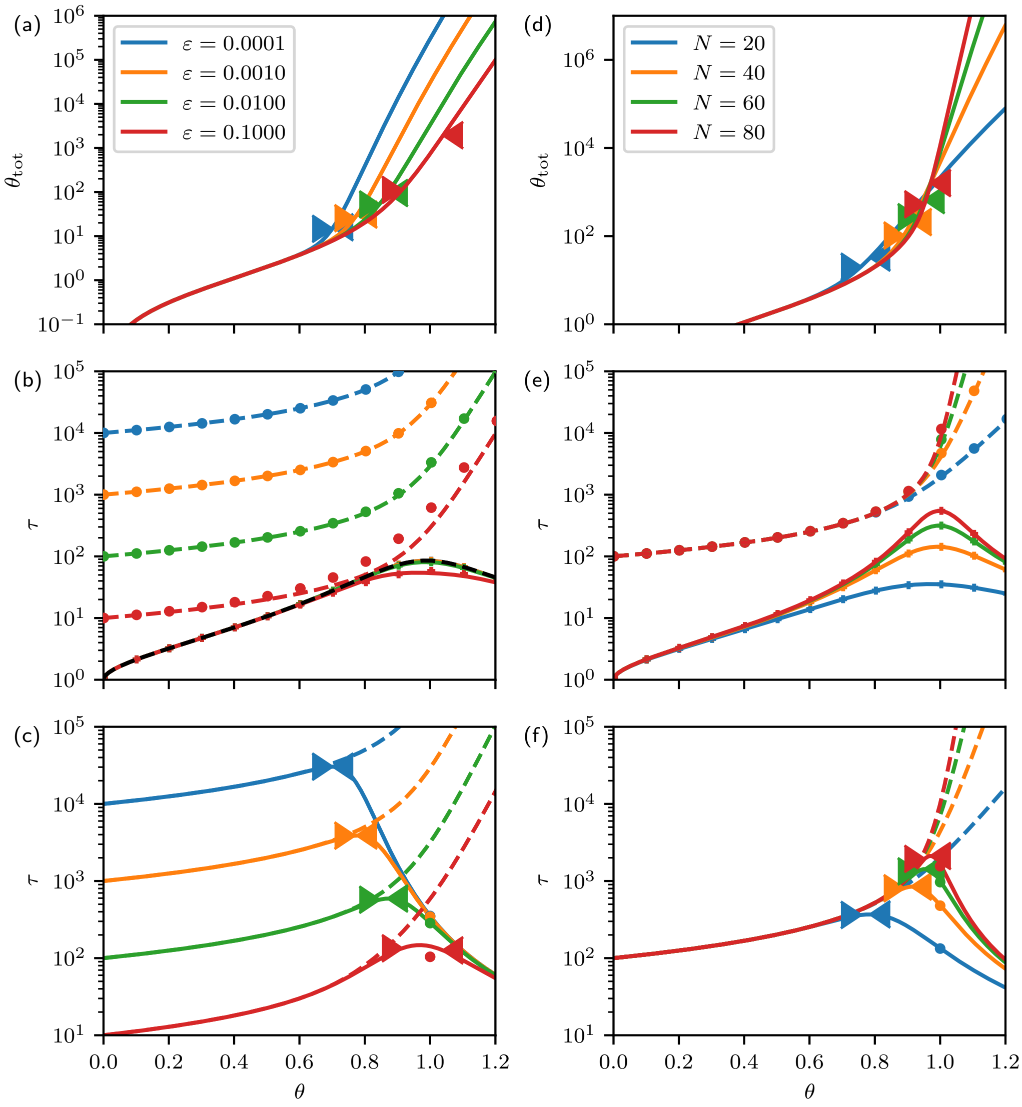

Figure 3.5.: Relation of total monomer to free monomer (a, d) and timescales τ (b, e) related to λ_0 (dashed lines and circles) and λ_1 (solid lines and crosses) as functions of θ. Lines denote the perturbative approximation, while markers denote the numerically determined value. The dashed black line denotes the timescale of λ_1 of the unperturbed system. Note that at free monomer concentrations where the dependency $\theta_{\mathrm{tot}}(\theta)$ becomes very steep the relaxation time scales become very long. (c, f) Relaxation times for the single cluster in an equilibrium solution (solid lines) compared to the relaxation of a system where the monomer concentration is held constant (dashed lines). The dots denote the perturbatively calculated value for $\theta = 1$ from equation (3.33). For (a-c) $N = 30$ and (d-f) $\varepsilon = 0.01$. The right pointed arrowheads denote the critical concentration θ_c, while the left pointed arrowheads denote the concentration θ_ε where half of all monomers are polymerized in maximum sized clusters.

N respectively. Decreasing ε shifts the CAC to lower values while leaving the scaling of $\theta_{\mathrm{tot}}(\theta)$ scaling at concentration lower than and also above the CAC more or less unchanged. Conversely, increases in N shift the CAC to higher values which approach 1, while also steepening the scaling at reduced monomer concentrations beyond the CAC. Interestingly, for decreasing ε, θ_c and θ_ε move closer together which is consistent with the notion, that for decreasing ε the amount of maximum size clusters becomes more important overall.

Figs. 3.5(b) and (e) show the longest two relaxation times τ_0 and τ_1 for the bulk solution. Consistent with the approximation in eqn. (3.23) for high and low θ the scaling of the longest timescale τ_0 does not change much with varying ε. The absolute value however increases strongly with decreasing ε. Also, similar to the control curve θ_{tot}, changes in the maximum cluster size N do not change the behavior much for low θ but the scaling for high θ changes as we could see in eqn. (3.23). The second longest timescale τ_1 rises with increasing θ to a maximum which is typically close to $\theta = 1$. This is also the behavior of the unperturbed system, i.e. this timescale does not show qualitative differences which arise by the perturbation. For increasing N the maximum becomes more pronounced and sharp. We finally compare the longest relaxation timescale of the bulk solution with that of the single cluster. This is summarized in Figs. 3.5(c,f). Remarkably, the longest relaxation time scale of both systems agree for low monomer concentration. At some monomer concentration this behavior stops. While the relaxation time of the bulk continues to increase monotonically, the relaxation time for the single cluster reaches a maximum τ_{max} at θ_{max}, beyond which it decreases again. This also leads to the observation that at the concentration θ_{max} the bulk system always relaxes more slowly than the single cluster probability. Interestingly, the monomer concentration at this maximum is very close to the critical concentration θ_c. As shown in Fig. 3.5(c), the maximum is shifted to lower monomer concentration and increased in magnitude by increasing the stability of the maximum sized cluster (i.e. by decreasing ε). Increasing the maximum cluster size asymptotically shifts the maximum towards $\theta = 1$ in addition to increasing its magnitude (see Fig. 3.5(f)).

Fig. 3.6 quantifies the qualitative observations on the relation of bulk system to the single cluster dynamics at the monomer concentration θ_{max} from Figs. 3.5(c) and (f). Fig. 3.6(a) compares the critical concentration θ_c (dotted lines) with the maximum relaxation time concentration θ_{max} for a range of maximum cluster sizes N as a function of the stability parameter of the maximum sized cluster ε. For all ε the two values are very close to each other, for very low ε (i.e. a very stable maximum sized cluster) the agreement becomes especially good. This is also illustrated in Fig. 3.6(d) where θ_{max} and θ_c (dotted lines) are shown as a function of maximum cluster size

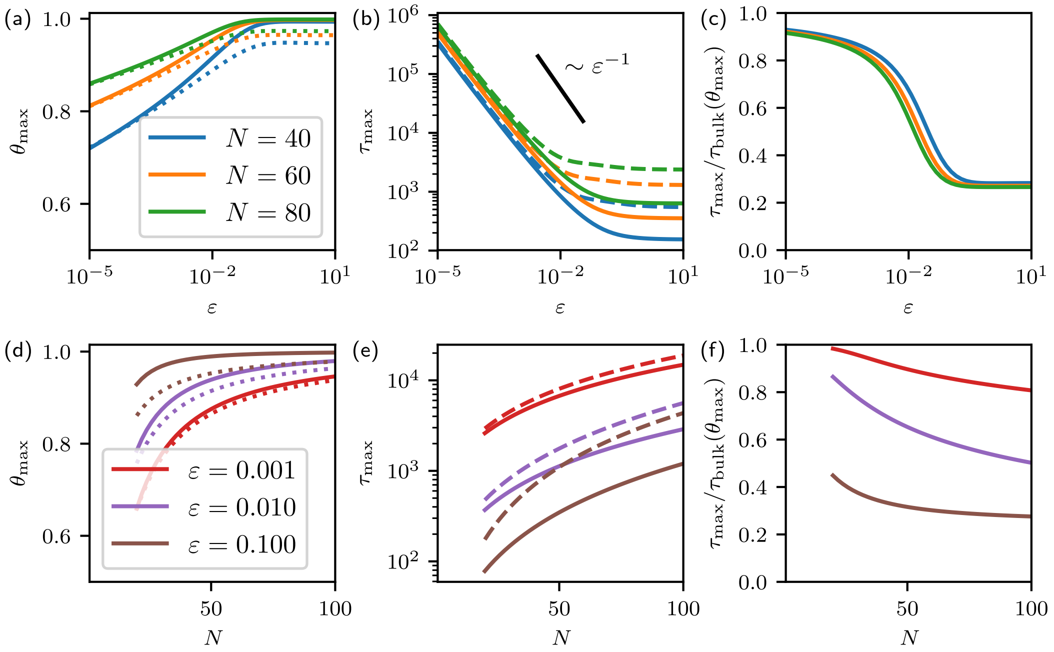

Figure 3.6.: Maximum relaxation time τ_{max} w.r.t. θ as functions of ε and maximum cluster size N. (a, d) Reduced concentration θ yielding maximum relaxation time θ_{max} of the single cluster dynamics. The dotted line denotes the critical concentration θ_c. (b, e) Maximum relaxation time τ_{max} of the single cluster dynamics (solid lines) and relaxation time of the bulk system at θ_{max} (dashed lines). (c, f) Ratio of maximum single cluster dynamics timescale and appropriate bulk timescale.

N for a range of stability parameters ε. Fig. 3.6(b) shows the associated maximum relaxation time τ_{max} together with the relaxation time of the bulk at θ_{max} (dashed lines). The relaxation time decreases with decreasing stability of the maximum sized cluster (i.e. for increasing ε). For very low ε τ_{max} scales with a power law $\tau_{\mathrm{max}} \sim \varepsilon^{-\zeta}$ with $\zeta \lesssim 1$. This behavior is intuitive from the perturbative result in eqn. (3.23) for the bulk system, as $\theta_{\mathrm{max}} \ll 1$ for low enough ε. Since $\varepsilon \ll 1$ is required for the perturbative solution to be correct it is not surprising, that the power law stops being valid for $\varepsilon \gtrsim 10^{-2}$. Evidently, this behavior carries over to the single cluster dynamics. Fig. 3.6(c) shows the quotient of τ_{max} and the bulk relaxation time at the same monomer concentration $\tau_{\mathrm{bulk}}(\theta_{\mathrm{max}}) = \tau_0(\theta_{\mathrm{max}})$. We find typical values for the quotient which are $\gtrsim 0.25$ for higher ε and approach 1 for $\varepsilon \to 0$. In the intermittent regime $\varepsilon \sim 10^{-2}$ we see a quite abrupt change in the value of the quotient, which traces back to the power law $\sim \varepsilon^{-\zeta}$ being valid for higher ε for the single cluster than the bulk system (see Fig. 3.6(b)).

Fig. 3.6(e) shows the maximum relaxation time $\tau_{\max}$ as a function of maximum cluster size N for a range of ε. The relaxation time increases with size and while the bulk system relaxes more slowly than the single cluster, for low enough N it also increases more quickly in the bulk system than for the single cluster. Overall, this leads to the quotient of the two timescales decreasing with increasing cluster size as is shown in Fig. 3.6(f).

3.6. Relation to constant total concentration case

We now turn to the case where not the monomer concentration θ is held constant but θ_{tot}. The rough respective experimental protocol is:

1. Solve x amout of monomer in volume V of solvent
2. Wait and record concentration of n-mers

Here, the system of ordinary differential equations (ODEs) becomes nonlinear because of the time evolution equation for the monomer concentration. As polymerization of two monomers to a dimer is a two particle reaction, the polymerization speed of monomers is quadratic in monomer concentration. For this reason—and the fact that even if we were to linearize the system it would become too complicated to solve analytically—we base our investigations of this section on numerical solutions of the ODE system, which we compare to solutions of constant monomer concentration case.

Fig. 3.7(a) shows a solution of the Becker-Döring equations for a maximum size of $N = 10$ for a constant total concentration of $\theta_{\text{tot}} = 1000$. After an initial phase of relaxation of the monomer concentration (see Fig. 3.7(b)) the solution is described well by

$$\vec{\theta}(\tau) = \theta_{\text{eq}} - \sum_{n=0}^{N-2} C_n \vec{d_n} \mathrm{e}^{\lambda_n \tau - \tau_{\text{const}}}. \tag{3.34}$$

Here $\vec{d_n}$ and λ_n are the numerically determined eigenvectors and corresponding eigenvalues—these are sorted in descending order—of the Jacobian and τ_{const} is the time after which the further relaxation can be described well. Fig. 3.7(c) shows some examples of the eigenvectors. The coefficients C_n are chosen, such that at $\tau = \tau_{\text{const}}$ the numerical solution of the ODE match $\theta(\tau)$ from eqn. (3.34). One can clearly observe, that the lower the eigenvalue, i.e. the faster the relaxation time, the more often the eigenvectors change sign. This can be interpreted as follows, oscillations of different frequencies as eigenvectors of a system enable representing many different

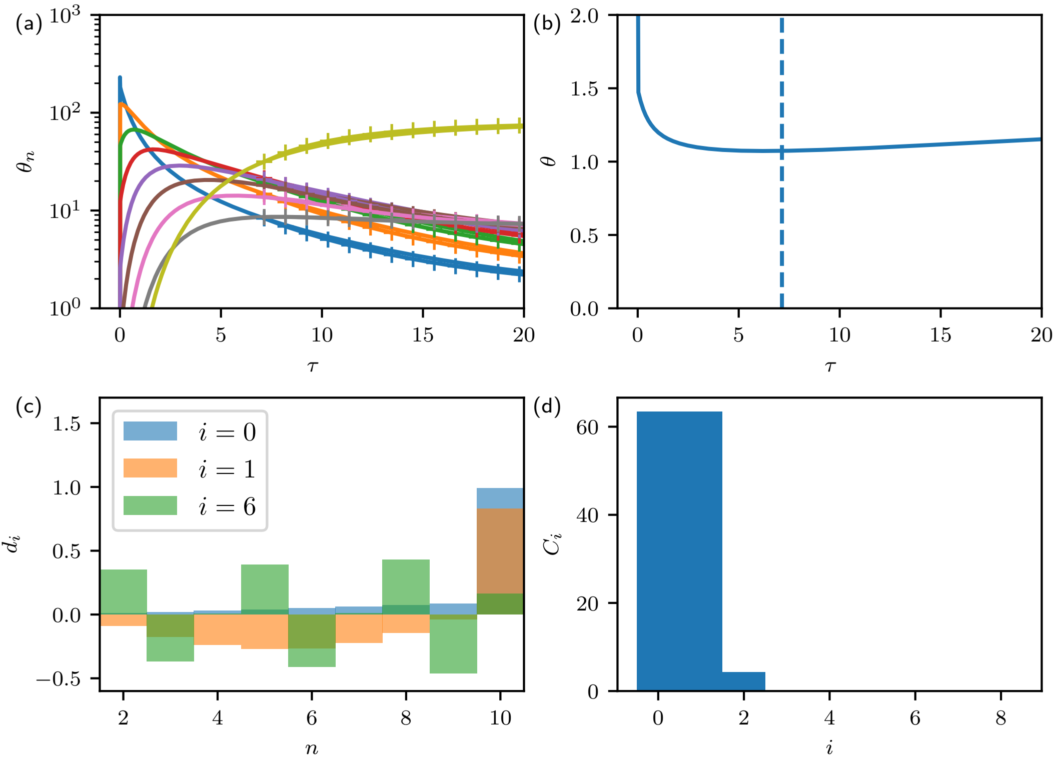

Figure 3.7.: Comparison of constant total concentration simulation to constant monomer situation with $\varepsilon = 0.1$ and $N = 10$ and $\theta(\tau = 0) = \theta_{\text{tot}} = 1000$. (a) Time course of concentrations of n-mers (from top to bottom on the left side $n = 2, ..., 10$). The solid lines denote the numerical solution of the ODE system, while the '+' markers indicate the linear relaxation close to equilibrium where the monomer concentration is assumed to be constant. (b) Time course of monomer concentration θ, the dashed line denotes the time τ_{const} at which changes in the monomer concentration become small. (c) Typical numerically determined eigenvectors of the linear system, where n denotes the according n-mer. $i = 0$ is the eigenvector with longest relaxation time. (d) Constants C_i given by the starting conditions at τ_{const}. Only the three slowest relaxation modes matter.

vectors as linear combinations of the eigenvectors. In this system the high frequency oscillations (the eigenvectors with highly negative eigenvalue) decay much faster in time, much like in the diffusion equation high spatial frequency distributions decay faster. This comparison is very intuitive in the sense, that the Becker-Döring model as-well as the diffusion equation are very local models. In the Becker-Döring equations the concentration of n-mers communicates with the concentration of m-mers via all the j-mers with size between n and m but no direct concentration fluxes between n- and m-mers exist if $|n - m| \neq 1$, similarly in the diffusion equation the differential operator dictates a local dynamic. The result of this in the Becker-Döring equation can be seen in Fig. 3.7(d). Here the coefficients C_n of eq. (3.34) are shown. Consistent with the previous argument, only the first three eigenvectors contribute to the result in a meaningful way. This illustrates that while oftentimes the time evolution of observables of experimental self-assembly studies can be described well by a sum of multiple saturating exponential functions we should not hope for this experimentally observed set of relaxation timescales to be exhaustive. Instead, there will often be processes with timescales which are hidden because they are smaller than the time the monomer concentration needs to relax to its equilibrium value. These faster processes in the model presented here are ones, that locally smooth out the concentration profile $\vec{\theta}$.

3.7. Conclusion

This chapter introduced a version of the Becker-Döring equation that serves as a simple model system for self-assembling systems that reach a fully assembled state, which is stabilized. Similar to other studies of the Becker-Döring equations with a maximum cluster, here we also found an appreciable gap between characteristic timescales which indicates the existence of metastable solutions [167, 168, 173].

More importantly, the relation between the stochastic dynamics of a single cluster in an equilibrated solution was compared to the dynamics of the bulk system. The graph θ_{tot} vs. θ in Fig. 3.5(a) and (d) shows how the total amount of monomer scales with the amount of free monomer in solution. It can be viewed as a control curve that is probed when performing a polymerization experiment i.e. insert θ_{tot} monomers to achieve an equilibrium behavior characterized with monomer concentration θ. The relation becomes very steep where finite size clusters tend to form often; which makes it a priori quite likely that experiments are carried out close to this concentration, the CAC.

Interestingly, at concentrations near the CAC the relaxation time of the single cluster system is maximal (see Fig. 3.5(c) and (f)). When comparing the relaxation of the a single complex to the relaxation time of the bulk system it becomes clear, that the relaxation time of the bulk system with constant monomer concentration will typically be an upper bound to the relaxation time of the single complex. For particularly small maximum size clusters that are also very stable, the relaxation times at the CAC of single cluster and bulk dynamics approximately equal. For system sizes studied here, the differences between the two relaxation times were always less than an order or magnitude.

These findings have implications on the comparison of single cluster simulations, that are often performed due to limited computational resources, to the dynamics of self-assembly experiments, where it is very difficult to follow a single cluster, but much simpler to gauge the average molar weight of the clusters by light scattering [54, 165, 174]. If a monomer concentration vs. relaxation timescale of the single complex can be obtained for a given model and typical relaxation timescale for the experimental system are known, this allows for a rough estimation of the on- *and* off-rate. One should find the maximum relaxation time $\tau_{\mathrm{max}}(\theta_{\mathrm{max}})$ in units of inverse off-rate which is related to the experimental value t_{exp} by

$$\tau_{\mathrm{max}} k_{\mathrm{off}} \lesssim t_{\mathrm{exp}}. \tag{3.35}$$

For the typical on-rate $k_{\mathrm{on}} c_{\mathrm{max}}$ at the CAC it follows that

$$k_{\mathrm{on}} c_{\mathrm{max}} = k_{\mathrm{off}} \theta_{\mathrm{max}} \lesssim \theta_{\mathrm{max}} \frac{t_{\mathrm{exp}}}{\tau_{\mathrm{max}}}, \tag{3.36}$$

which introduces bounds for both on- and off-rate, that become better approximations as maximum cluster size decreases and maximum cluster stability increases.

4. Mechanosensitive self-assembly of myosin II minifilaments

Self-assembly and force generation are two central processes in biological systems that usually are considered in separation. However, the signals that activate non-muscle myosin II molecular motors simultaneously lead to self-assembly into myosin II minifilaments as well as progression of the motor heads through the crossbridge cycle. Here we investigate theoretically the possible effects of coupling these two processes. Our assembly model, which builds upon a consensus architecture of the minifilament, predicts a critical aggregation concentration at which the assembly kinetics slows down dramatically. The combined model predicts that increasing actin filament concentration and force both lead to a decrease in the critical aggregation concentration. We suggest that due to these effects, myosin II minifilaments in a filamentous context might be in a critical state that reacts faster to varying conditions than in solution. We finally compare our model to experiments by simulating fluorescence recovery after photobleaching.

The results of this chapter have been published in Physical Review E [175].

4.1. Introduction

Molecular motors powered by ATP-consumption are ubiquitous in living organisms, converting chemical energy into movement and force at the right time and place [176]. The most important molecular motor for force generation is the two-headed non-processive molecular motor myosin II, which occurs in many different variants. In skeletal muscle, hundreds of skeletal myosin II motors are assembled into the thick filament that forms the core of the sarcomere. Large assemblies of the corresponding myosin II variants also exist in cardiac and smooth muscle. In non-muscle cells, however, non-muscle myosin II assembles into much smaller groups, so-called myosin II minifilaments, that due to their small size can be dynamically regulated to generate forces on demand, in particular in the actomyosin cortex and in stress fibers [49, 51]. Very importantly for the way myosin II minifilaments function, it is not only force generation, but also assembly that is regulated in non-muscle cells. In particular, the Rho-pathway leading to myosin II minifilament activation has two branches, one regulating actin assembly through the formin mDia1 and one leading to phosphorylation of the myosin II regulatory chain [86, 87]. This in turn leads both to myosin II assembly and cycling of the motor heads. Together, these different elements make sure that myosin II minifilaments are assembled in a functional state in which motor heads and actin filaments work together synergistically. However, because assembly and force generation of non-muscle myosin II minifilaments are usually studied in isolation, no quantitative understanding exists for how these two processes are coupled in cells. Here we introduce and analyze a mathematical model for this purpose.

Regarding force generation, we start from earlier models of force generation, which occurs by myosin cycling through a set of mechanochemical states, as first formalized by Huxley [61]. Briefly, myosin binds to actin, then the lever arm performs the powerstroke, the myosin detaches from actin and the lever arm resets. This cycle is powered by ATP-hydrolysis and each of these states corresponds to a step in the hydrolysis cycle. Cross-bridge models are master equation models using this discrete sets of states, and have been used with great success to study a variety of effects that arise due to the mechanochemistry of molecular motors [68, 69, 71, 73–75, 77]. One important aspect is the realization that myosin II acts as a catch bond, which means that bond lifetime is increased under mechanical force [4, 64]. This leads to accumulation of myosin to stressed parts of the actin network [177]. Earlier we have incorporated the catch bond character of myosin II in a master equation approach for minifilaments and showed that it can explain many aspects of cellular mechanosensitivity [70].

While the force generating aspect of myosin II has been studied and modeled in great detail, the literature describing the dynamic self-assembly of myosin II minifilaments is less developed. For myosin II minifilaments from the amoeba Dictyostelium, a very detailed model has been developed, that however incorporates some biological details that do not necessarily apply to other minifilament systems [4, 177–180]. Here we aim at a more generic model in the spirit of the aggregation-fragmentation theory by Smoluchowski [105] and Becker and Döring [111], which is the standard model for assembly processes. Our starting point is the observation that non-muscle myosin II minifilaments from human cells assemble to a stereotypic size of 28 to 30 molecules, corresponding to a linear size around 300 nm [34, 54]. Thus, they are an example for molecular assemblies of well-defined size, similar to e.g. virus capsids, whose assembly has been modeled before in great detail [100, 163, 181, 182]. The very regular architecture of the virus capsids could be determined by electron microscopy, which motivated self-assembly models that were built upon the neighborhood relations of the constituents of the capsid. It has been argued that assembly of finite-sized complexes works best if the cluster size distribution is relatively flat with peaks only for the monomer and complete complexes [183]. Other examples for self-assembling protein complexes that have been modeled include clathrin coats, adhesion complexes, cytoskeletal fibers and chromatin [103].

In order to model myosin II self-assembly in detail, we use the observation that non-muscle myosin II assembles into bipolar filaments of approximately 30 proteins by electrostatic interactions of the coiled-coil tail domain, where electric charges are periodically arranged and support both parallel and anti-parallel alignment of rods [55]. Binding energies have been estimated to be about $35\,k_BT$ at zero ionic strength, however, due to the low screening length in cytoplasma ($\sim 1\,\mathrm{nm}$ at $100\,\mathrm{mM}$ NaCl) for physiological conditions, we expect and employ much lower binding energies in our model. Different options for rod arrangement within a bipolar filament have been proposed for muscle myosins of various species [58, 184]. The three-dimensional structures of the side regions of bipolar filaments of muscle cells from different species have been reconstructed from cryo-electron microscopy images with a resolution of $\sim 2\,\mathrm{nm}$ [81, 185]. This quasi-atomic resolution has been able to be achieved using the known helicity of and periodicity within the side regions of the muscle bipolar filament. In these region myosin heads project out from the core, which is made up of the myosin tails, at equidistantly recurring axial levels, so called crowns [186]. Between two subsequent crowns there is typically a well defined axial twist that varies between species. Potentially due to the missing spatial periodicity in the bare zone, until now it has only been possible to reconstruct the bare zone of bipolar filaments with a resolution of $\sim 5\,\mathrm{nm}$ which does not suffice to identify individual myosin tails [187]. The authors could nevertheless show that the bare zone consists of multiple protofilaments interacting with each other. Here we will use this molecular information to develop an assembly model that takes this known molecular information into account, but on the other side is generic enough to describe myosin II minifilaments from different species. We then couple it to our crossbridge model for force generation and analyze the combined model in great detail. Finally we will discuss its relation to experimental data.

This chapter is organized as follows. We first introduce our model as a graph. Growth of a minifilament is identified with increasing occupancy of the nodes of this graph. For a given cluster, we then assume actin binding and force generation through motor cycling. We analyze the dynamics of the combined model and identify steady states. We find that at a certain monomer concentration the relaxation time increases dramatically. We explore the equilibrium properties of the model as a function of applied force and monomer concentration around this concentration, revealing that already unloaded actin facilitates minifilament assembly, with applied

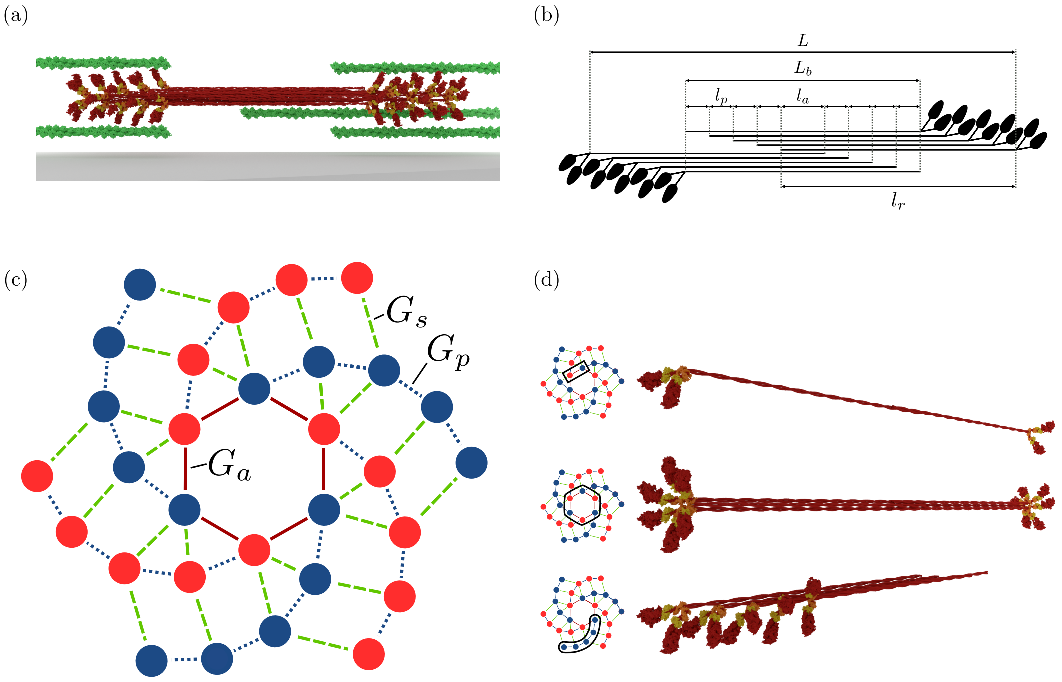

Figure 4.1.: Assembly model. (a) Artistic 3D rendering of a myosin minifilament that contracts actin fibres. (b) Schematic representation of a slice consisting of two anti-parallel protofilaments with indicated lengths (minifilament length L, bare zone length L_b, parallel stagger l_p, anti-parallel stagger l_a and rod length l_r). (c) The graph on which the assembly occurs. The light red and the dark blue discs represent sites with opposing myosin heads. The solid red lines in the middle represent strong interactions between anti-parallel myosin rods, the dotted blue lines represent interactions caused by a favorable parallel overlap of myosin rods and the dashed green lines represent weak anti-parallel interactions. (d) Artistic representation of intermediates (right), with corresponding regions of the graph indicated (left). (top) Initial nucleation seed of two anti-parallel molecules. (middle) Inner core of the minifilament containing three of the nucleation seeds. (bottom) One protofilament.

force enhancing this effect. In addition we produce fluorescence recovery after photobleaching (FRAP) trajectories which can be compared to experiments.

4.2. Models and methods

4.2.1. Minifilament organization

Fig. 4.1(a) shows an artistic representation of a myosin II minifilament that is contracting opposing actin filaments. The number of myosin II molecules in a minifilament has been estimated to be between 28 and 30 [34, 54], from which we take the later value, because it allows for a more symmetric cluster architecture. Each myosin is a hexamer comprised of two myosin heavy chains, two essential light chains and two regulatory light chains. The heavy chain globular region (i.e. the myosin head) can bind to actin filaments and displace them by undergoing a powerstroke in the neck region behind the head region. The two heavy chains form a long and relatively stiff rod due to hydrophobic interactions. To the outside, this rod carries a very specific pattern of charged amino acids which leads to favorable interactions with other myosin rods at well-defined staggering distances [54, 55, 58]. The most important one seems to be the anti-parallel overlap at $l_a = 45$ nm, which establishes the basic bipolar structure of the minifilament. The most favorable parallel staggers are at 14.3 nm and 43 nm. Here we focus on the first one, $l_p = 14.3$ nm. Fig. 4.1(b) shows a schematic two-dimensional representation of the most likely arrangement of myosin II rods in a slice through the minifilament given these two prominent staggers. With the rod length $l_r = 160$ nm, the overall minifilament length is $L = 2l_r - l_a = 275$ nm and the length of the bare zone (no myosin heads) is $L_b = L - 8l_p = 160$ nm, in good agreement with electron microscopy data [54]. Note that three such slices have to be combined to give the full minifilament with 30 molecules.

In order to represent the full three-dimensional structure of the minifilament, we represent it by the graph shown in Fig. 4.1(c). Here the two opposing directions of the rods are represented by two different colors for the nodes. The core of the filament is defined by six rods forming a hexagon, with three rods from each direction. They are held together by the anti-parallel overlap with staggering length l_a and we assign a binding energy of G_a to this kind of bond. From each of the six rods in the core, one string with four additional rods of the same orientation spirals out to the periphery. These five rods define the five crowns and together our graph contains the $2 \times 3 \times 5 = 30$ molecules assumed in our model. Note that two neighboring spirals together form the slice shown in Fig. 4.1(b). The spiraling rods are held together by the parallel stagger with l_p and we assign a binding energy G_p to these bonds. Because intermediates with both anti-parallel and parallel staggers have been observed and in the absence of further information, here we assume that G_a and G_p have similar values. Note that the three-dimensional structure does not change the linear lengths L and L_b for the minifilament and the bare zone given above. Finally we note that our graph from Fig. 4.1(c) requires anti-parallel rods of not so favorable staggers to be in close proximity. Although not directly observed experimentally yet, these interactions must be present in order to fulfill the geometrical constraint that the bare zone is roughly six times as thick as the diameter of one myosin tail while maintaining an architecture which is organized from a core that is located in the center of the minifilament. We note that a central core and thereby very accessible side regions explain the relatively fast exchange times that have been measured with FRAP [90, 143] and also the dynamic rearrangements of minifilaments observed in live cell microscopy with structured illumination [188]. We assign a relatively low binding energy G_s to this kind of bonds.

Although our model is a strong simplification, it captures all the geometrical properties known from the literature. We note that it is highly likely that real minifilaments are more disordered than assumed here. For example, we do not expect all six rods in the core to be exactly aligned, because they form a tight bundle in which also next-nearest neighbors are relevant and which might use some of the other staggers known for myosin [55]. It is also known that different species form different staggers and have different rod architectures. The graphical model suggested here should be considered to be a consensus architecture that captures most of the known general features of myosin II minifilaments.

4.2.2. Minifilament assembly

We now use the graph introduced in Fig. 4.1(c) to define the minifilament growth dynamics. Starting from one myosin molecule in the core, the minifilament most likely polymerizes by recruiting new myosin molecules onto neighboring sites. Thus the growth dynamics can be represented by populating more and more of the nodes of the graph. Fig. 4.1(d) shows different intermediates of the assembly process, both as subsets of the graph and as artistic representations in space. We assume that association is diffusion-limited, with a rate k_{on} that does not depend on the binding energy gained, but is proportional to the concentration of myosin molecules. Dissociation corresponds to turning an occupied site into an unoccupied one. Assuming detailed balance, this occurs with a rate

$$k_{\text{off}} = k_{\text{off}}^0 \exp\left(-\frac{n_s G_s + n_p G_p + n_a G_a}{k_B T}\right) \tag{4.1}$$

that is dependent on the number of each particular bonds (n_s, n_p, n_a) that are broken due to the removal of the dissociating myosin II molecule. If a myosin dissociates from the minifilament such that two separate patches are generated, we remove the patch that does not contain the central region of the graph. Our growth model is now complete and can be simulated using the Gillespie algorithm for reaction kinetics [189].

Table 4.1.: Parameters used in the simulation of minifilament assembly and force generation.

Parameter	Symbol	Value	References
Transition	k_{01}	0.2	[72]
rates [s^{-1}]	$k_{20,0}$	0.35	[72]
	Δ_c	0.92	[72]
Force scales	F_c	1.66	[72]
[pN]	F_s	10.35	[72]
Energy scales	G_a	3	our estimate
[$k_B T$]	G_p	3	our estimate
	G_s	1	our estimate

4.2.3. Crossbridge model

The crossbridge cycle of a single myosin II protein is modeled according to the Parallel Cluster Model (PCM) [68, 69]. In the PCM, the crossbridge cycle is described by a three-state system as depicted schematically in Fig. 4.2(a). The first state of the PCM is the unbound state (UB) of myosin. From there a myosin head can bind to actin into the weakly bound state (WB). Now the lever arm can swing backwards which reversibly transitions the myosin head to the post-powerstroke state (PPS). This transition is very fast (milliseconds). Finally, from the PPS state myosin can unbind from actin via two different reaction paths, namely the catch-path and the slip path. The reaction rate along the catch-path decreases exponentially with increasing force, while along the slip-path it increases exponentially. The model summarizes these effects into a cumulative rate that depends on the force that the myosin-actin bond retains, i.e.

$$k_{20}(F) = k_{20,0}\left[\Delta_c \exp\left(-\frac{F}{F_c}\right) + (1-\Delta_c)\exp\left(\frac{F}{F_s}\right)\right], \tag{4.2}$$

where Δ_c is the fraction of myosin heads that use the catch-path to unbind at zero force, F_c and F_s are the critical forces for the catch-path and the slip-path, respectively, and $k_{20,0}$ is the rate at zero force. The inverse of the rate, i.e. the mean dwell time, is shown in Fig. 4.2(b). Here the typical time scale is larger than seconds.

When part of an ensemble is retaining a force, it is assumed that, by consecutive unbinding and rebinding of the heads, the strain of all motors that are in the same mechanochemical state is the same. Thus, the strain only depends on the current state of the ensemble (i.e. how many motors are in each state of the crossbridge cycle) and not on the history of the filament. In this manner the model describes an

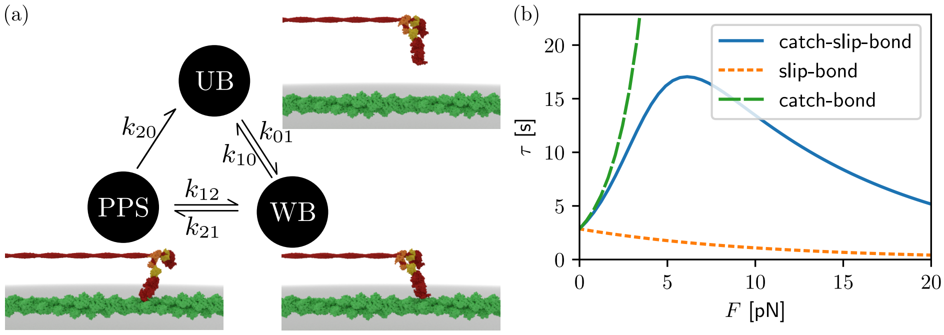

Figure 4.2.: Parallel Cluster Model (PCM) for force generation. (a) The PCM considers the three most important states of the crossbridge cycle. The reaction rates k_{01} and k_{10} are constant, while the rate k_{20} depends on force as given in (4.2). The rates k_{12}, k_{21} are high compared to the other rates. (b) Mean dwell time of a single myosin head on actin assuming catch-slip bond ($\Delta_c = 0.92$), a pure slip bond ($\Delta_c = 0$) and a pure catch-bond ($\Delta_c = 1$).

ensemble of N motors where $i \leq N$ motors are in an actin bound state and $j \leq i$ motors have performed the powerstroke. Hereby it is possible to calculate the strain x_{ij} of the weakly bound motors when the cluster is balancing against an external force F_{ext} yielding $x_{ij} = (F_{\text{ext}} - jkd)/ik$, where k is the spring constant of the neck linkers and d the length of the powerstroke.

The high transition rates between the PPS state and the WB state compared to the unbinding rates allow to maintain a local thermal equilibrium (LTE) between the two bound states. The probability for j motors being in the PPS state, when i are bound, follows the Boltzmann distribution $p(j|i) = \exp(-E_{ij}/k_B T)/Z$, with the partition sum Z. The energy $E_{ij} = E_{\text{el}} + jE_{\text{pp}} + E_{\text{ext}}$ is the sum of the elastic energy $E_{\text{el}} = k[(i-j)x_{ij}^2 + j(x_{ij} + d)^2]/2$ stored in the neck linkers, the free energy bias towards the PPS state $E_{pp} \approx -60\,\text{pN}\,\text{nm}$ and the contribution of any conservative external force field E_{ext}. For a non-conservative constant force – as discussed here – $E_{\text{ext}} = 0$.

LTE of the bound states allows us to average over all possible numbers of motors j in the PPS, thus making it possible to describe the probability of i motors bound to actin in the one-step master equation

$$\frac{\mathrm{d}}{\mathrm{d}t} p_i = r(i+1)p_{i+1} + g(i-1)p_{i-1} - [r(i) + g(i)]p_i \,. \tag{4.3}$$

As $N - i$ motors can bind, the binding rate $g(i)$ is given by $g(i) = (N-i)k_{01}$. Unbinding is possible from the WB state and the PPS state such that the rate reads $r(i,j) = (i-j)k_{10} + jk_{20}(f(i,j))$, where $f(i,j) = (F_{\text{ext}} - dk(i-j))/i$ is the force that is retained by one motor in the PPS state. Averaging over j yields $r(i) = \sum_j p(j|i)r(i,j)$. In the case of constant non-conservative forces, this sum has been found to be approximated well by $r(i) = r(i,i)$ [69]. The model depends strongly on the chosen rates. Here we use the rates that we have previously used to study non-muscle myosin IIB [71], which is considered to be the main isoform responsible for maintaining long lasting forces [59].

4.2.4. Coupling of self-assembly and force generation

Each occupied site of the self-assembly model can be in one of the three states of the crossbridge model. The two sub-ensembles with the different orientations (blue and red in the graph) work against each other in a tug-of-war situation which has been modeled before with the PCM for fixed minifilament sizes [70]. This implies that force can be generated only if both sides are attached to actin. Here we assume that for each two-headed myosin molecule, only one head can be active at a given time, as experiments have suggested that one of the two heads mainly optimizes the force generating action of the other, while not being active itself [190, 191]. Thus from the 60 heads, only 30 are considered in our model. To complete the model, we now have to couple the minifilament to a specific mechanical environment. Here we choose to work with a constant force ensemble, in contrast to an elastic environment with own stiffness. In this way, we can avoid any dependence of our model on neck linker stiffness, whose effective value is known to depend on context [64, 192]. Earlier, neck linker stiffness values have been used that lead to strong occupancy of the PPS states [68–70]. In the combined model, actin-bound motors cannot dissociate from the ensemble directly, but must first unbind from actin by going into the UB state. This makes dissociation of the actin bound motors a two-step process that depends on features of both models.

4.2.5. Mean-field theory

In order to obtain an intuition for the behavior of the system it is instructive to coarse grain the assembly model to one variable. We consider one side of the minifilament, e.g. all myosin monomers with heads pointing to the right in Fig. 4.1(a), and denote its size with N. A monomer addition scheme for polymerization means

$$H_N + H_1 \underset{\alpha_{N+1}}{\overset{\beta}{\rightleftharpoons}} H_{N+1}\,, \tag{4.4}$$

where H_1, H_N, H_{N+1} represent monomers, N-mers and $(N+1)$-mers, respectively, and β and α_{N+1} are the association and dissociation rates for the half-filament. The equilibrium size distribution for this model is solved recursively via detailed balance:

$$p_{N+1} = \frac{\beta}{\alpha_{N+1}} p_N \, . \tag{4.5}$$

If we now require the dissociation rates α_N of the monomer addition scheme to be such that the equilibrium size distribution of one side of the minifilament assembly model from section 4.2.2 is reproduced, equation (4.5) provides a conditional equation for the dissociation rates α_N if β is given. The rate β however is not known since the total association rate depends on the current assembly state of the minifilament. We assume $\beta = 3k_{\text{on}}$, as each side of the graph is made up of three protofilaments. Additionally, matching with the assumption that actin-bound motors cannot dissociate from the ensemble, the dissociation rate has to be weighted by the fraction $(N-i)/N$ of motors in the UB state.

Now, the state of the filament can be projected to two integers per side of the filament, the cluster size N and the number of actin bound motors i. The master equation for one side of the filament is

$$\begin{aligned} \frac{\mathrm{d}}{\mathrm{d}t} p_{N,i} = &- \left(\alpha_N \frac{N-i}{N} + \beta_N \right) p_{N,i} \\ &+ \alpha_{N+1} \frac{N+1-i}{N+1} p_{N+1,i} + \beta_{N-1} p_{N-1,i} \\ &- (r_i + g_{N,i}) p_{N,i} + r_{i+1} p_{N,i+1} + g_{N,i-1} p_{N,i-1} \, , \end{aligned} \tag{4.6}$$

where $\beta_N = 3\ k_{\text{on}}$ if $1 \leq N \leq 14$ and zero otherwise. The α_N are chosen as explained after Eq.(4.5) if $2 \leq N \leq 15$ and zero otherwise. These rules ensure that the normalization of the probability $p_{N,i}(t)$ is time-independent in the allowed domain $1 \leq N \leq 15$ and $0 \leq i \leq N$. From the master equation (4.6) it is possible to construct a mean-field description. Starting from

$$\begin{aligned} \left\langle \frac{\mathrm{d}}{\mathrm{d}t} N \right\rangle &= \sum_{N,i} N \frac{\mathrm{d}}{\mathrm{d}t} p_{N,i} \\ \left\langle \frac{\mathrm{d}}{\mathrm{d}t} i \right\rangle &= \sum_{N,i} i \frac{\mathrm{d}}{\mathrm{d}t} p_{N,i} \end{aligned} \tag{4.7}$$

and shifting summation indices and Taylor expanding around $(\langle N \rangle, \langle i \rangle)$ yields

$$\begin{aligned} \langle \dot{N} \rangle &= \beta - \alpha(\langle N \rangle) \frac{\langle N \rangle - \langle i \rangle}{\langle N \rangle} + \mathcal{O}(\sigma_N^2 + \sigma_i^2 + \mathrm{cov}(N,i)) \\ \langle \dot{i} \rangle &= (\langle N \rangle - \langle i \rangle) k_{01} - \langle i \rangle k_{20}(F/\langle i \rangle) + \mathcal{O}(\sigma_N^2 + \sigma_i^2 + \mathrm{cov}(N,i)) \, . \end{aligned} \tag{4.8}$$

It is possible to compute the time development of the second central moments. These however depend on third central moments, resulting in a closure problem. In the following the second central moments are dropped for simplicity.

From equation (4.8) it is possible to calculate the two nullclines of the system

$$\begin{aligned}\langle N\rangle_{\langle\dot{i}\rangle=0} &= \langle i\rangle\left(1+\frac{k_{20}(F/\langle i\rangle)}{k_{10}}\right)\\ \langle i\rangle_{\langle\dot{N}\rangle=0} &= \langle N\rangle\left(1-\frac{\beta}{\alpha(\langle N\rangle)}\right)\,.\end{aligned} \tag{4.9}$$

4.2.6. FRAP-experiments

The presented model allows for performing *in silico* FRAP experiments by associating another Boolean variable to every occupied site that indicates whether the associated myosin is fluorescently labeled. By starting the Monte Carlo simulation from a non-fluorescent state drawn from the equilibrium distribution and filling up holes that form after dissociation of one molecule with new, fluorescent myosin proteins, FRAP traces can be obtained by calculating the time course of the ensemble average of the number of fluorescently labeled sites.

4.3. Results

4.3.1. Assembly dynamics

We first discuss the assembly model based on the graphical model from Fig. 4.1(c), that is we do not consider yet the coupling to the motor model. We simulated the mean number of assembled myosins N (maximal value 30) for the model described in section 4.2.2 using the Gillespie algorithm and the parameter values from Table 4.1. Fig. 4.3(a) shows the mean trajectory and its standard deviation. We see that the mean assembly dynamics can be described well by an exponentially saturating function $N_a\left(1-\exp(-\tau/\tau_0)\right)+1$, where $\tau = tk_{\text{off}}^0$ is the dimensionless time. Note that the minimal cluster size at $\tau = 0$ has to be 1.

Fig. 4.3(b) shows the plateau value $N_{\text{plat}} = N_a + 1$ as a function of the dimensionless association rate $\kappa = k_{\text{on}}/k_{\text{off}}^0$. One sees that the larger the association rate, the more the mean size N_{plat} approaches the maximal value 30, and that the function has a hyperbolic character, indicating a crossover at the inflection point. Fig. 4.3(c) shows the variance of N, which has a clear peak at a critical value $\kappa_c = 0.018$, indicating a transition between partially and fully assembled minifilaments. Fig. 4.3(d) shows the relaxation time τ as a function of association rate κ, which again has a clear peak at $\kappa_c = 0.018$ (with value $\tau \approx 800$). We interpret these results as crit-

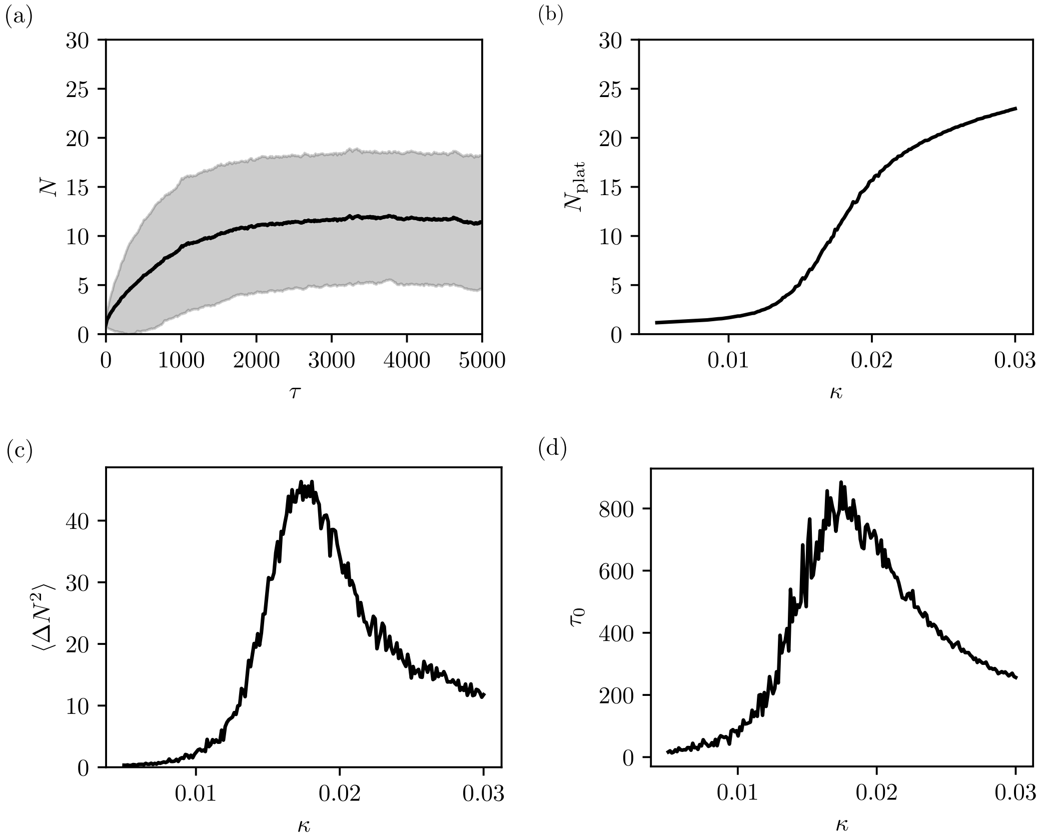

Figure 4.3.: Assembly dynamics. (a) Time course of the mean minifilament size for dimensionless association rate $\kappa = 0.018$ (black line) with standard deviation (grey area). (b) Mean number of assembled myosins as a function of κ. (c) Variance of N as a function of κ. A peak at $\kappa_c \approx 0.018$ indicates the transition between partially and fully assembled minifilaments. (d) Relaxation time of the minifilament as a function of κ as obtained from a saturating exponential fit to the mean size of an assembling cluster.

ical slowing down. Because the association rate κ is proportional to the myosin II concentration in solution, the critical association rate κ_c corresponds to a critical aggregation concentration (CAC). In the following, we will investigate our model around this critical point.

From the stochastic simulations, we can also obtain the full cluster size probability distribution. From here on, we will still simulate the full minifilament, but only show results for one half, because the two halves are statistically equivalent. Thus from here on the maximal cluster size is 15. The size distribution for a half-filament is shown in Fig. 4.4(a). At association rates below the critical value κ_c,

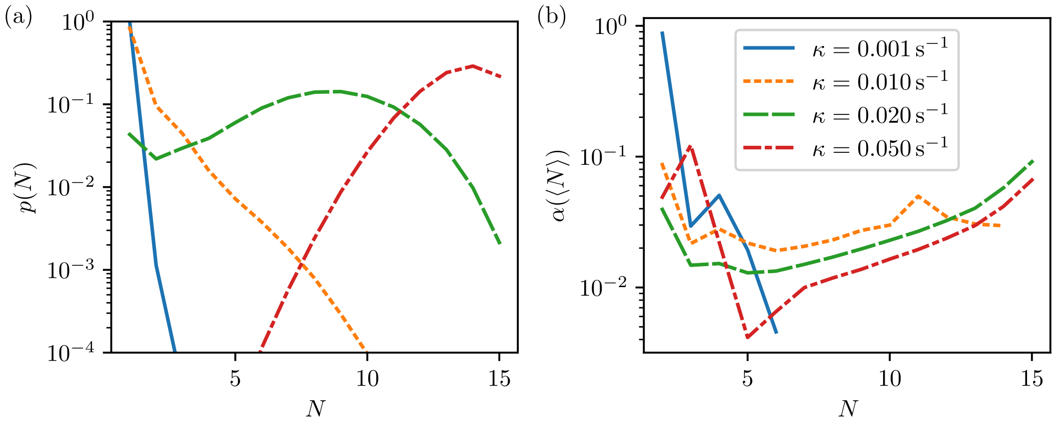

Figure 4.4.: Equilibrium distribution p and dissociation rates α as a function of association rate κ. (a) Equilibrium distribution $p(N)$ of the assembly model for different values of κ. (b) Resulting dissociation rates $\alpha(\langle N\rangle)$ (compare eqn. (4.5)) that are used in the mean-field model or in a coarse grained model.

the distributions are approximately exponential. At the critical association rate, the distribution becomes very broad. Above the critical value, a clear maximum emerges close to full assembly. As explained in section 4.2.5, from these distributions one can calculate effective equilibrium constants (eq. (4.5)) that map the graphical model to a monomer addition scheme. Fig. 4.4(b) shows the effective off-rate α_N obtained from equation (4.5). These are used in the mean field approach in the following.

4.3.2. Steady state results

We now investigate the full model that couples assembly and force generation. Starting from here we stop using dimensionless quantities, since the dynamics of the myosin crossbridge cycle are experimentally measured for specific isoforms and we choose to study the effects on non-muscle myosin IIB, where the fraction of time a single myosin head is attached to actin (the so-called duty ratio) is comparatively high [71]. In addition, we utilize the assembly rates documented in table 4.1 (justified later in section 4.3.3). In order to obtain a complete understanding of our combined model, we investigate how the mean values of the number of assembled motors N and the mean values of the number of bound motors i of one side of the filament change with association rate k_{on} and force F. In addition, we record the variances of these quantities, because this indicates transitions between different regimes. The corresponding results are shown in Fig. 4.5(a). Here we also show the values of the critical association rate: the solid and dashed lines show these transitions with and without motor cycle dynamics, respectively. While the dashed line corresponds to

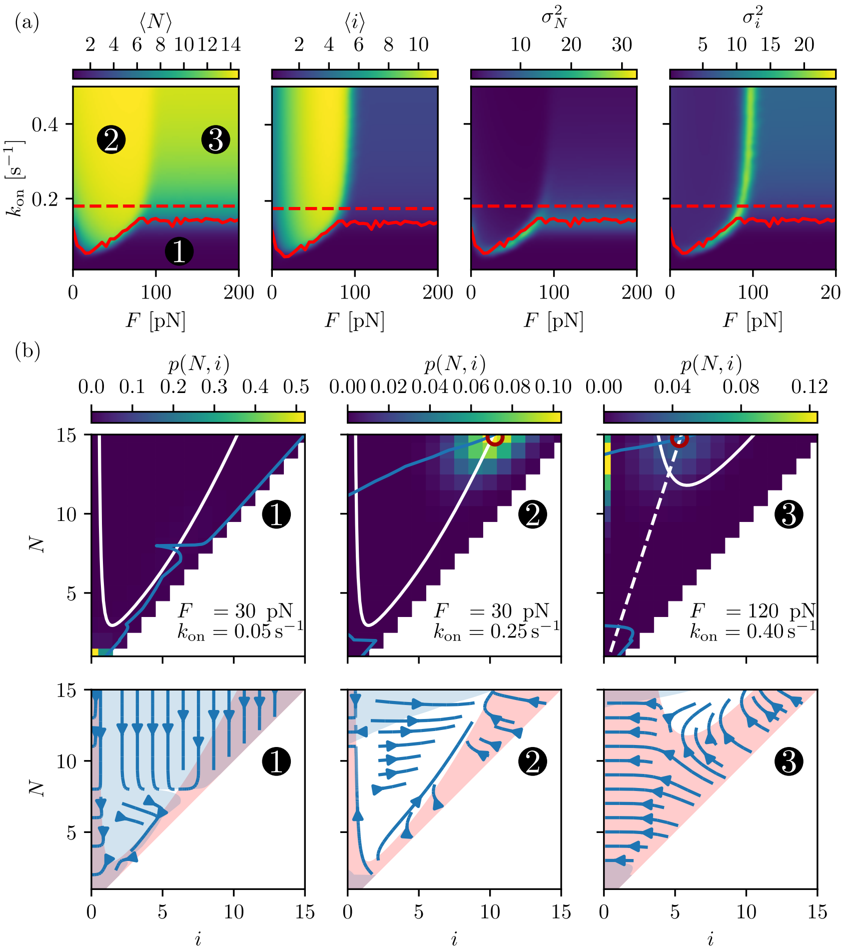

Figure 4.5.: Steady states. (a) Mean-values and variances of the full model for different forces F and on-rate k_{on} ($k_{\text{off}}^0 = 10\,\text{s}^{-1}$). The red dashed line represents the critical on-rate k_{on} for a cluster without actin, whereas the solid line represents the critical on-rate as a function of force. (b) Equilibrium distribution $p(i, N)$ (top row) and phase portrait (bottom row) in the 3 different regions. In the top row the solid white line depicts the nullcline of i whereas the blue line depicts the nullcline of N. The dashed white line depicts the nullcline of i at zero force. The red circles denote stable fixed points of the meanfield theory for the indicated force (middle) and zero force (right). The phase portraits (bottom row) illustrate how a change in force and on-rate affects the flow lines (blue) and the nullclines (red region $\langle \dot{i} \rangle < 0$, blue region $\langle \dot{N} \rangle < 0$).

the results from section 4.3.1, for the full model we numerically searched for the maximal relaxation time. From Fig. 4.5(a) we see that there exist three different regimes (marked by labels 1, 2 and 3) which are separated by small parameter regions with high variance in either the cluster size N or the number of actin bound motors i. The solid line for the critical values for the relaxation times nicely corresponds to the transition region defined by the variance in N. The dashed line from the assembly model is always higher, suggesting that actin binding lowers the CAC.

We now discuss the three different regimes identified in Fig. 4.5(a) in more detail. The regime 1 at low association rates k_{on} is characterized by a small mean cluster size $\langle N \rangle$. Due to low association, there are not enough monomers to support an assembled minifilament. At higher association rate and up to medium forces, regime 2 emerges, in which minifilaments are typically assembled and attached to actin with both sides. The border of this region to the prior one is convex, indicating that the catch-slip bond mechanism facilitates assembly under medium forces by increasing the amount of actin-bound myosin that is unable to dissociate from the minifilament. At higher forces and high on-rates, there is regime 3, in which the minifilaments are typically assembled, however, the number of actin bound motors i of the half-filament is reduced to half the value which one would obtain with $F = 0\,\mathrm{pN}$. The underlying reason is that now the slip pathway dominates and therefore one half of the minifilament unbinds, while the other side binds without force.

In order to understand why these three regimes form, in Fig. 4.5(b) we show the probability distributions $p(N, i)$ for cluster size N and bound motors i. In addition we show the phase portraits of the deterministic (mean-field) system described in section 4.2.5. As shown at the left side of Fig. 4.5(b), the half-filament is of size 1 at low monomer concentration and force. In the corresponding phase portrait one can see that the regime 1 forms because the net flux of the system is always directed either towards lower size N or lower actin-bound myosin heads i which enhances each other in the model. Although the phase portrait shows a node at $(N \approx 8, i \approx 6)$, the proximity to a saddle makes it unstable to noise.

The regime 2, in which both sides of the filament are attached, is shown in the middle of Fig. 4.5(b) and is characterized by a stable fixpoint at large N and i with a large basin of attraction. This leads to a maximum in the equilibrium distribution at the boundary $N = 15$. In regime 2, the force is sufficiently small so that the motors are stabilized by their catch behavior.

In regime 3, there are two populations: one at $i = 0$ and the other distributed around the nullcline of i at zero force. This indicates that the minifilament is not fully attached to actin, but only attached with one side and hence is not sustaining a force. At this high level of force, the slip pathway dominates and the mean field description fails, because it only describes one half-filament and assumes that the force can be applied. This would not happen for a pure catch bond and our results for this case are shown as Fig. A.1 in the appendix. Then minifilaments can assemble at very low on-rate, just as long as the force is high enough. Additionally, there is no region where only one side of the filament is attached, but both sides are typically attached at the same time.

In summary, the force-dependence of the distributions indicates that with increased force, the probability for the system to be near the assembled maximum of the distribution increases. At high forces this probability decreases again. This behavior is illustrated in Fig. A.2 where the probability that the system is of size $N \geq 8$ is shown.

4.3.3. Comparison with experiments

As described in section 4.2.6, by using the proposed model, it is possible to predict trajectories of FRAP experiments from the model. We investigated the effect of different forces with or without the crossbridge cycle, of which the latter mimics myosins heads that are blocked in the unbound state (experimentally this can be achieved by using the pharmacological inhibitor blebbistatin [193]). Fig. 4.6(a) shows the mean number of fluorescent proteins in a minifilament $\langle N(t) \rangle$ starting the dynamical self-assembly simulation with a non-fluorescent minifilament drawn from the appropriate equilibrium distribution. Similar to the fluorescence intensity in FRAP experiments, $\langle N(t) \rangle$ is a saturating and monotonously increasing function of time that can be described by a saturating exponential.

When fitting an exponential function of type $N_a(1-\exp(-t/\tau))$ to the fluorescence recovery traces at different forces and different on-rates close to the critical on-rate for the minifilament without actin, we choose $k_{\mathrm{off}}^0 = 10\,\mathrm{s}^{-1}$ such that we obtain values close to the recovery times measured in cells [90, 143] (see Fig. 4.6(b)). We note that the recovery times calculated here are on the lower end of the wide spectrum of reported experimental values, indicating that k_{off}^0 should be seen as an upper bound. For increasing force the fluorescence recovery time increases until it reaches a maximum at around 80 pN from where it drops down to a constant value. This constant value is always higher than the fluorescence recovery time for minifilaments without actin, underlining once again that at very high forces one side of the minifilament is attached. If pure catch bonds are used to simulate the motor dynamics, the fluorescence recovery time rises monotonically with force, underlining that the drop we observe at intermediate forces for the catch-slip bond occurs due to the instability of slip bonds beyond a certain force. With our choice for the value of k_{off}^0, we revisit Fig. 4.3(d), which indicates the maximum relaxation time is $t_0 \gtrsim 80s$, consistent with light scattering measurements in *in vitro* assembly assays [54] ($t_{\mathrm{exp}} \approx 580\,\mathrm{s}$).

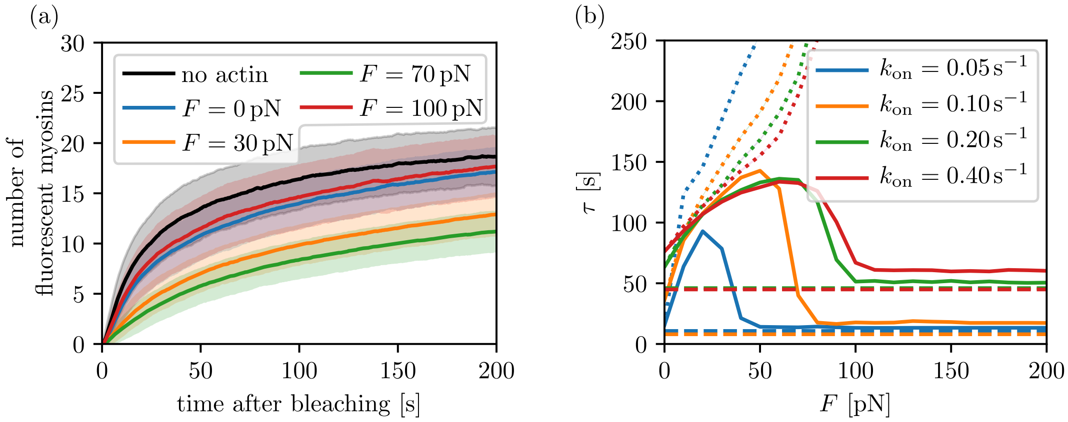

Figure 4.6.: (a) Time-dependent mean number of fluorescently labeled myosin proteins per minifilament starting from a non-fluorescent minifilament drawn from the equilibrium distribution at $k_{\mathrm{on}} = 0.4\,\mathrm{s}^{-1}$ for different forces and with the myosins heads blocked in the unbound state. The transparently colored regions denote the region of one standard deviation. (b) Results for fitting functions of type $N(1-\exp(-t/\tau))$ to the mean number of fluorescently labeled myosins for different on-rates and forces. The dashed lines indicate the fluorescence recovery if the motor cycle is turned off, which is always significantly faster, even at forces where the minifilament is not bound to actin on both sides but typically only on one. The dotted lines indicate the result when using pure catch-bonds.

4.4. Discussion

In this chapter we have proposed an assembly model of myosin II filaments, that explains the mechanosensivity of myosin II self-assembly by coupling assembly and motor activity in one model. In particular, we suggested a graph representing the consensus architecture of human myosin II minifilaments. Although myosin II minifilaments tend to differ in the details of their architecture from species to species, our approach is very generic and does not depend much on the details of this graph (Figs. A.3 and A.4 in the supplement). We investigate the dynamical model on this graph in a range around a critical aggregation concentration (CAC), which we identified by critical slowing down. We identified and characterized three regimes. Finally we performed FRAP simulations that yielded recovery times which we used to find plausible assembly rates.

It is a common feature of self-assembling systems that, as soon as the equilibrium concentration of free monomers is beyond a threshold, i.e. the CAC, it does not increase much anymore with added total monomer, since the added monomer goes mainly towards forming additional assembled structures [171]. Myosin minifilaments do not form an exception here, as has been experimentally shown [84]. This means, that a system of assembling myosin tunes itself, such that forming new filaments becomes very slow after the equilibrium concentration has been reached. However, this is only valid for solutions without actin. Our simulation results suggest that in contact with actin the assembly could be facilitated by coupling assembly to force generation. This leads to the CAC of minifilaments being lowered locally near actin filaments, in agreement with experimental observations [194]. If the solution can support the assembly of minifilaments already without actin, i.e. the concentration of monomers is near the CAC, minifilaments operating on actin might associate new myosin molecules with the critical association rate of the solution, which is well above the critical association rate of the minifilaments that are attached to actin. This mechanism in conjunction with regulation of the equilibrium between assembly-competent and incompetent myosin II [49] yields a system that can show a very dynamic response to change of external conditions. In addition, it explains the known mechanoaccumulative behavior of myosin II [9].

Since blebbistatin, an often utilized small molecule inhibitor of myosin, blocks the myosin II head domain mainly in an actin-detached state [193], the assembly-enhancing effect of actin, that our model predicts, could be experimentally investigated using already available methods [143]. Hence, the model assumption that a myosin II protein is not able to dissociate from its respective minifilament when its head is bound to actin can in principle be verified.

We were not able to fully explain the wide spectrum of recovery rates reported by changes in retained force alone. Instead, also other mechanisms will be involved. However the rates we extract are consistent with light scattering data from *in vitro* assembly assays, where assembly has turned out to be slower by a factor of 7 than our lower bound. This seemingly large deviation should however be put into perspective by noting that live cell FRAP experiments [90, 143] were used to obtain absolute rates, which then were used to compare the model to *in vitro* experiments [54], that in addition have been conducted at a 17 °C lower temperature. In order to test our predictions in quantitative detail, one had to conduct FRAP-experiments under controlled loading conditions.

Our model suggests that the strong force-dependence of minifilament self-assembly arises due to the catch-bond characteristic of unbinding myosin from actin after performing the powerstroke. This constellation, where self-assembly of a motor complex is markedly affected by the binding dynamics to its track, is not unique to myosin II. Another interesting example is the bacterial flagellar motor (BFM), which in contrast to myosin II is a rotary motor, but similar to minifilaments is a complex with multiple load bearing elements (i.e. stators). It has been shown that increasing load (i.e. torque) increases the amount of stators in the BFM [195]. Later studies have suggested this to be due to the dissociation rate of the stators decreasing with increased torque [40, 196], i.e. the BFM also implements a catch bond which modulates self-assembly. The catch bond feature is also central to the function of actomyosin, where it modulates the transient response to mechanical stress and guides accumulation of myosin to stressed parts of the actin network [4, 64]. We conclude that the interplay of assembly and force generation described here might be at play in other protein clusters that have to function under mechanical load.

5. Rheology of mixed motor ensembles

The rheology of biological cells is not only determined by their cytoskeletal networks, but also by the molecular motors that crosslink and contract them. Recently it has been found that the assemblies of myosin II molecular motors in non-muscle cells are mixtures of fast and slow motor variants. Using computer simulations and a mean field theory of a crossbridge model for myosin II motors, we show that such motor ensembles effectively behave as active Maxwell elements. We calculate storage and loss moduli as a function of the model parameters and show that the rheological properties cross over from viscous to elastic as one increases the ratio of slow to fast motors. This suggests that cells tune their mechanical properties by regulating the composition of their myosin assemblies.

This chapter is partly based on a paper that is currently in preparation [197].

5.1. Introduction

The rheology of animal cells is essential for many physiological functions, including the function of epithelial and endothelial cell layers under continous loading, e.g. in lung, skin, intestines or vasculature. It is also essential for single cell processes such as cell migration and division, which are characterised by large-scale flows and deformations. For these reasons, single cells and cell ensembles have been widely studied using rheological approaches as commonly applied in materials science [122, 127, 148, 150, 198, 199] (see section 2.3.3 for more details on experimental methods). Cells typically show a wide relaxation spectrum indicating the relevance of different time scales. Often power-law relaxation spectra have been reported [148, 198], which can be related to soft glassy rheology [126], but there is also evidence for an upper cut-off at a maximum relaxation time [122]. Despite this complexity of cell rheology, however, for many purposes linear viscoelasticity has turned out to be a surprisingly good description of the effective mechanical properties of cells and cell monolayers [2, 200–205].

Cells control their mechanical properties mainly by changing the assembly status and activity of their actomyosin cytoskeleton. Although much is known about the effective rheology of these networks [152, 206], it is less clear how the microscopic properties of the different types of myosin motors contribute to cell rheology. Recently, it has been found that cells co-assemble fast and slow isoforms of myosin II [88, 89]. While the fast myosin II isoform A is mainly found at the front of the cell, where fast assembly and flow is required, the slow myosin II isoform B is incorporated towards the back, where strong and long-lasting forces are required. Here, we explore the intriguing possibility that cells control their rheology by differential assembly of their myosin assemblies. We address this important question theoretically by using a microscopic crossbridge model for small ensembles of myosin motors, which earlier has been applied only to ensembles of one isoform [71, 72]. By extending this framework to mixed ensembles and calculating their complex modulus, we show that such assemblies operate as active Maxwell elements that can tune their rheology from viscous to elastic by increasing the ratio of slow versus fast motors.

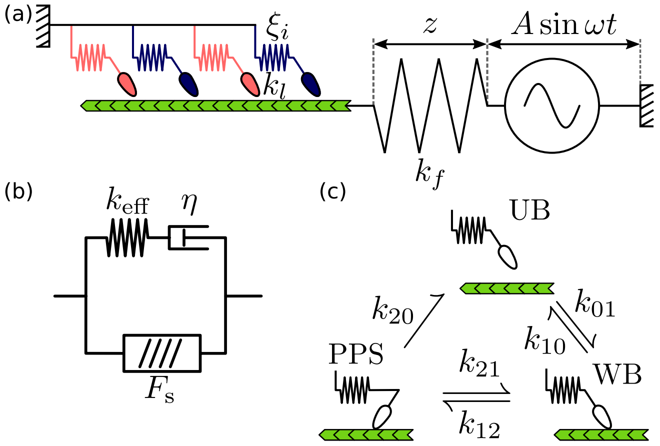

Figure 5.1.: Model. (a) Scheme used for rheology simulations of myosin II ensembles. Myosin crossbridges with individual motor strains ξ_i and linker stiffness k_l. z and $A \sin \omega t$ are the strain on the elastic environment and the oscillatory manipulation. Blue and red myosin crossbridges denote the fast and slow isoforms A and B, respectively. (b) Maxwell element in parallel with active force F_s with spring constant k_{eff} and friction coefficient η pulling on a linear spring with constant k_f. (c) Crossbridge model illustrating the mechanochemical rates and states.

5.2. Mechanical setup & simulation

Fig. 5.1(a) shows a schematic representation of the situation that we analyze here. A central spring with extension z and spring constant k_f is pulled from two sides. On the right hand side, we have a mechanical motor that pulls with fixed frequency ω and amplitude A. On the left hand side, we have a small ensemble of N myosin II motor heads that walk towards the barbed end of an actin filament. For the myosin

II minifilaments in non-muscle cells, we typically would have $N = 15$. From these N motor heads, N_a are assumed to be of isoform A. Then $N_b = N - N_a$ are of isoform B.

We first demonstrate that this setup should effectively behave like an active Maxwell element as shown in Fig. 5.1(b). The Maxwell element is the simplest possible viscoelastic model and features a spring with spring constant k_{eff} and a dashpot with friction coefficient η in series; in an active Maxwell model, there is a constant pull F_s operating in parallel. We assume that the motor ensemble depicted in Fig. 5.1(a) should have a well-defined force-velocity relation $v(F)$, with a free velocity v_0 at $F = 0$ and vanishing velocity at the stall force $F = F_s$. Moreover, the motor ensemble should have an effective spring constant k_{eff}. With all motors having the same crossbridge spring constant k_l, this should simply be $k_{\text{eff}} = ik_l$, with i being the average number of bound motors. This leads to a differential equation for extension z

$$\dot{z} = \kappa \left[v(k_f z) + A\omega \cos(\omega t) \right], \; \kappa = \frac{k_{\text{eff}}}{k_{\text{eff}} + k_f} \; . \tag{5.1}$$

After expanding the force-velocity relation around the stall force F_s with a slope $v'(F_s) = -1/\eta$, we easily can solve this equation:

$$\begin{aligned} z(t) &= \frac{F_s}{k_f} + C \exp\left(\frac{\kappa k_f}{\eta} t \right) \\ &+ \frac{\omega \kappa A}{\sqrt{\omega^2 + (\kappa k_f/\eta)^2}} \sin(\omega t - \delta), \; \tan\delta = \frac{\kappa k_f}{\omega \eta} \; . \end{aligned} \tag{5.2}$$

We obtain three terms, each with a clear physical meaning. The first term is the constant pull of the active Maxwell element, arising from the stall force as expected. The second term is initial relaxation with a constant C determined by the initial conditions. The third term is our most important result: the system response is oscillatory with the same frequency as the external perturbation, but with a loss angle δ that depends on the details of the motor ensemble. The calculated oscillations correspond to a complex modulus

$$G^* = \frac{\kappa k_f \omega^2 \eta^2}{(\kappa k_f)^2 + \omega^2\eta^2} + \mathrm{i} \frac{(\kappa k_f)^2 \omega \eta}{(\kappa k_f)^2 + \omega^2 \eta^2} \tag{5.3}$$

which is exactly the result for a Maxwell model, with effective spring constant κk_f and friction coefficient η.

In order to validate our prediction that motor ensembles should effectively behave as active Maxwell systems, we conducted computer simulations of a detailed crossbridge model for myosin II as shown in Fig. 5.1(c). If successful, such an approach allows us to predict how the effective rheological properties of the system depend on both the microscopic rates of the single motors and the ensemble parameters N_a and N_b. In our model, each of the N crossbridges of the ensemble is in one of three mechanochemical states that are connected by force dependent transition rates [71]. The transition from the unbound (UB) to the weakly bound (WB) state occurs with rate $k_{01} = 0.2\,\mathrm{s}^{-1}$. The strain-dependent reverse rate $k_{10}(\xi) = k_{10}^0 \exp k_l\xi^+/f_s$, where $k_{10}^0 = 0.004\,\mathrm{s}^{-1}$ is the rate at zero strain, $k_l = 0.3\,\mathrm{pN/nm}$ is the crossbridge stiffness and $\xi^+ = \max(0,\xi)$ is the positive part of the crossbridge strain ξ. The transitions between the WB and the post-powerstroke (PPS) states is governed by the difference in elastic energy stored in the crossbridges ΔE_{el} and the change in chemical energy $\Delta G = -60\,\mathrm{pN\,nm}$. The rates considered here are $k_{12/21} = k_{\mathrm{ps}} \exp(\pm\beta(\Delta E_{\mathrm{el}}{+}\Delta G)/2)$ with $k_{\mathrm{ps}} = 1000\,\mathrm{s}^{-1}$. Finally, the unbinding from the post-powerstroke state is modeled as a *catch-slip* bond, i.e. $k_{20}(\xi) = k_{20}^{0a/b}(\Delta_c \exp -k_l\xi^+/f_c + \Delta_s \exp k_l\xi^+/f_s)$. Here $\Delta_c = 0.92$ is the fraction following the *catch-path* at zero force with force scale $f_c = 1.66\,\mathrm{pN}$, $\Delta_s = 0.08$ is the fraction following the *slip-path* at zero force with force scale $f_s = 10.55\,\mathrm{pN/nm}$. For the faster NM IIA motors we use $k_{20} = 1.71\,\mathrm{s}^{-1}$, while for the slower NM IIB we use $k_{20} = 0.35\,\mathrm{s}^{-1}$. By mixing N_a NM IIA and N_b NM IIB motors, we can explore how the mixing ratio determines the effective rheology of motor ensembles.

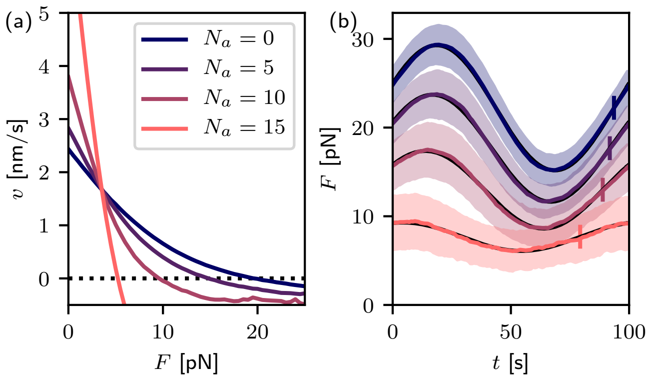

Figure 5.2.: Computer simulations of crossbridge model for $N = 15$ motor heads. (a) Force velocity relations. Zero crossings define the stall force F_s and the (negative) linear slope around this point the friction coefficient η. Throughout this section the fraction of NM IIA motors is color coded as a gradient from dark blue for $N_a = 0$ to light red for $N_a = N$. (b) Overall system response. The colored areas denote the region of one standard deviation. The black lines denote the fits with $\sin(\omega t - \delta) + \mathrm{const.}$, while the colored vertical tics serve as indicators of where a non phase lagged sine oscillation starts.

Fig. 5.2(a) shows that indeed our microscopic model leads to well-defined force-velocity relations, which define both the stall force F_s and the effective friction coefficient η. We clearly see that as the number of fast motors N_a is increased, F_s and η decrease. Fig. 5.2(b) shows that, as predicted by Eq. (5.2), the system response is oscillatory and can be fit well with a sine wave (black lines), but with a varying lag phase. We see that the loss angle δ increases while the oscillatory component of the force F^* and the constant offset force F_s decrease with increasing NM IIA content. This suggests that the system crosses over from elastic to viscous as the myosin IIB motors are replaced by myosin IIA motors.

In order to achieve an accurate mapping between the microscopic motor rates and the effective Maxwell rheology, we next developed a self-consistent mean field treatment of our crossbridge model for motor ensembles [68, 69]. As before, we assume equal load sharing between all bound motors. In steady state binding and unbinding from the track is balanced. Assuming the powerstroke is performed immediately after binding and approximating the stall force of the ensemble as the sum of the single motor stall forces $\hat{F}_s = k_l d$ for all bound motors $F_s \approx i\hat{F}_s$ we find the self-consistent number of bound motors at stall force

$$i(\hat{F}_s) = \frac{k_{01} N}{k_{20}(d) + k_{01}}. \tag{5.4}$$

Using the speed when all i bound motors are in the pps. state in the parallel cluster model (PCM), given by [69]

$$v_i(F) = (N - i) k_{01} \frac{id - F/k_l}{i(i+1)} \tag{5.5}$$

we can now give the friction coefficient η and the effective spring constant κk_f as functions of the mechanochemical rates, the environmental stiffness k_f and the ensemble size N

$$\kappa k_f = \frac{k_l N}{1 + \frac{k_{20}(d)}{k_{01}} + \frac{k_l N}{k_f}} \tag{5.6}$$

$$\eta = \frac{k_l i(\hat{F}_s)(i(\hat{F}_s) + 1)}{(N - i(\hat{F}_s)) k_{01}}. \tag{5.7}$$

To approximate the quantities for motor ensembles with heterogeneous composition, we use the harmonic mean of off-rates of the two considered isoforms

$$k_{20}^{0}(N_a, N_b) = \frac{N_a + N_b}{N_a/k_{20}^{0a} + N_a/k_{20}^{0b}}, \tag{5.8}$$

with N_a, k_{20}^{0a}, N_b, k_{20}^{0b} the total number and the off-rates of NM IIA and B heads, respectively. This follows the intuition, that the average dwell time of a motor head on the track is the pivotal quantity. We note, that this approach is not the only possibility to combine NM IIA and IIB using this approximation. However, since k_{20}^{a0} and k_{20}^{b0} do not differ too much from each other, it is quite successful. In section 5.3 we outline a different linear mean-field theory that can be used if k_{20}^{a0} and k_{20}^{b0} differ too much from each other. In addition, we note that this mean field approximation should carry over to passive crosslinkers by setting the powerstroke distance $d = 0$.

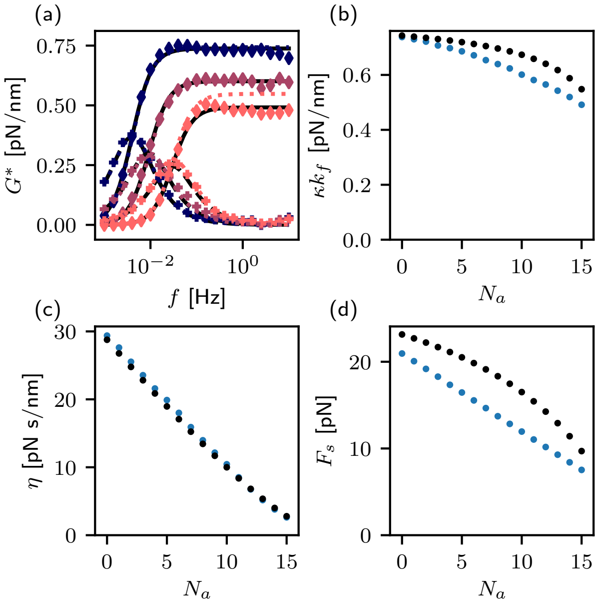

Figure 5.3.: Mechanical response depends on ensemble isoform content for an ensemble of size $N = 15$ with $k_f = 1\,\mathrm{pN/nm}$. (a) The dynamic modulus G^* of a ensembles with $N_a \in \{0, 10, 15\}$ (dark blue, light violet, light red). The diamonds and crosses denote the storage and loss as determined from the simulation, respectively, while the black lines are Maxwell model fits. The dotted colored lines are the result of the mean field approximation. (b, c, d) Effective spring constant κk_f, friction coefficient η and ensemble stall force F_s as a function of NM IIA content N_a. Blue and black circles denote the results obtained from the simulation and the mean field approximation, respectively.

In accordance to eqn. (5.3) Figs. 5.3(b) and (c) show the effective spring constant κk_f of the motor ensemble and its environment and the friction coefficient η as calculated from a fit of the Maxwell element eqn. (5.3) to the simulation results, alongside the theoretical prediction from the mechanochemical rates (eqns. (5.6) and (5.7), respectively). The effective spring constant decreases slightly with increasing NM

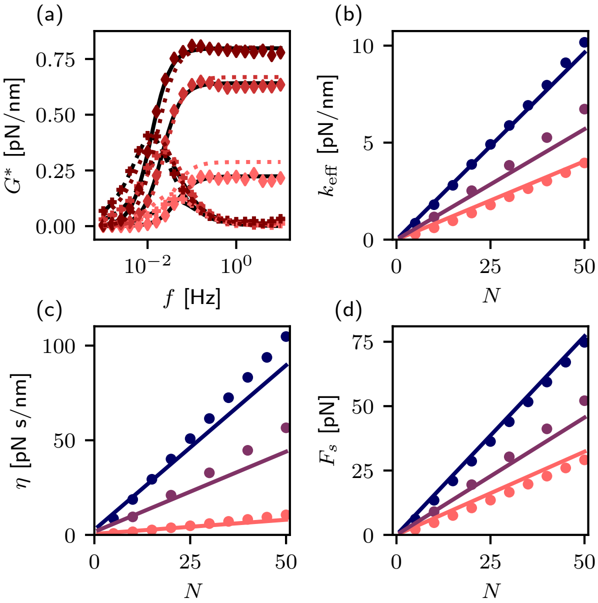

Figure 5.4.: Mechanical response dependence on ensemble size. (a) Dynamic modulus for NM IIA ensembles of size $N = N_a \in \{5, 25, 50\}$ (light to dark red) with $k_f = 1\,\mathrm{pN/nm}$ (for symbol description see Fig. 5.3(a)). (b, c, d) motor ensemble spring constant k_{eff}, friction coefficient η and ensemble stall force F_s as a function of ensemble size N for $N_a \in \{0, N/2, N\}$ (dark blue, violet, light red). Dots and lines represent the simulation and mean field approximation, respectively.

IIA content which is consistent with the lower duty ratio of a single NM IIA motor compared to NM IIB. The friction coefficient decreases markedly with increasing NM IIA starting from $\eta \approx 30\,\mathrm{pN\,s/nm}$ without NM IIA and ending at $\eta \approx 2\,\mathrm{pN\,s/nm}$ with purely NM IIA for a motor ensemble with 15 motors. The stall force F_s goes from $\sim 20\,\mathrm{pN/nm}$ for ensembles of purely NM IIB to $\sim 10\,\mathrm{pN/nm}$ for purely NM IIA, as shown in Fig. 5.3(d).

We also investigate the size dependence of the mechanical response, which is summarized in Fig. 5.4. Ensemble spring constant $k_{\mathrm{eff}} = ik_l$, Stall force F_s and friction coefficient η rise linearly with size. This suggests, that one can think of a single motor of the ensemble as an active Maxwell element which in the context of the ensemble is in parallel to others. The linear relationships also motivate calculating the effective Young's modulus $E = k_{\mathrm{eff}} l/\pi r^2$, the bulk viscosity $Y = \eta l/\pi r^2$ and the active stress $\sigma_a = F_s/\pi r^2$ generated by a one half minifilament of length $l \approx 150\,\mathrm{nm}$ with a typical crosssectional radius of $r \approx 20\,\mathrm{nm}$, i.e. the distance the heads typically splay outward from the center of the filament with $N = 15$ motors [54]. We find

$E = 160$ .. $460\,\mathrm{kPa}$, $Y = 0.45$ .. $4.8\,\mathrm{MPa\,s}$ and $\sigma_a = 2$ .. $5\,\mathrm{kPa}$ for pure NM IIA and NM IIB ensembles, respectively.

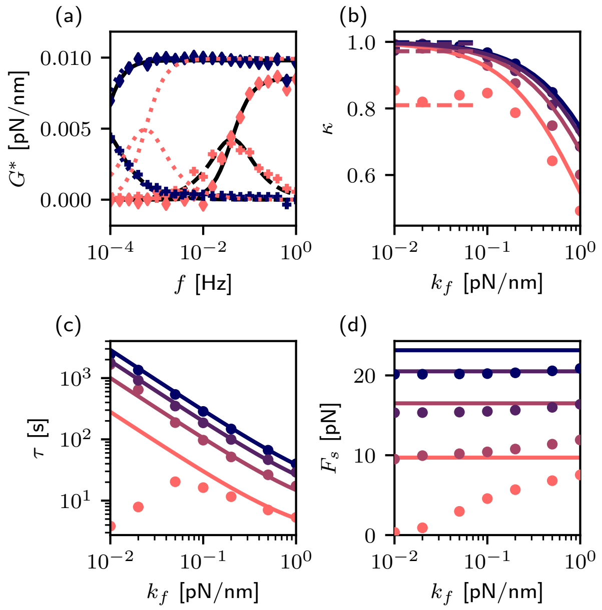

Figure 5.5.: Mechanical response dependence on elastic environment. (a) Dynamic modulus for NM IIA and NM IIB ensembles of size $N = 15$ at $k_f = 0.01\,\mathrm{pN/nm}$ (dark blue, light red) (for symbol description see Fig. 5.3(a)). (b, c, d) κ, friction coefficient η and ensemble stall force F_s as a function of environment stiffness k_f for $N_a \in \{0, 5, 10, 15\}$ (dark blue, dark violet, light violet, light red). Dots and lines represent the simulation and mean field approximation, respectively. Dashed lines represent the expected duty ratio ρ of the ensemble at $F = 0$.

The mechanical response also depends on the stiffness of the elastic environment k_f as shown in Fig. 5.5. Typically, the timescale $\tau = \eta/(\kappa k_f)$ and stiffness normalized to the environment stiffness κ decrease with increasing environment stiffness. In most cases, also the force does not depend much on the stiffness. Interestingly, the mean field approximation fails for NM IIA ensembles of size $N = 15$ for environments less stiff than $k_f = 0.1\,\mathrm{pN/nm}$. In this case $\kappa < 1$ for $k_f \to 0$, which is not included in the mean field theory due to implicitly assuming that at least one motor is bound at all times. If no motor is bound $\kappa = 0$, while if at least one motor is bound $\kappa = 1$. Thus, the mean value can be approximated by $\kappa = \rho = 1 - [k_{20}^0/(k_{20}^0 + k_{01})]^N$, where ρ is the duty ratio of the ensemble at $F = 0$, i.e. the probability that at least one motor is bound at a given time. Here, the mean field theory also overestimates the timescale τ and stall force F_s. The timescale of the NM IIA ensemble reaches a maximum at $k_f \approx 0.05\,\mathrm{pN/nm}$ and falls off to higher and lower stiffnesses. The stall force rises with environment stiffness.

5.3. An alternative mean-field approach

Above we noted, that the mean-field approach used until now where mixed motor ensembles were approximated by taking the harmonic mean of the isoform-dependent off-rates k_{20}^{a0} and k_{20}^{b0} (see eq. (5.8)), which follows from intuition about the cross-bridge cycle. Taking a more mechanical perspective one can also think of a mixed motor ensemble as two directly coupled ensembles with different mechanical properties working in parallel, as shown in the inset of Fig. 5.6. Naively, one could now use eqs. (5.4) and (5.7), replace N with N_a and N_b, respectively in order to calculate the stall forces, the effective stiffnesses ensembles and the effective friction coefficients of the two ensembles. While the mean number of bound motors at stall force $i(\hat{F}_s)$ scales linearly with ensemble size, the friction coefficient only does so approximately for large ensembles. For small ensembles, in particular the first motors added to the cluster effectively contribute more towards the friction coefficient than the later added ones. Therefore, it is more instructive to calculate the friction coefficient per motor for the limit of an infinitely large cluster and use this value as the friction coefficient per motor when determining the mechanical properties of the two coupled ensembles. It is given by

$$\tilde{\eta}_{a/b} = \lim_{N\to\infty} \frac{\eta_{\text{eff}}(N)}{N} = \frac{k_{01}k_l}{k_{20}(d)(k_{20}^{a/b}(d) + k_{01})}. \tag{5.9}$$

The complex modulus of each ensemble is then the Maxwell modulus

$$G^*_{a/b}(\omega) = \frac{k_{\text{eff}}(N_{a/b}\tilde{\eta}_{a/b}\omega)^2 + i\omega k_{\text{eff}}^2 N_{a/b}\tilde{\eta}_{a/b}}{(N_{a/b}\tilde{\eta}_{a/b}\omega)^2 + k_{\text{eff}}^2}. \tag{5.10}$$

The total complex modulus of the system, i.e. the mixed ensemble with the serially attached external spring, then follows

$$G^*(\omega) = \left[(G^*_a(\omega) + G^*_b(\omega))^{-1} + k_f^{-1}\right]^{-1}. \tag{5.11}$$

As a proof of concept Fig. 5.6 shows the complex modulus of an ensemble of $N_a = 10$ NM IIA and $N_b = 1$ NM IIB, however here the off-rate of the slower motor has been set to $k_{20}^{b0} = 0.05\,\text{s}^{-1}$, thereby leading to an appreciable distance in timescales of the two motors and two distinct peaks in the imaginary part of the complex modulus.

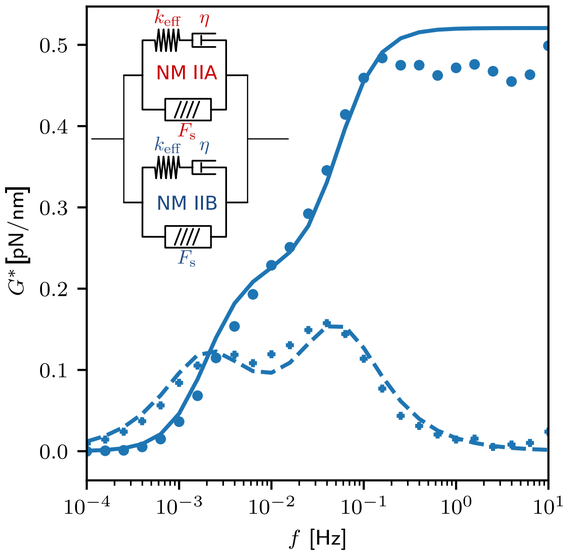

Figure 5.6: Complex modulus of an ensemble of $N_b = 1$ and $N_a = 10$, where the slower motor has been made slower by adapting $k_{20}^{0b} = 0.05\,\mathrm{s}^{-1}$. One can clearly see two distinct peaks in the imaginary part of the complex modulus G^*, as a result of two parallely arranged active Maxwell materials with distinct characteristic times. Points denote results from the full simulation of the crossbridge cycle, while the solid and dotted line denotes the mean-field result for the storage and loss modulus, respectively.

5.4. Nonlinear behavior

Until now, only relatively small changes in force $\Delta F \lesssim 10\,\mathrm{pN}$ have been considered. If the amplitude is increased further, the linear theory does not produce valid results anymore, which is a typical restriction of linear theories. A nonlinear mean field time evolution equation that can in principle account for effects arising due to higher amplitude can be given by combining eqs. (4.8), (5.1) and (5.5) to

$$\begin{aligned} \frac{\mathrm{d}i}{\mathrm{d}t} &= (N-i)k_{01} - ik_{20}(k_f z/i) + \mathcal{O}(\sigma_i^2 + \sigma_z^2 + \mathrm{cov}(i,z)) \\ \frac{\mathrm{d}z}{\mathrm{d}t} &= \kappa\left[(N-i)k_{01}\frac{id - k_f z/k_l}{i(i+1)} + A\omega\cos(\omega t)\right] + \mathcal{O}(\sigma_i^2 + \sigma_z^2 + \mathrm{cov}(i,z)). \end{aligned} \tag{5.12}$$

As these equations are difficult to analyze analytically, we turn to numerical methods. In particular, eqs. (5.12) are solved by an expicit adaptive Runge-Kutta method of order five as implemented in the *scipy* package for scientific computing in Python [207]. Throughout this section we simulate an ensemble of $N = N_b = 15$ NM IIB motors as an example until the oscillation does not depend on initial conditions anymore. The results are summarized in Fig. 5.7. Fig. 5.7(a) shows the mean number of actin bound motors as a function of time and indeed – as assumed in the previous section – the change in number of bound motors i over time is negligible for low amplitudes. At larger amplitudes the number of bound motors oscillates around a mean value. Similar to the force response as shown in Fig. 5.7(b). The phase angle between these oscillations depends on frequency. At low frequencies the phase of the

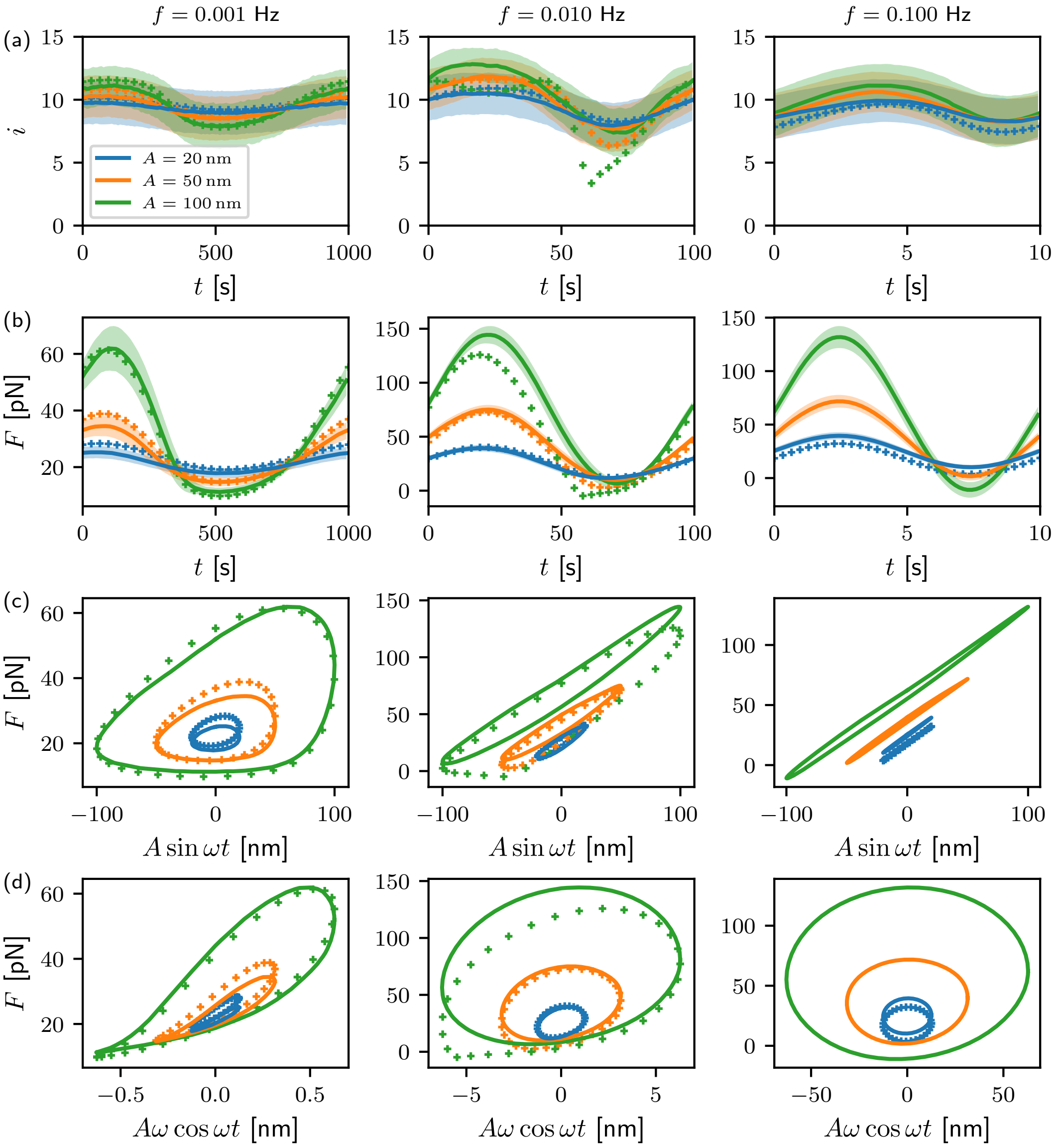

Figure 5.7.: Increased amplitudes make the system depart form linear response. Crosses denote the numeric solution of the mean-field equation (5.12), lines denote the mean according to the simulation and the colored surface denotes the region of one standard deviation. Here simulations of $N = N_b = 15$ NM IIB motors are shown. (a) Oscillatory response of the mean number of bound motors. Note that for very low frequencies the response becomes strongly non-sinusoidal. (b) Time-dependent force response of the system. (c) Trajectory of strain imposed by the motor versus the total force. (d) Trajectory of the strain rate imposed by the motor versus the total force.

Figure 5.7 *(previous page)*: For purely harmonic oscillations (c) and (d) should show only ellipses, while this is approximately true for low amplitude this breaks down at higher amplitudes. Note that the trajectories furthermore do not exhibit odd symmetry, indicating that the motor ensemble can be understood as an anisotropic material.

oscillation in i follows the oscillation of force rather closely implying that the typical time the motor ensemble needs to reach its steady state is much shorter than an oscillation period. At high frequencies this changes however, as the peak in number of bound motors lags behind the force slightly.

The force response departs most obviously from a harmonic oscillation at low frequencies and high amplitudes as shown in Fig. 5.7 at frequency $f = 0.001\,\mathrm{Hz}$ and amplitude $A = 100\,\mathrm{nm}$. Here the oscillation is deformed such that the maximum the oscillation passes through is sharper, while the minimum is less defined.

Fig. 5.7(c) and (d) shows diagrams that are also referred to as Pipkin diagrams [208]. The elastic Pipkin diagram, i.e. Fig. 5.7(c), shows the trajectory of *strain* imposed on the system by the motor against the force response, while the viscous Pipkin diagram , i.e. Fig. 5.7(d), shows the trajectory of *strain rate* imposed on the system by the motor against the force response. In the elastic Pipkin diagram straight lines indicate the response of a purely elastic material, while in the viscous Pipkin diagrams are indicative of a purely viscous material. Linear viscoelastic materials show ellipses in the Pipkin diagram with major axes that are neither aligned with x- nor with y-axis. Accordingly, for low amplitudes we observe trajectories that are close to ellipses while the higher the amplitude of the imposed strain becomes, the more deformed they become. In typical large amplitude rheological measurements investigating the response of a material to shear, where the material response to oscillatory strain is assumed to have odd symmetry – as the direction of applied stress should not change the material response in isotropic materials – only odd harmonics contribute to the response [209]. If no odd symmetry is exhibited by the trajectories in the Pipkin diagrams it follows that the material is anisotropic, as observed here, where the system responds stronger to stretching than to compression.

All trajectories that are observed here are closed loops indicating that, unsurprisingly, the force response of the system is periodic. As the response is also smooth, it can be described as a Fourier series. The response to the oscillatory strain depicted in Fig. 5.1 can therefore be described by

$$z = \sum_{n=0}^{\infty} A \left[G_n'(\omega, A) \sin(n\omega t) + G_n''(\omega, A) \cos(n\omega t) \right] . \tag{5.13}$$

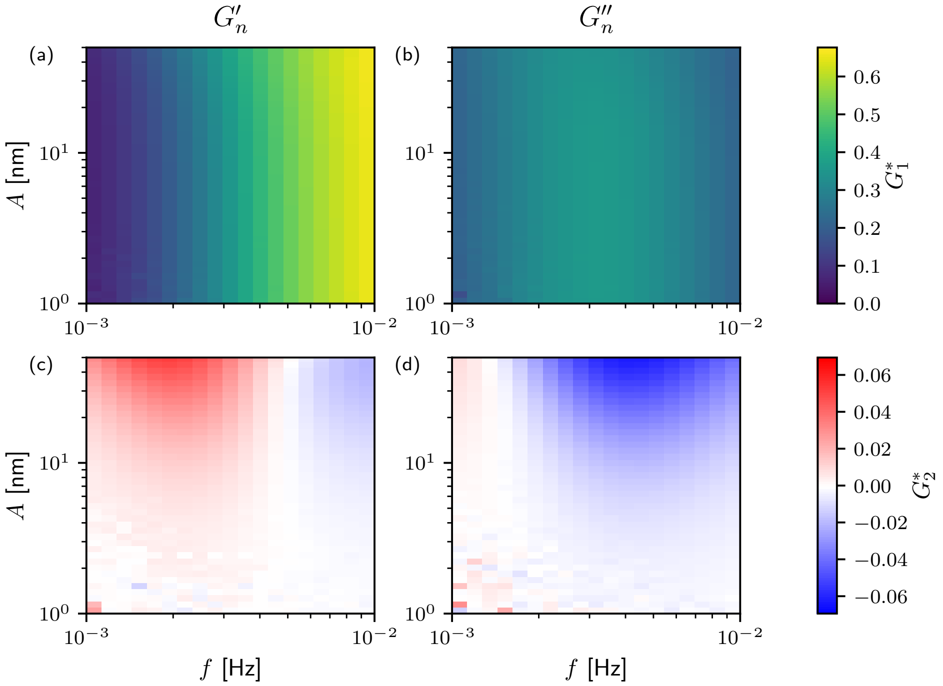

Figure 5.8.: Fourier analysis of the force response of the mean-field equation. The first harmonic of the in phase response $G'_1(f, A)$ (a), as well as the first harmonic of the out of phase response $G''_1(f, A)$ (b) are independent of amplitude in the region shown and match that shown in Fig. 5.3 in the studied paramter regime. (c, d) Fourier coefficients of the second harmonic, indicating a response that is dependent on the direction of deformation at higher amplitudes A.

If the response is linear, all terms with $n > 1$ must vanish. For $n = 0$ only $G''_0(\omega, A)$ is relevant and together with the amplitude $AG''_0(\omega, A)$ can be interpreted as a constant offset. The $n = 1$ terms can be identified with storage and loss modulus, respectively. Since trajectories in the Pipkin diagrams are not ellipses, the first higher order terms that contribute are G'_2 and G''_2. As the full simulation of the crossbridge cycle and the oscillatory perturbation is computationally very expensive, we here turn to the mean field theory which gives reasonable results in the frequency interval $f = 0.001 \sim 0.01\,\text{Hz}$ for amplitudes $A \leq 50\,\text{nm}$. We fit eq. (5.13) (stopping the sum at $n = 2$) to one oscillation period of the mean field solution to obtain the Fourier coefficients. The results are shown in Fig. 5.8. In detail, Fig. 5.8(a) and (b) show the Fourier coefficients of the base frequency. These turn out to be independent of amplitude A in the parameter regime investigated and, as expected, match the complex modulus of the Maxwell model from Fig. 5.3. The Fourier coefficients of the second harmonic are shown in Fig. 5.8(c) and (d). Combined, they indicate, that there is an anisotropic response of the system dependent on the direction of deformation, that becomes appreciable for higher amplitudes. On their own, the Fourier coefficients as well as their cause are however difficult to understand. As a toy model, suppose we apply an oscillatory strain $x = \tilde{A}\sin(\omega t)$ to a nonlinear spring with force extention relation $F(x) = k_1 x + k_2 x^2$. Trigonometric identities then imply that the force response is

$$F(t) = \frac{1}{2}\tilde{A}^2 k_2 + \tilde{A} k_1 \sin(\omega t) - \frac{1}{2}\tilde{A}^2 k_2 \cos(2\omega t). \tag{5.14}$$

Comparison of coefficients with eq. (5.13) implies for the second harmonic oscillation that $\sqrt{G_2'^2 + G_2''^2} = \tilde{A} k_2/2$.

But how does this relate to the system studied here? Of course, and in contrast to the toy model, due to the viscoelastic nature of the system, there is a loss angle between imposed strain and output stress. If we however take the oscillation of force as given and investigate the response of the neck linker strain to the force, we can gain further insight. If we assume, that relaxation of the bound motors to their steady states given the force applied to the system is fast, such that the number of bound motors relaxes to its steady state value instantaneously, one can formally write the number of bound motors as a function of force $i(F)$. This assumption is valid at low frequencies, where the number of bound motors and the force oscillate in phase (see Fig. 5.7(a) and (b). Any change in force ΔF can now be related to a change of neck linker strain Δx

$$\Delta F(\Delta x) = i(F_s + \Delta F) k_l \Delta x = k_l \Delta x \left(i(\hat{F_s}) + \Delta i(\Delta F) \right). \tag{5.15}$$

If we now interpret $\Delta i(\Delta F)$ as the oscillation amplitude of the number of bound motors, this implies, that $k_l \Delta i$ is the elastic nonlinearity in the crossbridge ensemble. Thereby we should expect the whole system with the external spring in series with the motor ensemble to have a non-linear contribution of

$$k_2 \approx \frac{\Delta i k_l k_f}{i(F_s) k_l + k_f}, \tag{5.16}$$

which together with our nonlinear spring toy model suggests, that as long as our assumption holds, the amplitude in the oscillation of bound motors Δi should be related to the magnitude of the second harmonic of the force oscillation by

$$\sqrt{G_2'^2 + G_2''^2} \approx \frac{K}{2} \frac{\Delta i k_l k_f}{i(F_s) k_l + k_f}, \tag{5.17}$$

with proportionality constant K. Fig. 5.9(a) shows an example frequency $f =$

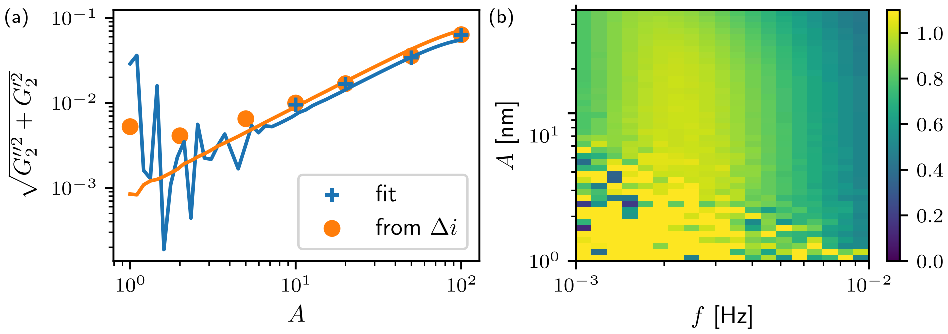

Figure 5.9.: Relation of oscillation amplitude of bound motors Δi and the contribution of the second harmonic to the force oscillation. (a) For frequency $f = 0.001\,\mathrm{Hz}$ eq. (5.17) holds well. Symbols denote results derived from the full simulation, while solid lines denote results from the mean-field equation. Blue relates to the left side of (5.17) while orange relate to the right side. (b) Dependence of K on amplitude and frequency as a result of the mean field theory. In the regime, where the mean field equations apply, K mainly depends on frequency.

$0.001\,\mathrm{Hz}$ where this proportionality holds quite well for the mean-field equation and the full model. Fig. 5.9(b) shows the proportionality factor K for different frequencies and amplitudes as a result of numerically solving the mean field equation (5.12). It is mostly independent of A as assumed by our calculation and mainly depends on the frequency f, as expected from the approximation. While at this point the meaning of the proportionality factor K which has units of an inverse spring constant, this result suggests, that the nonlinear behavior that the system exhibits is due to the force dependent transition rates. The catch-bond that is implemented in crossbridge cycle in the detachment from the post powerstroke state (PPS) thus leads to compression-softening and -fluidizing as well as stretch-stiffening and -hardening.

5.5. Conclusion

In this chapter, we proposed a theory that relates a stochastic crossbridge model to an active linear viscoelastic model, which thereby predicts rheological properties from microscopic chemical rates and showcased what we can learn about the two myosin isoforms NMII A/B using this approach. In brief, NM IIA behaves more fluidlike than NM IIB, stiffer elastic environments lead to a more fluid response and increasing the number of crossbridges yields an increasingly solid behavior. In addition we gave an outlook into the anisotropic nonlinear behavior of the system, that resists stretching more than it does compression.

In the context of live-cell experiments studying the implications of our theory seems most promising in the context of stress fiber microsurgery assays [154]. Here, stress fibers are cut by laser ablation and the viscoelastic recoil is recorded. The recoil can be divided into an instaneous, presumably elastic and an exponential relaxation with a typical time scale of several seconds to minutes. Corresponding with the heterogeneous distribution of NM IIA/B within cells measured relaxation times differ significantly with location and stress fiber type [159, 210]. Strikingly, the relaxation time of mature stress fibers, which normally contain a mix of NM IIA and B, can be reduced by suppressing NM IIB gene expression [211]. Additionally, as the stiffness of a fiber with constant elastic modulus and cross sectional area decreases with increasing length, the notion, that stress fibers of increasing length show increasing relaxation times [157], is also consistent with our model predictions (see Fig. 5.5(c)).

The response to cutting of stress fibers motivates modeling stress fibers as a standard linear solid with additional active stress. This has been demonstrated recently by mechanically isolating stress fibers in live cell experiments with microsurgery and subsequent micromanipulation with soft cantilevers [155]. The model presented here, in conjunction with this experimental result suggests, that in stress fibers contractile myosin II minifilaments should not only be in series with passive crosslinkers, but also in parallel. This may be a key ingredient of a future model explaining the currently observed inconsistency [24] between predictions of maximum force of molecular motors from crossbridge models $\sim 50\,\mathrm{pN}$ and chemical rates and the typical traction force of stress fibers of $\sim 10\,\mathrm{nN}$ [156].

In general, proteins are thought to have been optimized by evolution for their specific task. The different tasks at hand specifically for myosin II pertain to different spatiotemporal localizations of NM IIA/B [212, 213]: there is more NM IIA in transverse arcs than NM IIB and vice versa in ventral stress fibers. In turn, transverse arcs are thought to flatten the lamellum at the advancing edge of migrating cells [21], while ventral stress fibers produce the traction forces that are needed for detaching the trailing edge of the cell, which are typically much larger than in other stress fibers [23]. These different tasks surely bear different challenges with differing optimal solutions. We conclude that the cytoskeleton should be seen as a system consisting of many different components whose chemical properties, such as binding affinities, have been tuned such that the mechanical properties arising as described here result in optimal performance.

6. Tension Viscosity Model

This chapter follows up on the tradition of models explaining the circular arc that is often observed in peripheral stress fibers that bridge a non-adhesive region [128, 130, 214–216]. Much like previous models, it explains the experimentally observed correlation between spanning distance and arc radius of peripheral stress fibers, but adding a dynamical twist. The model assumes, that experimentally observed peripheral stress fibers are in a steady state, where contraction by motors with distinct force velocity relation is balanced with stress fiber elongation at both ends by polymerization of additional actin fibers. While this chapter introduces the model and analyzes the stability of the steady states theoretically, the model is applied to experiments in chapter 7.

6.1. Introduction

In deformable materials, such as biological cells, solid bodies or even soap bubbles the shapes we observe typically are generated by a stable balance of forces of some sort. Be it a balance of body forces and contact forces in the Hertz Problem [217], the balance of pressure and surface tension in the forming of a soap bubble or the intricate interplay of surface tension, bending energy and osmotic pressure determining the shape of red blood cells [218]. Adherent cells, which can be thought of as a two dimensional contractile sheet, show a similarly interesting phenomenon of invaginated peripheral stress fibers between focal adhesions. These invaginations arise due to balancing of forces along the stress fiber. The shape that is observed is a result of a balance of the contractile force along the peripheral stress fiber with the force that is applied to the fiber from the environment. A surface tension in the environment which leads to forces with non zero normal part to the stress fiber can only be balanced by a curved stress fiber when assuming negligible bending rigidity [128, 130, 214, 219, 220]. Circular arcs arise, when this surface tension is isotropic [128, 130, 214], while elliptical arcs should form if the tension within the cell has a preferred direction [219]. Experimentally it has been found, that often the radius of the circular arc is correlated positively with the distance between the associated focal adhesions [128, 130], which can be explained by an elastostatic theory for the stress fiber. Similar results have been obtained theoretically when investigating active cable networks, that additionally show fundamental properties of the cytoskeleton such as robustness of cell shape to the detailed topology of the network [215].

Here, instead of assuming a static elasticity of the stress fiber, we approach the tension generation from a dynamical perspective. Stress fibers are organized similar to muscle sarcomeres. Regions of alternating actin polarity are alternatingly crosslinked by passive crosslinkers such as α-actinin, and active myosin II motors, which can additionally contract the anti-parallel fibers [51, 143]. Therefore the number of motors in series scales linearly with stress fiber length, but the contraction force is independent of length as experimental evidence suggests [221]. In essence there are two dynamical processes that occur within a stress fiber. These are firstly, the contraction by molecular motors and secondly actin polymerization at the focal adhesions which leads to a flow of material towards the center of the stress fiber [2, 143, 222–224]. In a steady state situation these two processes, polymerization and contraction have to be balanced. In this chapter we develop a dynamical model for the peripheral stress fiber which balances the force that is produced dynamically by the interplay of polymerization and contraction against the isotropic surface tension from the inside of the cell. This model which depends on the mechanical properties of the molecular motors will allow us to explain shape differences that arise from differences in the force-velocity relations of the different isoforms of myosin II [66, 71, 72] that produce the active contractile stress.

6.2. Active contractile flows may control cell shape

As stated above, the model we introduce here considers the interplay of three processes, as visualized in Fig. 6.1:

1. Sarcomeric contraction by serially arranged molecular motors with speed $v(F, L)$, that may depend on tension F within the stress fiber and length L of the stress fiber
2. Actin polymerization at the focal adhesions with speed $v_p(F, L)$, that in principle may also depend on the tension F within the stress fiber and length L of the stress fiber
3. Balance of an isotropic surface tension σ from the cell surface with the tension F inside the stress fiber, by curving the stress fiber into a circular arc of radius $R = F/\sigma$, a modified Laplace law [128, 214].

The two velocities lead to a length change

$$\dot{L} = v_p(F, L) - v(F, L) \tag{6.1}$$

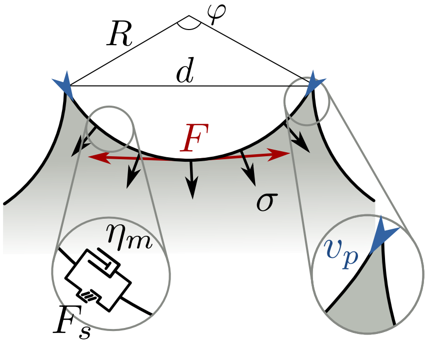

Figure 6.1: Model sketch. A peripheral stress fiber forms a circular arc by balance of surface tension σ and tension F within the stress fiber. This tension is generated by the interplay of contractile elements that are arranged in series along the stress fiber and polymerization of additional actin filaments.

of the stress fiber, which is the central dynamic equation that we study here.

From the knowledge that the contractile speed of molecular motors can be modeled by a force velocity relation of type

$$v_m(F) = \frac{1}{\eta_m}(F_s - F) \tag{6.2}$$

with motor stall force F_s and effective friction coefficient η_m for a sarcomeric unit of reference length L_0, linear scaling of contraction speed with stress fiber length implies for a stress fiber of length L

$$\frac{v_m}{L_0} = \frac{v(F,L)}{L} \Leftrightarrow v(F,L) = \frac{L}{\eta_0}(F_s - F). \tag{6.3}$$

Here η_0 is the friction coefficient of the stress fiber normalized to the length, such that the stress fiber contracts faster when it is longer. This is the contraction speed of the molecular motors inside the stress fiber.

For the polymerization speed of actin at the focal adhesions we here investigate two different force dependencies: Constant, i.e. independent of force, and linear with force. The related velocities $v_p(F,L)$ are given in the according sections.

The line tension we obtain from the interplay of contraction and polymerization can now be related to the circular arc radius R with the modified Laplace Law

$$R = \frac{F}{\sigma}, \tag{6.4}$$

where σ is the contractile surface tension. This defines how surface tension and line tension within the stress fiber is balanced and shows, that the tension-dependencies in the dynamic equation (6.1) are in fact dependencies on radius of curvature R, that in turn will depend on the length of the stress fiber and the spanning distance d.

Thus, to close eq. (6.1) to a well defined equation of motion, a geometric formula that relates these quantities is required. Stress fiber length L and the radius R are

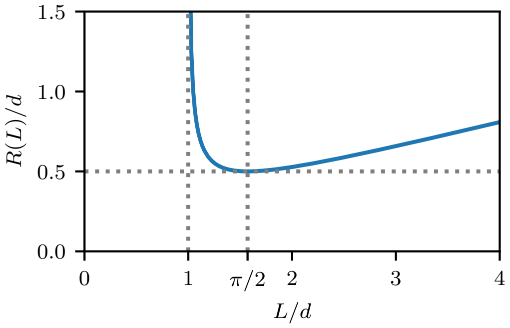

Figure 6.2: The arc radius $R(L)$ is a function of arc length L on the interval $L \in (d, \infty)$. For $L < \pi/2$ it is monotonically decreasing for $L > \pi/2$ it increases monotonically. Normalizing R and L to the spanning distance d yields a universal result.

trivially related with the central angle φ by $L = R\varphi$. The central angle is in turn dependent on spanning distance d and radius of curvature R by the trigonometric functions. Overall

$$L = \begin{cases} 2R \arcsin \frac{d}{2R} & 0 \leq \varphi \leq \pi \\ 2R(\pi - \arcsin \frac{d}{2R}) & \pi \leq \varphi \leq 2\pi \end{cases} \tag{6.5}$$

relates spanning distance, radius of curvature and stress fiber length. While circular arcs with larger central angle than π have not been observed experimentally, from geometrical deliberations they are also permissible. For completeness, they are also considered here. The function $R(L)$ that will be important for studying the dynamics is implicitly given by eqn. (6.5) and is visualized in Fig. 6.2. The relation becomes independent of spanning distance d, if distances are measured in units of d. For small central angles (i.e. large radii) eq. (6.5) can be approximated by $L = d$. Since $\sin\varphi/2 = d/2R$, the relative error of this approximation is given by

$$\frac{\Delta L}{L} = \frac{2R \arcsin \frac{d}{2R} - d}{2R \arcsin \frac{d}{2R}} = 1 - \frac{2}{\varphi} \sin \frac{\varphi}{2} < 0.1 \qquad \text{if} \qquad \varphi \leq \frac{\pi}{2}. \tag{6.6}$$

6.2.1. Constant polymerization speed

We now study the first case, a constant polymerization speed, $v_p(F) = v_{\text{const}}$. Using eqs. (6.3) together with the Laplace Law (6.4) and the constant polymerization speed in eq. (6.1) we arrive at

$$\dot{L} = -\frac{L}{\eta_0}(F_s - \sigma R(L)) + v_{\text{const}}. \tag{6.7}$$

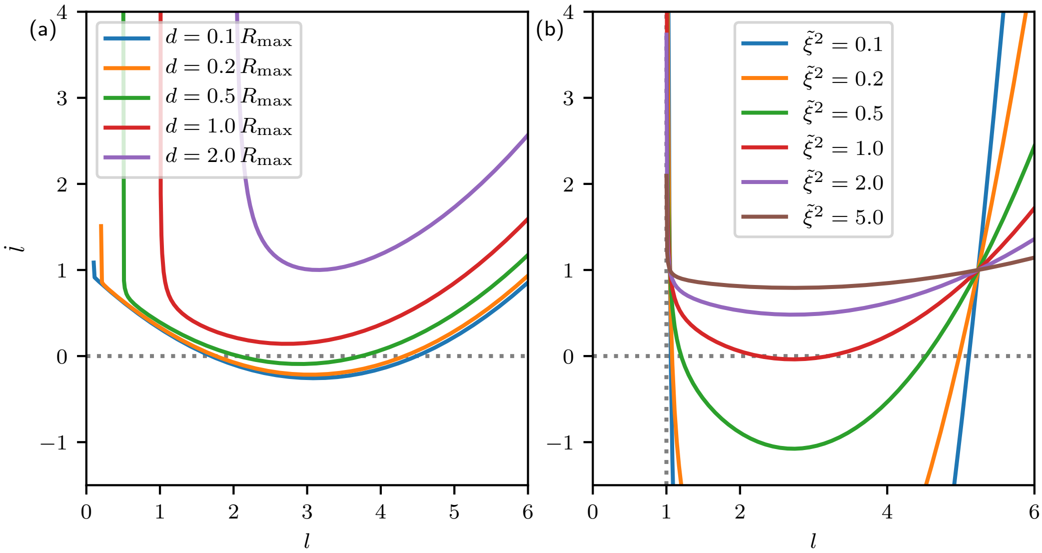

Figure 6.3.: Stability analysis, $\dot{l}$ as a function of l. (a) $\dot{l}$ for a range of spanning distances $\tilde{d}$ for $\tilde{\xi} = 1.1$. For small spanning distances there are two steady states, the one at lower l is stable, while the other one is instable. For increasing d the system approaches a saddle-node distribution, beyond which both steady states vanish and the length of the peripheral arc increases indefinitely. (b) $\dot{l}$ for a range of $\tilde{\xi}$ and spanning distance $\tilde{d} = 1$. Similarly for increasing $\tilde{\xi}$ the two steady states vanish in a saddle node bifurcation.

By measuring distance in units of $R_{\max} = F_s/\sigma$ and time in units of $\tau = R_{\max}/v_{\text{const}}$ we can nondimensionalize this equation of motion for the length of the peripheral arc L with result

$$\dot{l} = -\frac{l}{\tilde{\xi}^2}(1 - r(l)) + 1,$$
$$\text{with } \tilde{\xi} = \frac{\xi}{R_{\max}} = \frac{\sqrt{\frac{v_{\text{const}}\eta_0}{\sigma}}}{R_{\max}},\ r\left(l = \frac{L}{R_{\max}}\right) = \frac{R(L)}{R_{\max}} \text{ and } l = \frac{L}{R_{\max}}. \tag{6.8}$$

For a stability analysis of possible steady states, $\dot{l}$ is visualized in Fig. 6.3 as a function of l. For low spanning distances $\tilde{d} = d/R_{\max}$ and $\tilde{\xi}$ we find there exist two steady states. The ones at smaller and larger arc length are stable and unstable respectively. There is a bifurcation point at some $(\tilde{d}_{\text{crit}},\ \tilde{\xi}_{\text{crit}})$, where the two steady states merge into one metastable steady state. Increasing either $\tilde{d}$ or $\tilde{\xi}$ leads to a completely instable system, in which the arc length increases indefinitely.

The steady states can formally be found by setting $\dot{l} = 0$. From this we can also find a conditional equation for the steady state radius. We find

$$r = 1 - \tilde{\xi}^2/l, \text{ or in dimensional quantities} \tag{6.9}$$

$$R = R_{\text{max}} - \frac{\xi^2}{L}. \tag{6.10}$$

From these equations it becomes clear, that the process depends on two different length scales namely R_{max}, the 2D-Laplace radius, and ξ, which depends on the slope of the length nomalized force-velocity relation of the stress fiber, the polymerization speed at the focal adhesions and the surface tension.

Together with the geometrical relation (6.5) this equation can be solved implicitly or alternatively one can use the approximation $L = d$ for small central angles. Using $\sin\varphi/2 = \tilde{d}/2r$ in eq. (6.9) we find

$$\tilde{\xi}^2 + \frac{\left(\tilde{d} - \sin\varphi/2\right)^2}{\frac{\sin^2\varphi/2}{\varphi}} = 1, \tag{6.11}$$

i.e. given that there is a stable solution, the central angle φ as a function of $(\tilde{\xi}, \tilde{d})$ will have elliptical contour lines with ellipse centers at $(0, \sin\varphi/2)$ and major/minor axes of $\sin(\varphi/2)/\sqrt{\varphi}$ and 1. In particular for the exact relation, this means that there is a lower as well as an upper bound for the spanning distance and associated radius, where polymerization speed and contraction speed can be balanced for arcs with central angle $0 \leq \varphi \leq \pi$

$$R_{\text{high/low}} = \frac{R_{\text{max}}}{2} \pm \sqrt{\left(\frac{R_{\text{max}}}{2}\right)^2 - \frac{\xi^2}{\pi}} \text{ and } d_{\text{high/low}} = R_{\text{max}} \pm \sqrt{R_{\text{max}}^2 - \frac{4\xi^2}{\pi}}. \tag{6.12}$$

Above the upper bound and below the lower bound the stable steady states are either arcs with central angle $\varphi > \pi$ or there exist no stable steady states. The solutions are shown later in Figs. 6.5(a) and (b) as well as the phase diagram which is shown in Fig. 6.5(c) in section 6.2.3.

6.2.2. Force-dependent polymerization speed

We now study the second case, where we assume, that actin filaments are polymerized at the focal adhesions with linearly increasing speed, when increasing the force

$$v_p = \frac{F}{\eta_f}. \tag{6.13}$$

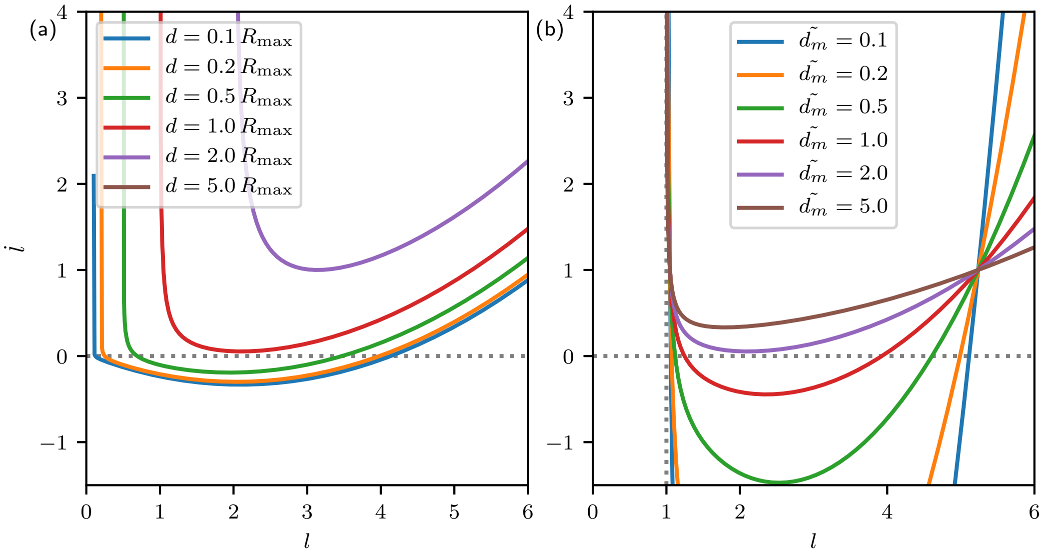

Figure 6.4.: Stability analysis, $\dot{l}$ as a function of l. (a) $\dot{l}$ for a range of spanning distances d for $\tilde{d_m} = 2$. For small spanning distances there are two steady states, the one at lower l is stable, while the other one is instable. For increasing d the system approaches a saddle-node distribution, beyond which both steady states vanish and the length of the peripheral arc increases indefinitely. (b) $\dot{l}$ for a range of $\tilde{d_m}$ and spanning distance $d = R_{\max}$. Similarly for increasing $\tilde{\xi}$ the two steady states vanish in a saddle node bifurcation.

Again using eqs. (6.3) together with the Laplace Law (6.4) we now obtain

$$\dot{L} = -\frac{L}{\eta_0}(F_s - \sigma R(L)) + \frac{\sigma R(L)}{\eta_f}. \tag{6.14}$$

We again nondimensionalize the equation of motion by measuring distance in units of $R_{\max} = F_s/\sigma$ and time in units of $\tau = \eta_f/\sigma$ with result

$$\dot{l} = -\frac{l}{\tilde{d_m}}(1-r) + r, \text{ with } \tilde{d_m} = \frac{d_m}{R_{\max}} = \frac{\eta_0}{\eta_f R_{\max}}. \tag{6.15}$$

Fig. 6.4 shows $\dot{l}$ as a function of l. We find very similar qualitative results as in the case of constant polymerization speed, i.e. there is a saddle-node bifurcation at a certain $(\tilde{d}, \tilde{d_m})$, where increasing either $\tilde{d_m}$ or $\tilde{d}$ leads to a complete destabilization of the system. Also here the fiber grows indefinitely.

We again formally find the steady states by setting $\dot{l} = 0$ and derive a conditional equation for the steady state radius from the geometric relation (6.5). We arrive at

$$r = \frac{l}{\tilde{d}_m + l}, \text{ or in dimensional quantities} \tag{6.16}$$

$$R = \frac{L}{d_m + L} R_{\max}. \tag{6.17}$$

This coincidentally is a mechanical analogon to the Michaelis-Menten kinetics with radius R corresponding to reaction rate, $R_{\max}$ corresponding to the maximum reaction rate, arc length L corresponding to the substrate concentration, d_m corresponding to the Michaelis constant, which is the arc length of half maximal radius. Here the two competing length scales are again the 2D-Laplace radius $R_{\max}$ and the ratio of the slopes of the length normalized force-velocity relation of the fiber and the force-velocity relation of the focal adhesion.

Using $\varphi r = l$ and $\sin \varphi/2 = d/2r$ in eq. (6.16) we find

$$\tilde{d} = 2 \sin \frac{\varphi}{2} \left(1 - \frac{\tilde{d}_m}{\varphi} \right), \tag{6.18}$$

i.e. the contour lines of the central angle φ as a function of $(\tilde{d}, \tilde{d}_m)$ are linear functions. In particular for central angles $0 < \varphi < \pi$ we find a maximum spanning distance

$$d_{\text{high}} = 2(R_{\max} - \frac{d_m}{\pi}). \tag{6.19}$$

At higher spanning distances the central angle $\varphi > \pi$, i.e. the central angle $\varphi > \pi$. At some $d_{\text{crit}} > d_{\text{high}}$ the steady states cease to exist. The solutions are shown in Fig. 6.5(d) and (e) together with the the emerging phase diagram in Fig. 6.5(f) in section 6.2.3.

6.2.3. Comparison of $R(d)$ relation

In Fig. 6.5 we compare typical relations of arc radius R to the spanning distance d, which is the relation that is best accessible experimentally and give phase diagrams indicating whether the system is stable and if so, whether the central angle φ is larger or smaller than π.

The constant polymerization speed model for small $\tilde{\xi}$ leads to $R(d)$ relations that for small d curving upward and reach the line of minimal radius $R_{\min} = d/2$ at d_{low} as shown in Fig. 6.5(a). In this region $\varphi > \pi$. Beyond this point $\varphi < \pi$ and the radius increases monotonically into a plateau region. Near d_{high} the slope of $R(d)$ increases again (here again $\varphi > \pi$) until d_{crit}, where the stable steady state ceases to exist. At

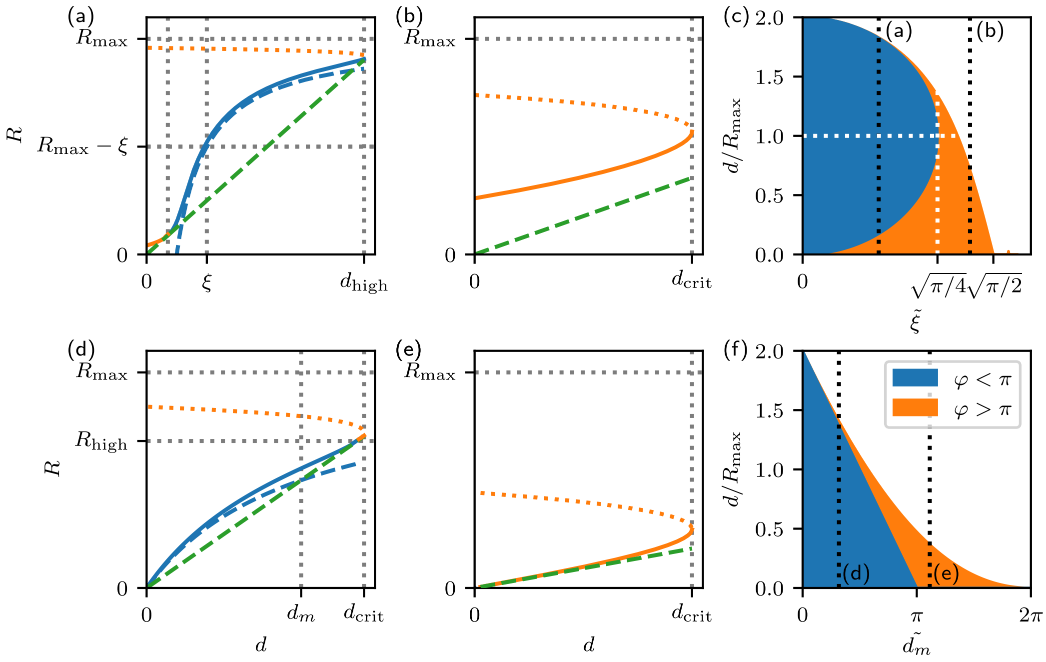

Figure 6.5.: Comparison of $R(d)$ relationship and phase diagram for the two models. Blue solid lines are related to stable steady state lengths, where the arc is smaller than a half cicle, while dashed blue lines represent the result with approximation $\arcsin x = x$. Solid orange lines represent stable steady states where the arc is bigger than a half circle and dotted orange lines represent instable steady states. The dashed green line denotes $d = 2R$, which corresponds to the circle of smallest radius by geometry. The colors in the phase diagrams represent parameter regions, where stable solutions can be found and represent arcs that are smaller (blue) and bigger (orange) than half circles respectively. In the white area the arc curls inward and increases its radius indefinitely. Constant polymerization speed: (a) $\tilde{\xi} = 0.5$ (b) $\tilde{\xi} = 1.1$ (c) Phase diagram. (d) $\tilde{d_m} = 1$ (e) $\tilde{d_m} = 3.5$ (f) Phase diagram.

the value $\tilde{\xi}$ used in Fig. 6.5(a) this region is too small to visualize appropriately. At these parameters the approximation yields reasonable results compared to the exact solution, as long as the central angle $\varphi < \pi$.

For a higher $\tilde{\xi} > \sqrt{\pi/4}$ (where the discriminant in eqn. (6.12) becomes negative) the steady state always relates to an arc with $\varphi > \pi$. Correspondingly, the $R(d)$ relation curves upward throughout all spanning distances d until the critical spanning distance d_{crit}, where the saddle-node bifurcation occurs, which is shown in Fig. 6.5b.

The phase diagram of the constant polymerization model is shown in Fig. 6.5(c). For spanning distances greater than $2R_{\max}$ no steady states occur. This is consistent with the notion, that the interplay of polymerization at the focal adhesion and con-

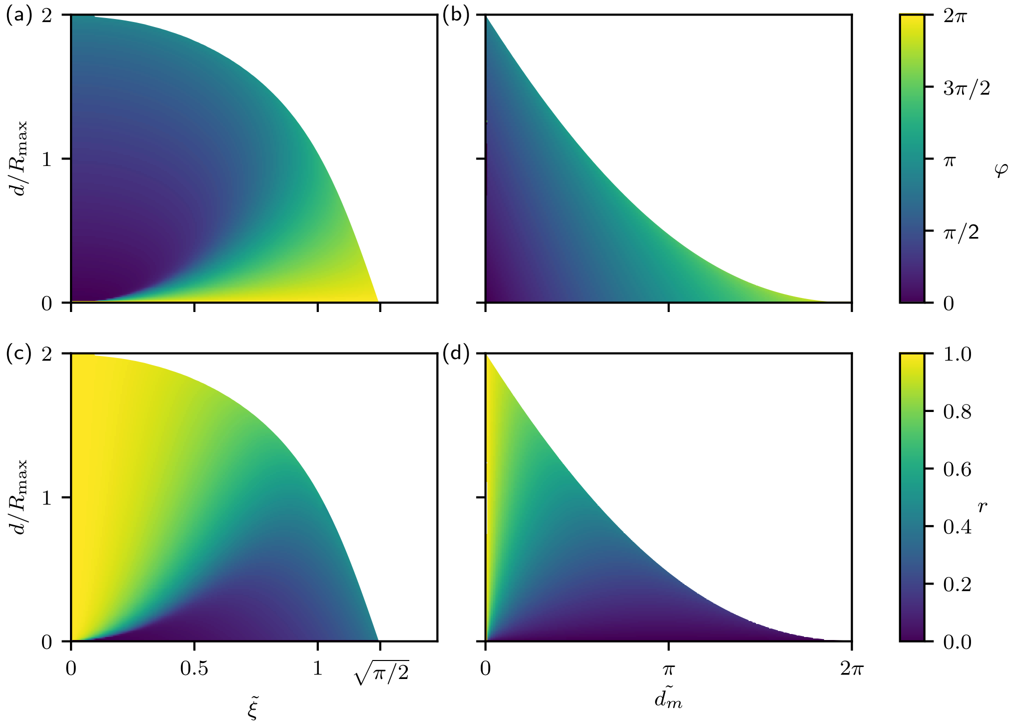

Figure 6.6.: Central angle φ and dimensionless radius r as a function of spanning distance and polymerization length scales. Left: Constant polymerization speed, right: force-dependent polymerization speed.

traction within the fiber always reduces the force within the fiber below the stall force of the motors. For increasing $\tilde{\xi}$ the maximum spanning distance d_{crit} decreases until it reaches zero at $\tilde{\xi} = \sqrt{\pi/2}$. This value can be can be calculated by setting $l = 2\pi r$ in eqn. (6.9) and solving for r. The solutions for r are only real for $\tilde{\xi} \leq \sqrt{\pi/2}$. While the regions of stability could only be determined numerically, the region, where the peripheral arc's central angle $\varphi < \pi$ was determined analytically (see eqn. (6.12)) and follows an elliptical shape as all contour lines of φ (compare eq. 6.11).

For the force-dependent polymerization rate model we find $R(d)$ relations that always start at $R(0) = 0$. From there, the function increases monotonically while curving downward and approaching a plateau for low d_m. At d_{high} the function stops approaching the plateau and the central angles $\varphi > \pi$. Shortly after, at d_{crit}, the saddle-node bifurcation occurs and at higher spanning distances d no steady state exists anymore. This behavior is visualized in Fig. 6.5(d). At the chosen parameters, $d_{\text{high}} \approx d_{\text{crit}}$ for this reason the region where central angles $\varphi > \pi$ is very small. At these parameters the approximation yields reasonable results compared to the exact solution for spanning distances that are not too large.

At higher $\tilde{d_m} \geq \pi$, the central angle $\varphi > \pi$. The $R(d)$ relation again starts at zero for zero spanning distance and curves upward until reaching the critical value for d where the steady states do not exist anymore as shown in Fig. 6.5(e).

Fig. 6.5(f) summarizes this behavior in a phase diagram. The region of stability, as before, is bounded by $d \leq 2R_{\text{max}}$, which is the result for polymerization speed zero or $\eta_f \to \infty$. Increasing $\tilde{d_m}$ leads to a decrease of the maximum spanning distance d_{crit}. For $\tilde{d_m} < \pi$ arcs with central angles $\varphi < \pi$ occur at $d < d_{\text{high}}$ while central angles $\varphi > \pi$ at values $d_{\text{high}} < d < d_{\text{crit}}$. For $\pi \leq \tilde{d_m} \leq 2\pi$ only arcs with $\varphi > \pi$ are observed. At $d_m = 2\pi$ the only configuration that is stable is a full circle, accordingly with spanning distance $d = 0$.

Fig. 6.6 summarizes the dependencies of the central angle φ and the radius r on the spanning distance and the respective additional length scale $\tilde{\xi}$ and $\tilde{d_m}$. Indeed, apart from the quantitative results and shapes of the stable domain, the qualitative behavior is similar. At very low values of the additional length scales the modified Laplace Law recovered and at high polymerization speeds that however still allow for stable stationary solutions of the dynamical equation, the radius approaches zero for the force dependent polymerization, while it remains finite for the constant polymerization speed model.

The key difference between the two models is the following: The constant polymerization speed model predicts arcs with central angles $\varphi > \pi$ for small *and* large spanning distances as long as the polymerization length scale is small enough. In the force dependent polymerization model central angles that are larger than π only occur at large enough spanning distances.

6.3. Summary

This chapter introduced two similar contour models that take into account the dynamic interplay of surface tension, force produced by motors and self-assembly of additional actin filaments at focal adhesions for the maintenance of peripheral stress fibers. The model results depend strongly on the properties of the motors that reside in the stress fibers and therefore could be a valuable tool when quantitatively studying cell shape in conditions with varying quantities of the respective NM II isoforms.

Both studied models show a very similar behavior if the polymerization speed of actin at the focal adhesions is rather slow, which is the typical experimental condition in live cell experiments, where one finds values of $\sim 1\,\text{nm/s}$ [2, 222, 223]. In the following chapter however we restrict the analysis of experimental data to the force-dependent model consistent with an optogenetic study showing an increased centripetal flow of cytoskeletal material towards the inside after activation of the center of the stress fiber [2].

In contrast to other contour models in two dimensions, where the contour shape results from a static (and sometimes elastic) balance of forces [128, 214, 219, 220], in these models the steady state is characterized by a dynamic balance of inflow of cytoskeletal material at the boundary points, the focal adhesion and disassembly by contraction all along the stress fiber. It can therefore be interpreted as another model system, where self-assembly and mechanical processes may occur with temporal overlap. This is similar to myosin minifilaments that are also an example for self assembling complexes that turn over their constituents during the mechanical process they are designed to perform (see chapter 4). In contrast, here the number of constituents is much larger, indicating that we can turn to a deterministic description of the interplay of mechanics and self-assembly.

7. Interplay of non-muscle myosin II isoforms in live-cells

This chapter is based on a preprint from a collaboration with experimentalists, with the working title *"Distinct roles of non-muscle myosin II isoforms A and B for establishing cell morphology: dynamic generation of tension versus elastic stability"* [225]. Here, I focus on the application of the mathematical models to the experimental data but still follow the biophysical narrative of the preprint. More experimental details can be found in the publication or in Kai Weißenbruch's PhD thesis [226].

7.1. Introduction

The morphology of non-muscle cells depends strongly on dynamics in the actin cytoskeleton, where non-muscle myosin II (NM II) minifilaments contract and crosslink actin filaments by hydrolysis of ATP. This active interplay of NM II and actin is critical during processes that involve cellular shape changes, such as cell migration or spreading [49]. As these processes have spatio-temporally different mechanical requirements, the dynamic tension generation and longer lasting tension maintenance have to be precisely tuned.

To accomplish this, mammalian cells can express up to three different isoforms of NM II, that have been introduced in section 2.1.3: NM IIA, NM IIB and NM IIC. In brief, NM IIA contracts much faster than NM IIB when no force is applied, but NM IIB can withstand much higher forces due to its higher affinity for actin after the first powerstroke [71, 72, 227, 228], while not much details are known for NM IIC. In addition, several cell culture studies have shown, that isoforms A and B can co-assemble into mixed, heterotypic filaments containing both NM IIA and NM IIB [88, 229].

Micropatterned substrates (see also section 2.3.1) are an ideal tool to quantitatively analyze cellular morphogenesis as they can normalize cell shape [230] sometimes to such an extent, that the cell shape can be described well by only a handful of numbers [128]. This is in stark contrast to the high diversity of cell shapes that occur on unpatterned substrates. In an early study this approach has been used to quanitify the positioning of cell organelles, such as the golgi, centrosome or the nucleus [231].

Another study discovered, that cells can span accross regions that are nonadhesive by forming stress fibers that invaginate while spanning over these regions [135]. Later work has investigated these so called peripheral stress fibers more quantitatively on dot-shaped micropatterns [128]. The experiments show that cell shape is determined by a balance of surface tension in the cell and a line tension in the cell contour, as described by a modified Laplace law. Additionally, the experiments revealed a correlation of spanning distance and radius of curvature of the invaginated stress fiber, which was theoretically interpreted by the interplay of a tensional element and an elastic element in the line tension in the tension elasticity model (TEM). The underlying molecular mechanism for these elements however remain unclear. We therefore asked, whether NM II isoforms could contribute differentially to the observed cell shape by virtue of their different mechanochemical properties and from there arising different force-velocity relations [71].

To investigate the specific functions of the two NM II isoforms our experimental collaborators generated two knock-out (KO) cell lines NM IIA-KO and NM IIB-KO from the U2OS cell line, which is widely used to study stress fiber dynamics [20], using the CRISPR/Cas9 genome editing system [232]. For quantitative analysis they used cross shaped adhesive micropatterns that, similar to dot-patterns, lead to invaginated arcs, but with more continuously distributed spanning distances. Phenotypical investigation of the cells shows, that NM IIA initiates tension generation by forming filaments containing only NM IIA. Without NM IIA cells neither able to form mature stress fibers nor focal adhesions, which underlines the pioneering role NM IIA has also shown in system such as developing cardiomyocytes [60]. Knock-out of NM IIB in contrast leads to much less pronounced changes. Quantitative analysis using the cross-shaped micropatterns strikingly reveals that knock-out of NM IIB prevented the correlation between spanning distance and arc radius from occuring. This can be understood in terms of the dynamic variant of the TEM, that accounts for the faster crossbridge cycle of NM IIA compared to NM IIB which was analyzed theoretically in chapter 6. Furthermore, and as suggested by the self-assembly model introduced in chapter 4, our FRAP-experiments show that the exchange dynamics of NM II also depends on the specifics of the crossbridge cycle.

In summary, we have found signatures of the isoform specific crossbridge cycle in live cells by a combination of theoretical modeling and experiments; particularly, by studying the quantitative phenotype of peripheral stress fibers and the turnover behavior of each isoform. Together our results underline that NM IIA and NM IIB have complementary roles in establishing the morphology of single cells that are reflected by the interplay of the self-assembly and the isoform specific crossbridge cycle of NM II. Fast NM IIA is responsible for tension generation, while slower

NM IIB is responsible for the upkeep of this tension, thereby providing stability to longer lasting structures.

7.2. Phenotypical characterization of NM II-KO and NM IIB-KO cell lines

First, the effect of NM IIA and B-KO was investigated on homogeneously protein coated coverslip by visualizing stress fibers and focal adhesions by staining for actin and paxillin, which are known to depend on actomyosin contractility [49]. As discussed in section 2.1.1, migratory cells can form different types of stress fibers. In U2OS wild type (WT) cells we observe dorsal stress fibers, connected to one focal adhesion, as well as transverse arcs located near the leading edge and ventral stress fibers that are connected to focal adhesions at both ends (see Fig. 7.1(a)), as previously described in the literature [20]. KO of NM IIA led to a severe disruption of the actin cytoskeleton leading to a branched phenotype of the cell body, with no dorsal stress fibers and no transverse arcs as shown in Fig. 7.1. The stress fibers that remain can be best classified as ventral stress fibers, due to them being connected to two focal adhesions, and occur much lower in number. Additionally, NM IIA-KO cells only show very small focal adhesions localized mainly along the leading edges. NM IIB-KO cells show a much less pronounced change in phenotype compared to NM IIA-KO as shown in Fig. 7.1(c). All stress fiber types are observed, however their distribution within the cell was sometimes disrupted.

We quantified the observed phenotypes by measuring the area of each focal adhesion, the number of focal adhesions per cell and the number of focal adhesions normalized to each cell's area. We found, that the number of focal adhesions per cell was significantly reduced by NM IIA-KO, with no significant difference between WT and NM IIB-KO as shown in Fig. 7.1(d). Fig. 7.1(e) shows the cell average of the focal adhesion area. HereNM IIA-KO cells showed a significant reduction compared to the WT, but we found no significant difference between NM IIB-KO and the two other cell lines. Consistent with the lack of difference between cell areas (not shown), the number density of focal adhesions showed a significant reduction by NM IIA-KO (see Fig. 7.1(f). Fig. 7.1(g) shows that the normalized distribution of focal adhesion areas follows an exponential distribution, which, consistent with the mean area shown in Fig. 7.1(e) has a much lower spread for NM IIA-KO compared to WT.

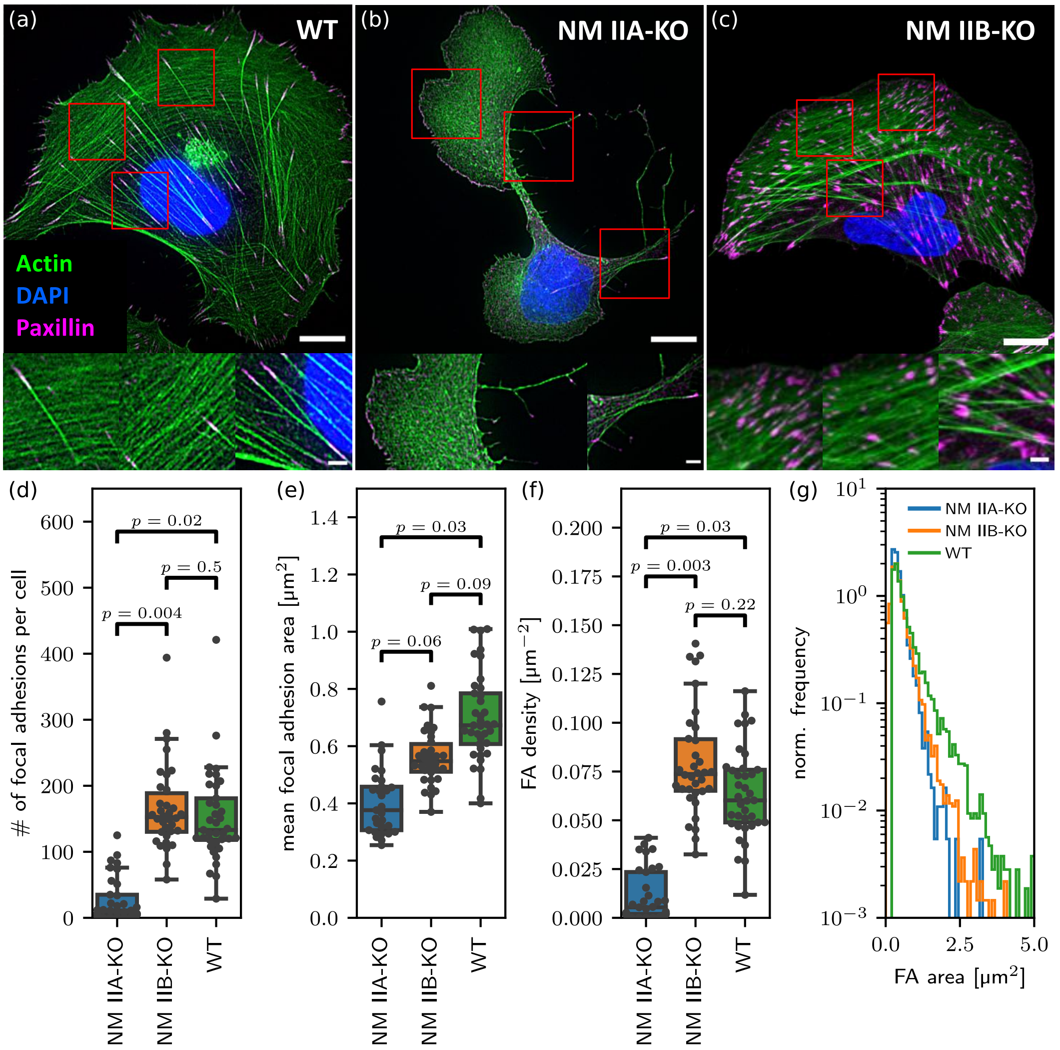

Figure 7.1.: Phenotypical changes induced by NM IIA and NM IIB-KO in stress fiber and focal adhesion formation. (a) USOS wildtype cells show clearly distinguishable dorsal stress fibers, transversal arcs and ventral stress fibers. Elongated clusters of paxillin indicate the presence of mature focal adhesions at the distal end of dorsal stress fibers aswell as both ends of ventral stress fibers. (b) NM IIA-KO leads to drastic changes in the phenotype marked by the loss of most stress fibers and mature focal adhesions. (c) NM IIB-KO leads to only mild phenotypical change, where ventral stress fibers and transversal arcs are unspecifically distributed within the cell. The number of focal adhesions per cell (d), the mean area of the focal adhesions (e), and the number density of focal adhesions (f) are reduced significantly for NM IIA cells compared to the WT. (g) Focal adhesion sizes are approximately exponentially distributed. WT cells show the highest spread followed by NM IIB-KO and finally NM IIA-KO cells. Adapted from [225].

7.3. Quantitative analysis of NM II A/B-KO phenotypes show signatures of isoform-specific force-velocity relation

We let the cells spread on adhesive micropatterns with cross-shapes and – as expected – observed that four invaginated circular arcs form at the periphery, as shown in Fig. 7.2(a) through (c). The occurence of circular arcs has been explained before by models that assume a balance between surface tension generated in the actin cortex and line tension generated in peripheral stress fibers [128, 130, 214]. Quantitative image analysis has revealed a positive correlation between spanning distance d and arc radius R and has been interpreted as evidence for an elastic nature of the stress fibers [128]. Here we follow this earlier work, but explore a more dynamical approach that allows us to focus on the role of the different myosin II isoforms, which are known to have very different rates in their crossbridge cycles. We also find such a correlation for WT and NM IIA-KO cells as shown in Figs. 7.2(a) and (b), respectively. KO of NM IIB however disrupts this correlation as visualized in Fig. 7.2(c).

To explain this result theoretically, we consider the model introduced in section 6.2.2, that describes the stress fiber as a contractile structure that sustains a continuous transport of cytoskeletal material from the focal adhesion towards the center of the stress fiber as visualized in Fig. 7.2(d). This flow in stress fibers can be observed experimentally and like retrograde flow is believed to be driven both by actin polymerization in the focal adhesions and myosin force in the stress fiber [2, 143, 222–224]. Therefore, it should depend on the details of the myosin II isoforms residing in the stress fibers. As described in chapter 5, stress fibers should contract faster at low forces if the isoform ratio favors NM IIA. Like muscle, mature stress fibers are organized with sarcomeric arrangements of the myosin motors [51, 143]. Accordingly, the number of serially arranged motor ensembles increases linearly with stress fiber length and stress fiber contraction speed should increase with length. The stall force F_s however should not depend on stress fiber length because in a one-dimensional system, each sarcomere feels the same force. Indeed, the linear scaling between contraction speed and length as well as the length-independence of the stall force have been observed experimentally for reconstituted stress fibers [221]. We also assume that the flow of stress fibers out of focal adhesions increases with force in the stress fiber as demonstrated by optogenetics [2]. Finally, we assume that the force in the contour is related to its radius by the Laplace equation [128, 214].

In chapter 6 we have defined a dynamical model with these ingredients for invaginated arcs. We then have identified its steady states that should correspond to the stationary shapes observed in the experiments. The mathematical analysis gave the

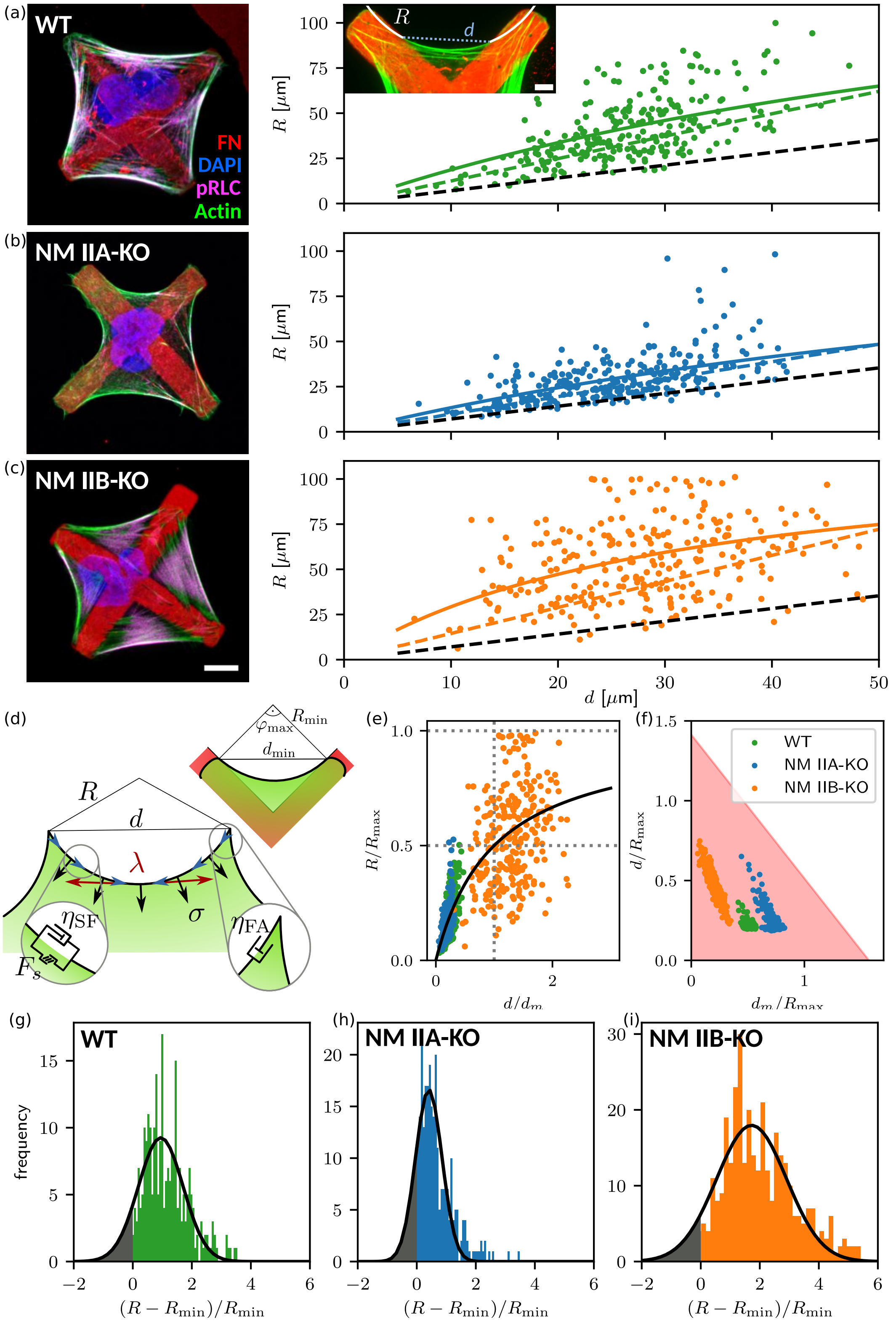

Figure 7.2.: NM II-KO phenotypes on cross patterns.

Figure 7.2 *(previous page)*: (a-c) Phenotypes and quantification of R-d relations. (d) Model sketch of the modified TEM. Circular arcs form from the balance of line tension λ and surface tension σ. The blue arrows indicate the inward flow of cytoskeletal material. The inset visualizes the geometry of peripheral stress fibers with maximum central angle. (e) Normalizing experimental results using the respective fit parameters yields a master curve. NM IIB-KO cells fall into the plateau regime of the Michaelis-Menten analogon, WT and NM IIB-KO into the linear regime. (f) $d_m/R_{\max}$ vs ratio of maximum observed spanning distance and $R_{\max}$. The region marked in red denotes the theoretical prediction where the central angle of the arc is smaller than 90°. Points denote bootstrapped fit results. Solid lines denote the bootstrapped mean fit of the model sketched in (d), dashed colored lines denote fits of the tension control TEM. (g-i) Distributions of differences between observed radius and minimum allowed radius normalized to the minimum allowed radius resemble cut-off gaussian distributions, we can estimate the fraction of non-formed arcs by calculating the grey area. Adapted from [225].

following approximate relation between R and d

$$R(d) = \frac{d}{d_m + d} R_{\max} \tag{7.1}$$

which is formally similar to a Michaelis-Menten relation, with maximal radius $R_{\max} = F_\mathrm{s}/\sigma$, given by the ratio of stall force F_s and surface tension σ. It can be interpreted as the radius that would be observed if there was no reduction of tension by the polymerization at the focal adhesions. The spanning distance at half maximal radius is found to be $d_m = \eta_\mathrm{SF}/\eta_\mathrm{FA}$ and determines whether the force is bounded by the contraction speed of the fiber or by the maximum force F_s that can be produced. If the spanning distance is small against d_m, the observed radius is dependent on the length of the stress fiber, while at spanning distances that are large against d_m, the radius depends primarily on surface tension and the stall force that can be generated by the motors.

We also note that due to geometrical constraints, the circular arcs on our cross pattern can have a central angle of up to 90°, as indicated in the inset of Fig. 7.2(d). If angle were larger, peripheral arcs would have to span across adhesive regions of the substrate, which was never observed. This maximally allowed central angle leads to a minimal possible radius given the spanning distance d as $R_{\min} = d/\sqrt{2}$.

We fitted eq. 7.1 to the experimental data and obtained reasonable agreement (see Fig. 7.2(a)-(c)). We find mean fit parameters from bootstraps: WT: $R_{\max} = (199 \pm 8)$ µm, $d_m = (100 \pm 7)$ µm ; NM IIA-KO: $R_{\max} = (190 \pm 30)$ µm, $d_m = (134 \pm 20)$ µm;

NM IIB-KO: $R_{\max} = (100 \pm 20)\,\mu\text{m}$, $d_m = (20 \pm 10)\,\mu\text{m}$. Note that the fits have been constrained such that $R_{\max}$ and d_m are always smaller than 200 µm, since the radii and spanning distances we observe are well below 200 µm. Standard deviations are calculated from bootstraps. These results are consistent with the experimental finding that NM IIA motors, which are the only motors present in NM IIB-KO cells, are weaker but faster than NM IIB motors. A mix of both as is present in WT cells leads to intermediate motor strenghts and speeds [66, 71, 72]. By rescaling the experimental values using the fit parameters, the points roughly follow a master curve which is shown in Fig. 7.2(e). This illustrates that the data we have obtained for NM IIB-KO cells lies in the plateau region of the Michaelis Menten curve, while the data we collected for the other cells lies in the linear regime.

We have theoretically predicted the region in $(d_m/R_{\max}, d/R_{\max})$ where the central angle is lower than 90°, i.e. permissible by our cross pattern (see Fig. 7.2 (f)), by using eq. (6.18). This region is triangular; bounded by an upper spanning distance $d/R_{\max}$. For each cell line, we show the bootstrapped results of the maximum spanning distance and the fit parameters in this space. We see, that the cell lines are sorted along the x-axis from NM IIB-KO to NM IIA-KO, with NM IIA-KO being closest to the edge of the theoretically permissible region, which is consistent with the fact that in these cells we sometimes find, that arcs do not form. We explore this phenomenon further by analyzing the distribution of arc radii. Fig. 7.2 (g)-(i) shows that the distribution of the difference of observed radius to the minimum radius normalized to the minimum radius approximately follows a Gaussian distribution, that is however cut off at zero difference. For the approximately linear $R(d)$ relations, we can interpret this spread as a Gaussian fluctuation of the maximum radius $R_{\max}$. Assuming the cut off part of the distribution relates to the fraction of arcs that have not formed despite possible from the cell spread on the cross, we find there should be approximately 10%, 18% and 7% non formed arcs for WT, NM IIA-KO and NM IIB-KO cells respectively. These estimates should be considered as upper bounds, since we have not considered the error in measurement, which will increase the variance of the shown distributions. Consistently, we observe non-formed arcs only in NM IIA-KO cells. In these cells we observe this 13% of the time.

To get another perspective on these results, we fit the original TEM [128] to the data, which assumes a static elastic fiber with no contributions by flow. The model additionally assumes that the rest length scales linearly with the spanning distance with a factor α. Using this model it is possible to determinde upper bounds for the scaling factor α. For the different cell types we find mean values: WT: $\alpha = 1.029 \pm 0.003$, NM IIA-KO: $\alpha = 1.051 \pm 0.004$, NM IIB-KO: $\alpha = 1.021 \pm 0.005$ (Standard deviations are calculated from bootstraps). These results suggest, that the more influence NM IIA has on the cell, the more the rest length of the stress fiber is regulated to be smaller, by actomyosin contraction. This is consistent with the interpretation of the results obtained in the here introduced dynamical model.

7.4. Isoform specific differences in turn-over depend on the crossbridge cycle

Having found a signature of the isoform specific crossbridge cycle which leads to distinct force-velocity relations in mixed minifilaments depending on the isoform content (see chapter 5) in the quantitative phenotype, we turn to FRAP experiments probing the turnover dynamics of NM II. Motivated by the theoretical result from section 4.3.3 that NM II turnover may depend on force and also be modulated by the isoform specific crossbridge cycle, we performed FRAP experiments in reconstituted cells. These were prepared from NM IIA-KO and NM IIB-KO cells by reintroducing a fluorescently labeled version of the missing isoform. Exemplary image sequences of the FRAP experiment of the isoforms A and B are shown in Figs. 7.3 (a) and (b), respectively. Image sequences like these are analyzed by fitting the normalized intensity

$$I(t) = \delta(1 - \exp -t/\tau) \tag{7.2}$$

to the trajectory after correcting for photobleaching and drift of the region of interest as described in detail in the appendix (see section A.3.2). We find a wide spread of recovery trajectories for both investigated isoforms of NM II (see Figs. 7.3(c) and (f)). Consistent with previous experiments, NM IIA shows a much faster exchange dynamics than NM IIB [90, 143]. For NM IIA we find a distribution of recovery times τ and mobile fractions δ with means and standard deviations $\tau = (69 \pm 53)\,\mathrm{s}$ and $\delta = (0.63 \pm 0.29)$. For NM IIB we find $\tau = (230 \pm 140)\,\mathrm{s}$ and $\delta = (0.47 \pm 0.28)$. Inhibition of myosin crossbridge cycle by para-aminoblebbistatin, a photostable and non-fluorescent blebbistatin derivative [193, 233], leads to only miniscule changes in the FRAP of NM IIA, as visualized in Fig. 7.3(d). Here we find $\tau = (52 \pm 30)\,\mathrm{s}$. The FRAP dynamics of NM IIB however is accelerated by para-aminoblebbistatin and we here find $\tau = (63 \pm 44)\,\mathrm{s}$ and $\delta = (0.64 \pm 0.33)$. The fit results are summarized in scatter plots in Fig. 7.3(e) for NM IIA and Fig. 7.3(h) for NM IIB. For a better comparison of the results for both isoforms, boxplots of the recovery time and mobile fraction of all four experiments are shown in Figs. 7.3(i) and (j), respectively.

Since recovery time and mobile fraction are not statistically independent variables as they arise from the same fit and are correlated, as shown in Figs. 7.3(e) and (h), we compare the joint distribution of mobile fraction and recovery time by a two-dimensional version of the Kolmogorov-Smirnoff test, the Peacock test [234, 235]. The p-values are indicated in Figs. 7.3(i) and (j). Note that the reported values are the same in both figures, as the joint distribution is compared. The statistical test shows, that of the four experiments only untreated NM IIB resulted in significantly different distributions of recovery time and mobile fraction. In particular, since the recovery times of NM II become independent of isoform if treated with para-aminoblebbistatin and since blebbistatin is known to inhibit the phosphate release in the crossbridge cycle [193, 236], this experimental result suggests that self-assembly of NM II depends on the mechanochemistry of actomyosin, as already proposed in chapter 4.

Aiming for a mechanistic understanding of this effect, we extend the graph based assembly model introduced in chapter 4 to allow for mixed isoform minifilaments. Fig. 7.4(a) visualizes the graph on which the assembly occurs. The assembly follows similar rules as introduced in section 4.2.2, i.e. the association rate of each site with neighboring occupied sites is constant and the dissociation rate is governed by eq. (4.1), as long as the motor head of the associated myosin is not attached to actin. Overall turnover is thereby reduced by actin bound myosins. Reminiscent of the extension of the Ising model to a Potts model, now however each site can not only be occupied or unoccupied, but has three possible states in total, unoccupied, occupied by NM IIA and occupied by NM IIB. The assembly model now by principle has to define separate association rates for of NM IIA and NM IIB which are defined by

$$k_{\text{on}}^{a/b} = \Delta_{a/b} k_{\text{on}}, \tag{7.3}$$

where k_{on} is the total association rate and $\Delta_{a/b}$ can be interpreted as the relative amounts of NM IIA and B in solution, with $\Delta_a + \Delta_b = 1$. In principle, also the dissociation rate could depend on isoform, as binding energies of the assembly depend on specifics of the charge distribution along the myosin coiled-coil [55, 237], however – favoring model simplicity – we here assume the dissociation rate does not depend on isoform. Following the argument about the CAC from chapter 4, we use a dimensionless association-rate $\kappa = k_{\text{on}}/k_{\text{off}}^0 = 0.017$, which implies a concentration very close to, but below the CAC of myosin in solution without the stabilizing effect of the crossbridge cycle. This is consistent with the idea, that cells will not assemble myosin minifilaments if there is no actin that can be contracted. FRAP of one minifilament is simulated as described before in section 4.2.6, by associating an addition Boolean value to each occupied space indicating whether the associated myosin is fluorescent. The inset of Fig. 7.4(a) visualizes the two step process of replacement

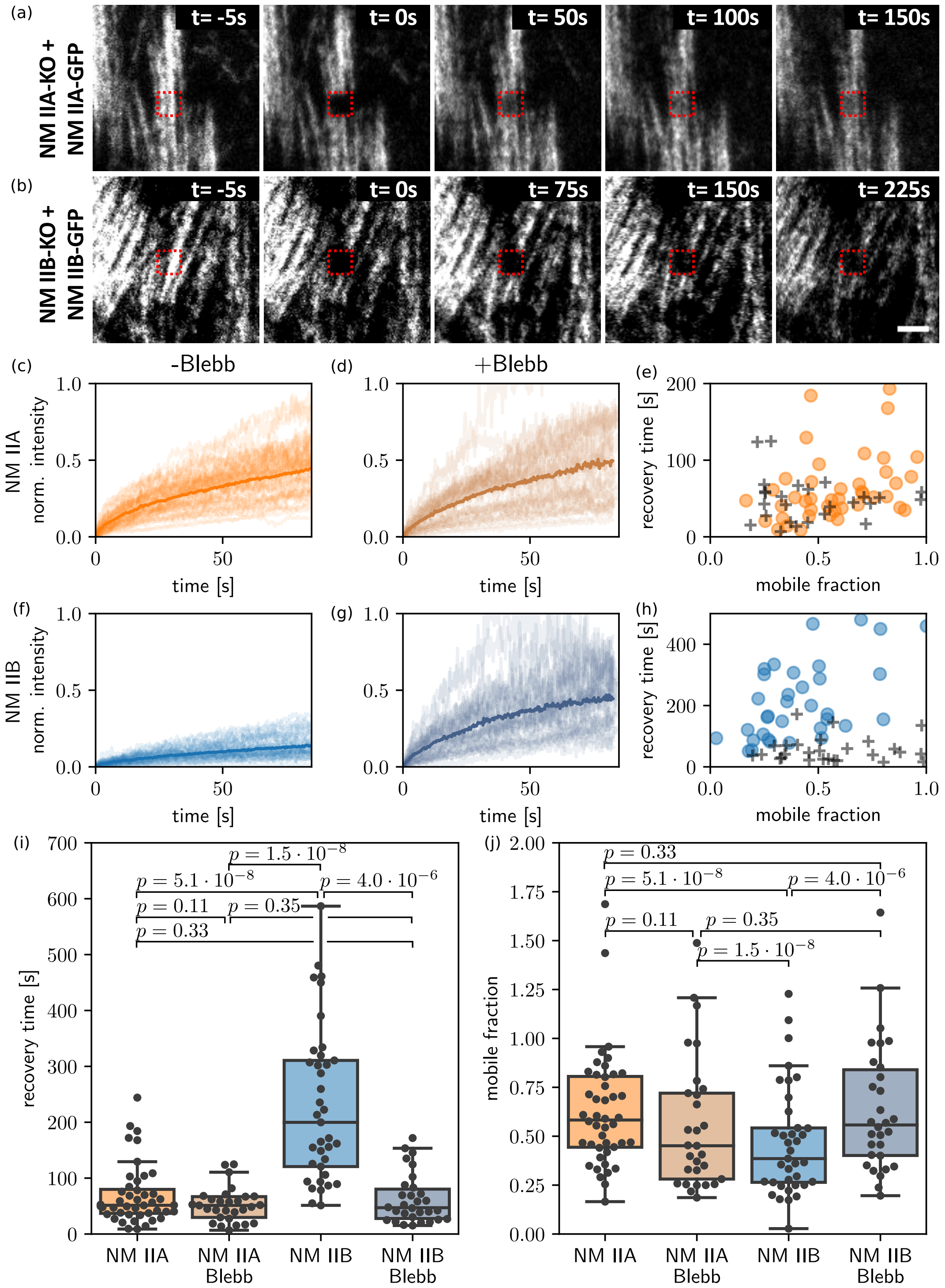

Figure 7.3.: FRAP recovery time difference between NM II isoforms is abolished by inhibition with blebbistatin. (a,b) Exemplary FRAP image sequence showing qualitatively faster exchange dynamics for NM IIA. (c,d,f,g) Normalized FRAP dynamics of NM IIA and B in the absence and presence of photostable

Figure 7.3 *(previous page)*: para-aminoblebbistatin. Transparent lines denote singular measurements of the normalized intensity, solid lines represent the mean normalized intensity. (e,f) Scatter plot of NM IIA and B fitted recovery time and mobile fraction in the absence (transparent circles) and presence (gray pluses) of para-aminoblebbistatin. Boxplots of recovery time (i) and mobile fraction (j) in the four experimental conditions. p-values denote the result of a Peacock-test comparing the two-dimensional distribution of mobile fraction and recovery timescale. Adapted from [225].

of a non-fluorescent myosin with a fluorescent one.

The experiments with fluorescent NM IIA and B are performed in different cell lines: NM IIA experiments are conducted with NM IIA-KO cells with reintroduced, but fluorescently tagged NM IIA, while NM IIB experiments are conducted using NM IIB-KO, with reintroduced fluorescent NM IIB. Accordingly, we consider simulations of the two systems separately in simulations where NM IIA is assumed to be fluorescent, we assume $\Delta_a = 0.9$, while we use $\Delta_b = 0.3$, as NM IIA is more abundantly available in the U2OS cells used here [88]. The ratio will most likely also depend on the specific cell studied, miniscule changes to these values however do not change the qualitative result of the simulation.

The crossbridge cycle of the model is visualized in Fig. 7.4(b). Myosin heads bind from the unbound state to a weakly bound state with rate $k_{01} = 0.2\,\mathrm{s}^{-1}$ that is non-stereospecifically bound to actin [236] and therefore is very prone to direct unbinding events, which occur with rate $k_{10} = 0.4\,\mathrm{s}^{-1}$. From this weakly bound state, the powerstroke occurs quickly, with rate $k_{12} = 1.4 \cdot 10^6\,\mathrm{s}^{-1}$ [71, 72]. This is the rate that is strongly reduced by the presence of blebbistatin, as it is also linked to the phosphate release. When simulating FRAP in the presence of blebbistatin we use $k_{12}^{\mathrm{Blebb}} = 1.5\,\mathrm{s}^{-1}$ [236]. After having performed the powerstroke, myosin can either return to the weakly bound state with relatively small rate k_{21} or it can unbind from actin with a force- and isoform-dependent rate

$$k_{20}^{a/b}(F) = k_{20}^{0a/0b}[\Delta_c \exp(-k_l \xi_i / f_c) + (1 - \Delta_c) \exp(-k_l \xi_i / f_s)]. \tag{7.4}$$

The model additionally considers a tug-of-war situation between the two sides of the minifilament, which is depicted Fig. 7.4(c). The minifilament works against two external springs with strains z_- and z_+, respectively. In addition, each side of the minifialment consists of a variable number of NM IIA and NM IIB motors N_a^-, N_b^-, N_a^+ and N_b^+, respectively, that are dynamcially exchanged according to the rules of the assembly model. At all times the forces acting on the myosin heads of each sides has to be balanced against the force in the external springs. Balancing of the

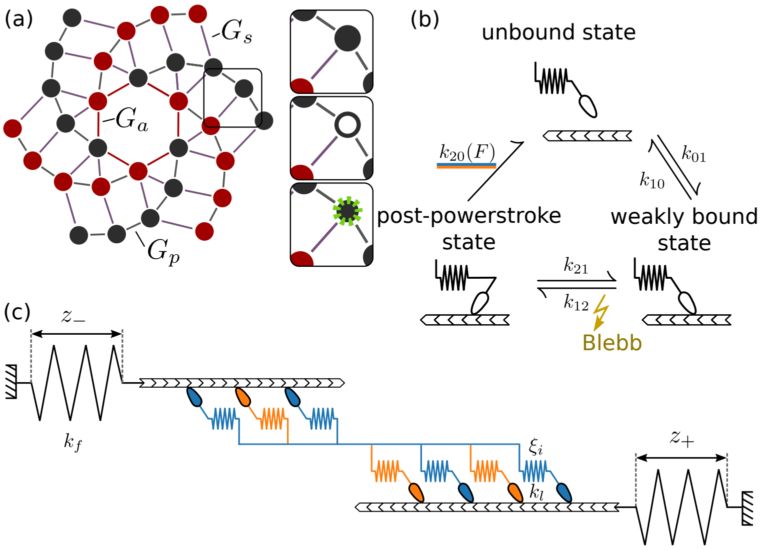

Figure 7.4.: Simulating FRAP of NM II hetero-filaments. (a) Graph of the assembly model. Red and gray circles denote NM II monomers with heads pointing to either direction of the minifilament, while violet, red and gray lines denote bonds with differing associated bond energies G_a, G_p and G_s. The inset illustrates the two-step process of exchanging a non-fluorescent monomer with a fluorescent molecule (green). (b) The crossbridge cycle is modeled by three mechanochemical states, the unbound state, the weakly bound state and the post-powerstroke state. k_{01}, k_{10} and k_{21} are assumed to be constant and independent of isoform, $k_{20}(F)$ depends on force and isoform and k_{12} is decreased strongly in the presence of blebbistatin. (c) NM II motors of either side of the minifilament work against each other in a tug-of-war, straining external springs with spring constant k_f in the process. The simulation considers individual strains ξ_i for each neck linker, with spring constant k_l.

forces is described in detail in the appendix in section A.3.3. The stochastic model can now be simulated using the Gillespie algorithm [189]. All model parameters are summarized in Table A.1 in the appendix.

After an initial burn-in time, the number of NM IIA and NM IIB fluorescent myosins N^j_{pre} in the minifilament is recorded at one time-step before the bleach time in NM IIA and NM IIB FRAP simulations. At the time of photobleaching, all assembled myosin are set to be non-fluorescent. Newly assembling proteins from that point on however are fluorescent, which over time leads to an increase in the number of fluorescent myosin $N^j_{\text{fluor}}(t)$, which is also recorded. We now simulate these systems until the time after bleach matches, the time the respective FRAP experiment has been conducted. As myosin minifilaments are very small, we assume multiple minifilaments are recorded in the region of interest that was recorded. Accordingly, $n = 4$

independent simulations of one minifilament showing the time-dependent number of fluorescent myosin monomers were used to obtain one normalized FRAP trajectory that can be compared to the experiment by

$$I_{\mathrm{sim}}(t) = \frac{\sum_{j=1}^{n} N^{j}_{\mathrm{fluor}}(t)}{\sum_{j=1}^{n} N^{j}_{\mathrm{pre}}}. \tag{7.5}$$

We started by simulating NM IIA in the absense of blebbistatin and obtain trajectories comparable to the experiment, as shown in Fig. 7.5(a) by using an association rate of $k_{\mathrm{on}} = 5\,\mathrm{s}^{-1}$, which is reasonably close to the value estimated in chapter 4. After this, we simulated NM IIA in the presence blebbistatin, which had little effects on the dynamics, as in the experiment. We further quantified this by fitting eq. (7.2) to the simulated trajectories. The results of the fits to simulation data are visualized in Fig. 7.5(c). As in the experiment, mobile fraction and recovery timescale are correlated with each other. In absence of blebbistatin, myosin II cycles through the states shown in Fig. 7.4 in a clockwise fashion. Since $k_{12} \ggg k_{12}^{\mathrm{Blebb}}$, this does not occur as regularly when considering the presence of blebbistatin. Instead, the specific transition rates between unbound and weakly bound state are probed much more, because the weakly bound state becomes more populated in the presence of blebbistatin. As the rates used here lead to similar overall duty ratios of NM IIA, independent of blebbistatin presence, the recovery dynamics is not affected much. Overall for NM II we find mean timescales and standard deviations of $\tau_a = (61 \pm 30)\,\mathrm{s}$ and $\tau_a^{Blebb} = (64 \pm 81)\,\mathrm{s}$ and mobile fractions of $\delta_a = 0.53 \pm 0.12$ and $\delta_a^{\mathrm{Blebb}} = 0.62 \pm 0.4$, similar to the experiments.

Turning to NM IIB, as expected from the higher duty ratio of the NM IIB, we find a slower recovery dynamic compared to NM IIA. The trajectories are shown in Fig. 7.5(d). In contrast to NM IIA, reduction of the powerstroke rate to k_{12}^{Blebb} here markedly quickens the dynamics of turnover as shown in Fig. 7.5(e). In Fig. 7.5(f) the fitted mobile fraction and recovery time are summarized for NM IIB in the absence and presence of blebbistatin. The two different point clouds are clearly discernible from each other. Quantitatively our simulations for NM IIB yield mean recovery times and standard deviations of $\tau_b = (145 \pm 129)\,\mathrm{s}$ and $\tau_b^{\mathrm{Blebb}} = (62 \pm 54)\,\mathrm{s}$ and mean mobile fractions and standard deviations of $\delta_b = 0.54 \pm 0.27$ and $\delta_b^{\mathrm{Blebb}} = 0.52 \pm 0.29$. These results are visualized in boxplots in Figs. 7.5(g) and (h). Overall for NM IIB the result for the fluorescence recovery in the absence of blebbistatin does not match the experiment exactly, however the simulation captures the qualitative behavior of NM IIB in response to blebbistatin well. Using a slower detachment rate from the

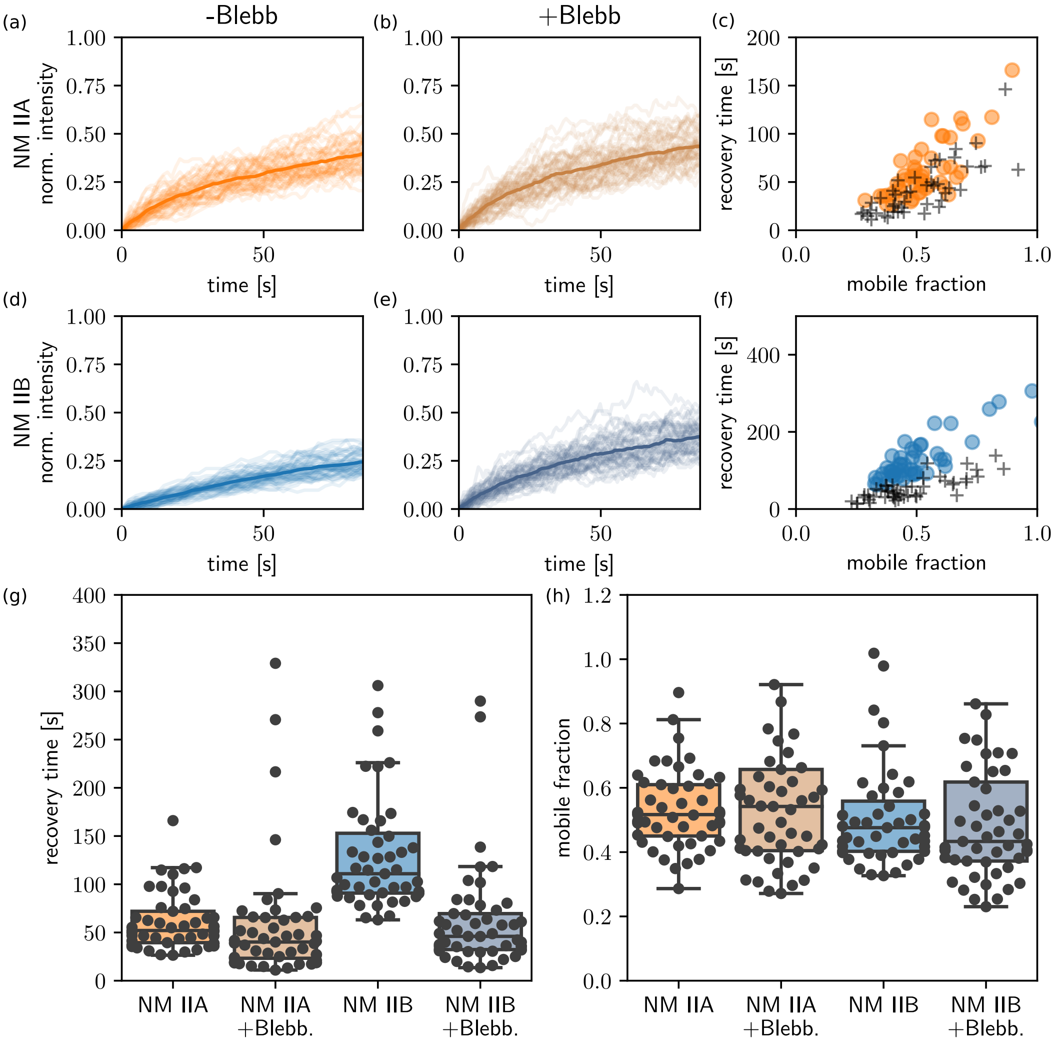

Figure 7.5.: The assembly model can qualitatively explain the experimental experimental findings. (a,b,d,e) Simulated FRAP trajectories of NM IIA and B with powerstroke rate k_{12} for (-Blebb) column and k_{12}^{Blebb} for (+Blebb) column. (c,f) Scatter plot of mobile fraction and recovery time as fitted from the simulated data for NM IIA and B, respectively. (g,h) Visualization of recovery times and mobile fractions as boxplots. The parameters used for the simulation are given in the appendix (Table A.1).

post powerstorke state $k_{20}^{0b} = 0.15\,\mathrm{s}^{-1}$ gives better quantitative results for NM IIB, while not changing much for the results of NM IIA as shown in Fig. A.5 in the appendix. This may indicate, that the mechanochemistry of NM IIB depends even more strongly on force than assumed until now. However, due to the complexity of the system it is difficult to come up with a definite explanation of the difference.

7.5. Discussion

The experimental results together with the theoretical interpretations presented in this chapter highlight the complementary mechanochemistry of the two isoforms: The fast NM IIA and the slower but stronger NM IIB. While NM IIA with its high velocity at low forces typically acts as an initiator of contraction in dynamic situations as in the transverse arcs at the lamellum, NM IIB with its lower velocity but higher stall force gives stability to longer lasting structures such as ventral stress fibers in the center of the cell [90]. Interestingly, these mechanical dynamics are also reflected by the dynamics of self-assembly of the two isoforms. Our FRAP results indicate, that this close relation of mechanical dynamics and self-assembly dynamics is neither by design nor by chance, but by a coupling of the crossbridge cycle to the self-assembly dynamics in which actin takes the role of a stabilizing template.

Using cross shaped micropatterns produced by microcontact printing, we found that the previously reported correlation of arc radius R and spanning distance d of peripheral stress fibers [128] depended critically on the presence of the NM IIB isoform. The phenotypes of invaginated stress fibers were explained by the contour model introduced in chapter 6, which explains the observed arcs as steady states determined by three mayor factors. These are firstly myosin contractility-dependent self-assembly of actin filaments at the focal adhesions at either end of the stress fiber, that has previously been observed experimentally [2, 222, 223], secondly the force-velocity relation, that is well known to be explained by the characteristic crossbridge cycle of each NM II isoform [71, 72], and lastly cortical tension.

In the FRAP experiment, we also found signatures of the different biochemical properties as suggested by the theory presented in chapter 4. Consistent with previous reports of FRAP experiments on NM IIA and B [90, 91, 143] our experiment also found that NM IIA fluorescence recovery occurs much faster than NM IIB, which could at least partly be linked to the differences in the crossbridge cycle transition rates that have been measured experimentally [227, 228]. The differences in FRAP dynamics were leveled by treatment with a photostable and non-fluorescent derivative of blebbistatin [233]. In particular the FRAP dynamics of NM IIB was sped up to be as quick as NM IIA, while NM IIA FRAP dynamics did not show a significant reaction to treatment with the blebbistain derivative. While the model of mechanosensitive assembly reasonably explains the observed results, in light of super-resolution microscopy data, indicating that treatment by blebbistatatin decreases the cortical network density [14], this is a surprising result, as a denser network typically hinders diffusion, which should slow down the fluorescence recovery. Consistent with the notion, that NM IIB assembly is affected more than NM II by addition of blebbistatin, as indicated by the reduced exchange time, solubility assays have also shown a much stronger increase in solubility of NM IIB after treatment of cells with blebbistatin [91].

Overall, both the micropattern experiment and the FRAP experiment show signatures of the isoform specific crossbridge cycle of NM II where it modulates the self-assembly of actin filaments and the NM II minifilament itself.

8. Conclusion

Mechanical stability and the ability to interact with its mechanical environment is given to cells by a dynamic self-assembled superstructure, the cytoskeleton. Thus, the central processes generating the cell mechanical behavior have to integrate chemical quantities such as reaction rates of cytoskeletal constituents and mechanical properties such as forces generated by molecular motors. In this thesis I studied such processes by developing and analyzing mathematical models specifically addressing the interplay of self-assembly and mechanics. In particular together with experimental collaborators, we could show, that self-assembly and mechanical processes are tightly intertwined in NM II minifilaments as well as whole stress fibers.

Chapter 3 started from the Becker-Döring equations to explore how the assembly dynamics of a solution near equilibrium of many self-assembling structures relates to the stochastic size dynamics of one single cluster in an equilibrated solution. Here I focused on clusters with finite size, where the fully assembled cluster is stabilized by a low dissociation rate of monomers, and a constant free monomer concentration which leads to a linear system of dynamical equations. Using a linear perturbative approach I calculated the eigenvalues of the Jacobian that governs the time-evolution of concentrations in this system. These eigenvalues can be interpreted as inverse relaxation timescales. Comparison with numerical calculations showed reasonable agreement. Furthermore I quantified – mostly numerically – the eigenvalues of the single cluster size dynamics' master-equation. Here I found a phenomenon of critical slowing down at a certain on-rate, where the relaxation timescales reach a maximum at the onset of assembly. Interestingly, this maximum was related very closely to the CAC, which was defined as the monomer concentration, where the scaling of the relation of free monomers to total monomers in the system changes dramatically. Experiments showing stable assembly of clusters will be close to this concentration. In the model system studied, the longest timescale of the entire system was an upper bond to the maximum relaxation time of the single cluster dynamics, becoming very close for very low free monomer concentrations. This could be used to give lower bounds on association and dissociation rates of theoretical assembly models given experimental data describing the dynamics. Further research could more thoroughly investigate how these findings transfer to the case where not free monomer concentration is held constant, but the total amount of monomers in the system.

Chapter 4 introduced a self-assembly model of NM II minifilaments that is based on a consensus architecture of the minifilament. This model couples self-assembly and force generation of NM II in the intuitive fashion, that myosins can only unbind from the minifilament if it currently is not in an actin bound state of its cross-bridge cycle. Similar to chapter 3 there is a critical on-rate where assembly slows down dramatically which marks the onset of assembly. Analysis of the parameter space showed that this concentration depends on force and is reduced by the coupling of self-assembly and the cross-bridge cycle, illustrating that actin and force may stabilize myosin II minifilaments. In addition, a mean-field model, that mapped the complexity of the graph into rates of a monomer addition scheme, could explain the qualitatively different behaviors of the system in the different parameter regimes by the occurrence of saddle-node bifurcations. The model used here also allowed for simulating FRAP experiments, which, consistent with the general behavior of the system, showed a slower dynamics at higher forces. In turn, if no interaction with actin was simulated the FRAP became faster, which was later backed up by experiments, discussed in chapter 7, using the pharmacological inhibitor blebbistatin, that specifically inhibits the cross-bridge cycle.

Chapter 5 investigated the mechanical response of a mixed motor ensemble containing the fast and slow isoforms of NM IIA and B to an oscillatory strain. This simulation, which was motivated by typical rheological experiments, showed that the mechanical response of the mixed motor ensemble could be modeled as active Maxwell element. Increasing the ratio of slow to fast isoforms led to a transition of viscous to elastic behavior. As expected, the complex modulus scaled linearly with system size. These findings are also captured by a mean-field theory that assumes a linear force-velocity relation, with a finite free velocity at zero force and a finite stall force at which the velocity becomes zero. The slope of the force velocity relation and the stall force were estimated from a self-consistent approximation based on the PCM. While the ensemble responded approximately linear to small oscillatory strain, large amplitude oscillations revealed the anisotropic property of stretch strengthening and compression weakening which should be attributed to the catch-bond behavior of myosin implemented in the simulation. Further investigations should be complemented by appropriate experiments that probe the response of myosin motor ensembles to oscillatory strain.

Chapter 6 introduces a dynamical model for peripheral stress fiber shape. As in previous models, cortical tension is assumed to be isotropic, as well as the tension within the stress fiber which has to be constant throughout the stress fiber, due to force balancing. Motivated by the rheology of mixed motor ensembles, as discussed in chapter 5, but neglecting the short timescale behavior of the active Maxwell model proposed therein, the stress fiber is modeled as a viscous contractile material that is renewed at both ends and turns over its elements by a flow of material towards its center. As previous models, also this model predicts correlation of the arc radius and the spanning distance of the stress fiber, this is however also dependent on the effective friction coefficient of the stress fiber material, which showed a pronounced myosin isoform-dependence in the analysis of chapter 5. Future models could aim to extend the framework of dynamic contour models to transiently allow for less restrictive shapes than circles by introducing additional viscous forces that lift the requirement for a spatially constant line tension. This could help shed light on shape responses of the contour to transient stimulation of contractility.

Chapter 7 discusses results of a collaboration, where biological experiments with live-cells expressing either both or only one of the two NM II isoform A and B could be studied using the models introduced in chapter 4 and 6. Both models explain the phenomena observed in a manner that is consistent with the known motor properties of the NM II isoforms A and B. Further research could study the stress fiber dynamics of the generated cell lines by investigating the forces more quantitatively which would help make more quantitative statements on the mechanical properties of these cells.

In conclusion, this thesis expands further on the perspective that self-assembling structures performing mechanical work may show signatures of the self-assembly dynamics in the mechanical process and vice versa also signatures of the mechanical process could show in the self-assembly dynamics.

A. Appendix

A.1. List of abbreviations

ATP adenosine triphosphate

ADP adenosine diphosphate

CAC critical aggregation concentration

ECM extra cellular matrix

ELC essential light chain

FRAP fluorescence recovery after photobleaching

GFP green fluorescent protein

KO knock-out

MLCK myosin light-chain kinase

NM II non-muscle myosin II

ODE ordinary differential equation

PCM parallel cluster model

PDMS	polydimethylsiloxane
PPS	post powerstroke state
RLC	regulatory light chain
ROCK	Rho-associated kinase
SIM	structured illumination microscopy
TEM	tension elasticity model
WT	wild type

A.2. Supplementary figures to chapter 4

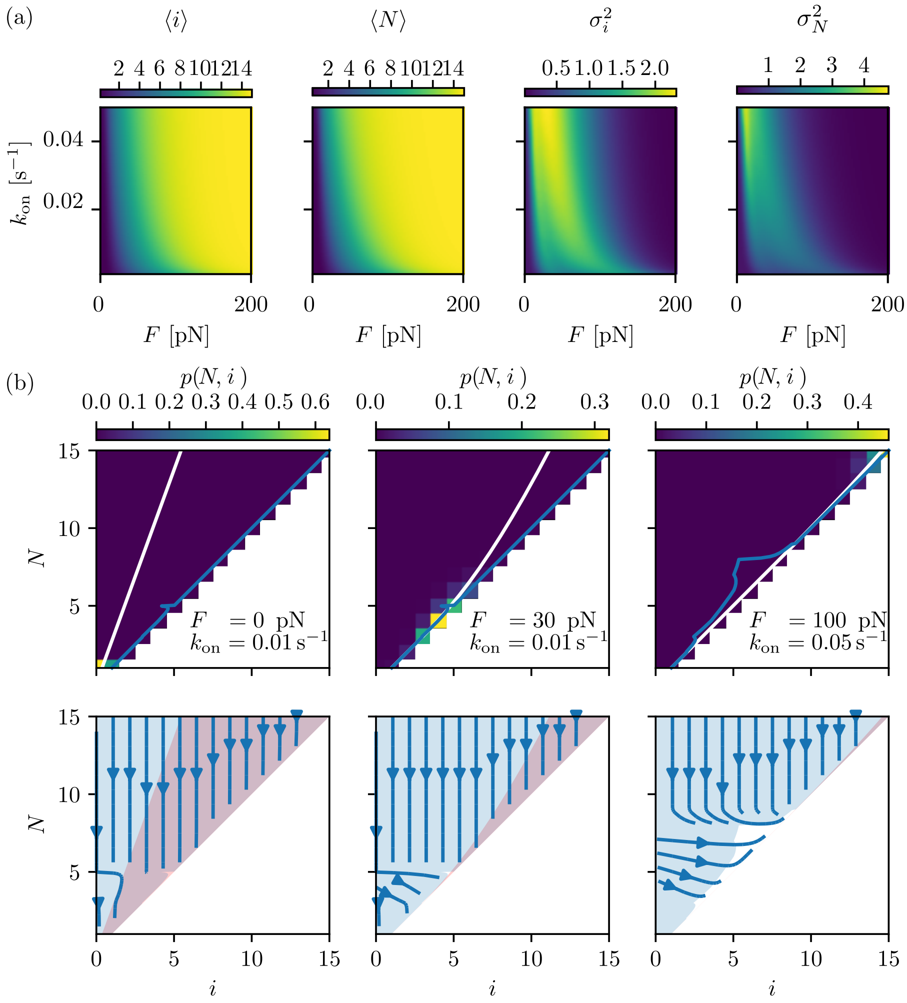

Figure A.1.: Steady states. (a) Mean-values and variances of the full model for different forces and on-rates ($k_{\mathrm{off}}^0 = 10\,\mathrm{s}^{-1}$). Here the results are shown for catch bonds only. (b) Phase portraits for selected parameters for pure catch bonds. In this case force can be sufficient to assemble the minifilament even if the on-rates are very small.

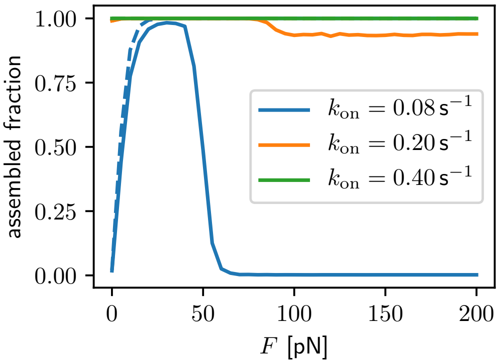

Figure A.2.: The fraction of half-minifilaments with a size $N \geq 8$ for different on-rates. Solid lines denote the simulations with catch-slip bonds, while dashed lines denote the ones with pure catch bonds (the orange and green dashed lines are both at 1).

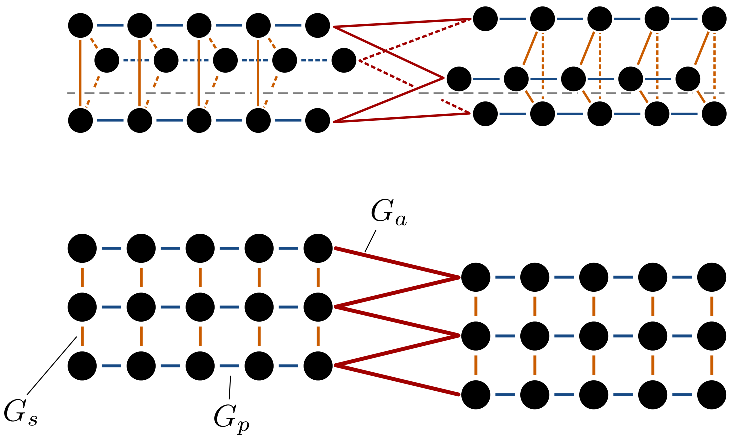

Figure A.3.: Alternative graph topology, which yields the results shown in Fig. A.4. The top schematic illustrates the connectivity to be similar to the vertices of 2 prisms that have been axially rotated against each other by 180°. Cutting the bonds along the gray dotted line yields the unwrapped graph on the bottom.

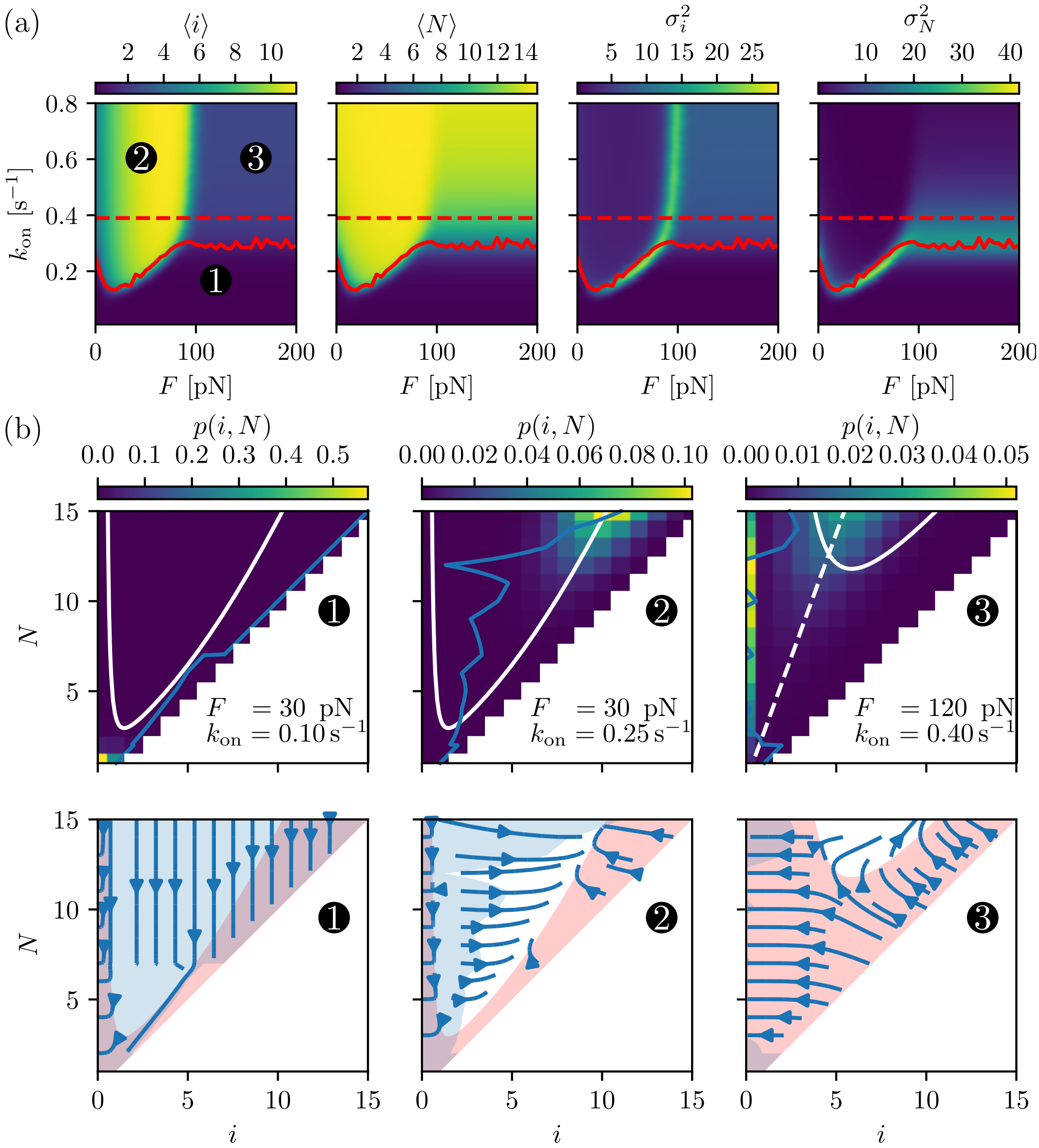

Figure A.4.: Same quantities as Fig. 5 (main text) for the graph shown in Fig. A.3 ($k^0_{\mathrm{off}} = 20\,\mathrm{s}^{-1}$), giving similar results as the main model.

A.3. Supplemental material to chapter 7

A.3.1. Focal adhesion quantification

Quantification of FAs was performed using the pixel classification functunality of the image analysis suite ilastik [238]. First, ilastik was trained to mark the cell area. In a separate classification project ilastik was trained to discern between FA and non-FA. The segmentations were exported in the .npy file format for analysis in custom scripts. To determine the number of FAs connected component analysis was applied to the segmented FAs as implemented in openCV 3.4.1 [239].

A.3.2. FRAP analysis

To correct for drift, the feature detection and matching ORB-algorithm [240], as implemented in *openCV* [239], was applied to a temporal gaussian filtered image series. In slices of 20 frames, features were detected and matched. Matches were used to determine a shift per frame. This shift per frame was used to align the original videos such that the regions of interest do not move, which was implemented in custom scripts. Two square regions of interest were defined in ImageJ: The bleach spot and a reference spot with similar pre-bleach intensity. In these regions the intensity was recorded as I_{bleach}, $I_{\text{prebleach}}$, I_{ref}, $I_{\text{ref,prebleach}}$ the intensity of the bleached spot after bleaching, the mean intensity before bleaching, the intensity of the reference spot after bleaching and the mean intensity before bleaching respectively. The intensity was normalized and corrected for unwanted photobleaching with

$$I_{\text{norm}} = \frac{I_{\text{bleach}}(t) - I_{\text{bleach}}(0)}{I_{\text{prebleach}}} \frac{I_{\text{ref,prebleach}}}{I_{\text{ref}}(t)} \tag{A.1}$$

The normalized intensities were fit to $I_{\text{fit}}(t) = \delta(1 - \exp(-t/\tau))$. The fit values were reported as recovery time and mobile fraction. Resulting distributions where compared using the Peacock test [234, 235].

A.3.3. Balancing of Forces

Here the procedure of balancing the forces in a tug-of-war of myosin motors as shown in Fig. 7.4(c) is given following [241]. Consider the two external springs with strain z_- and z_+ and spring constant k_f and the two ensembles working against each other in a tug-of-war of i_- and i_+ actin bound myosin heads with neck linker stiffness k_l

and strains $\{\xi_j^-\}$ and $\{\xi_j^+\}$. The force balance then reads

$$F = k_f z_+ = \sum_{j=0}^{i_-} k_l \xi_- = \sum_{j=0}^{i_+} k_l \xi_+ = k_+ z_+. \tag{A.2}$$

After an event that disrupts this force balance, e.g. one motor performing a powerstoke, the transient force balance is compensated by movement of the minifilament position Δz and the change of the strains on the external springs Δz_- and Δz_+. With now unbalanced strains $\{\xi_j^-\}$, $\{\xi_j^+\}$, z_- and z_+ the force balance reads

$$\begin{aligned} k_f(z_- + \Delta z_-) &\overset{!}{=} \sum_{j=1}^{i_-} k_l(\xi_j^- + \Delta z - \Delta z_-) \\ \overset{!}{=} \sum_{j=1}^{i_+} k_l \left(\xi_j^+ + \Delta z - \Delta z_-\right) &\overset{!}{=} k_f(z_+ + \Delta z_+). \end{aligned} \tag{A.3}$$

As long as $i_+ \neq 0$ or $i_- \neq 0$ this can be solved for Δz, Δz_- and Δz_+

$$\Delta z = \frac{\Sigma_- - \Sigma_+ - i_+ \Delta z_+ + i_- \Delta z_-}{i_+ + i_-} \tag{A.4}$$

$$\Delta z_+ = \frac{-k_f^2 z_+(i_+ + i_-) - k_l k_f i_+ i_- z_+ + k_l k_-(i_+\Sigma_- + i_-\Sigma_+ + i_+ i_- z_-)}{k_f^2(i_+ + i_-) + 2k_l k_f i_+ i_-} \tag{A.5}$$

$$\Delta z_- = \frac{-k_f^2 z_-(i_+ + i_-) - k_l k_f i_+ i_- z_- + k_l k_+ + (i_+\Sigma_- + i_-\Sigma_+ + i_+ i_- z_+}{k_f^2(i_+ + i_-) + 2k_l k_f i_+ i_-} \tag{A.6}$$

where we introduced the sum of strains on either side of the minifilament $\sum_{j=1}^{i_\pm} \xi_j^\pm = \Sigma_\pm$. Overall neck linker strains and strains of the external springs have to be updated by

$$z_\pm \rightarrow z_\pm + \Delta z_\pm \tag{A.7}$$

$$\xi_j^\pm \rightarrow \xi_j^\pm \mp \Delta z - \Delta z_\pm. \tag{A.8}$$

This is valid as long as at least one motor is bound to the track. If this does not hold anymore, all force is released and the system resets to $\Delta z_\pm = \xi_i^\pm$.

A.3.4. FRAP simulation

Table A.1.: Parameters used in the FRAP simulation.

Parameter	Symbol	Value	Comments
Transition rates [s^{-1}]	k_{20}^{a0}	1.71	[71, 72]
	k_{20}^{a0}	0.35	[71, 72]
	k_{01}	0.2	[71, 72]
	k_{10}	0.4	a non-stereospecific actin bound state is probed most in the presence of blebbistatin [236]
	k_{12}	$4 \cdot 10^6$	[71, 74]
	k_{12}^{Blebb}	1.5	[236]
	k_{21}	0.7	[71, 74]
Association rate [s^{-1}]	k_{on}	5	Fit such, that NM IIA timescale matches the experiment
Dimensionless association rate	$\kappa = k_{\mathrm{on}}/k_{\mathrm{off}}^0$	0.017	Below the critical aggregation without actin dynamics [175]
Catch-path fraction	Δ_c	0.92	[71, 72]
Isoform fractions	Δ_a	0.9	When simulating FRAP of NM IIA
	Δ_b	0.3	When simulating FRAP of NM IIB
Neck-linker stiffness [pN/nm]	k_l	0.7	[71, 72]
Powerstroke distance [nm]	d	8	[68, 69, 74]
Binding energies [k_BT]	G_a	3	[175]
Binding energies [k_BT]	G_p	3	[175]
Binding energies [k_BT]	G_s	1	[175]
External springs [pN/nm]	k_f	4	At high enough values, this parameter does not impact the quantitative results [70]

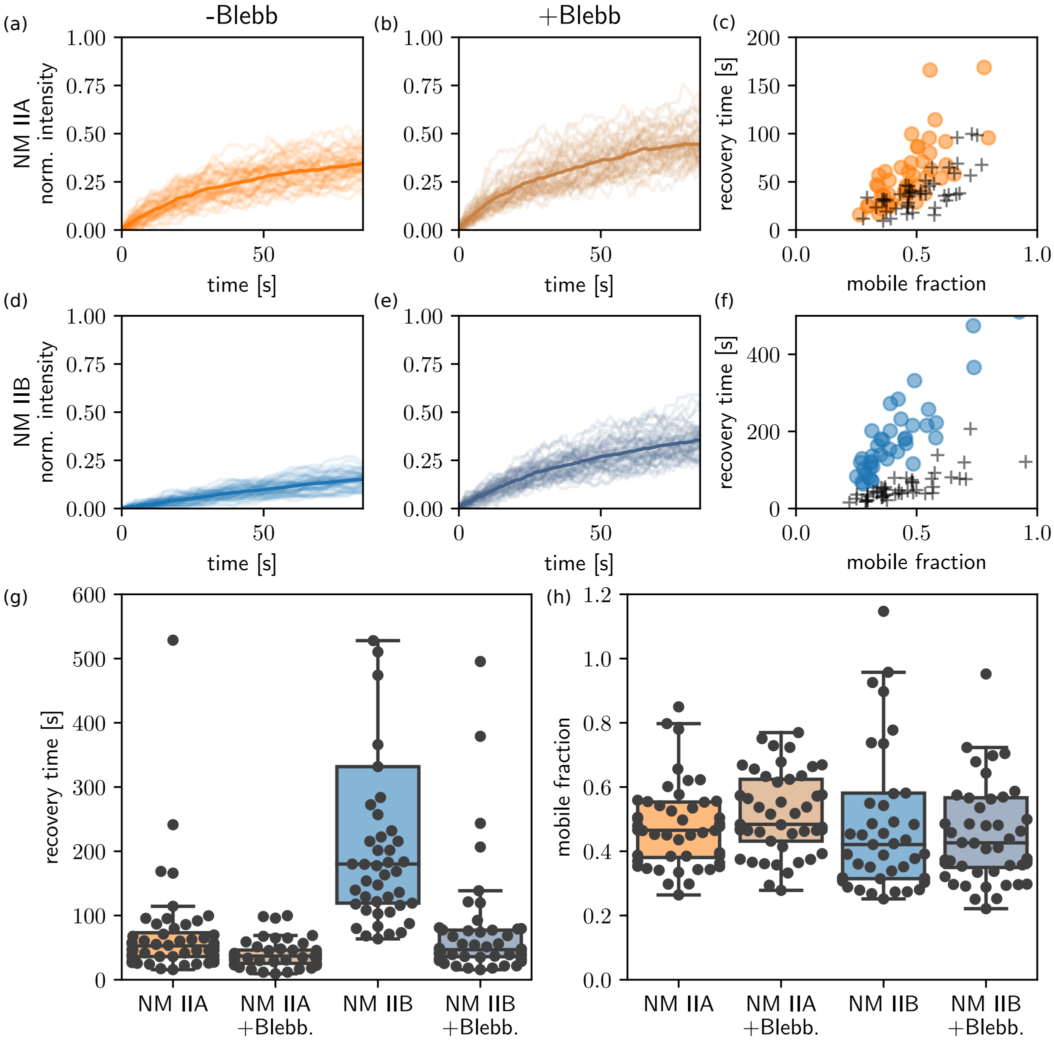

Figure A.5.: Same simulation as Fig. 7.5 but $k_{20}^{b} = 0.15\,\mathrm{s}^{-1}$ with minimal effect on NM IIA recovery but increasing the NM IIB recovery time to values comparable to the experiment. (a,b,d,e) Simulated FRAP trajectories of NM IIA and B with powerstroke rate k_{12} for (-Blebb) column and k_{12}^{Blebb} for (+Blebb) column. (c,f) Scatter plot of mobile fraction and recovery time as fitted from the simulated data for NM IIA and B, respectively. (g,h) Visualization of recovery times and mobile fractions as boxplots.

Bibliography

[1] Ulrich Schwarz. Physik der Zelladhäsion. *Physik Journal*, 14(7), 2015. (Cited on page 1.)

[2] Patrick W. Oakes, Elizabeth Wagner, Christoph A. Brand, Dimitri Probst, Marco Linke, Ulrich S. Schwarz, Michael Glotzer, and Margaret L. Gardel. Optogenetic control of RhoA reveals zyxin-mediated elasticity of stress fibres. *Nature Communications*, 8, 2017. ISSN 20411723. `DOI:10.1038/ncomms15817`. (Cited on pages 1, 23, 73, 90, 99, 100, 105, and 116.)

[3] Andrea C. Scheiwe, Stephanie C. Frank, Tatjana J. Autenrieth, Martin Bastmeyer, and Martin Wegener. Subcellular stretch-induced cytoskeletal response of single fibroblasts within 3D designer scaffolds. *Biomaterials*, 44:186–194, 2015. ISSN 18785905. `DOI:10.1016/j.biomaterials.2014.12.018`. (Cited on page 1.)

[4] Tianzhi Luo, Krithika Mohan, Vasudha Srivastava, Yixin Ren, Pablo a. Iglesias, and Douglas N. Robinson. Understanding the cooperative interaction between myosin II and actin cross-linkers mediated by actin filaments during mechanosensation. *Biophysical Journal*, 102 (2):238–247, 2012. ISSN 00063495. `DOI:10.1016/j.bpj.2011.12.020`. (Cited on pages 1, 54, and 71.)

[5] Navish Wadhwa, Rob Phillips, and Howard C. Berg. Torque-dependent remodeling of the bacterial flagellar motor. *Proceedings of the National Academy of Sciences*, 116(24):11764–11769, jun 2019. ISSN 0027-8424. `DOI:10.1073/PNAS.1904577116`. (Cited on pages 1, 2, 12, and 21.)

[6] Nicoletta I. Petridou, Zoltán Spiró, and Carl Philipp Heisenberg. Multiscale force sensing in development. *Nature Cell Biology*, 19(6):581–588, 2017. ISSN 14764679. `DOI:10.1038/ncb3524`. (Cited on page 1.)

[7] Elizabeth C. Lessey, Christophe Guilluy, and Keith Burridge. From mechanical force to RhoA activation. *Biochemistry*, 51(38):7420–7432, 2012. ISSN 00062960. `DOI:10.1021/bi300758e`. (Cited on page 1.)

[8] Xuefeng Zhu, Kun Li, Peng Zhang, Jie Zhu, Jintao Zhang, Chao Tian, and Shengchun Liu. Implementation of dispersion-free slow acoustic wave propagation and phase engineering with helical-structured metamaterials. *Nature Communications*, 7(May), 2016. ISSN 20411723. `DOI:10.1038/ncomms11731`. (Cited on page 1.)

[9] Eric S S. Schiffhauer, Tianzhi Luo, Krithika Mohan, Vasudha Srivastava, Xuyu Qian, Eric R R. Griffis, Pablo A A. Iglesias, and Douglas N N. Robinson. Mechanoaccumulative Elements of the Mammalian Actin Cytoskeleton. *Current Biology*, 26(11):1473–1479, 2016. ISSN 09609822. `DOI:10.1016/j.cub.2016.04.007`. (Cited on pages 1, 2, and 70.)

[10] Evgeni V. Sokurenko, Viola Vogel, and Wendy E. Thomas. Catch-Bond Mechanism of Force-Enhanced Adhesion: Counterintuitive, Elusive, but ... Widespread? *Cell Host and Microbe*, 4 (4):314–323, oct 2008. ISSN 19313128. `DOI:10.1016/j.chom.2008.09.005`. (Cited on page 1.)

[11] Bruce Alberts. *Molecular Biology of the Cell.* Garland Science, nov 2014. ISBN 0815344325. (Cited on pages 5, 8, 9, 10, 14, 16, and 27.)

[12] Rob Phillips. *Physical Biology of the Cell*. Garland Science, oct 2012. ISBN 9780815344506. (Cited on pages 5, 7, 8, 11, and 12.)

[13] Florian Huber, Adeline Boire, Magdalena Preciado López, and Gijsje H Koenderink. Cytoskeletal crosstalk: when three different personalities team up. *Current Opinion in Cell Biology*, 32:39–47, feb 2015. ISSN 09550674. DOI:10.1016/j.ceb.2014.10.005. (Cited on page 6.)

[14] Ke Xu, Hazen P. Babcock, and Xiaowei Zhuang. Dual-objective STORM reveals three-dimensional filament organization in the actin cytoskeleton. *Nature Methods*, 9(2):185–188, 2012. ISSN 15487091. DOI:10.1038/nmeth.1841. (Cited on pages 6 and 117.)

[15] Kruno Vukušić, Renata Buđa, Agneza Bosilj, Ana Milas, Nenad Pavin, and Iva M. Tolić. Microtubule Sliding within the Bridging Fiber Pushes Kinetochore Fibers Apart to Segregate Chromosomes. *Developmental Cell*, 43(1):11–23.e6, 2017. ISSN 18781551. DOI:10.1016/j.devcel.2017.09.010. (Cited on page 6.)

[16] Ernest Latorre, Sohan Kale, Laura Casares, Manuel Gómez-González, Marina Uroz, Léo Valon, Roshna V. Nair, Elena Garreta, Nuria Montserrat, Aránzazu del Campo, Benoit Ladoux, Marino Arroyo, and Xavier Trepat. Active superelasticity in three-dimensional epithelia of controlled shape. *Nature*, 563(7730):203–208, nov 2018. ISSN 0028-0836. DOI:10.1038/s41586-018-0671-4. (Cited on pages 6 and 9.)

[17] James R. Sellers. Myosins: A diverse superfamily, 2000. ISSN 01674889. (Cited on pages 7 and 12.)

[18] Benoit Rogez, Laeschkir Würthner, Anastasiia B. Petrova, Felix B. Zierhut, Dario Saczko-Brack, Maria Ana Huergo, Christopher Batters, Erwin Frey, and Claudia Veigel. Reconstitution reveals how myosin-VI self-organises to generate a dynamic mechanism of membrane sculpting. *Nature Communications*, 10(1):1–11, 2019. ISSN 20411723. DOI:10.1038/s41467-019-11268-9. (Cited on page 7.)

[19] Laurent Blanchoin, Gaëlle Letort, Hajer Ennomani, Laurène Gressin, and Manuel Théry. Dynamic reorganization of the actin cytoskeleton. *F1000Research*, 4(0):1–11, 2015. ISSN 1759796X. DOI:10.12688/f1000research.6374.1. (Cited on page 7.)

[20] Sari Tojkander, Gergana Gateva, and Pekka Lappalainen. Actin stress fibers - Assembly, dynamics and biological roles. *Journal of Cell Science*, 125(8):1855–1864, 2012. ISSN 00219533. DOI:10.1242/jcs.098087. (Cited on pages 8, 102, and 103.)

[21] Dylan T. Burnette, Lin Shao, Carolyn Ott, Ana M. Pasapera, Robert S. Fischer, Michelle A. Baird, Christelle Der Loughian, Helene Delanoe-Ayari, Matthew J. Paszek, Michael W. Davidson, Eric Betzig, and Jennifer Lippincott-Schwartz. A contractile and counterbalancing adhesion system controls the 3D shape of crawling cells. *Journal of Cell Biology*, 205(1):83–96, 2014. ISSN 15408140. DOI:10.1083/jcb.201311104. (Cited on pages 8 and 88.)

[22] Masahiro Kuragano, Taro Q. P. Uyeda, Keiju Kamijo, Yota Murakami, and Masayuki Takahashi. Different contributions of nonmuscle myosin IIA and IIB to the organization of stress fiber subtypes in fibroblasts. *Molecular Biology of the Cell*, 29(8):mbc.E17–04–0215, apr 2018. ISSN 1059-1524. DOI:10.1091/mbc.E17-04-0215. (Cited on pages 8 and 18.)

[23] Jérôme R.D. Soiné, Christoph A. Brand, Jonathan Stricker, Patrick W. Oakes, Margaret L. Gardel, and Ulrich S. Schwarz. Model-based Traction Force Microscopy Reveals Differential Tension in Cellular Actin Bundles. *PLoS Computational Biology*, 11(3):1–16, 2015. ISSN 15537358. DOI:10.1371/journal.pcbi.1004076. (Cited on pages 8 and 88.)

[24] Ariel Livne and Benjamin Geiger. The inner workings of stress fibers - From contractile machinery to focal adhesions and back. *Journal of Cell Science*, 129(7):1293–1304, apr 2016. ISSN 14779137. `DOI:10.1242/jcs.180927`. (Cited on pages 8 and 88.)

[25] Steven P. Gross. Hither and yon: A review of bi-directional microtubule-based transport. *Physical Biology*, 1(2), 2004. ISSN 14783975. `DOI:10.1088/1478-3967/1/2/R01`. (Cited on page 8.)

[26] Valeria Levi, Anna S. Serpinskaya, Enrico Gratton, and Vladimir Gelfand. Organelle transport along microtubules in Xenopus melanophores: Evidence for cooperation between multiple motors. *Biophysical Journal*, 90(1):318–327, 2006. ISSN 00063495. `DOI:10.1529/biophysj.105.067843`. (Cited on page 9.)

[27] Johanna Block, Viktor Schroeder, Paul Pawelzyk, Norbert Willenbacher, and Sarah Köster. Physical properties of cytoplasmic intermediate filaments. *Biochimica et Biophysica Acta - Molecular Cell Research*, 1853(11):3053–3064, 2015. ISSN 18792596. `DOI:10.1016/j.bbamcr.2015.05.009`. (Cited on page 9.)

[28] Clément Y.J. Hémonnot, Monika Mauermann, Harald Herrmann, and Sarah Köster. Assembly of Simple Epithelial Keratin Filaments: Deciphering the Ion Dependence in Filament Organization. *Biomacromolecules*, 16(10):3313–3321, 2015. ISSN 15264602. `DOI:10.1021/acs.biomac.5b00965`. (Cited on page 9.)

[29] Charlotta Lorenz, Johanna Forsting, Anna V. Schepers, Julia Kraxner, Susanne Bauch, Hannes Witt, Stefan Klumpp, and Sarah Köster. Lateral Subunit Coupling Determines Intermediate Filament Mechanics. *Physical Review Letters*, 123(18):188102, 2019. ISSN 10797114. `DOI:10.1103/PhysRevLett.123.188102`. (Cited on page 9.)

[30] Daniela Stock, Keiichi Namba, and Lawrence K. Lee. Nanorotors and self-assembling macromolecular machines: The torque ring of the bacterial flagellar motor. *Current Opinion in Biotechnology*, 23(4):545–554, 2012. ISSN 09581669. `DOI:10.1016/j.copbio.2012.01.008`. (Cited on page 10.)

[31] Allison M. Gicking, Weihong Qiu, and William O. Hancock. Mitotic kinesins in action: diffusive searching, directional switching, and ensemble coordination. *Molecular Biology of the Cell*, 29(10):1153–1156, 2018. ISSN 19394586. `DOI:10.1091/mbc.E17-10-0612`. (Cited on pages 10 and 11.)

[32] Bruce T. Seet, Ivan Dikic, Ming Ming Zhou, and Tony Pawson. Reading protein modifications with interaction domains. *Nature Reviews Molecular Cell Biology*, 7(7):473–483, 2006. ISSN 14710072. `DOI:10.1038/nrm1960`. (Cited on pages 10 and 11.)

[33] Claudia Veigel, Stephan Schmitz, Fei Wang, and James R. Sellers. Load-dependent kinetics of myosin-V can explain its high processivity. *Nature Cell Biology*, 7(9):861–869, 2005. ISSN 14657392. `DOI:10.1038/ncb1287`. (Cited on pages 11 and 31.)

[34] Richard Niederman and Thomas D. Pollard. Human platelet myosin: II. In vitro assembly and structure of myosin filaments. *Journal of Cell Biology*, 67(1):72–92, oct 1975. ISSN 15408140. `DOI:10.1083/jcb.67.1.72`. (Cited on pages 11, 15, 35, 54, and 57.)

[35] Patricia A. Conrad, Kenneth A. Giuliano, Greg Fisher, Kathleen Collins, Paul T. Matsudaira, and D. Lansing Taylor. Relative distribution of actin, myosin I, and myosin II during the wound healing response of fibroblasts. *Journal of Cell Biology*, 120(6):1381–1391, 1993. ISSN 00219525. `DOI:10.1083/jcb.120.6.1381`. (Cited on page 11.)

[36] Martin Lenz, Todd Thoresen, Margaret L. Gardel, and Aaron R. Dinner. Contractile units in disordered actomyosin bundles arise from f-actin buckling. *Physical Review Letters*, 108(23): 1–5, 2012. ISSN 00319007. `DOI:10.1103/PhysRevLett.108.238107`. (Cited on page 11.)

[37] Julio M Belmonte, Maria Leptin, and François Nédélec. A theory that predicts behaviors of disordered cytoskeletal networks. *Molecular Systems Biology*, 13(9):941, 2017. ISSN 1744-4292. `DOI:10.15252/msb.20177796`. (Cited on page 11.)

[38] Martin Lenz. Geometrical origins of contractility in disordered actomyosin networks. *Physical Review X*, 4(4):1–9, 2014. ISSN 21603308. `DOI:10.1103/PhysRevX.4.041002`. (Cited on page 11.)

[39] Samantha Stam, Simon L. Freedman, Shiladitya Banerjee, Kimberly L. Weirich, Aaron R. Dinner, and Margaret L. Gardel. Filament rigidity and connectivity tune the deformation modes of active biopolymer networks. *Proceedings of the National Academy of Sciences of the United States of America*, 114(47):E10037–E10045, 2017. ISSN 10916490. `DOI:10.1073/pnas.1708625114`. (Cited on page 11.)

[40] Ashley L Nord, Emilie Gachon, Ruben Perez-Carrasco, Jasmine A Nirody, Alessandro Barducci, Richard M Berry, and Francesco Pedaci. Catch bond drives stator mechanosensitivity in the bacterial flagellar motor. *Proceedings of the National Academy of Sciences*, 114(49): 12952–12957, dec 2017. ISSN 0027-8424. `DOI:10.1073/pnas.1716002114`. (Cited on pages 12 and 71.)

[41] T. Hodge and M. J.T.V. Cope. A myosin family tree. *Journal of Cell Science*, 113(19): 3353–3354, 2000. ISSN 00219533. (Cited on page 13.)

[42] Enrique M. De La Cruz and E. Michael Ostap. Relating biochemistry and function in the myosin superfamily, feb 2004. ISSN 09550674. (Cited on pages 12 and 16.)

[43] S. Schiaffino and C. Reggiani. Myosin isoforms in mammalian skeletal muscle. *Journal of Applied Physiology*, 77(2):493–501, 1994. ISSN 87507587. `DOI:10.1152/jappl.1994.77.2.493`. (Cited on page 12.)

[44] Dirk Pette and Robert S. Staron. Myosin isoforms, muscle fiber types, and transitions. *Microscopy Research and Technique*, 50(6):500–509, 2000. ISSN 1059910X. `DOI:10.1002/1097-0029(20000915)50:6<500::AID-JEMT7>3.0.CO;2-7`. (Cited on page 12.)

[45] Lana M. Pollock, Shih Wei Chou, and Brian M. McDermott. My oh my(osin): Insights into how auditory hair cells count, measure, and shape. *Journal of Cell Biology*, 212(2):135–137, 2016. ISSN 15408140. `DOI:10.1083/jcb.201512086`. (Cited on page 12.)

[46] Uri Manor, Andrea Disanza, M'Hamed Grati, Leonardo Andrade, Harrison Lin, Pier Paolo Di Fiore, Giorgio Scita, and Bechara Kachar. Regulation of stereocilia length by myosin XVa and whirlin depends on the actin-regulatory protein Eps8. *Current Biology*, 21(2):167–172, 2011. ISSN 09609822. `DOI:10.1016/j.cub.2010.12.046`. (Cited on page 12.)

[47] Michael J. Greenberg, Göker Arpağ, Erkan Tüzel, and E. Michael Ostap. A Perspective on the Role of Myosins as Mechanosensors. *Biophysical Journal*, 110(12):2568–2576, 2016. ISSN 15420086. `DOI:10.1016/j.bpj.2016.05.021`. (Cited on page 12.)

[48] Peter G. Gillespie and Ulrich Müller. Mechanotransduction by Hair Cells: Models, Molecules, and Mechanisms. *Cell*, 139(1):33–44, 2009. ISSN 00928674. `DOI:10.1016/j.cell.2009.09.010`. (Cited on page 12.)

[49] Miguel Vicente-Manzanares, Xuefei Ma, Robert S. Adelstein, and Alan Rick Horwitz. Nonmuscle myosin II takes centre stage in cell adhesion and migration. *Nature Reviews Molecular Cell Biology*, 10(11):778–790, 2009. ISSN 1471-0072. `DOI:10.1038/nrm2786`. (Cited on pages 12, 16, 17, 18, 19, 53, 70, 101, and 103.)

[50] K. M. Trybus. Myosin V from head to tail. *Cellular and Molecular Life Sciences*, 65(9):1378–1389, 2008. ISSN 1420682X. `DOI:10.1007/s00018-008-7507-6`. (Cited on page 13.)

[51] Kinjal Dasbiswas, Shiqiong Hu, Frank Schnorrer, Samuel A. Safran, and Alexander D. Bershadsky. Ordering of myosin II filaments driven by mechanical forces: experiments and theory. *Philosophical Transactions of the Royal Society B: Biological Sciences*, 373(1747):20170114, may 2018. ISSN 0962-8436. `DOI:10.1098/rstb.2017.0114`. (Cited on pages 14, 53, 90, and 105.)

[52] P. Vibert and L. Castellani. Substructure and accessory proteins in scallop myosin filaments. *Journal of Cell Biology*, 109(2):539–547, 1989. ISSN 00219525. `DOI:10.1083/jcb.109.2.539`. (Cited on page 14.)

[53] Zhongjun Hu, Dianne W. Taylor, Michael K. Reedy, Robert J. Edwards, and Kenneth A. Taylor. Structure of myosin filaments from relaxed Lethocerus flight muscle by cryo-EM at 6 Å resolution. *Science Advances*, 2(9), 2016. ISSN 23752548. `DOI:10.1126/sciadv.1600058`. (Cited on pages 14 and 15.)

[54] Neil Billington, Aibing Wang, Jian Mao, Robert S Adelstein, and James R Sellers. Characterization of three full-length human nonmuscle myosin II paralogs. *Journal of Biological Chemistry*, 288(46):33398–33410, 2013. ISSN 00219258. `DOI:10.1074/jbc.M113.499848`. (Cited on pages 14, 15, 35, 51, 54, 57, 68, 70, and 79.)

[55] Derek Ricketson, Christopher A Johnston, and Kenneth E Prehoda. Multiple tail domain interactions stabilize nonmuscle myosin II bipolar filaments. *Proceedings of the National Academy of Sciences of the United States of America*, 107(49):20964–9, 2010. ISSN 1091-6490. `DOI:10.1073/pnas.1007025107`. (Cited on pages 14, 55, 57, 58, and 110.)

[56] Takashi Nakasawa, Masayuki Takahashi, Fumiko Matsuzawa, Seiichi Aikawa, Yuki Togashi, Takayuki Saitoh, Akihiko Yamagishi, and Michio Yazawa. Critical regions for assembly of vertebrate nonmuscle myosin II. *Biochemistry*, 44(1):174–183, 2005. ISSN 00062960. `DOI:10.1021/bi048807h`. (Cited on page 14.)

[57] Ravid Straussman, John M. Squire, Ami Ben-Ya'acov, and Shoshana Ravid. Skip residues and charge interactions in myosin II coiled-coils: Implications for molecular packing. *Journal of Molecular Biology*, 353(3):613–628, 2005. ISSN 00222836. `DOI:10.1016/j.jmb.2005.08.010`. (Cited on page 14.)

[58] J. M. Squire. General model of myosin filament structure. III. Molecular packing arrangements in myosin filaments. *Journal of Molecular Biology*, 77(2):291–323, 1973. ISSN 00222836. `DOI:10.1016/0022-2836(73)90337-9`. (Cited on pages 15, 55, and 57.)

[59] Maria S. Shutova and Tatyana M. Svitkina. Mammalian nonmuscle myosin II comes in three flavors. *Biochemical and Biophysical Research Communications*, 506(2):394–402, 2018. ISSN 10902104. `DOI:10.1016/j.bbrc.2018.03.103`. (Cited on pages 15, 17, 18, 19, and 61.)

[60] Aidan M. Fenix, Abigail C. Neininger, Nilay Taneja, Karren Hyde, Mike R. Visetsouk, Ryan J. Garde, Baohong Liu, Benjamin R. Nixon, Annabelle E. Manalo, Jason R. Becker, Scott W. Crawley, David M. Bader, Matthew J. Tyska, Qi Liu, Jennifer H. Gutzman, and Dylan T. Burnette. Muscle-specific stress fibers give rise to sarcomeres in cardiomyocytes. *eLife*, 7:1–33, 2018. ISSN 2050084X. `DOI:10.7554/eLife.42144`. (Cited on pages 15 and 102.)

[61] A F Huxley. Muscle structure and theories of contraction. *Progress in biophysics and biophysical chemistry*, 7:255–318, 1957. (Cited on pages 15 and 54.)

[62] Sarah F. Wulf, Virginie Ropars, Setsuko Fujita-Becker, Marco Oster, Goetz Hofhaus, Leonardo G. Trabuco, Olena Pylypenko, H. Lee Sweeney, Anne M. Houdusse, Rasmus R. Schröder, and Ronald D. Vale. Force-producing ADP state of myosin bound to actin. *Proceedings of the National Academy of Sciences of the United States of America*, 113(13):E1844–E1852, 2016. ISSN 10916490. `DOI:10.1073/pnas.1516598113`. (Cited on pages 15 and 16.)

[63] Caspar Rüegg, Claudia Veigel, Justin E. Molloy, Stephan Schmitz, John C. Sparrow, and Rainer H.A. Fink. Molecular motors: Force and movement generated by single myosin II molecules. *News in Physiological Sciences*, 17(5):213–218, 2002. ISSN 08861714. `DOI:10.1152/nips.01389.2002`. (Cited on page 15.)

[64] Claudia Veigel, Justin E. Molloy, Stephan Schmitz, and John Kendrick-Jones. Load-dependent kinetics of force production by smooth muscle myosin measured with optical tweezers. *Nature Cell Biology*, 5(11):980–986, nov 2003. ISSN 1465-7392. `DOI:10.1038/ncb1060`. (Cited on pages 15, 18, 54, 61, and 71.)

[65] Tomonobu M. Watanabe, Atsuko H. Iwane, Hiroto Tanaka, Mitsuo Ikebe, and Toshio Yanagida. Mechanical characterization of one-headed Myosin-V using optical tweezers. *PLoS ONE*, 5(8), 2010. ISSN 19326203. `DOI:10.1371/journal.pone.0012224`. (Cited on page 15.)

[66] Luca Melli, Neil Billington, Sara A. Sun, Jonathan E. Bird, Attila Nagy, Thomas B. Friedman, Yasuharu Takagi, and James R. Sellers. Bipolar filaments of human nonmuscle myosin 2-A and 2-B have distinct motile and mechanical properties. *eLife*, 7:1–25, 2018. ISSN 2050084X. `DOI:10.7554/eLife.32871`. (Cited on pages 15, 90, and 108.)

[67] Lewis S. Mosby, Nikolas Hundt, Gavin Young, Adam Fineberg, Marco Polin, Satyajit Mayor, Philipp Kukura, and Darius V. Köster. Myosin II Filament Dynamics in Actin Networks Revealed with Interferometric Scattering Microscopy. *Biophysical Journal*, 2020. ISSN 15420086. `DOI:10.1016/j.bpj.2020.02.025`. (Cited on page 15.)

[68] Thorsten Erdmann and Ulrich S. Schwarz. Stochastic Force Generation by Small Ensembles of Myosin II Motors. *Physical Review Letters*, 108(18):188101, 2012. ISSN 00319007. `DOI:10.1103/PhysRevLett.108.188101`. (Cited on pages 15, 54, 59, 61, 77, and 130.)

[69] Thorsten Erdmann, Philipp J Albert, and Ulrich S Schwarz. Stochastic dynamics of small ensembles of non-processive molecular motors: the parallel cluster model. *The Journal of chemical physics*, 139(17):175104, 2013. ISSN 1089-7690. `DOI:10.1063/1.4827497`. (Cited on pages 15, 22, 54, 59, 61, 77, and 130.)

[70] Philipp J Albert, Thorsten Erdmann, and Ulrich S Schwarz. Stochastic dynamics and mechanosensitivity of myosin II minifilaments. *New Journal of Physics*, 16(9):093019, 2014. ISSN 1367-2630. `DOI:10.1088/1367-2630/16/9/093019`. (Cited on pages 15, 54, 61, and 130.)

[71] Thorsten Erdmann, Kathrin Bartelheimer, and Ulrich S. Schwarz. Sensitivity of small myosin II ensembles from different isoforms to mechanical load and ATP concentration. *Physical Review E*, 94(5):052403, nov 2016. ISSN 2470-0045. `DOI:10.1103/PhysRevE.94.052403`. (Cited on pages 15, 18, 54, 61, 65, 74, 76, 90, 101, 102, 108, 112, 116, and 130.)

[72] Samantha Stam, Jon Alberts, Margaret L. Gardel, and Edwin Munro. Isoforms Confer Characteristic Force Generation and Mechanosensation by Myosin II Filaments. *Biophysical Journal*, 108(8):1997–2006, apr 2015. ISSN 0006-3495. `DOI:10.1016/J.BPJ.2015.03.030`. (Cited on pages 15, 18, 59, 74, 90, 101, 108, 112, 116, and 130.)

[73] Thomas Duke. Cooperativity of myosin molecules through strain-dependent chemistry. *Philosophical transactions of the Royal Society of London. Series B, Biological sciences*, 355(1396): 529–38, 2000. ISSN 0962-8436. DOI:10.1098/rstb.2000.0594. (Cited on pages 15 and 54.)

[74] Andrej Vilfan and Thomas Duke. Instabilities in the Transient Response of Muscle. *Biophysical Journal*, 85(2):818–827, aug 2003. ISSN 0006-3495. DOI:10.1016/S0006-3495(03)74522-6. (Cited on pages 15, 54, and 130.)

[75] Sam Walcott, David M. Warshaw, and Edward P. Debold. Mechanical coupling between myosin molecules causes differences between ensemble and single-molecule measurements. *Biophysical Journal*, 103(3):501–510, aug 2012. ISSN 00063495. DOI:10.1016/j.bpj.2012.06.031. (Cited on pages 15 and 54.)

[76] Sam Walcott and Neil M. Kad. Direct Measurements of Local Coupling between Myosin Molecules Are Consistent with a Model of Muscle Activation. *PLoS Computational Biology*, 11(11):1–20, 2015. ISSN 15537358. DOI:10.1371/journal.pcbi.1004599. (Cited on page 15.)

[77] Lennart Hilbert, Shivaram Cumarasamy, Nedjma B. Zitouni, Michael C. Mackey, and Anne-Marie Lauzon. The Kinetics of Mechanically Coupled Myosins Exhibit Group Size-Dependent Regimes. *Biophysical Journal*, 105(6):1466–1474, sep 2013. ISSN 00063495. DOI:10.1016/j.bpj.2013.07.054. (Cited on pages 15 and 54.)

[78] Zsombor Balassy, Anne Marie Lauzon, and Lennart Hilbert. Spreading of perturbations in myosin group kinetics along actin filaments. *Proceedings of the National Academy of Sciences of the United States of America*, 116(35):17336–17344, 2019. ISSN 10916490. DOI:10.1073/pnas.1904164116. (Cited on page 15.)

[79] H. Lee Sweeney and Anne Houdusse. Structural and Functional Insights into the Myosin Motor Mechanism. *Annual Review of Biophysics*, 39(1):539–557, 2010. ISSN 1936-122X. DOI:10.1146/annurev.biophys.050708.133751. (Cited on page 15.)

[80] James W. McNamara, Amy Li, Cristobal G. dos Remedios, and Roger Cooke. The role of super-relaxed myosin in skeletal and cardiac muscle. *Biophysical Reviews*, 7(1):5–14, 2014. ISSN 18672469. DOI:10.1007/s12551-014-0151-5. (Cited on page 16.)

[81] John L. Woodhead, Fa Qing Zhao, Roger Craig, Edward H. Egelman, Lorenzo Alamo, and Raúl Padrón. Atomic model of a myosin filament in the relaxed state. *Nature*, 436(7054): 1195–1199, 2005. ISSN 00280836. DOI:10.1038/nature03920. (Cited on pages 17 and 55.)

[82] Lorenzo Alamo, Dan Qi, Willy Wriggers, Antonio Pinto, Jingui Zhu, Aivett Bilbao, Richard E Gillilan, Songnian Hu, and Ra??l Padr??n. Conserved Intramolecular Interactions Maintain Myosin Interacting-Heads Motifs Explaining Tarantula Muscle Super-Relaxed State Structural Basis. *Journal of Molecular Biology*, 428(6):1142–1164, 2016. ISSN 10898638. DOI:10.1016/j.jmb.2016.01.027. (Cited on page 17.)

[83] Shixin Yang, Kyoung Hwan Lee, John L Woodhead, Osamu Sato, Mitsuo Ikebe, and Roger Craig. The central role of the tail in switching off 10S myosin II activity. 151(9):1081–1093, 2019. (Cited on page 17.)

[84] Xiong Liu, Neil Billington, Shi Shu, Shu Hua Yu, Grzegorz Piszczek, James R. Sellers, and Edward D. Korn. Effect of ATP and regulatory light-chain phosphorylation on the polymerization of mammalian nonmuscle myosin II. *Proceedings of the National Academy of Sciences of the United States of America*, 114(32):E6516–E6525, 2017. ISSN 10916490. DOI:10.1073/pnas.1702375114. (Cited on pages 17 and 69.)

[85] M S Shutova and T M Svitkina. Common and Specific Functions of Nonmuscle Myosin II Paralogs in Cells. *Biochemistry. Biokhimiia*, 83(12):1459–1468, dec 2018. ISSN 1608-3040. `DOI:10.1134/S0006297918120040`. (Cited on page 17.)

[86] Anne J Ridley. Rho GTPase signalling in cell migration. *Current Opinion in Cell Biology*, 36:103–112, oct 2015. ISSN 09550674. `DOI:10.1016/j.ceb.2015.08.005`. (Cited on pages 18 and 54.)

[87] Alexander D. Bershadsky, Christoph Ballestrem, Letizia Carramusa, Yuliya Zilberman, Benoit Gilquin, Saadi Khochbin, Antonina Y. Alexandrova, Alexander B. Verkhovsky, Tom Shemesh, and Michael M. Kozlov. Assembly and mechanosensory function of focal adhesions: Experiments and models. *European Journal of Cell Biology*, 85(3-4):165–173, 2006. ISSN 01719335. `DOI:10.1016/j.ejcb.2005.11.001`. (Cited on pages 18 and 54.)

[88] Jordan R. Beach, Lin Shao, Kirsten Remmert, Dong Li, Eric Betzig, and John A. Hammer. Nonmuscle myosin II isoforms coassemble in living cells. *Current Biology*, 24(10): 1160–1166, 2014. ISSN 09609822. `DOI:10.1016/j.cub.2014.03.071`. (Cited on pages 18, 74, 101, and 112.)

[89] Jordan R. Beach and John A. Hammer. Myosin II isoform co-assembly and differential regulation in mammalian systems. *Experimental Cell Research*, 334(1):2–9, 2015. ISSN 10902422. `DOI:10.1016/j.yexcr.2015.01.012`. (Cited on pages 18 and 74.)

[90] Maria S Shutova, Sreeja B Asokan, Shefali Talwar, Richard K Assoian, James E Bear, and Tatyana M Svitkina. Self-sorting of nonmuscle myosins IIA and IIB polarizes the cytoskeleton and modulates cell motility. *The Journal of cell biology*, 216(9):2877–2889, sep 2017. ISSN 1540-8140. `DOI:10.1083/jcb.201705167`. (Cited on pages 18, 19, 58, 68, 70, 109, and 116.)

[91] Joshua C. Sandquist and Anthony R. Means. The C-Terminal Tail Region of Nonmuscle Myosin II Directs Isoform-specific Distribution in Migrating Cells. *Molecular Biology of the Cell*, 19(12):5156–5167, dec 2008. ISSN 1059-1524. `DOI:10.1091/mbc.e08-05-0533`. (Cited on pages 18, 19, 116, and 117.)

[92] Miguel Vicente-Manzanares, Margaret A. Koach, Leanna Whitmore, Marcelo L. Lamers, and Alan F. Horwitz. Segregation and activation of myosin IIB creates a rear in migrating cells. *Journal of Cell Biology*, 183(3):543–554, 2008. ISSN 00219525. `DOI:10.1083/jcb.200806030`. (Cited on page 19.)

[93] NG Van Kampen. *Stochastic processes in physics and chemistry*. North Holland, 2007. (Cited on page 19.)

[94] Carsten Timm. Random transition-rate matrices for the master equation. *Physical Review E - Statistical, Nonlinear, and Soft Matter Physics*, 80(2):1–14, 2009. ISSN 15393755. `DOI:10.1103/PhysRevE.80.021140`. (Cited on page 21.)

[95] A. Berman and R.J. Plemmons. *Nonnegative Matrices in the Mathematical Sciences*. Society for Industrial and Applied Mathematics, 1994. (Cited on page 21.)

[96] Thorsten Erdmann and Ulrich S Schwarz. Stochastic dynamics of adhesion clusters under shared constant force and with rebinding. *Journal of Chemical Physics*, 121(18):8997–9017, 2004. ISSN 00219606. `DOI:10.1063/1.1805496`. (Cited on page 21.)

[97] T Erdmann and U S Schwarz. Stability of Adhesion Clusters under Constant Force. *Physical Review Letters*, 92(10):108102–1, 2004. ISSN 00319007. `DOI:10.1103/PhysRevLett.92.108102`. (Cited on pages 21 and 22.)

[98] Felix Frey, Falko Ziebert, and Ulrich S. Schwarz. Stochastic dynamics of nanoparticle and virus uptake. *Physical Review Letters*, 122(8):88102, 2019. ISSN 10797114. `DOI:10.1103/PhysRevLett.122.088102`. (Cited on page 21.)

[99] Felix Frey, Falko Ziebert, and Ulrich S. Schwarz. Dynamics of particle uptake at cell membranes. *Physical Review E*, 100(5):1–18, 2019. ISSN 24700053. `DOI:10.1103/PhysRevE.100.052403`. (Cited on page 21.)

[100] Michael F. Hagan. Modeling Viral Capsid Assembly. *Advances in chemical physics*, 155:1, 2014. ISSN 0065-2385. `DOI:10.1002/9781118755815.CH01`. (Cited on pages 21 and 54.)

[101] Johanna Funk, Felipe Merino, Larisa Venkova, Lina Heydenreich, Jan Kierfeld, Pablo Vargas, Stefan Raunser, Matthieu Piel, and Peter Bieling. Profilin and formin constitute a pacemaker system for robust actin filament growth. *eLife*, 8:1–34, 2019. ISSN 2050084X. `DOI:10.7554/eLife.50963`. (Cited on page 21.)

[102] Thomas Tørring, Niels V. Voigt, Jeanette Nangreave, Hao Yan, and Kurt V. Gothelf. Advances in DNA-based nanotechnology themed issue Guest editors Eugen Stulz , Guido Clever , Mitsuhiko Shionoya and. *Chem. Soc. Rev.*, 40(12):5621–5928, 2011. (Cited on page 21.)

[103] Anne E Hafner, Johannes Krausser, and Anđela Šarić. Minimal coarse-grained models for molecular self-organisation in biology. *Current Opinion in Structural Biology*, 58:43–52, oct 2019. ISSN 0959-440X. `DOI:10.1016/J.SBI.2019.05.018`. (Cited on pages 21 and 55.)

[104] Paul Smith, Piet J. Lemstra, and Jacques P.L. Pijpers. Tensile Strength of Highly Oriented Polyethylene - 2. Effect of Molecular Weight Distribution. *Journal of polymer science. Part A-2, Polymer physics*, 20(12):2229–2241, 1982. ISSN 04492978. `DOI:10.1002/pol.1982.180201206`. (Cited on page 22.)

[105] MV Smoluchowski. An experiment on mathematical theorization of coagulation kinetics of the colloidal solutions. *Zeitschrift fur physikalisch Chemie*, 92:129–168, 1917. (Cited on pages 22 and 54.)

[106] Jonathan A.D. Wattis. An introduction to mathematical models of coagulation-fragmentation processes: A discrete deterministic mean-field approach. *Physica D: Nonlinear Phenomena*, 222(1-2):1–20, 2006. ISSN 01672789. `DOI:10.1016/j.physd.2006.07.024`. (Cited on pages 22 and 35.)

[107] F. P. da Costa. Mathematical Aspects of Coagulation-Fragmentation Equations. volume 2, pages 83–162. 2015. `DOI:10.1007/978-3-319-16121-1_5`. (Cited on page 22.)

[108] Heinrich C.R. Klein and Ulrich S. Schwarz. Studying protein assembly with reversible Brownian dynamics of patchy particles. *Journal of Chemical Physics*, 140(18), 2014. ISSN 00219606. `DOI:10.1063/1.4873708`. (Cited on page 22.)

[109] Heinrich C.R. Klein, Paul Guichard, Virginie Hamel, Pierre Gönczy, and Ulrich S. Schwarz. Computational support for a scaffolding mechanism of centriole assembly. *Scientific Reports*, 6:1–9, 2016. ISSN 20452322. `DOI:10.1038/srep27075`. (Cited on page 22.)

[110] Pierre Gönczy. Towards a molecular architecture of centriole assembly. *Nature Reviews Molecular Cell Biology*, 13(7):425–435, 2012. ISSN 14710072. `DOI:10.1038/nrm3373`. (Cited on page 22.)

[111] R. Becker and W. Döring. Kinetische Behandlung der Keimbildung in übersättigten Dämpfen. *Annalen der Physik*, 416(8):719–752, 1935. ISSN 15213889. `DOI:10.1002/andp.19354160806`. (Cited on pages 23, 35, 36, and 54.)

[112] J M Ball, J Carr, and O Penrose. The Becker-Döring cluster equations: Basic properties and asymptotic behaviour of solutions. *Communications in Mathematical Physics*, 104(4): 657–692, 1986. ISSN 00103616. `DOI:10.1007/BF01211070`. (Cited on page 23.)

[113] Jonathan A D Wattis and John R King. Asymptotic solutions of the Becker–Doring equations. *J. Phys. A*, 31:7169–7189, 1998. (Cited on page 23.)

[114] J. Carr and R. M. Dunwell. Asymptotic behaviour of solutions to the Becker-Döring equations. *Proceedings of the Edinburgh Mathematical Society*, 42(2):415–424, 1999. ISSN 0013-0915. `DOI:10.1017/s0013091500020344`. (Cited on page 23.)

[115] M. Castelnovo, T. Verdier, and L. Foret. Comparing open and closed molecular self-assembly. *EPL*, 105(2), 2014. ISSN 02955075. `DOI:10.1209/0295-5075/105/28006`. (Cited on page 23.)

[116] Timothée Verdier, Lionel Foret, and Martin Castelnovo. Modeling the Kinetics of Open Self-Assembly. *Journal of Physical Chemistry B*, 120(26):6411–6420, 2016. ISSN 15205207. `DOI:10.1021/acs.jpcb.6b03899`. (Cited on page 23.)

[117] Hiroaki Ito, Ryo Murakami, Shinya Sakuma, Chia Hung Dylan Tsai, Thomas Gutsmann, Klaus Brandenburg, Johannes M.B. Pöschl, Fumihito Arai, Makoto Kaneko, and Motomu Tanaka. Mechanical diagnosis of human erythrocytes by ultra-high speed manipulation unraveled critical time window for global cytoskeletal remodeling. *Scientific Reports*, 7(October 2016):1–14, 2017. ISSN 20452322. `DOI:10.1038/srep43134`. (Cited on page 23.)

[118] Marion Geerligs, Gerrit W.M. Peters, Paul A.J. Ackermans, Cees W.J. Oomens, and Frank P.T. Baaijens. Linear viscoelastic behavior of subcutaneous adipose tissue. *Biorheology*, 45(6):677–688, 2008. ISSN 0006355X. `DOI:10.3233/BIR-2008-0517`. (Cited on page 23.)

[119] Arne Schäfer and Manfred Radmacher. Influence of myosin II activity on stiffness of fibroblast cells. *Acta Biomaterialia*, 1(3):273–280, 2005. ISSN 17427061. `DOI:10.1016/j.actbio.2005.02.004`. (Cited on page 23.)

[120] Kathleen M Van Citters, Brenton D Hoffman, Gladys Massiera, and John C Crocker. The Role of F-Actin and Myosin in Epithelial Cell Rheology. *Biophysical Journal*, 91(10):3946–3956, 2006. ISSN 0006-3495. `DOI:10.1529/biophysj.106.091264`. (Cited on page 23.)

[121] Chii J. Chan, Andrew E. Ekpenyong, Stefan Golfier, Wenhong Li, Kevin J. Chalut, Oliver Otto, Jens Elgeti, Jochen Guck, and Franziska Lautenschläger. Myosin II activity softens cells in suspension. *Biophysical Journal*, 108(8):1856–1869, 2015. ISSN 15420086. `DOI:10.1016/j.bpj.2015.03.009`. (Cited on page 23.)

[122] Elisabeth Fischer-Friedrich, Yusuke Toyoda, Cedric J. Cattin, Daniel J. Müller, Anthony A. Hyman, and Frank Jülicher. Rheology of the Active Cell Cortex in Mitosis. *Biophysical Journal*, 111(3):589–600, aug 2016. ISSN 15420086. `DOI:10.1016/j.bpj.2016.06.008`. (Cited on pages 23, 31, and 73.)

[123] F. Mainardi. *Fractional Calculus and Waves in Linear Viscoelasticity: An Introduction to Mathematical Models*. Imperial College Press, 2010. ISBN 9781848163300. (Cited on pages 23, 24, and 26.)

[124] Christian Friedrich. *Understanding Viscoelasticity*, volume 13. 2019. ISBN 9783319619996. `DOI:10.1515/arh-2003-0033`. (Cited on page 23.)

[125] M. Caputo and F. Mainardi. Linear models of dissipation in anelastic solids. *La Rivista del Nuovo Cimento*, 1(2):161–198, apr 1971. ISSN 1826-9850. `DOI:10.1007/BF02820620`. (Cited on page 24.)

[126] Peter Sollich. Rheological constitutive equation for a model of soft glassy materials. *Physical Review E - Statistical Physics, Plasmas, Fluids, and Related Interdisciplinary Topics*, 58(1): 738–759, 1998. ISSN 1063651X. `DOI:10.1103/PhysRevE.58.738`. (Cited on pages 25 and 73.)

[127] Philip Kollmannsberger and Ben Fabry. Linear and Nonlinear Rheology of Living Cells. *Annual Review of Materials Research*, 41(1):75–97, 2011. ISSN 1531-7331. `DOI:10.1146/annurev-matsci-062910-100351`. (Cited on pages 25, 31, 32, and 73.)

[128] Ilka B Bischofs, Franziska Klein, Dirk Lehnert, Martin Bastmeyer, and Ulrich S Schwarz. Filamentous network mechanics and active contractility determine cell and tissue shape. *Biophysical Journal*, 95(7):3488–3496, oct 2008. ISSN 15420086. `DOI:10.1529/biophysj.108.134296`. (Cited on pages 27, 28, 89, 90, 100, 101, 102, 105, 108, and 116.)

[129] Ana Joaquina Jimenez, Chiara de Pascalis, Gaelle Letort, Benoit Vianay, Robert D. Goldman, Michel Bornens, Matthieu Piel, Laurent Blanchoin, and Manuel Théry. Acto-myosin network geometry defines centrosome position. *bioRxiv*, page 2020.01.07.896969, 2020. `DOI:10.1101/2020.01.07.896969`. (Cited on page 27.)

[130] Christoph A. Brand, Marco Linke, Kai Weißenbruch, Benjamin Richter, Martin Bastmeyer, and Ulrich S. Schwarz. Tension and Elasticity Contribute to Fibroblast Cell Shape in Three Dimensions. *Biophysical Journal*, 113(4):770–774, 2017. ISSN 15420086. `DOI:10.1016/j.bpj.2017.06.058`. (Cited on pages 27, 89, and 105.)

[131] Reza Zandi Shafagh, Alexander Vastesson, Weijin Guo, Wouter Van Der Wijngaart, and Tommy Haraldsson. E-Beam Nanostructuring and Direct Click Biofunctionalization of Thiol-Ene Resist. *ACS Nano*, 2018. ISSN 1936086X. `DOI:10.1021/acsnano.8b03709`. (Cited on page 27.)

[132] Ravi S. Kane, Shuichi Takayama, Emanuele Ostuni, Donald E. Ingber, and George M. Whitesides. Patterning proteins and cells using soft lithography. *Biomaterials*, 20(23-24):2363–2376, 1999. ISSN 01429612. `DOI:10.1016/S0142-9612(99)00165-9`. (Cited on pages 27 and 28.)

[133] Dong Qin, Younan Xia, and George M. Whitesides. Soft lithography for micro- and nanoscale patterning. *Nature Protocols*, 5(3):491–502, 2010. ISSN 17542189. `DOI:10.1038/nprot.2009.234`. (Cited on page 27.)

[134] Rahul Singhvi, Amit Kumar, Gabriel P. Lopez, Gregory N. Stephanopoulos, Daniel I.C. Wang, George M. Whitesides, and Donald E. Ingber. Engineering cell shape and function. *Science*, 264(5159):696–698, 1994. ISSN 00368075. `DOI:10.1126/science.8171320`. (Cited on page 28.)

[135] Manuel Théry, Anne Pépin, Emilie Dressaire, Yong Chen, and Michel Bornens. Cell distribution of stress fibres in response to the geometry of the adhesive environment. *Cell Motility and the Cytoskeleton*, 63(6):341–355, 2006. ISSN 08861544. `DOI:10.1002/cm.20126`. (Cited on pages 28 and 102.)

[136] Kristopher A. Kilian, Branimir Bugarija, Bruce T. Lahn, and Milan Mrksich. Geometric cues for directing the differentiation of mesenchymal stem cells. *Proceedings of the National Academy of Sciences of the United States of America*, 107(11):4872–4877, 2010. ISSN 00278424. `DOI:10.1073/pnas.0903269107`. (Cited on page 28.)

[137] Jenny Fink, Manuel Théry, Ammar Azioune, Raphael Dupont, François Chatelain, Michel Bornens, and Matthieu Piel. Comparative study and improvement of current cell micropatterning techniques. *Lab on a Chip*, 7(6):672–680, 2007. ISSN 14730189. `DOI:10.1039/b618545b`. (Cited on page 28.)

[138] Jacques J Neefjes and Eric A J Reits. From fixed to FRAP: measuring protein mobility and activity in living cells. *Nature Cell Biology*, 3(June):E145–E147, 2001. (Cited on page 28.)

[139] D. Axelrod, D. E. Koppel, J. Schlessinger, E. Elson, and W. W. Webb. Mobility measurement by analysis of fluorescence photobleaching recovery kinetics. *Biophysical Journal*, 16(9):1055–1069, 1976. ISSN 00063495. `DOI:10.1016/S0006-3495(76)85755-4`. (Cited on pages 28 and 29.)

[140] J. Chloë Bulinski, D. J. Odde, B. J. Howell, T. D. Salmon, and C. M. Waterman-Storer. Rapid dynamics of the microtubule binding of ensconsin in vivo. *Journal of Cell Science*, 114 (21):3885–3897, 2001. ISSN 00219533. (Cited on page 28.)

[141] Brian L. Sprague, Robert L. Pego, Diana A. Stavreva, and James G. McNally. Analysis of binding reactions by fluorescence recovery after photobleaching. *Biophysical Journal*, 86(6): 3473–3495, 2004. ISSN 00063495. `DOI:10.1529/biophysj.103.026765`. (Cited on pages 28 and 29.)

[142] Nicole O. Taylor, Ming Tzo Wei, Howard A. Stone, and Clifford P. Brangwynne. Quantifying Dynamics in Phase-Separated Condensates Using Fluorescence Recovery after Photobleaching. *Biophysical Journal*, 117(7):1285–1300, 2019. ISSN 15420086. `DOI:10.1016/j.bpj.2019.08.030`. (Cited on page 29.)

[143] Shiqiong Hu, Kinjal Dasbiswas, Zhenhuan Guo, Yee-han Tee, Visalatchi Thiagarajan, Pascal Hersen, Teng-leong Chew, Samuel A Safran, Ronen Zaidel-bar, and Alexander D Bershadsky. Long-range self-organization of cytoskeletal myosin II filament stacks. *Nature Cell Biology*, 19(2), 2017. `DOI:10.1038/ncb3466`. (Cited on pages 30, 58, 68, 70, 90, 105, 109, and 116.)

[144] Michael Krieg, Gotthold Fläschner, David Alsteens, Benjamin M. Gaub, Wouter H. Roos, Gijs J.L. Wuite, Hermann E. Gaub, Christoph Gerber, Yves F. Dufrêne, and Daniel J. Müller. Atomic force microscopy-based mechanobiology. *Nature Reviews Physics*, 1(1):41–57, 2019. ISSN 25225820. `DOI:10.1038/s42254-018-0001-7`. (Cited on page 31.)

[145] Ning Wang, James P. Butler, and Donald E. Ingber. Mechanotransduction across the cell surface and through the cytoskeleton. *Science*, 260(5111):1124–1127, 1993. ISSN 00368075. `DOI:10.1126/science.7684161`. (Cited on page 31.)

[146] Andreas R. Bausch, Florian Ziemann, Alexei A. Boulbitch, Ken Jacobson, and Erich Sackmann. Local measurements of viscoelastic parameters of adherent cell surfaces by magnetic bead microrheometry. *Biophysical Journal*, 75(4):2038–2049, 1998. ISSN 00063495. `DOI:10.1016/S0006-3495(98)77646-5`. (Cited on page 31.)

[147] Furqan M. Fazal and Steven M. Block. Optical tweezers study life under tension. *Nature Photonics*, 5(6):318–321, 2011. ISSN 17494885. `DOI:10.1038/nphoton.2011.100`. (Cited on page 31.)

[148] Martial Balland, Nicolas Desprat, Delphine Icard, Sophie Féréol, Atef Asnacios, Julien Browaeys, Sylvie Hénon, and Franaçois Gallet. Power laws in microrheology experiments on living cells: Comparative analysis and modeling. *Physical Review E - Statistical, Nonlinear, and Soft Matter Physics*, 74(2), 2006. ISSN 15502376. `DOI:10.1103/PhysRevE.74.021911`. (Cited on pages 32 and 73.)

[149] N. Desprat, A. Guiroy, and A. Asnacios. Microplates-based rheometer for a single living cell. *Review of Scientific Instruments*, 77(5), 2006. ISSN 00346748. `DOI:10.1063/1.2202921`. (Cited on page 32.)

[150] Pablo Fernández and Albrecht Ott. Single cell mechanics: Stress stiffening and kinematic hardening. *Physical Review Letters*, 100(23), jun 2008. ISSN 00319007. `DOI:10.1103/PhysRevLett.100.238102`. (Cited on pages 32 and 73.)

[151] Denis Wirtz. Particle-Tracking Microrheology of Living Cells: Principles and Applications. *Annual Review of Biophysics*, 38(1):301–326, 2009. ISSN 1936-122X. `DOI:10.1146/annurev.biophys.050708.133724`. (Cited on page 32.)

[152] Daisuke Mizuno, Catherine Tardin, C. F. Schmidt, and F. C. MacKintosh. Nonequilibrium mechanics of active cytoskeletal networks. *Science*, 315(5810):370–373, 2007. ISSN 00368075. `DOI:10.1126/science.1134404`. (Cited on pages 32 and 73.)

[153] P. Howell. *Applied Solid Mechanics*. Cambridge University Press, 2008. ISBN 9780521854894. (Cited on page 32.)

[154] Sanjay Kumar, Iva Z. Maxwell, Alexander Heisterkamp, Thomas R. Polte, Tanmay P. Lele, Matthew Salanga, Eric Mazur, and Donald E. Ingber. Viscoelastic retraction of single living stress fibers and its impact on cell shape, cytoskeletal organization, and extracellular matrix mechanics. *Biophysical Journal*, 90(10):3762–3773, 2006. ISSN 00063495. `DOI:10.1529/biophysj.105.071506`. (Cited on pages 32, 33, and 88.)

[155] Céline Labouesse, Chiara Gabella, Jean Jacques Meister, Benoît Vianay, and Alexander B. Verkhovsky. Microsurgery-aided in-situ force probing reveals extensibility and viscoelastic properties of individual stress fibers. *Scientific Reports*, 6, mar 2016. ISSN 20452322. `DOI:10.1038/srep23722`. (Cited on pages 33 and 88.)

[156] Elena Kassianidou and Sanjay Kumar. A biomechanical perspective on stress fiber structure and function, 2015. ISSN 18792596. (Cited on pages 33 and 88.)

[157] Elena Kassianidou, Christoph A. Brand, Ulrich S. Schwarz, and Sanjay Kumar. Geometry and network connectivity govern the mechanics of stress fibers. *Proceedings of the National Academy of Sciences of the United States of America*, 114(10):2622–2627, mar 2017. ISSN 10916490. `DOI:10.1073/pnas.1606649114`. (Cited on pages 33 and 88.)

[158] Julien Colombelli, Achim Besser, Holgar Kress, Emmanuel G. Reynaud, Philippe Girard, Emmanuel Caussinus, Uta Haselmann, John V. Small, Ulrich S. Schwarz, and Ernst H.K. Stelzer. Erratum: Mechanosensing in actin stress fibers revealed by a close correlation between force and protein localization (Journal of Cell Science vol. 122 (1665-1679)). *Journal of Cell Science*, 122(11):1928, 2009. ISSN 00219533. `DOI:10.1242/jcs.054577`. (Cited on page 33.)

[159] Kandice Tanner, Aaron Boudreau, Mina J. Bissell, and Sanjay Kumar. Dissecting regional variations in stress fiber mechanics in living cells with laser nanosurgery. *Biophysical Journal*, 99(9):2775–2783, 2010. ISSN 15420086. `DOI:10.1016/j.bpj.2010.08.071`. (Cited on pages 33 and 88.)

[160] Timothée Vignaud, Calina Copos, Christophe Leterrier, Qingzong Tseng, Laurent Blanchoin, Alex Mogilner, Manuel Théry, and Laetitia Kurzawa. Stress fibers are embedded in a contractile cortical network. *bioRxiv*, page 2020.02.11.944579, 2020. `DOI:10.1101/2020.02.11.944579`. (Cited on page 33.)

[161] Benedikt Sabass, Margaret L. Gardel, Clare M. Waterman, and Ulrich S. Schwarz. High resolution traction force microscopy based on experimental and computational advances. *Biophysical Journal*, 94(1):207–220, 2008. ISSN 00063495. `DOI:10.1529/biophysj.107.113670`. (Cited on page 33.)

[162] L. Ts Adzhemyan, Yu A. Eroshkin, A. K. Shchekin, and I. A. Babintsev. Improved kinetic description of fast relaxation of cylindrical micelles. *Physica A: Statistical Mechanics and its Applications*, 518:299–311, 2019. ISSN 03784371. `DOI:10.1016/j.physa.2018.11.057`. (Cited on page 35.)

[163] Adam Zlotnick. To Build a Virus Capsid: An Equilibrium Model of the Self Assembly of Polyhedral Protein Complexes. *Journal of Molecular Biology*, 241(1):59–67, aug 1994. ISSN 0022-2836. `DOI:10.1006/JMBI.1994.1473`. (Cited on pages 35 and 54.)

[164] O. Penrose. The Becker-Döring equations at large times and their connection with the LSW theory of coarsening. *Journal of Statistical Physics*, 89(1-2):305–320, 1997. ISSN 00224715. `DOI:10.1007/BF02770767`. (Cited on page 35.)

[165] Adam Zlotnick, Jennifer M. Johnson, Paul W. Wingfield, Stephen J. Stahl, and Dan Endres. A theoretical model successfully identifies features of hepatitis B virus capsid assembly. *Biochemistry*, 38(44):14644–14652, 1999. ISSN 00062960. `DOI:10.1021/bi991611a`. (Cited on pages 35 and 51.)

[166] Joanna Masel, Vincent A.A. Jansen, and Martin A. Nowak. Quantifying the kinetic parameters of prion replication. *Biophysical Chemistry*, 77(2-3):139–152, 1999. ISSN 03014622. `DOI:10.1016/S0301-4622(99)00016-2`. (Cited on page 35.)

[167] J. Carr, D. B. Duncan, and C. H. Walshaw. Numerical approximation of a metastable system. *IMA Journal of Numerical Analysis*, 15(4):505–521, 1995. ISSN 02724979. `DOI:10.1093/imanum/15.4.505`. (Cited on pages 35 and 50.)

[168] Dugald B. Duncan and Rachel M. Dunwell. Metastability in the classical, truncated Becker-Döring equations. *Proceedings of the Edinburgh Mathematical Society*, 45(3):701–716, 2002. ISSN 00130915. `DOI:10.1017/S0013091500000882`. (Cited on pages 35 and 50.)

[169] John S. Schreck and Jian Min Yuan. A kinetic study of amyloid formation: Fibril growth and length distributions. *Journal of Physical Chemistry B*, 117(21):6574–6583, 2013. ISSN 15205207. `DOI:10.1021/jp401586p`. (Cited on page 35.)

[170] Claudio Soto. Unfolding the role of protein misfolding in neurodegenerative diseases. *Nature Reviews Neuroscience*, 4(1):49–60, 2003. ISSN 14710048. `DOI:10.1038/nrn1007`. (Cited on page 35.)

[171] Jacob N. Israelachvili. *Intermolecular and surface forces / Jacob N. Israelachvili.* Academic Press London ; San Diego, 2nd ed. edition, 1991. ISBN 0123751810. (Cited on pages 36 and 69.)

[172] Wen Chyuan Yueh. Eigenvalues of several tridiagonal matrices. *Applied Mathematics E - Notes*, 5:66–74, 2005. ISSN 16072510. (Cited on page 44.)

[173] Vincent Ssemaganda and Gerald Wamecke. Existence of metastable solutions for a thermodynamically consistent Becker-Döring model. *Journal of Applied Analysis*, 19(1):91–124, 2013. ISSN 14256908. `DOI:10.1515/jaa-2013-0009`. (Cited on page 50.)

[174] P. Debye. Molecular-weight determination by light scattering. *Journal of Physical and Colloid Chemistry*, 51(1):18–32, 1947. ISSN 00223654. `DOI:10.1021/j150451a002`. (Cited on page 51.)

[175] Justin Grewe and Ulrich S. Schwarz. Mechanosensitive self-assembly of myosin ii minifilaments. *Phys. Rev. E*, 101:022402, Feb 2020. `DOI:10.1103/PhysRevE.101.022402`. (Cited on pages 53 and 130.)

[176] J. Howard. *Mechanics of Motor Proteins and the Cytoskeleton*. Sinauer Associates, Publishers, 2001. ISBN 9780878933341. (Cited on page 53.)

[177] Tianzhi Luo, Krithika Mohan, Pablo A. Iglesias, and Douglas N. Robinson. Molecular mechanisms of cellular mechanosensing. *Nature Materials*, 12(11):1064–1071, nov 2013. ISSN 1476-1122. `DOI:10.1038/nmat3772`. (Cited on page 54.)

[178] R K Mahajan and J D Pardee. Assembly mechanism of Dictyostelium myosin II: regulation by K+, Mg2+, and actin filaments. *Biochemistry*, 35(48):15504–15514, 1996. ISSN 0006-2960. `DOI:10.1021/bi9618981`. (Cited on page 54.)

[179] Yixin Ren, Janet C. Effler, Melanie Norstrom, Tianzhi Luo, Richard a. Firtel, Pablo a. Iglesias, Ronald S. Rock, and Douglas N. Robinson. Mechanosensing through Cooperative Interactions between Myosin II and the Actin Crosslinker Cortexillin I. *Current Biology*, 19 (17):1421–1428, 2009. ISSN 09609822. `DOI:10.1016/j.cub.2009.07.018`. (Cited on page 54.)

[180] Tianzhi Luo and Douglas N Robinson. Kinetic Monte Carlo simulations of the assembly of filamentous biomacromolecules by dimer addition mechanism. *RSC advances*, 5(6):3922–3929, 2015. ISSN 2046-2069. `DOI:10.1039/c4ra09189b`. (Cited on page 54.)

[181] D. C. Rapaport. Self-assembly of polyhedral shells: A molecular dynamics study. *Physical Review E*, 70(5):051905, nov 2004. ISSN 1539-3755. `DOI:10.1103/PhysRevE.70.051905`. (Cited on page 54.)

[182] Blake Sweeney, Tiequan Zhang, and Russell Schwartz. Exploring the parameter space of complex self-assembly through virus capsid models. *Biophysical journal*, 94(3):772–783, 2008. ISSN 00063495. `DOI:10.1529/biophysj.107.107284`. (Cited on page 54.)

[183] Marvin A. Boettcher, Heinrich C.R. Klein, and Ulrich S. Schwarz. Role of dynamic capsomere supply for viral capsid self-assembly. *Physical Biology*, 12(1):16014, 2015. ISSN 14783975. `DOI:10.1088/1478-3975/12/1/016014`. (Cited on page 55.)

[184] M W Chew and J M Squire. Packing of alpha-helical coiled-coil myosin rods in vertebrate muscle thick filaments. *Journal of structural biology*, 115(3):233–249, 1995. ISSN 10478477. `DOI:10.1006/jsbi.1995.1048`. (Cited on page 55.)

[185] Hind A Al-Khayat, Robert W Kensler, John M Squire, Steven B Marston, and Edward P Morris. Atomic model of the human cardiac muscle myosin filament. *Proceedings of the National Academy of Sciences of the United States of America*, 110(1):318–23, 2013. ISSN 1091-6490. `DOI:10.1073/pnas.1212708110`. (Cited on page 55.)

[186] John M Squire. Muscle myosin filaments: cores, crowns and couplings. *Biophysical reviews*, 1(3):149, sep 2009. ISSN 1867-2450. `DOI:10.1007/s12551-009-0017-4`. (Cited on page 55.)

[187] Hind A AL-Khayat, Robert W Kensler, Edward P Morris, and John M Squire. Three-dimensional structure of the M-region (bare zone) of vertebrate striated muscle myosin filaments by single-particle analysis. *Journal of Molecular Biology*, 403(5):763–776, 2010. ISSN 00222836. `DOI:10.1016/j.jmb.2010.09.025`. (Cited on page 55.)

[188] Jordan R. Beach, Kyle S. Bruun, Lin Shao, Dong Li, Zac Swider, Kirsten Remmert, Yingfan Zhang, Mary A. Conti, Robert S. Adelstein, Nasser M. Rusan, Eric Betzig, and John A. Hammer. Actin dynamics and competition for myosin monomer govern the sequential amplification of myosin filaments. *Nature Cell Biology*, 19(2):85–93, February 2017. ISSN 1465-7392. `DOI:10.1038/ncb3463`. (Cited on page 58.)

[189] Daniel T. Gillespie. A general method for numerically simulating the stochastic time evolution of coupled chemical reactions. *Journal of Computational Physics*, 22(4):403–434, dec 1976. ISSN 00219991. `DOI:10.1016/0021-9991(76)90041-3`. (Cited on pages 58 and 113.)

[190] M. J. Tyska, D. E. Dupuis, W. H. Guilford, J. B. Patlak, G. S. Waller, K. M. Trybus, D. M. Warshaw, and S. Lowey. Two heads of myosin are better than one for generating force and motion. *Proceedings of the National Academy of Sciences of the United States of America*, 96 (8):4402–4407, 1999. ISSN 00278424. `DOI:10.1073/pnas.96.8.4402`. (Cited on page 61.)

[191] Neil M Kad, Arthur S Rovner, Patricia M Fagnant, Peteranne B Joel, Guy G Kennedy, Joseph B Patlak, David M Warshaw, and Kathleen M Trybus. A mutant heterodimeric myosin with one inactive head generates maximal displacement. *Journal of Cell Biology*, 162 (3):481–488, aug 2003. ISSN 00219525. `DOI:10.1083/jcb.200304023`. (Cited on page 61.)

[192] Motoshi Kaya and Hideo Higuchi. Nonlinear elasticity and an 8-nm working stroke of single myosin molecules in myofilaments. *Science (New York, N.Y.)*, 329(5992):686–9, aug 2010. ISSN 1095-9203. `DOI:10.1126/science.1191484`. (Cited on page 61.)

[193] Mihály Kovács, Judit Tóth, Csaba Hetényi, András Málnási-Csizmadia, and James R. Seller. Mechanism of blebbistatin inhibition of myosin II. *Journal of Biological Chemistry*, 279(34): 35557–35563, 2004. ISSN 00219258. `DOI:10.1074/jbc.M405319200`. (Cited on pages 68, 70, 109, and 110.)

[194] D. Applegate and J. D. Pardee. Actin-facilitated assembly of smooth muscle myosin induces formation of actomyosin fibrils. *Journal of Cell Biology*, 117(6):1223–1230, 1992. ISSN 00219525. `DOI:10.1083/jcb.117.6.1223`. (Cited on page 70.)

[195] Murray J Tipping, Nicolas J Delalez, Ren Lim, Richard M Berry, and Judith P Armitage. Load-dependent assembly of the bacterial flagellar motor. *mBio*, 4(4):e00551–13, aug 2013. ISSN 21612129. `DOI:10.1128/mBio.00551-13`. (Cited on page 70.)

[196] Navish Wadhwa, Rob Phillips, and Howard C. Berg. Torque-dependent remodeling of the bacterial flagellar motor. *Proceedings of the National Academy of Sciences*, 116(24):11764–11769, June 2019. ISSN 0027-8424, 1091-6490. `DOI:10.1073/pnas.1904577116`. (Cited on page 71.)

[197] Ulrich S. Grewe, Justinand Schwarz. Rheology of mixed motor ensembles. *In preparation*, 2020. (Cited on page 73.)

[198] Ben Fabry, Geoffrey N. Maksym, James P. Butler, Michael Glogauer, Daniel Navajas, and Jeffrey J. Fredberg. Scaling the Microrheology of Living Cells. *Physical Review Letters*, 87 (14):148102, sep 2001. ISSN 0031-9007. `DOI:10.1103/PhysRevLett.87.148102`. (Cited on page 73.)

[199] Alexandre Micoulet, Joachim P. Spatz, and Albrecht Ott. Mechanical response analysis and power generation by single-cell stretching. *ChemPhysChem*, 6(4):663–670, 2005. ISSN 14394235. `DOI:10.1002/cphc.200400417`. (Cited on page 73.)

[200] Mirjam Mayer, Martin Depken, Justin S. Bois, Frank Jülicher, and Stephan W. Grill. Anisotropies in cortical tension reveal the physical basis of polarizing cortical flows. *Nature*, 467(7315):617–621, 2010. ISSN 00280836. `DOI:10.1038/nature09376`. (Cited on page 73.)

[201] Xavier Serra-Picamal, Vito Conte, Romaric Vincent, Ester Anon, Dhananjay T. Tambe, Elsa Bazellieres, James P. Butler, Jeffrey J. Fredberg, and Xavier Trepat. Mechanical waves during tissue expansion. *Nature Physics*, 8(8):628–634, 2012. ISSN 17452481. `DOI:10.1038/nphys2355`. (Cited on page 73.)

[202] Romaric Vincent, Elsa Bazellières, Carlos Pérez-González, Marina Uroz, Xavier Serra-Picamal, and Xavier Trepat. Active Tensile Modulus of an Epithelial Monolayer. *Physical Review Letters*, 115(24):1–5, 2015. ISSN 10797114. `DOI:10.1103/PhysRevLett.115.248103`. (Cited on page 73.)

[203] Arnab Saha, Masatoshi Nishikawa, Martin Behrndt, Carl Philipp Heisenberg, Frank Jülicher, and Stephan W. Grill. Determining Physical Properties of the Cell Cortex. *Biophysical Journal*, 110(6):1421–1429, 2016. ISSN 15420086. `DOI:10.1016/j.bpj.2016.02.013`. (Cited on page 73.)

[204] Medhavi Vishwakarma, Jacopo Di Russo, Dimitri Probst, Ulrich S. Schwarz, Tamal Das, and Joachim P. Spatz. Mechanical interactions among followers determine the emergence of leaders in migrating epithelial cell collectives. *Nature Communications*, 9(1), 2018. ISSN 20411723. `DOI:10.1038/s41467-018-05927-6`. (Cited on page 73.)

[205] Tom P.J. Wyatt, Jonathan Fouchard, Ana Lisica, Nargess Khalilgharibi, Buzz Baum, Pierre Recho, Alexandre J. Kabla, and Guillaume T. Charras. Actomyosin controls planarity and folding of epithelia in response to compression. *Nature Materials*, 19(1):109–117, 2020. ISSN 14764660. `DOI:10.1038/s41563-019-0461-x`. (Cited on page 73.)

[206] C. P. Broedersz and F. C. MacKintosh. Modeling semiflexible polymer networks. *Reviews of Modern Physics*, 86(3):995–1036, jul 2014. ISSN 0034-6861. `DOI:10.1103/RevModPhys.86.995`. (Cited on page 73.)

[207] Pauli Virtanen, Ralf Gommers, Travis E. Oliphant, Matt Haberland, Tyler Reddy, David Cournapeau, Evgeni Burovski, Pearu Peterson, Warren Weckesser, Jonathan Bright, Stéfan J. van der Walt, Matthew Brett, Joshua Wilson, K. Jarrod Millman, Nikolay Mayorov, Andrew R. J. Nelson, Eric Jones, Robert Kern, Eric Larson, CJ Carey, İlhan Polat, Yu Feng, Eric W. Moore, Jake Vand erPlas, Denis Laxalde, Josef Perktold, Robert Cimrman, Ian Henriksen, E. A. Quintero, Charles R Harris, Anne M. Archibald, Antônio H. Ribeiro, Fabian Pedregosa, Paul van Mulbregt, and SciPy 1. 0 Contributors. SciPy 1.0: Fundamental Algorithms for Scientific Computing in Python. *Nature Methods*, 2020. `DOI:https://doi.org/10.1038/s41592-019-0686-2`. (Cited on page 82.)

[208] A.C. Pipkin. *Lectures on viscoelasticity theory*. Number Bd. 7,Teil 1 in Applied mathematical sciences. Springer-Verlag, 1986. ISBN 9783540963455. (Cited on page 84.)

[209] Randy H. Ewoldt, A. E. Hosoi, and Gareth H. McKinley. New measures for characterizing nonlinear viscoelasticity in large amplitude oscillatory shear. *Journal of Rheology*, 52(6): 1427–1458, 2008. ISSN 0148-6055. `DOI:10.1122/1.2970095`. (Cited on page 84.)

[210] Stacey Lee, Elena Kassianidou, and Sanjay Kumar. Actomyosin stress fiber subtypes have unique viscoelastic properties and roles in tension generation. *Molecular Biology of the Cell*, 29(16):1992–2004, aug 2018. ISSN 1059-1524. `DOI:10.1091/mbc.E18-02-0106`. (Cited on page 88.)

[211] Ching Wei Chang and Sanjay Kumar. Differential Contributions of Nonmuscle Myosin II Isoforms and Functional Domains to Stress Fiber Mechanics. *Scientific Reports*, 5(August): 1–13, 2015. ISSN 20452322. `DOI:10.1038/srep13736`. (Cited on page 88.)

[212] Kangji Wang, Carsten Wloka, and Erfei Bi. Non-muscle Myosin-II Is Required for the Generation of a Constriction Site for Subsequent Abscission. *iScience*, 13:69–81, 2019. ISSN 25890042. `DOI:10.1016/j.isci.2019.02.010`. (Cited on page 88.)

[213] Kei Yamamoto, Kohei Otomo, Tomomi Nemoto, Seiichiro Ishihara, Hisashi Haga, Akira Nagasaki, Yota Murakami, and Masayuki Takahashi. Differential contributions of nonmuscle myosin IIA and IIB to cytokinesis in human immortalized fibroblasts. *Experimental Cell Research*, 376(1):67–76, mar 2019. ISSN 10902422. `DOI:10.1016/j.yexcr.2019.01.020`. (Cited on page 88.)

[214] Roy Bar-Ziv, Tsvi Tlusty, Elisha Moses, Samuel A. Safran, and Alexander Bershadsky. Pearling in cells: A clue to understanding cell shape. *Proceedings of the National Academy of Sciences of the United States of America*, 96(18):10140–10145, 1999. ISSN 00278424. `DOI:10.1073/pnas.96.18.10140`. (Cited on pages 89, 90, 100, and 105.)

[215] P. Guthardt Torres, I. B. Bischofs, and U. S. Schwarz. Contractile network models for adherent cells. *Physical Review E - Statistical, Nonlinear, and Soft Matter Physics*, 85(1):1–13, 2012. ISSN 15393755. `DOI:10.1103/PhysRevE.85.011913`. (Cited on pages 89 and 90.)

[216] Philipp J. Albert and Ulrich S. Schwarz. Dynamics of cell shape and forces on micropatterned substrates predicted by a cellular Potts model. *Biophysical Journal*, 106(11):2340–2352, 2014. ISSN 15420086. `DOI:10.1016/j.bpj.2014.04.036`. (Cited on page 89.)

[217] Lev Davidovich Landau, Evgeny M Lifshitz, JB Sykes, WH Reid, and Ellis H Dill. Theory of elasticity. *PhT*, 13(7):44, 1960. (Cited on page 89.)

[218] Gerhard Gompper and Michael Schick. *Soft Matter, Volume 4: Lipid Bilayers and Red Blood Cells*, volume 4. Wiley-VCH, 2006. (Cited on page 89.)

[219] Wim Pomp, Koen Schakenraad, Hayri E. Balcloğlu, Hedde Van Hoorn, Erik H.J. Danen, Roeland M.H. Merks, Thomas Schmidt, and Luca Giomi. Cytoskeletal Anisotropy Controls Geometry and Forces of Adherent Cells. *Physical Review Letters*, 121(17):1–5, 2018. ISSN 10797114. `DOI:10.1103/PhysRevLett.121.178101`. (Cited on pages 89 and 100.)

[220] Luca Giomi. Contour Models of Cellular Adhesion. *Advances in Experimental Medicine and Biology*, 1146:13–29, 2019. ISSN 22148019. `DOI:10.1007/978-3-030-17593-1_2`. (Cited on pages 89 and 100.)

[221] Todd Thoresen, Martin Lenz, and Margaret L Gardel. Thick Filament Length and Isoform Composition Determine Self-Organized Contractile Units in Actomyosin Bundles. *Biophysj*, 104(3):655–665, 2013. ISSN 0006-3495. `DOI:10.1016/j.bpj.2012.12.042`. (Cited on pages 90 and 105.)

[222] Nicole Endlich, Carol A. Otey, Wilhelm Kriz, and Karlhans Endlich. Movement of stress fibers away from focal adhesions identifies focal adhesions as sites of stress fiber assembly in stationary cells. *Cell Motility and the Cytoskeleton*, 64(12):966–976, 2007. ISSN 08861544. `DOI:10.1002/cm.20237`. (Cited on pages 90, 99, 105, and 116.)

[223] Robert J. Russell, Alexandria Y. Grubbs, Sunil P. Mangroo, Sandra E. Nakasone, Richard B. Dickinson, and Tanmay P. Lele. Sarcomere length fluctuations and flow in capillary endothelial cells. *Cytoskeleton*, 68(3):150–156, 2011. ISSN 19493584. `DOI:10.1002/cm.20501`. (Cited on pages 90, 99, 105, and 116.)

[224] Sari Tojkander, Gergana Gateva, Amjad Husain, Ramaswamy Krishnan, and Pekka Lappalainen. Generation of contractile actomyosin bundles depends on mechanosensitive actin filament assembly and disassembly. *eLife*, 4:1–28, 2015. ISSN 2050-084X. `DOI:10.7554/elife.06126`. (Cited on pages 90 and 105.)

[225] Kai Weißenbruch, Justin Grewe, Kathrin Stricker, Laurent Baulesch, Ulrich S. Schwarz, and Martin Bastmeyer. Distinct roles of non-muscle myosin II isoforms A and B for establishing cell morphology: dynamic generation of tension versus elastic stability. *In preparation*, 2020. (Cited on pages 101, 104, 107, and 112.)

[226] Kai Weißenbruch. *Adaption der Zellmorphologie durch Aktomyosin-Kontraktilität auf mikrostrukturierten Zellkultursubstraten.* PhD thesis, Karlsruhe Institut für Technologie, Germany, 2019. (Cited on page 101.)

[227] Fei Wang, Mihály Kovács, Aihua Hu, John Limouze, Estelle V. Harvey, and James R. Sellers. Kinetic mechanism of non-muscle myosin IIB. Functional adaptations for tension generation and maintenance. *Journal of Biological Chemistry*, 278(30):27439–27448, 2003. ISSN 00219258. `DOI:10.1074/jbc.M302510200`. (Cited on pages 101 and 116.)

[228] Mihály Kovács, Fei Wang, Aihua Hu, Yue Zhang, and James R. Sellers. Functional divergence of human cytoplasmic myosin II. Kinetic characterization of the non-muscle IIA isoform. *Journal of Biological Chemistry*, 278(40):38132–38140, 2003. ISSN 00219258. `DOI:10.1074/jbc.M305453200`. (Cited on pages 101 and 116.)

[229] Maria S. Shutova, Waldo A. Spessott, Claudio G. Giraudo, and Tatyana Svitkina. Endogenous species of mammalian nonmuscle myosin IIA and IIB include activated monomers and heteropolymers. *Current Biology*, 24(17):1958–1968, 2014. ISSN 09609822. `DOI:10.1016/j.cub.2014.07.070`. (Cited on page 101.)

[230] Sami Alom Ruiz and Christopher S. Chen. Microcontact printing: A tool to pattern. *Soft Matter*, 3(2):168–177, 2007. ISSN 1744683X. `DOI:10.1039/b613349e`. (Cited on page 101.)

[231] Manuel Théry, Victor Racine, Matthieu Piel, Anne Pépin, Ariane Dimitrov, Yong Chen, Jean Baptiste Sibarita, and Michel Bornens. Anisotropy of cell adhesive microenvironment governs cell internal organization and orientation of polarity. *Proceedings of the National Academy of Sciences of the United States of America*, 103(52):19771–19776, 2006. ISSN 00278424. `DOI:10.1073/pnas.0609267103`. (Cited on page 101.)

[232] Jennifer A. Doudna and Emmanuelle Charpentier. The new frontier of genome engineering with CRISPR-Cas9. *Science*, 346(6213), 2014. ISSN 10959203. `DOI:10.1126/science.1258096`. (Cited on page 102.)

[233] Boglárka H. Várkuti, Miklós Képiró, István Ádám Horváth, László Végner, Szilvia Ráti, Áron Zsigmond, György Hegyi, Zsolt Lenkei, Máté Varga, and András Málnási-Csizmadia. A highly soluble, non-phototoxic, non-fluorescent blebbistatin derivative. *Scientific Reports*, 6(April 2015):2–11, 2016. ISSN 20452322. `DOI:10.1038/srep26141`. (Cited on pages 109 and 116.)

[234] J. A. Peacock. Two-dimensional goodness-of-fit testing in astronomy. *Monthly Notices of the Royal Astronomical Society*, 202(3):615–627, 1983. ISSN 0035-8711. `DOI:10.1093/mnras/202.3.615`. (Cited on pages 110 and 128.)

[235] G. Fasano and A. Franceschini. A multidimensional version of the Kolmogorov–Smirnov test. *Monthly Notices of the Royal Astronomical Society*, 225(1):155–170, 1987. ISSN 0035-8711. `DOI:10.1093/mnras/225.1.155`. (Cited on pages 110 and 128.)

[236] Mohammad A. Rahman, Marko Ušaj, Dilson E. Rassier, and Alf Månsson. Blebbistatin Effects Expose Hidden Secrets in the Force-Generating Cycle of Actin and Myosin. *Biophysical Journal*, 115(2):386–397, jul 2018. ISSN 15420086. `DOI:10.1016/j.bpj.2018.05.037`. (Cited on pages 110, 112, and 130.)

[237] Tom Kaufmann and Ulrich S Schwarz. Electrostatic and bending energies predict staggering and splaying in nonmuscle myosin II minifilaments Author summary. *bioRxiv*, 2020. `DOI:10.1101/2020.03.20.000265`. (Cited on page 110.)

[238] Stuart Berg, Dominik Kutra, Thorben Kroeger, Christoph N. Straehle, Bernhard X. Kausler, Carsten Haubold, Martin Schiegg, Janez Ales, Thorsten Beier, Markus Rudy, Kemal Eren, Jaime I. Cervantes, Buote Xu, Fynn Beuttenmueller, Adrian Wolny, Chong Zhang, Ullrich Koethe, Fred A. Hamprecht, and Anna Kreshuk. ilastik: interactive machine learning for (bio)image analysis. *Nature Methods*, September 2019. ISSN 1548-7105. `DOI:10.1038/s41592-019-0582-9`. (Cited on page 128.)

[239] G. Bradski. The OpenCV Library. *Dr. Dobb's Journal of Software Tools*, 2000. (Cited on page 128.)

[240] Ethan Rublee, Vincent Rabaud, Kurt Konolige, and Gary Bradski. ORB: An efficient alternative to SIFT or SURF. *Proceedings of the IEEE International Conference on Computer Vision*, pages 2564–2571, 2011. `DOI:10.1109/ICCV.2011.6126544`. (Cited on page 128.)

[241] Marcel Weiß. Modelling the Interaction of Small Myosin II Ensembles with Their Physical Environment . Master's thesis, Ruprecht-Karls-Universität Heidelberg, Germany, 2016. (Cited on page 128.)

List of Publications

The following table lists the manuscripts which have been prepared during the course of this thesis.

1	Justin Grewe, Ulrich S. Schwarz **Mechanosensitive self-assembly of myosin II minifilaments** *Physical Review E* (2020): vol. 101, p. 022402	Chapter 4
2	Justin Grewe, Ulrich S. Schwarz **Rheology of mixed motor ensembles** *In preparation, 2020*	Chapter 5
3	Kai Weißenbruch, Justin Grewe, Ulrich S. Schwarz, Martin Bastmeyer **Distinct roles of non-muscle myosin II isoforms A and B for establishing cell morphology: dynamic generation of tension versus elastic stability** *In preparation, 2020*	Chapter 6 & 7

Danksagung

Bei meinem Betreuer Ulrich Schwarz bedanke ich mich ganz herzlich für seine wissenschaftliche Unterstüzung und Betreuung. Es war mir immer eine große Freude zusammen mit ihm in Diskussionen Ideen weiterzuentwickeln. Gleichzeitig konnte ich viel von ihm über Biophysik und wissenschaftliche Kommunikation lernen. Außerdem bedanke ich mich bei ihm, dass er alljährlich sicherstellt, dass die Arbeitsgruppe die Frühjahrsverhandlungen der DPG gemeinsam besuchen kann – sofern sie denn in natura stattfindet. Auch unsere erstaunlich erfolgreichen Jongliersessions zu unterschiedlichen Gelegenheiten werden mir mit Sicherheit lange in guter Erinnerung bleiben.

Rasmus Schröder danke ich für das Interesse an meiner Arbeit und die Bereitschaft sie als Zweitgutachter zu bewerten.

Ohne die biologischen Experimente von Kai Weißenbruch aus der Gruppe von Martin Bastmeyer in Karlsruhe hätte diese Arbeit deutlich weniger experimentellen Rückhalt. Bei Ihnen zwei bedanke ich mich für die gute Zusammenarbeit, sowie die Möglichkeit die Gruppe einige Wochen zu besuchen.

Ein großer Dank gilt der gesamten AG Schwarz vom Philosophenweg sowie vom Bioquant für das angenehme und freundschaftliche Miteinander. Bei Felix Frey bedanke ich mich für den häufigen Austausch und viele gut gemeinte Worte und Ratschläge. Bei meinen Bürokollegen Falko Ziebert, Dennis Wörthmüller, Felix Frey, Dimitri Probst und Robert Chojowski bedanke ich mich für die zahlreichen Kaffeepausen, in denen wir manch eine Idee entwickelt haben. Ein großer Dank gilt auch Julia Jäger und Nikolas Schnellbächer für die Organisation einiger gemeinsamer Konferenzreisen.

Den ehemaligen Bachelor der AG Schwarz Liam Russe, Susanna Fuhrmann, Stefan Maurer und Marina Savarino danke ich für die erfolgreiche Zusammenarbeit. Bei Tom Kaufmann bedanke ich mich für die zahlreichen myosinspezifischen, sowie fachfremden Diskussionen: wir waren in der Tat die Myosin Boys.

Für das sorgfältige Korrekturlesen meiner Arbeit möchte ich mich bei Dennis Wörthmüller, Felix Frey und Ines Schlotböller bedanken. Ganz besonders möchte ich mich bei meinen Eltern bedanken, ihr habt mich immer bedingungslos unterstützt! Von ganzem Herzen bedanke ich mich bei Ines Schlotböller für ihre aufmunternden Worte, ihre Geduld und ihr Vertrauen in mich.

Zu guter Letzt danke ich dem Structures Exzellenzcluster und der Landesgraduiertenförderung Baden-Württemberg für ihre finanzielle Unterstützung.